

DISSERTATION

Low Mass Dimuon Production in Proton-Nucleus Collisions at 400 GeV at the CERN-SPS

ausgeführt zum Zwecke der Erlangung des akademischen Grades eines Doktors der technischen Wissenschaften unter der Leitung von

Univ. Prof. Dr. DI Christian Fabjan

E141

Atominstitut der Österreichischen Universitäten

eingereicht an der Technischen Universität Wien
Fakultät für Physik

von

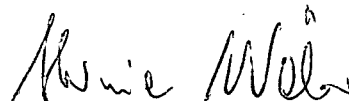
DI Hermine K. Wöhri

Matr. Nr. 9330330

CH-1217 Meyrin, Rue Virginio-Malnati 30

e-Mail: hermine.woehri@cern.ch

Wien, am 17. September 2004



Unser größter Feind ist die Langeweile.
Voltaire

Kurzfassung

Während der Juni 2002 Datennahme sammelte das NA60 Experiment 600 000 Dimuonen Trigger in inelastischen Proton-Kern Wechselwirkungen bei einer Strahlenergie von 400 GeV. Das verwendete Targetsystem bestand aus Beryllium, Indium und Plei Targets, jeweils mit ungefähr gleicher nuklearer Interaktionslänge, welche dem Strahl gleichzeitig ausgesetzt waren. Diese spezielle Anordnung erlaubte es, die nukleare Abhängigkeit des Wirkungsquerschnittes für die ω und ϕ Resonanzen zu bestimmen. Des Weiteren wurden die elementaren pp Wirkungsquerschnitte für die ρ , ω und ϕ Mesonen bei 400 GeV ermittelt. In der vorliegenden Doktorarbeit wird gezeigt, dass das Dimuon Massenspektrum durch bereits bekannte Quellen beschrieben werden kann. Mithilfe des η -Dalitz Zerfalls, welche das Dimuon Massenspektrum im Bereich 0.2–0.45 GeV dominiert, wurde versucht, auch den Wirkungsquerschnitt des η Mesons und dessen Abhängigkeit von der Massenzahl zu determinieren. Die erhaltenen Resultate werden im Rahmen bereits vorhandener Messungen von NA27, HELIOS-1 and CERES-TAPS diskutiert, welche meist durch Beobachtungen in anderen Zerfallskanälen erhalten wurden.

Die hierfür verwendeten Daten wurden mit dem neu gebauten Silizium Streifen-teleskop aufgenommen, dessen Prototyping, Testen, Montage und Betrieb auch Teil dieser Doktorarbeit war. Des Weiteren wird die Rohdatenanalyse dieses analog ausgelesenen Detektors präsentiert, gemeinsam mit dem Verhalten des Detektors während der Datennahme.

Schlüsselworte

Dimuonen Produktion; Fixed-target, 400 GeV; Elementare pp Wechselwirkungsquerschnitte der η , ρ , ω und ϕ Mesonen und deren nukleare Abhängigkeit;

Abstract

During the June 2002 run the fixed-target experiment NA60 collected around 600 000 dimuon triggers in proton-nucleus collisions at 400 GeV. The target system consisted of Beryllium, Indium and Lead targets, of roughly the same interaction length, simultaneously exposed to the beam. This specific setup allowed to study the nuclear dependence of the production cross-section of the ω and ϕ resonances. The elementary pp production cross-sections at 400 GeV for the ρ , ω and ϕ mesons are also presented. This thesis presents a general understanding of the collected dimuon mass spectra in terms of known sources. By using the η -Dalitz decay, dominating the 0.2–0.45 GeV mass range, an attempt was made to, furthermore, extract the η production cross-section and its nuclear dependence. The results are discussed in the framework of previous measurements, mostly obtained in different decay channels, performed by NA27, HELIOS-1 and CERES-TAPS.

These data were collected with the newly designed Silicon micro-strip tracking telescope of NA60, whose prototyping, testing, assembling and operation was also part of the present thesis. The raw data analysis of this analogue read-out detector is also presented, together with the detector's performance during this period of data taking.

Keywords

Dimuon production; Fixed-target, 400 GeV; Elementary pp production cross-section of η , ρ , ω , ϕ ; Nuclear dependence of light meson production.

Acknowledgements or “A PhD Student’s Diary”

During the past few years I have had the chance to work with many people; with some I collaborated during a limited amount of time, others have accompanied me over the whole lifetime as a PhD student. To *all* of them I want to say a truly “Thank You”, since I experienced a wonderful time. But let me start by addressing a few words to Carlos Lourenço, who supervised me over all these years and consciously guided the various steps during my PhD. I have never ever seen somebody as patient, helpful, constructive and motivating as Carlos. Through his fine sense of communicating with people he manages to always keep an excellent atmosphere within (and also outside) of our Collaboration. The many of you who know Carlos will certainly know what I mean. I can only express my sincere “thanks” to him.

During the very first months within NA60 I performed a simulation on the gas mixture of our Multi-Wire Proportional Chambers, where I could work with R. Veenhof, the author of the famous gas simulation package “Garfield”. I learnt about our chambers from the infinite knowledge and experience of J. Castor and J. Fargeix. In parallel I helped F. Bergsma to make a field map of our vertex magnet, PT7, whose experience I really appreciate. I would also like to thank W. Flegel for his support during this time. H. Brugger, cordially spent a significant time of his spare time at CERN to make an Autocad drawing of the new NA60 target region, including the PT7 magnet and the BeO / Al₂O₃ pre-absorber, which was deeply welcomed in the whole group. C. Theis then used his skills to make a 3D animation of Hannes’ design. Following these months I worked in the Cryo-Lab at CERN, where I met the help of several people, among them J.M. Rieubland and his group, V. Granata and S. Grohmann, who also helped me whenever I needed some practical “hints” or some theoretical understanding. I would like to thank our summer student J. Grognez for his simulations on heat transport through the Aluminium frame holding the microstrip sensors. While building the mechanical support for the microstrip detectors I had the pleasure to work with E. David, L. Kottelat, A. Domeniconi, A. Onnela and A. Placci from TA1. With great precision the team implemented the specific needs required for the support. At the time when we built, tested, assembled and operated the microstrip telescope I worked in a small team consisting of A. Boccardi, J. Buytaert, A. David, C. Lourenço, J. Lozano, besides myself. It was an intense time, full of debugging and I really appreciated the nice atmosphere in this group. S. Roe always had an open ear whenever we needed his help. In order to get the

whole telescope built we had the continuous support of I. McGill and C. Joram from the bonding lab and B. Herskind from the ATLAS-SCTA group, besides several portuguese summer students (R. Fradinho, P. Martins, A. Palha, I. Pereira, A. Silva, M. Silva), who helped us in the overall assembly. It is a special pleasure to thank J. Lozano, with whom I tested the chips, hybrids and sensors for the microstrip telescope, with whom I wrote the raw data analysis routines, with whom I spent sleepless nights in the counting room during the June 2002 data taking, with whom I looked at the raw data and who accompanied me also during the final data analysis as an always cheering-up office mate. I also appreciate the work of L. Figueira who, as a summer student in 2002, worked on a parameterisation of the observed noise pattern of the microstrip sensors. He also tried to convince me that Portuguese is an understandable language. When he went back to Lisbon the blackboard in our office was full with Portuguese and German (Austrian) expressions.

During all these years, but in particular during the (raw) data analysis phase, I had the continuous help of R. Shahoyan, with whom Carlos and me discussed many details of the present analysis. I also would like to express my special thanks to Ruben, since he not only is a person always present when help is needed, but also because of his patience and kindness. I also want to thank K. Banicz, S. Damjanovic, A. David, J. Heuser, M. Keil, H. Ohnishi, P. Sonderegger, H. Specht and R. Veenhof for their help and eagerness to discuss. A. Neves was a willing “teacher” during my first experience with C++. The help, but much more the motivating words of P. Martins, P. Parracho, P. Ramalhete and E. Tveiten, especially during the months of the data analysis period were highly welcome. Last but not least I want to thank L. Kluberg and P. Rosinsky without whom the experiment could not have taken a single dimuon trigger. I also would like to thank all the NA60 Collaborators, since I really appreciate the friendly environment. I apologise to all which I have not mentioned explicitly by their name.

In parallel to my thesis I was working on a review on “Heavy Flavour Production”. It was a pleasure to have collaborated with A. Devismes. The discussions with M. Mangano, A. Morsch, C. Salgado, J. Schuhkraft and P. Weilhammer are highly appreciated.

After this long list I finally want to thank C. Fabjan for being my doctor father over all these years, always supporting the many ideas which were explored during my PhD time. C. Fabjan ensured that I had the wonderful chance of performing my PhD thesis in the exceptional environment of a top level particle physics laboratory and, in particular, in one of the very few high energy physics experiments presently taking data at CERN. I also want to thank the supervisor of my diploma thesis, W. Majerotto, whom I highly esteem.

I want to thank the Austrian government (the Bundesministerium für Bildung, Wissenschaft und Kultur) for having funded most of the present research work. The financial help from the NA60 group through C. Lourenço and E. Radermacher and the effort of J. Seixas to obtain a scholarship from CFIF/IST Portugal to cover the remaining time of this work is highly appreciated.

Contents

Kurzfassung	i
Abstract	iii
Acknowledgements	v
1 Introduction and Physics Motivation	1
2 The NA60 Apparatus	7
2.1 General Overview	7
2.2 The Beam	9
2.3 The Muon Spectrometer and Trigger System	9
2.3.1 The Hadron Absorber	10
2.3.2 The Multi-Wire Proportional Chambers	11
2.3.3 The Trigger Hodoscopes	13
2.3.4 The Toroidal Magnet ACM	14
2.4 The Beam Tracker	16
2.5 The Target System	17
2.6 The PT7 Dipole Magnet	18
2.7 The Vertex Tracking Telescope	20
2.7.1 Overview and Geometry Aspects	20
2.7.2 The Silicon Pixel Telescope	21
2.8 The Interaction Counter	24
2.9 The ZDC and the Quartz Blade Detector	24
3 The NA60 Microstrip Telescope	27
3.1 Silicon Semiconductor Detectors	27
3.1.1 Energy-loss Distribution	29
3.2 The NA60 Microstrip Sensor	30
3.2.1 Sensor Technology	30
3.2.2 Tracking Requirements	31
3.2.3 Strip Segmentation	31
3.3 Read-out	34
3.3.1 Analogue versus Binary Read Out	34
3.3.2 Overview of the Read-out Chain	36

3.3.3	The Hybrid	36
3.3.4	The SCTA128VG Readout Chip	37
3.4	Mechanical Support and Installation	39
3.5	Power Distribution	41
3.6	Cooling Aspects	41
3.7	Assembly Tests Prior to the Data Taking	42
4	Raw Data Analysis of the Microstrip Sensors	45
4.1	Strips Numbering Convention	45
4.2	The Pedestals	46
4.3	The Noise	47
4.4	Common Mode	53
4.5	Strip Masking and Calibration Files	54
4.6	Digitisation	55
4.6.1	Fitting the Four Time Samples	55
4.6.2	Applying Simple Cuts to the Measured Values	57
4.6.3	Applying a Probability Cut	57
4.7	Performance in the June 2002 Run	57
4.7.1	Bias Voltage Scan	57
4.7.2	Strip Efficiency and Signal-To-Noise Ratio	58
4.7.3	Detector Setup, Behaviour and Stability	59
4.7.4	Occupancy Levels	61
4.7.5	Charge Sharing, Clusterisation	67
5	Data Reconstruction and Selection	69
5.1	Setup in the 400 GeV p-A 2002 Run	69
5.2	Data Reconstruction	70
5.2.1	Track Reconstruction	71
5.2.2	Vertex Finding	75
5.2.3	Dimuon Track Matching	80
5.2.4	A Typical Reconstructed Event	80
5.3	Data Selection and Luminosity Evaluation	81
5.3.1	Run and Burst Selection	81
5.3.2	Luminosity Evaluation	88
5.3.3	Selecting Dimuons from the Target Region	89
6	Expected Dimuon Sources	93
6.1	Light Meson Decays	93
6.1.1	The Pseudo-scalar Mesons, η and η'	94
6.1.2	The Light Vector Mesons: ρ , ω and ϕ	96
6.1.3	The Vector Dominance Model	96
6.1.4	Branching Ratios	96
6.1.5	Nuclear Dependence of the Production Cross-Sections	97
6.1.6	Transverse Momentum Distributions	98
6.1.7	Rapidity Distributions	99

6.1.8	Resonance Mass Line Shapes	100
6.1.9	Dimuon Mass Distribution for the Dalitz Decays	103
6.1.10	Distribution of the Decay Angles	104
6.2	Open Charm and Drell–Yan	106
6.2.1	The Drell–Yan process, DY	106
6.2.2	Open Charm	108
6.2.3	Nuclear Effects on the PDFs	110
6.3	The Generated Dimuon Mass Spectrum	111
7	Acceptances, Phase Space Window and Efficiencies	113
7.1	Reconstruction of the Monte Carlo events	113
7.2	Acceptances and the Phase Space Window	114
7.2.1	Dimuon Rapidity and $\cos\theta_{CS}$	114
7.2.2	Single Muon Pseudo-Rapidity, η	116
7.2.3	Dimuon m_{T-y} Correlation	117
7.2.4	Acceptances	118
7.3	Signal Detection Efficiencies	120
7.3.1	VT Track Reconstruction Efficiency	120
7.3.2	Matching Efficiency	122
7.3.3	Vertexing Efficiency	123
7.3.4	Integrated Efficiencies	125
7.4	Final Analysis Event Sample	126
8	Dimuon Analysis, Results and Discussion	133
8.1	Background	133
8.1.1	Introduction	133
8.1.2	Correlations at the Production Level	134
8.1.3	Correlations Induced by the Detector Conditions	136
8.1.4	Impact of the Muon Track Matching	138
8.2	Dimuon Kinematical Distributions	139
8.2.1	Dimuon Mass Resolution	139
8.2.2	Kinematical Distributions: Overview and $\cos\theta_{CS}$	141
8.2.3	ω and ϕ Rapidity Distributions	144
8.2.4	ω and ϕ Transverse Momentum Distributions	143
8.3	Analysis of Low Mass Dimuon Production	147
8.3.1	Nuclear Dependence of ω and ϕ Production	147
8.3.2	Very Low Mass Dimuons	149
8.4	Discussion and Conclusions	151
	Appendices	157
A.)	Dimuon Kinematics	157
B.)	Functional Form of the SCTA Output Signal	158
C.)	Parameterisation of the Strip Efficiencies	158
D.)	p_{T-y} Correlated Acceptances	162

Chapter 1

Introduction and Physics Motivation

The present work was performed within the framework of the NA60 experiment, which is a fixed target experiment at the CERN/SPS accelerator which studies prompt dimuon and open charm production in collisions induced by high energy proton and heavy-ion beams. The current chapter gives a short overview of the physics topics explored within NA60, with emphasis on the topics related to this thesis.

Normal nuclear matter is composed of quarks and gluons bound inside hadrons (mostly protons and neutrons exchanging pions). So far, these most fundamental particles have never been seen isolated, and seem to only exist *confined* inside the hadrons. However, it seems very natural to admit that the quarks and gluons will no longer be confined in individual hadrons if the protons and neutrons are violently compressed in high-energy nuclear collisions, resulting in a very dense and hot system of strongly interacting QCD matter. In such a system, the hadronic degrees of freedom should vanish and the quarks and gluons should behave similarly to the “free” electrons of a metal. These very simple arguments have been turned into robust statements by Lattice QCD calculations [1], which clearly predict that, above a critical temperature or energy density, strongly interacting matter undergoes a phase transition from hadronic matter to a new state, named Quark Gluon Plasma (QGP). In this new state, quarks and gluons are no longer confined into hadrons and chiral symmetry is restored. The search for experimental evidence establishing the existence of this QCD phase transition started at CERN in 1986, at the SPS, where several experiments were performed, with Oxygen, Sulphur and Lead ion beams, of up to 158 GeV per incident nucleon, in the case of Lead ions.

In the year 2000, four experiments started studying Gold-Gold collisions at the RHIC collider, in BNL, at much higher collision energies ($\sqrt{s} = 130$ GeV and $\sqrt{s} = 200$ GeV), and most of the SPS experiments had their last data taking period that year. However, it was also clear that the understanding of some of the most interesting observations made in the SPS heavy-ion program required further work, and this work had to be pursued at the SPS. Therefore, in spite of the severe financial constraints imposed by the construction of the LHC, a new experiment, NA60,

was exceptionally approved in that same year [2]. NA60 is fundamentally different from the previous experiments: rather than being an exploratory project, looking for whatever new phenomena may appear when approaching a new frontier in the energy density of strongly interacting matter, it was explicitly designed to clarify three specific questions raised by the previous experiments, all of them addressing physics topics accessible through the measurement of dileptons. These three questions are briefly summarised in the following paragraphs.

The NA38 and NA50 experiments studied J/ψ suppression, as a signature of the formation of a deconfined state. In Pb-Pb collisions the J/ψ production pattern, as a function of the collision centrality, shows that above a certain centrality threshold the J/ψ yield is considerably lower than expected from the “nuclear absorption” curve, derived from proton-nucleus and light-ion collisions [3]. One of the current interpretations of this result is that the dense and hot medium formed in the collisions dissolves the χ_c resonance, leading to the disappearance of the fraction ($\sim 30\%$) of J/ψ mesons that would otherwise originate from χ_c decays. However, there are several questions which remain open. What is the physics mechanism driving the suppression of the J/ψ meson? A thermal phase transition to a quark-gluon plasma or a geometrical transition (percolation) to a system of deconfined (but not necessarily in thermal equilibrium) partons? Is the suppression pattern determined by the (local) energy density reached in the collision? Or by the average length of nuclear matter traversed by the charmonium state? Or by the number of participant nucleons? And what is the role of the feed-down from χ_c decays in the observed suppression pattern?

The dimuon mass spectrum between the ϕ and J/ψ resonances is dominated by Drell-Yan and simultaneous semi-leptonic decays of D mesons. The superposition of these two sources describes the measurements done in p-A collisions, while in A-A collisions the dimuon mass spectrum shows an excess which increases with the number of nucleons participating in the interaction [4]. Two interpretations of this excess have been considered: it can be due to an unexpected enhancement of charm production or to thermal dimuons emitted from the QGP phase. We need improved measurements to distinguish them and clarify if we are seeing thermal dimuons from the Quark-Gluon Plasma or some anomaly in charm production in heavy-ion collisions.

The CERES experiment measured the dielectron invariant mass spectrum in Pb-Au collisions at 158 GeV per nucleon. A comparison with the expected sources, mainly light meson decays, showed an excess for masses above 200 MeV [5]. In the mass range 0.3–0.7 GeV, where the excess is most pronounced, the combined yield of the “hadronic cocktail” is exceeded by a factor $5.8 \pm 0.8 \pm 1.5$. This can be seen in Fig. 1.1 (right), showing the Pb-Au dielectron mass spectrum for the most central collisions. On the left hand side of this figure we can see the corresponding dimuon mass spectrum *before* background subtraction. Subtracting a rather large background (the signal-to-background ratio, including the observed excess, is 1/8), a net signal of 648 ± 105 e^+e^- pairs for $M > 200$ MeV is left. On the other hand, the proton-nucleus data, collected in p-Be and p-Au collisions at 450 GeV, are well described by the “hadronic cocktail”, see Fig. 1.2.

The observation done in Pb-Au collisions has been interpreted as an indication of

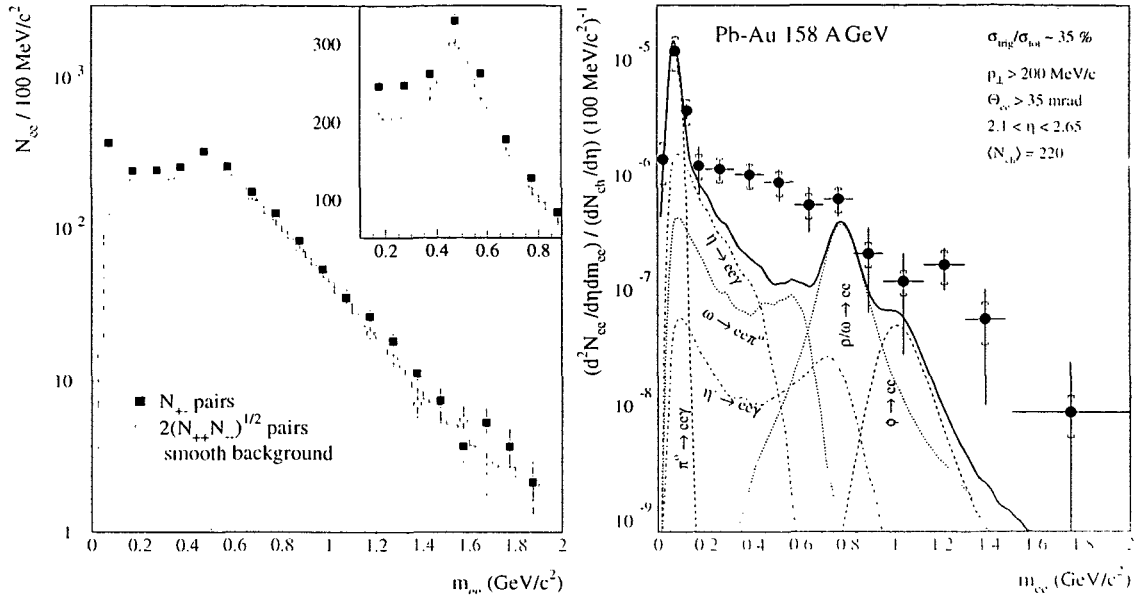


Figure 1.1: Dielectron mass spectrum collected by CERES in 158 GeV Pb-Au collisions, before (left) and after (right) background subtraction. Figures taken from Ref. [5].

changes in the mass and decay width of the ρ meson, maybe due to partial restoration of chiral symmetry. However, this result suffers from lack of statistics and a poor signal-to-background ratio. NA60 would like to clarify if the properties of the ρ meson are really modified in the strongly interacting dense medium created in heavy-ion collisions and, if so, whether this is indeed a signal of chiral symmetry restoration.

In order to significantly contribute to the clarification of these open questions, NA60 collected Indium-Indium collisions, at 158 GeV per incident nucleon, during a period of 5 weeks, at the end of 2003. The questions raised by the observations of CERES will be studied with considerable statistics (around 1 million signal events, thanks to the high luminosity and very selective dimuon trigger of NA60), a good mass resolution, around 20 MeV at masses of ~ 1 GeV, and a much better signal to background ratio than previous measurements. It is important to underline that the phase space coverage of NA60 extends down to zero transverse momentum even for dimuons of very low mass. The interpretation of the observations will also benefit from the study of the data in several bins of charged particle multiplicity, or forward hadronic energy, something that CERES did not do for lack of statistics.

Recent history has provided many examples which demonstrate that it is absolutely crucial to establish a robust reference baseline, essentially on the basis of *proton-nucleus* data, with respect to which we can identify patterns specific to the heavy-ion data, which may signal the formation of a new state of QCD matter. This requirement is even more important for the NA60 experiment, aimed at giving accurate answers to specific open questions rather than at “exploring new frontiers”.

While this is particularly true for the study of low mass dilepton production,

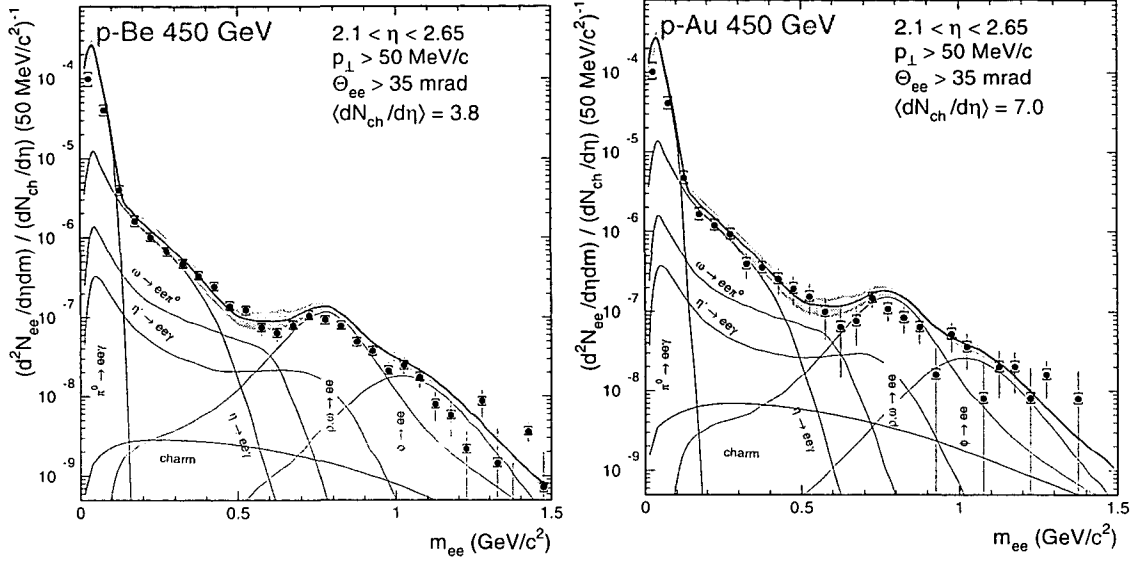


Figure 1.2: Dielectron mass spectra collected in p-Be (left) and p-Au (right) collisions at 450 GeV. Figures taken from Ref. [6].

there is some independent physics interest in this mass region for proton-induced interactions, linked to the historical puzzle of “anomalous lepton pair” production. The puzzle dates back to the mid-seventies and early eighties, when a series of publications, both on e^+e^- and on $\mu^+\mu^-$ pairs, reported an excess of the observed yield above the expectation from meson decays.

More recently, NA34/HELIOS-1 [7] showed, by direct measurements of certain Dalitz modes, that the yield of e^+e^- and $\mu^+\mu^-$ pairs in 450 GeV p-Be collisions could essentially be accounted for by meson decays, thereby ruling out the existence of such an anomaly. CERES made the measurements shown in Fig. 1.2 and NA38/NA50 reported the observation of a low-mass excess at $p_T > 1$ GeV/c [8].

This thesis reports on the data collected during a few days in 2002 with a proton beam of 400 GeV/c momentum, incident on several nuclear targets. The collected statistics, around 600 000 dimuon triggers, allows a reasonable study of low mass dimuon production. In this thesis we will extract the nuclear dependence of the production cross-sections of the ω and ϕ resonances, needed to correctly extrapolate the respective yields from the elementary pp cross-sections to the yields expected in heavy-ion collisions. Such a measurement requires different p-A collision systems and sufficient mass resolution to individually study the two resonances. The NA38/50 muon spectrometer has a relatively poor mass resolution for low mass dimuons, because the muons suffer considerable multiple scattering when crossing the 5 m thick hadron absorber. NA60 improved the mass resolution thanks to a Silicon tracking telescope, placed in the vertex region, *before* the hadron absorber. By matching the muon tracks, uniquely identified and tracked in the muon spectrometer, to reconstructed tracks in the vertex telescope, we improve the mass resolution, and the

signal-to-background ratio.

The specific physics requirements on our new detector and a detailed description of each detector component are given (Chapter 2). Special emphasis is given to the Microstrip Telescope in Chapter 3, with which the June 2002 data, used in this thesis, were collected. Chapter 4 then describes the microstrips' raw data analysis and the telescope's performance during the period of data taking. Chapter 5 outlines the data reconstruction procedure, the data selection and mentions the calculation of the integrated luminosities for each of the target materials. In view of understanding the collected dimuon spectrum, in Chapter 6 we will describe the various sources of muon pair production (η , ρ , ω , η' , ϕ , $D\bar{D}$ and Drell-Yan) which we have simulated and tracked through our apparatus. In Chapter 7 we use the Monte Carlo simulations to study particle acceptances and detection efficiencies, from the track reconstruction, track matching and vertexing efficiencies. Also in this chapter the final analysis event selection will be described, providing a sample of 13 500 opposite-sign and 800 like-sign dimuons for the physics data analysis. The final chapter (Chapter 8) starts with a discussion of the background and compares the kinematical distributions from the collected data with the reconstructed Monte Carlo simulations. It finishes by reporting our measurements of the nuclear dependence of the production cross-sections of the ω and ϕ mesons and by comparing our low mass dimuon continuum with the results of previous experiments.

Chapter 2

The NA60 Apparatus

2.1 General Overview

The purpose of the NA60 experiment is to accurately study dimuon production in proton-nucleus and heavy ion collisions. The highly selective dimuon trigger allows NA60 to look for processes of very low production cross-sections (roughly speaking, only one out of 100 thousand collisions are recorded). The produced dimuons are identified by the muon spectrometer, which is preceded by a hadron absorber that lets only muons pass. The drawback of this “muon filter” is that the muons undergo multiple scattering and energy loss which will affect the momentum and, hence, the dimuon mass resolution. To overcome this problem, NA60 measures the muons already *before* the absorber. This requires that the muon tracks are found among the many other charged particle tracks by a correct matching with the reconstructed tracks in the muon spectrometer. For this reason, the angles and momenta of charged particles must be known in the vertex region with sufficient accuracy. Measuring the particles’ momenta requires a magnetic field in the target region. The particle tracking in the vertex region is performed using a Silicon tracking telescope, made essentially of microstrip detectors in the proton runs and of pixel detectors in the heavy ion runs.

In order to distinguish *prompt* dimuons, as e.g. DY dimuons, from muons coming from mesons with a sufficiently long lifetime, as e.g. the D mesons, the interaction point and the impact parameter of the muon tracks have to be measured precisely. To measure the transverse coordinates of each incident beam particle we use a Beam Tracker, placed upstream of the target, which allows to determine the transverse coordinates of the interaction point with a resolution of $\sim 20 \mu\text{m}$. Combining this information with the reconstructed tracks of the Silicon tracking telescope allows to identify tracks from secondary vertices with an offset resolution of better than $40 \mu\text{m}$.

To estimate the centrality of the collision in heavy ion collisions, NA60 uses a zero degree calorimeter (ZDC) which measures the energy deposited by the non-interacting (spectator) nucleons.

Figure 2.1 gives an overview of the target region. In this photograph the beam comes from the right side and hits the Beam Tracker stations, placed inside a vacuum

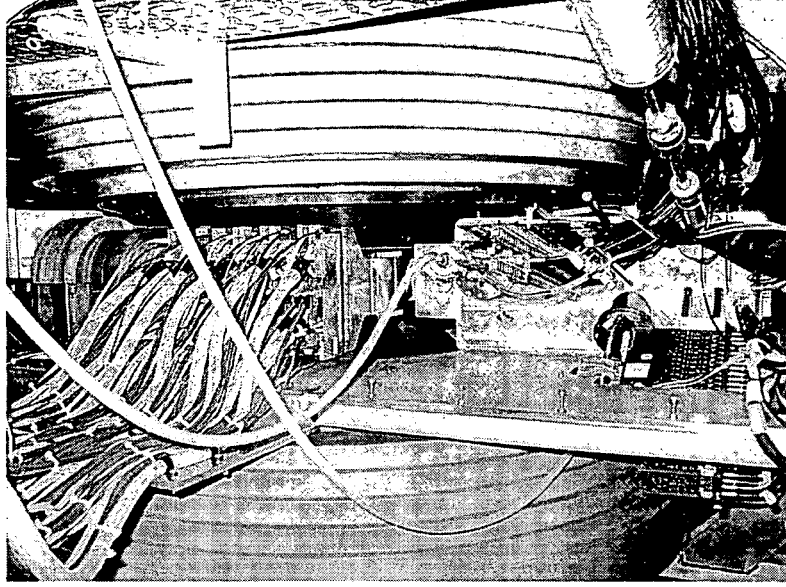


Figure 2.1: The NA60 target region.

cryostat box. Attached to this cryostat is the target box, holding the individual sub-targets. Between the magnetic coils of the vertex dipole magnet we see the read-out cards of the pixel vertex telescope. On the left hand side we see the beginning of the hadron absorber, the so-called “pre-absorber”.

Note that the term “muon spectrometer” designates the detector system *after* the hadron absorber, including the trigger hodoscopes, while we speak of the “vertex tracking telescope” when we mean the tracking elements in the vertex region. In the following we will use the expressions “Jura” and “Salève” sides, referring to the left and the right sides of the experiment with respect to the central vertical plane, when seen from the beam line looking downstream.

“Detector”	z [cm]	Δz [mm]	material
Beam Tracker 1	−30.0	0.4	Si
Beam Tracker 2	−10.0	0.4	Si
target 1–6	−2.0, −1.2, −0.4,	2.0	In, Be, Be
	0.4, 1.2, 2.0	2.0	Be, Pb, Be
microstrip telescope	7.6, 10.0, 11.2, 14.8,	0.3	Si
	23.0, 26.0, 34.0, 37.0, 40.0	0.3	Si
pixel plane	17.2	1.05	Si
Interaction Counter	42.5	20.0	scintillator

Table 2.1: Detectors in the vertex region during the June 2002 run. The centre of the vertex dipole magnet is located at $z = 20$ cm.

Table 2.1 gives the positioning of the detectors in the vertex region during the June 2002 run. The following sections describe the motivation, the design and performance

of specific components of the experiment, including the beam and the trigger system. After a short overview of the beam and the NA60 beam line, we will start with the muon spectrometer, which is the most important detector in this experiment. The subsequent sections then describe each detector in the sequence in which they are assembled along the beam line.

2.2 The Beam

NA60 collects data with proton and ion beams. While the proton beam has an energy of 400 GeV, the Indium beam has an energy of 158 GeV per nucleon. The energy of the Indium beam was chosen such that a *direct* comparison can be done with the Pb-data, previously taken by NA50, without any energy rescaling. The energy of the Pb-beam corresponds to 400 GeV per charged nucleon. In the test run of October 2002, NA60 had 5 days of beam time with a Lead beam of 30 GeV/nucleon followed by 5 days with 20 GeV/nucleon. The intensity of the proton beam used in 2002 was $\simeq 2 \cdot 10^8$ protons per burst, while the Indium data were taken with an intensity of $\simeq 5 \cdot 10^7$ ions per burst, where one burst lasted 4.8 and 6.2 s for the proton and ion beam, respectively.

The proton beam intensity is monitored by three “Argonia” ionisation chambers, placed upstream of the target. During the October 2001 commissioning run these detectors were calibrated by comparing the beam flux, measured by the Argonia, to the counts of a scintillator detector. Since the scintillator can be read out only at low intensities, the calibration was performed at an intensity of $\sim 10^6$ protons/burst. It is assumed that the Argonia are linear with intensity up to the higher values used in the experiment.

The NA60 experiment is situated in the CERN SPS North Area High Intensity Facility (NAHIF), in the ECN3 hall, and is served by the “P0” beam line. The extraction point from the SPS accelerator is located more than 1 km upstream of the NA60 target. Figure 2.2 gives an overview of the beam line, showing its collimators, and the bending and focusing magnets. The two horizontal dipole magnets “B8” and “B9”, situated ~ 320 m upstream from the NA60 target, direct the beam towards the NA60 target. The intensity of the beam is regulated by “Taxes” and Collimators.

2.3 The Muon Spectrometer and Trigger System

The muon spectrometer consists of four main elements: a hadron absorber, eight tracking multi-wire proportional chambers (MWPC), four trigger scintillator hodoscopes (R1-R4), the last one placed behind a 120 cm thick Iron wall, and an air core toroidal magnet (ACM) for the momentum measurement of the muons, see Fig. 2.3.

These components can be moved along the z -axis to ease maintenance and to keep the angular muon acceptance around mid-rapidity, in spite of small changes in the beam energy. In the current setup, the angular muon acceptance lies approximately

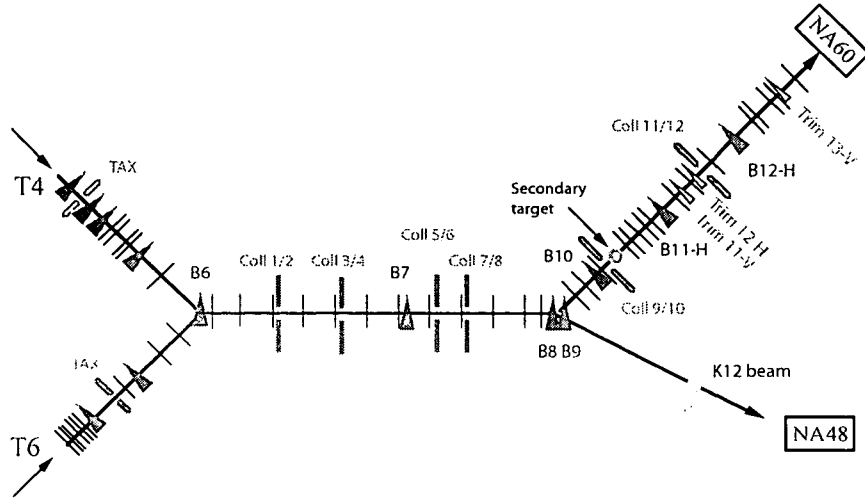


Figure 2.2: The beam line of the NA60 experiment.

in the range 35–120 mrad, as imposed by the magnet aperture. For beam energies of 158 and 400 GeV this corresponds roughly to one unit of rapidity at mid-rapidity, where particle production is most copious. The muon's acceptance also depends on the magnetic field and on the effective number of interaction lengths of the absorber. It is also affected by the trigger conditions.

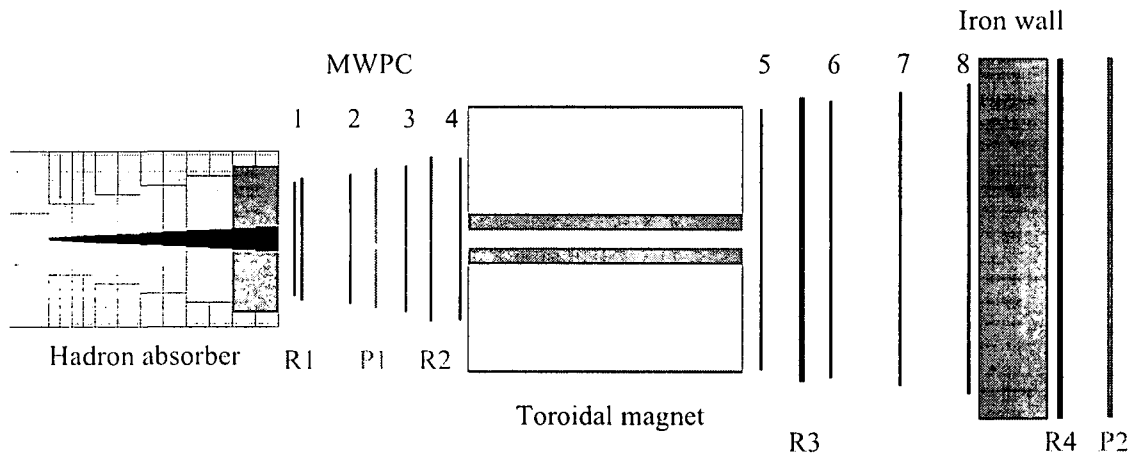


Figure 2.3: The muon spectrometer.

2.3.1 The Hadron Absorber

The muons are filtered out among the many other produced particles by the hadron absorber. This is a simple, but effective, “particle identification” system: particles that hit the R4 trigger hodoscope, by definition, are muons. Indeed, only muons (and

neutrinos) are penetrating enough to cross the pre-absorber, made of 41 cm BeO and 25.4 cm Al_2O_3 , the main absorber, 460 cm of graphite followed by 20 cm of Iron, and the 120 cm thick Iron wall, placed after the muon chambers so as to not degrade the tracking accuracy through multiple scattering, while ensuring a very clean muon trigger. Figure 2.4 shows the first part of the hadron absorber.

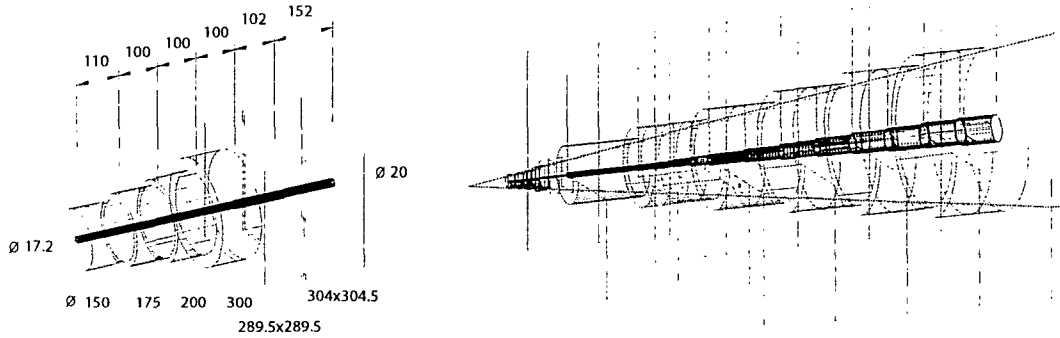


Figure 2.4: The hadron absorber consists of four slices of BeO and two of Al_2O_3 (left), followed by 460 cm of Carbon and 20 cm of Iron.

The hadron absorber starts as close as possible to the target, immediately after the vertex telescope, in order to stop a large fraction of pions and kaons from decaying into muons, and becoming a source of background.

The main absorber, placed between the target and the muon chambers, is made of materials with a low atomic number, Z , in order to minimise the multiple scattering induced on the traversing muons, and with the highest available densities, so as to stop the hadrons in a relatively small thickness. The beam is stopped in an “Uranium Plug”, indicated as the black cone in Fig. 2.3. The Carbon blocks are surrounded by cast Iron and concrete. The last 80 cm of the main absorber can be equipped in a modular way by 20 cm thick Iron and Carbon blocks. In the June 2002 proton run the main absorber was composed of 460 cm of Carbon, followed by 20 cm of Iron. A detailed study [9] has shown that 20 cm of Iron at the end of the absorber are sufficient to prevent the hadrons from polluting the first MWPC chambers.

Table 2.2 gives an overview of the location and thicknesses of the elements of the absorber for the June 2002 run.

Placing the last part of the absorber, the 1.2 m thick Iron wall, after the tracking stations and before the last trigger hodoscope ensures that no energetic punch-through hadrons give rise to a fake trigger, without contributing to the degradation of the tracks measured in the chambers.

2.3.2 The Multi-Wire Proportional Chambers

The muons which have crossed the main absorber are tracked in eight multi-wire proportional chambers, separated in two sets of 4 chambers by the toroidal magnet

material	ρ [g/cm ³]	z_{in} [cm]	Δz [cm]	λ_I [cm]	L/λ_I
BeO	2.81	43.6	41.0	35.85	1.14
Al ₂ O ₃	3.52	84.7	25.4	32.65	0.78
C	1.93	110.0	460.0	44.70	10.29
Fe	7.87	570.0	20.0	16.76	1.19
# interaction lengths in main absorber					13.4
Iron-Wall	7.87	1676.3	120.0	16.76	7.16
total number of interaction lengths					20.56

Table 2.2: Composition of the hadron absorber in the June 2002 setup. λ_I is the nuclear interaction length.

ACM (Air Core Magnet).

Each muon chamber consists of three independent tracking planes, interspaced by 2.2 cm, rotated by 60° with respect to each other, to allow a good measurement of one space point, see Fig. 2.5.

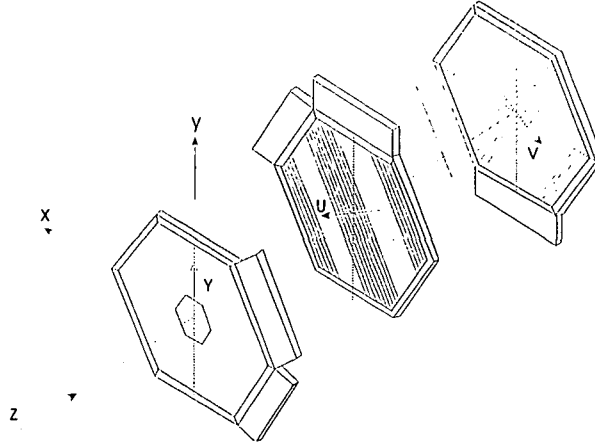


Figure 2.5: Each MWPC consists of three independent tracking planes. For visibility purposes the individual planes are shown well separated from one another.

The sensing elements of these chambers are gold-plated Tungsten anode wires with a diameter of $\sim 20 \mu\text{m}$, inter-spaced by 3 mm and sandwiched between two graphited Mylar cathode planes, 6 mm far away. The chambers have hexagonal shape and their transverse size increases with increasing distance from the target to cover the angular acceptance, defined by the aperture of the ACM magnet. The z -positions with respect to the target and the transverse size of all components of the muon spectrometer can be found in Table 2.3.

The tracking volume of the chambers is filled with a gas mixture, consisting of $\sim 80\%$ of Argon, of which 50% is flushed through 0.8% of Isopropyl alcohol (2-propanol), of 18% Isobutane $i\text{C}_4\text{H}_{10}$ used as a quencher and of 2% Tetrafluorethane

	z [cm]	Main characteristics
MWPC 1	615.8	448 wires per plane, $\varnothing = 134$ cm
R 1	629.6	6 \times 30 scintillator slabs of 1.05–3.45 cm width
MWPC 2	684.1	512 wires per plane, $\varnothing = 153$ cm
P 1	712.0	6 \times 8 scintillator elements; width: 2.73–13.65 cm
MWPC 3	748.7	576 wires per plane, $\varnothing = 172$ cm
R 2	761.0	6 \times 30 scintillator slabs of 1.25–3.35 cm width
MWPC 4	818.2	640 wires per plane, $\varnothing = 192$ cm
ACM	828.7–1311.7	
MWPC 5	1347.2	1024 wires per plane, $\varnothing = 306$ cm
R 3	1390.2	6 \times 23 scintillator slabs of 5.5 cm width
MWPC 6	1445.6	1088 wires per plane, $\varnothing = 326$ cm
MWPC 7	1544.1	1152 wires per plane, $\varnothing = 345$ cm
MWPC 8	1642.1	1216 wires per plane, $\varnothing = 364$ cm
Iron wall	1676.3–1796.3	
R 4	1800.7	6 \times 32 scintillator slabs of 5.5 cm width
P 2	1820.7	6 \times 8 scintillator elements; width: 8.10–47.50 cm

Table 2.3: Detector components of the muon spectrometer. The z values given refer to the centre of the respective device.

(commercial tradename: R134a), used as a “cleaning” gas. A gas mixer rack measures and controls the flow of the gas components. Each component enters the pressure regulator via an electro-valve and is then transported to a mass flow controller (MFC). The MFC measures the actual gas flow via comparison with an external reference value. The registered difference is then amplified and used to regulate the gas control valve. In this way the required contributions of the three components is obtained. Further mixing is performed by passing the gas through a “mixer tube”. Metal strips in this tube cause turbulences, which improve the mixture homogeneity.

Two gas distribution racks distribute the gas mixture to the various gas chambers. In total there are $8 \times 3 = 24$ independent gas volumes, since each of the eight chambers has three independent detection planes. Furthermore, the gas distributor measures the input and output flows for each chamber and calculates possible leaks. During the period when there is no beam the chambers remain permanently flushed with Argon. Each chamber volume can be purged independently. In order to detect gas leaks there are detection heads inside the racks. The outputs of the chambers are connected to the extraction ventilation system.

2.3.3 The Trigger Hodoscopes

The trigger system consists of four “R” hodoscopes, two before and two after the ACM magnet, made of scintillator slabs with a time resolution of around 2 ns. Like all other components of the muon spectrometer, the hodoscopes have hexagonal shape. All R-hodoscopes are designed in a similar way. The scintillator slabs of each sextant,

oriented parallel to the outer edges, become longer with increasing distance from the beam axis, see Fig. 2.6. The width of the slabs of the R1 and R2 hodoscopes

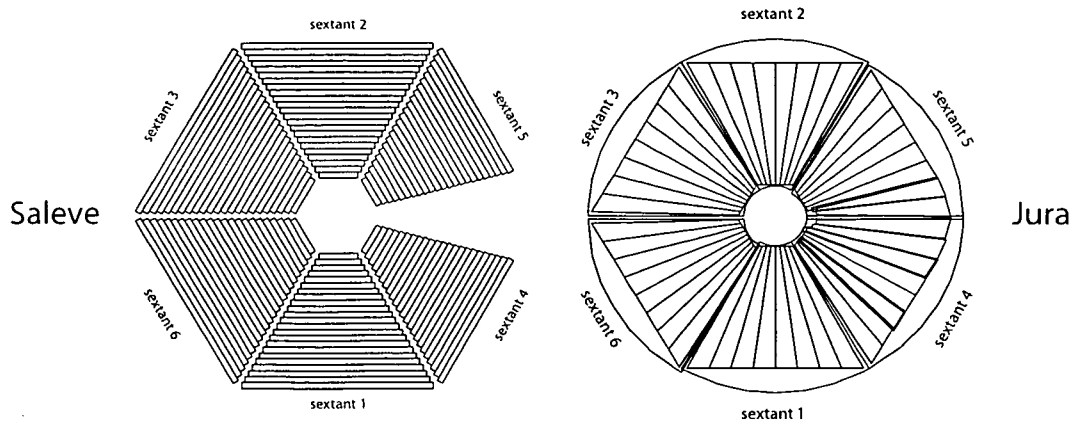


Figure 2.6: The segmented slabs of the R3 (left) and P1 (right) hodoscopes.

increases with the distance from the beam line so that a muon produced in the target which passes through slab i in R1 will also hit slab i in R2. In order to accommodate the spatial extent of the target and to allow for multiple scattering for low energetic muons, the combination of hitting slab i in R1 and $i - 1$ in R2 is also allowed. This “R1-R2 coincidence” for each muon is combined with the information from R3 and R4. The last trigger hodoscope, R4, is placed behind a 1.2 m thick Iron wall which absorbs remaining hadrons, thereby ensuring a clean (di)muon trigger. However, this implies that the muons must have a minimal momentum of ~ 5 GeV/c. The dimuon trigger then requires that the two muons pass through two different sextants. This requirement reduces the fraction of low mass muon pairs that give rise to a trigger, in order to not saturate the bandwidth of the data acquisition system (DAQ). The R3 hodoscope has a small inactive zone on the “Jura” side, called “Beam-Killer”, as can be seen in Fig. 2.6. Although the other trigger hodoscopes have no such dead areas, the muon acceptance is affected by this cut in sextants 4 and 5.

Furthermore, NA60 uses two so-called “P-hodoscopes”, P1 and P2. The former is placed before the ACM magnet, the latter after the Iron wall. They are used in special runs to measure the efficiency of the R1-R4 system. Their geometry is different from the R-hodoscopes. The scintillator slabs of each sextant are oriented radially, so that their width increases with increasing distance from the beam axis, see Fig. 2.6.

2.3.4 The Toroidal Magnet ACM

The magnetic field of the toroidal magnet ACM is produced between 6 radial Iron poles, which are 4 m long and cover 18° in azimuth. The magnet’s air gap starts at a radius of 29.5 cm. The outer radius is 154 cm. These two values are the ones determining the detector’s rapidity acceptance. Events with muons which cross one

of the Iron pieces are rejected from the physics analysis, since they have degraded momentum resolution, compared to the ones which traverse the air core between them.

The toroidal magnetic field is $1/r$ dependent, $\vec{B}(r) = B_0/r \cdot \vec{e}_\phi$. In Fig. 2.7 we can see the magnitude of the magnetic field in the air sectors for different distances from the beam-axis. The proportionality constant between the magnitude of the magnetic field and the radius is $B_0 = 0.219 \text{ Tm}$ for a current of 4000 A.

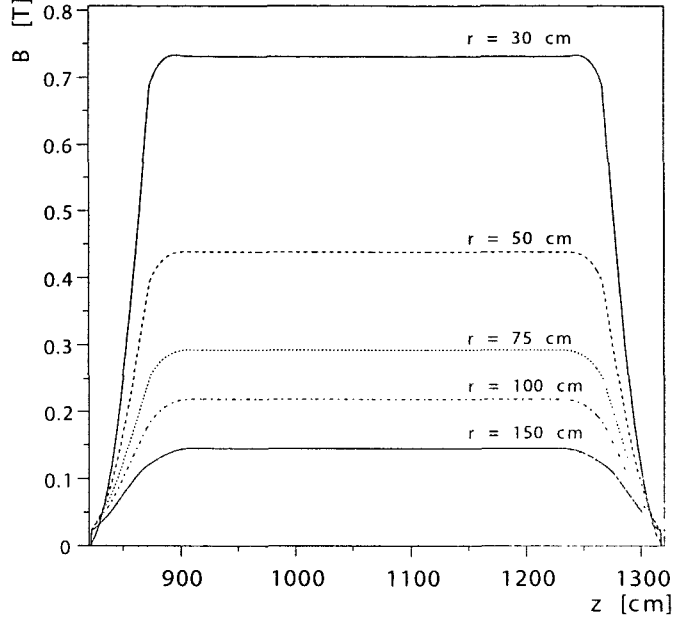


Figure 2.7: Magnitude of the toroidal field for various distances from the beam axis.

The bending power depends on the radial distance from the beam. For $r = 150, 100, 75$ and 30 cm we have $\int B \cdot dl = 0.64, 0.95, 1.89$ and 3.14 Tm , respectively.

Since the axis of the magnet is aligned along the beam axis the muons keep their azimuthal angle while changing their polar angle. The deflection angle, $\Delta\theta$, is inversely proportional to the particle's p_T ,

$$\Delta\theta = \frac{q \cdot B_0}{p_T} \ln(z_2/z_1), \quad (2.1)$$

where q is the particle's charge, and z_1, z_2 are the entrance and exit planes of the magnetic field, relative to the target position [10]. From this formula we see that for a given operation current, which sets the proportionality constant, B_0 , the expression $\Delta\theta \cdot p_T$ is constant. Therefore, by measuring the deflection angle the muons's transverse momenta can already be roughly calculated at the trigger level. This allows to select muons with a certain p_T and, hence, muon pairs with a given invariant mass, since the mass (in the acceptance window of the spectrometer) is roughly given by $M \approx p_{T,1} + p_{T,2}$. However, in order not to bias the collected data we have never applied any cut on the momenta of the muons at the trigger level.

The ACM current is pulsed, synchronised with the SPS cycle and is recorded burst by burst. For a more detailed description of the muon spectrometer, with all its components, see Refs. [11, 10].

2.4 The Beam Tracker

The purpose of the Beam Tracker is to provide the flight path of the incident beam particle in order to calculate the transverse coordinates of the interaction point. This is especially important for proton induced collisions, where the charged particle multiplicities are rather low. The smaller the number of tracks reconstructed in the vertex telescope, the smaller the “pointing accuracy” back to the individual sub-targets. The primary vertex identification can, hence, be improved if the transverse coordinates of the vertex can be provided independently. In heavy ion collisions, where hundreds of tracks are produced, the vertex reconstruction resolution, provided by the tracking telescope is already sufficient. However, the Beam Tracker’s information is very useful to speed up the vertex reconstruction. Furthermore, due to its good timing accuracy of 1.7 ns, its signal can be used to identify beam pile-up events.

The Beam Tracker was developed as a common project between the RD39 and NA60 Collaborations [12]. To measure the flight path of the beam particles, *two* tracking stations are needed. The NA60 Beam Tracker is made of 400 μm thick single sided Silicon microstrip detectors. Each sensor has 24 strips with a length of 1.2 cm and 50 μm pitch, surrounded by four wider strips on each side. To provide one space point, each tracking station consists of two sensors rotated by 90° . The two stations are interspaced by 20 cm and have a relative rotation of 45° to resolve hit ambiguities. Since the space available for installation is limited by the magnets’ coils, the station closer to the target (“station 2”), located at $z = -10$ cm, is placed at $+10^\circ$ with respect to the positive x axis, the one at $z = -30$ cm (“station 1”) at -35° .

In the proton runs, the strips are wire-bonded to a fast radiation hard pre-amplifier chip specially developed to run at cryogenic temperatures, with a double peak resolution of less than 10 ns. The modules used in the ion runs are essentially identical, except that the front-end chip is now replaced by a simple “pitch-adapter” circuit, since the signals are large enough to be sent directly to the fast amplifier cards sitting outside of the vacuum box. The amplified analog signals are then sent to the data acquisition system PC, placed in the counting room, through fast cabling and Multi-Hit Time Recorder (MHTR) FERA modules.

The detectors are placed in a vacuum box and run at 130 K to maximise the charge collection efficiency after collecting high radiation doses [13]. Their temperature is controlled by remotely setting the nitrogen flow in the cooling pipes and by continuously adjusting the power dissipated by heaters placed on the PCB. Figure 2.8 shows one Beam Tracker station, with a zoom onto the sensor on the right hand side.

In the first week of the June 2002 proton run, the Beam Tracker worked quite smoothly. In the second week, the sensors had to be exchanged due to radiation damage. The exchanged sensors of the station closer to the target did not work

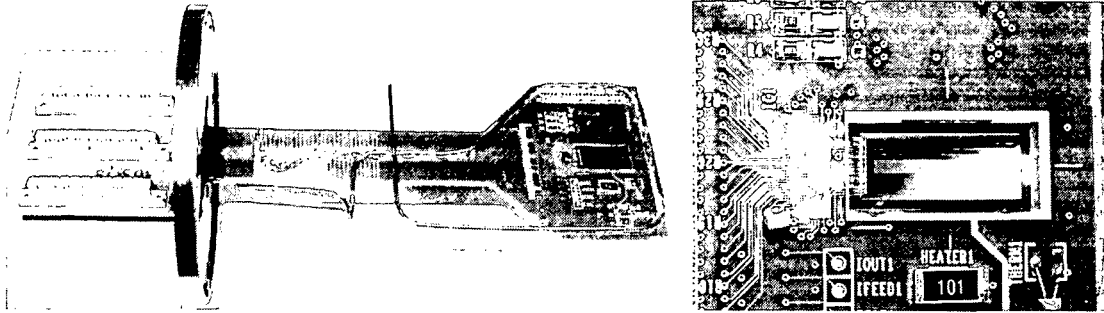


Figure 2.8: One Beam Tracker station. The sensors (zoomed view on the right side) are glued over a squared opening of the PCB, one on each side.

properly, so that this station is absent in the offline analysis.

2.5 The Target System

The NA60 experiment uses two different target systems; one in the proton runs, the other one in the ion runs. Since in the proton runs we want to study the nuclear dependence of the production cross-section of various particles, in particular of the ω , ϕ , χ_c and D mesons, we use three different target materials: Beryllium ($A = 9$), Indium ($A = 115$) and Lead ($A = 208$). Placing these different targets simultaneously into the beam allows to minimise systematic errors coming from luminosity calculations, which will affect all the targets in the same way. To have a symmetric collision system in the heavy ion runs, we use Indium targets with the Indium beam and Lead targets with the Lead beam.

In order to minimise the probability that the produced particles will re-interact or that the muons suffer multiple scattering in the target itself, we use several sub-targets separated along the beamline, which in sum give the same interaction length as one thick target. To minimise these problems further, in the Indium run NA60 uses sub-targets of 1 mm diameter only, apart from the very first sub-target.

The first target on the way of the proton beam is the Indium target, followed by three Beryllium sub-targets. Since we detect the χ_c in its radiative decay ($\chi_c \rightarrow J/\psi \gamma$), the Lead target, placed after the four preceeding sub-targets, serves as a converter for the photon. This, however, results in multiple scattering for the muons which are produced in the first sub-targets. After the Lead target we place a fourth Beryllium target, which cannot be used for the χ_c study, but provides a sample of dimuons unaffected by multiple scattering in the Lead target. All sub-targets have a diameter of 12 mm, with a thickness of 2 mm, and are inter-spaced by 8 mm. Using three Beryllium targets allows to obtain roughly the same number of interaction lengths as for the Indium and the Lead targets: $3 \times 2 \text{ mm Be} = 1.5\% \lambda_I$, $2 \text{ mm Indium} = 0.9\% \lambda_I$ and $2 \text{ mm Lead} = 1.2\% \lambda_I$.

The target system for the ion runs is different in the sense that it is placed in vacuum ($\sim 0.01 \text{ atm}$) to avoid collisions of the ion beam with nuclei from the air. In

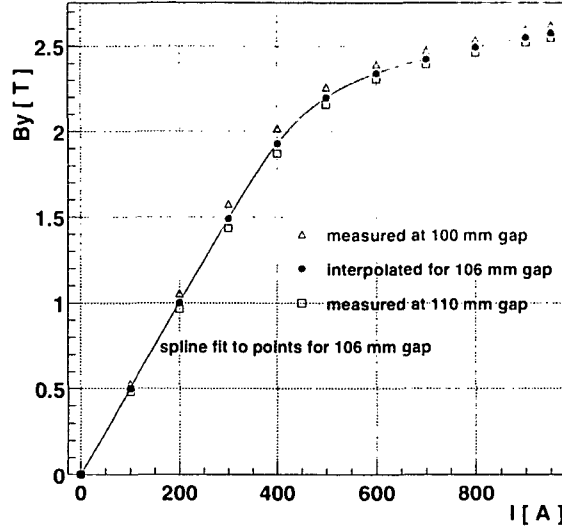


Figure 2.10: Magnetic field as a function of the current.

$B(r)/B(0)$ [%]	r [cm]	$B(r)$ [T]
100	0	2.52
90	15	2.27
50	27	1.26
10	51	0.25
1	79	0.025

Table 2.4: Magnetic field at various radii, with a current of 900 A, at the middle of the vertical gap.

of some of its operational characteristics are described in Ref. [14]. These measurements were parameterised and inserted into the NA60 detector simulation package, NA60root. Two alternative methods were applied to describe the field: a simple bi-linear interpolation of the measured values and a fitting function. Due to the dipole symmetry it suffices to consider two components: the vertical component B_y and the radial component B_r in the $x - z$ plane. By default, NA60root uses the former method.

To optimise the use of PT7's field, the tracking telescope for proton runs has a last station at 40 cm from the target. Starting from the target centre at $z = 0$ cm, this corresponds to a range in the magnets internal coordinate system of $-20 < z < +20$ cm. This range is longer than the plateau, seen in Fig. 2.11. Thus, along the flight path of a charged particle we have a rising and falling magnetic field. In such an inhomogeneous field, $B(l)$, the deflection angle $\Delta\theta$ is given by

$$\Delta\theta = \frac{0.3 \int_{-L/2}^{L/2} B(l) dl}{p_{\perp}}. \quad (2.2)$$

where L denotes the extent over which a charged particle experiences the magnetic field between its production point and the last tracking plane. p_{\perp} is the particle's

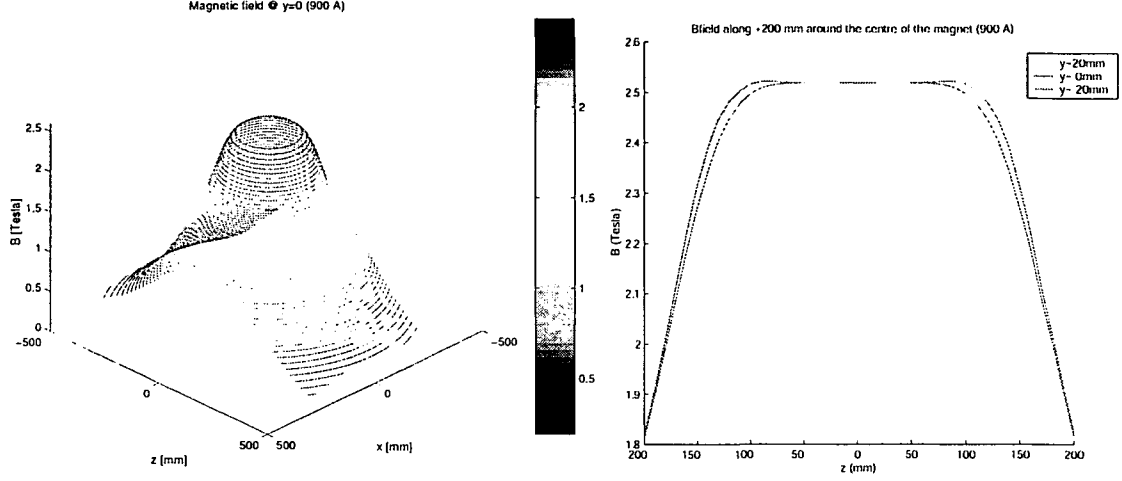


Figure 2.11: Magnetic field measured in the centre of the gap with a current of 900 A.

momentum transverse to the vertical field lines. The bending power of this magnet, integrated from the target to the last tracking plane, is 0.95 Tm for an operational current of 900 A (integrating from the target up to PT7’s “full range” gives a bending power of 1.25 Tm). To reduce systematic uncertainties, the polarity of the magnet is reversed every few runs. During the field mapping we verified that reversing the polarity leads to deviations of the magnetic field, if any, of smaller than 0.2%.

In a homogeneous magnetic field, the momentum resolution, σ_p/p , is given by [15],

$$\frac{\sigma_p}{p} = \frac{\sqrt{3}}{2} \sigma_x \frac{8p}{0.3BL^2}. \quad (2.3)$$

For an inhomogeneous magnetic field, the expression $BL^2/8$ should be replaced by $\int_0^{L/2} d\lambda \int_0^\lambda B(l)dl$. It degrades linearly with increasing momentum, p , it improves for higher magnetic fields, B , and it improves with the square of the tracking distance, L . σ_x denotes the position resolution of a single tracking station.

Before the installation of PT7 in the experimental zone ECN3, it has been seen that the field decreases by less than 0.08% in the first 10 hours of operation after which it remains stable. We have also seen that after three hours of operation the air in the magnet gap warms up by 2.5°C. On the shims the warm-up was 4.7°C.

2.7 The Vertex Tracking Telescope

2.7.1 Overview and Geometry Aspects

The purpose of the vertex tracking telescope is to track the secondary particles, including muons, produced as a result of an interaction in the target, before they enter in the hadron absorber. Out of the many uninteresting particles — in central heavy-ion collisions, hundreds of particles are emitted in the angular acceptance of the detector — the muons have to be unambiguously identified by matching with the tracks

reconstructed in the spectrometer. For the measurement of the χ_c in proton induced collisions also the electron-positron pairs coming from the converted photon have to be tracked. Apart from improving the mass resolution of the reconstructed dimuons, the tracking telescope in the vertex region allows us to distinguish prompt dimuons from displaced vertex muon pairs from D meson decays, which have a typical offset of a few hundred μm . This should clarify the unexplained enhancement of dimuons in the intermediate mass region, between the ϕ and J/ψ resonances, measured in S-U and Pb-Pb collisions at 200 GeV/nucleon and 158 GeV/nucleon, respectively [4]. Furthermore, the vertex telescope “identifies” the sub-target where the interaction took place, by finding the common origin of the *reconstructed* tracks.

NA60 uses either Silicon microstrip or Silicon pixel technology for the tracking elements in the target region. While the low charged particle multiplicities in proton induced collisions allow the use of microstrip detectors, the much higher particle densities reached in heavy ion collisions impose the exclusive use of Silicon pixel detectors. The microstrip and pixel planes were designed to fit in the gap of the PT7 magnet and to match the muon spectrometer’s angular acceptance. The spacing of the telescope planes was optimised to fulfill several requirements, given the available number of tracking planes. It should allow to

- extract the coordinates of the interaction point,
- measure the momenta and angles of the muons,
- determine the muon’s offsets,
- track the e^+e^- pair in the proton runs, coming from the converted γ of the χ_c ’s radiative decay.

The telescope is assembled in an overall support box, attached to the same table which supports the Beam Tracker, the target box and the Interaction Counter. The microstrip telescope is described in detail in the next chapter.

2.7.2 The Silicon Pixel Telescope

The Silicon pixel telescope [16] is made of small and large tracking planes, ranging from $z = 6.6$ cm to $z = 31.2$ cm, and is illustrated in Fig. 2.12.

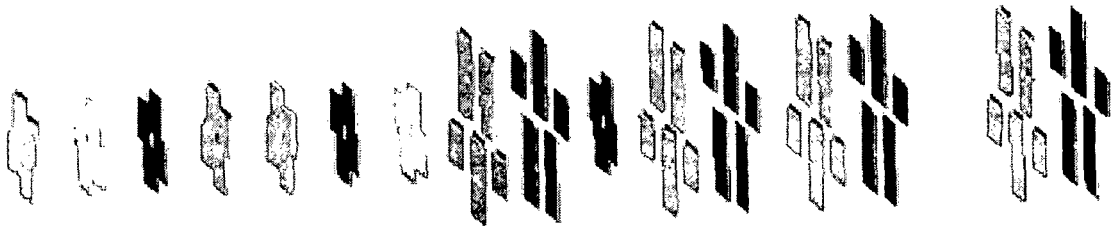


Figure 2.12: Illustration of the pixel telescope used in the October 2003 In-In run.

The small planes consist of 4 rectangular chips placed around a beam hole, while the large tracking stations are composed of two physical planes, each made of 8 chips. The tracking with pixel planes cannot be extended up to $z = 40$ cm, since even the large pixel planes would not cover the angular acceptance of the muon spectrometer. To improve the muon acceptance coverage a small pixel plane is placed close to the first large station, to cover its beam hole. From Fig. 2.13 we can see that the large tracking planes have a small area uncovered with sensors, along the horizontal axis, pointing towards the “Jura” side. This takes into account the acceptance gap of the muon spectrometer, in sextants 4 and 5 of the trigger hodoscopes. This figure shows the muon acceptance at $z = 30$ cm, overlapped on a 16 chips logical plane.

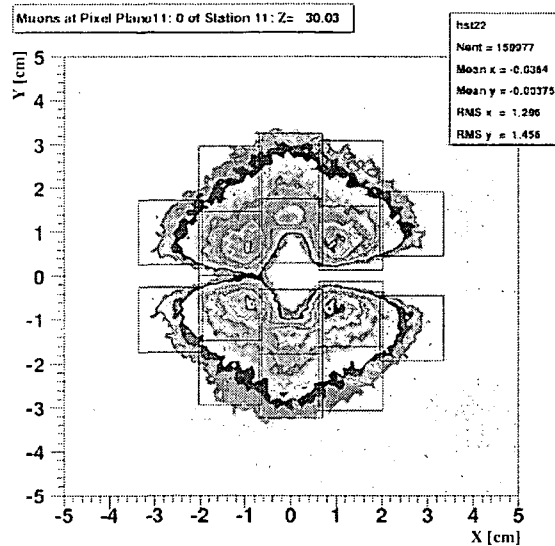


Figure 2.13: The configuration of the 16-chip planes, matching the acceptance of the muon spectrometer. The “Salève” side is on the left.

Each chip has 8192 pixels with an area of $425 \times 50 \mu\text{m}^2$, arranged in a matrix of 32 columns and 256 rows, giving a total active area of $13.6 \times 12.8 \text{ mm}^2$. Within a given plane, all chips are mounted with the same orientation, defining the plane as X or Y, depending on the orientation of the $50 \mu\text{m}$ side. To cover the full angular acceptance, some planes are inverted upside-down, having their back side facing the beam.

A pixel chip assembly is a $750 \mu\text{m}$ thick ALICE1LHCb pixel readout chip [17] bump-bonded to the $300 \mu\text{m}$ pixel sensor chip. The chips operate at a frequency of 10 MHz and have a read-out gate of 200 ns, because the NA60 trigger arrives asynchronous with respect to the chip’s clock. Such assemblies are glued on BeO or Al_2O_3 hybrids, which are placed on printed circuit boards (PCBs) to route the electrical lines out of the magnet’s gap. A zoomed view of a 4-chip plane and a fully assembled 8-chip plane can be seen in Fig. 2.14. The PCBs are mounted on Aluminium frames for mechanical support, and placed in slots of a support box that slides in the magnet gap. The modules are cooled by chilled water circulating in a copper tube attached to the backside of the hybrid.

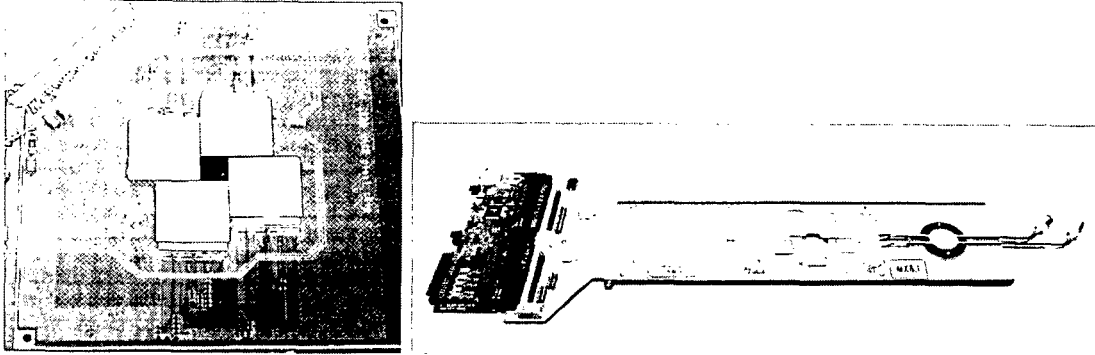


Figure 2.14: Zoomed view of a 4-chip plane, showing the sensor and read-out chips mounted on the ceramic hybrid (left) and a fully assembled 8-chip plane (right).

Being bump-bonded to the sensors the read-out chips are directly exposed to the many secondary particles produced as a result of a heavy ion collision. Since we want to study rare processes, we have to work with rather high interaction rates, of around 2 MHz. The operation in such a harsh environment imposes the exclusive use of radiation hard read-out chips. The chosen read-out chips have been shown to remain functional after radiation doses of at least 12 Mrad [18].

With a typical beam intensity of $5 \cdot 10^7$ ions per SPS cycle of 19.2 s we expect a 1 MeV neutron equivalent fluence of approximately $10^{13} n_{eq}/cm^2$ in the innermost pixels after 1 week of data taking. Given the strong radial dependence of the fluence, with more than a factor of 10 between different corners of the same sensor chip, we expect a very inhomogeneous radiation damage in the sensors. During the 40 days of the October 2003 In-In run we indeed saw a significant radiation damage, which required increasing the bias voltage up to 150 V, so that the detectors were efficiently working up to the end of the run.

Already during the October 2002 Pb-Pb run three pixel planes were successfully operated, without magnetic field. From these data we derived a spatial resolution along the $50 \mu m$ pixel direction of $8 \mu m$ [19]. From the reconstructed tracks we have obtained the z -vertex distribution, shown in Fig. 2.15 (left). We can clearly see that the tracks point back to the three Lead sub-targets and the exit window of the Beam Tracker. The measured distribution can be described by convoluting the thicknesses of the targets with a z -vertex resolution of around $200 \mu m$. We have, furthermore, correlated the transverse coordinates of the vertex measured by the pixel telescope with the one extracted from the Beam Tracker, see Fig. 2.15 (right). The correlation width is approximately $30 \mu m$, including both, the uncertainty of the Beam Tracker and the vertex resolution of the pixel telescope. Taking into account the Beam Tracker resolution of $20 \mu m$ we extract a resolution of around $20 \mu m$ on the determination of the transverse vertex coordinates by the pixel telescope.

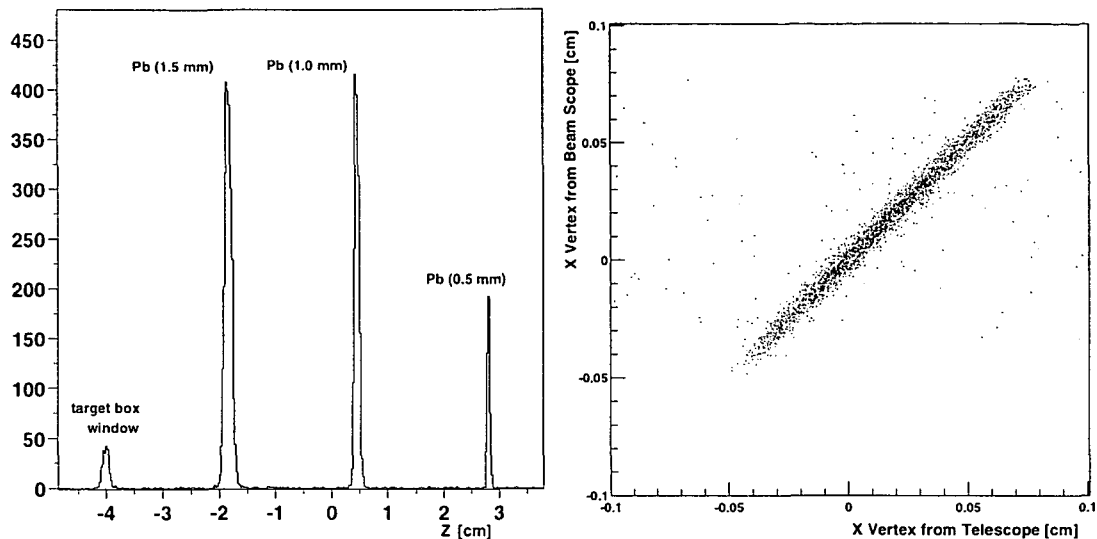


Figure 2.15: Left: z -vertex distribution, as determined from the pixel telescope. Right: Correlation of the x -vertex coordinate measured by the pixel telescope and with the Beam Tracker.

2.8 The Interaction Counter

The Interaction Counter is a small detector, placed between the Silicon tracking telescope and the hadron absorber, which gives a signal proportional to the multiplicity of the particles produced in the target region. It is made of two independent plastic scintillators, of $10 \times 16 \text{ cm}^2$ area and 10 mm thickness, preceded by a 5 mm thick Lead plate, and has a beam hole of 11 mm diameter. This Lead plate converts photons and, thereby, increases the collected signal by around 40%. Requiring a coincidence between the two scintillators rejects internal noise sources of the detectors or of the photo-multipliers. The very good time resolution of the scintillators is useful to identify interaction pile-up. However, the photomultipliers no longer work properly at interaction rates around or above 10 MHz.

2.9 The ZDC and the Quartz Blade Detector

In the ion runs it is crucial to have a measure of the *centrality* of the collision. For this purpose, NA60 uses a Zero Degree Calorimeter (ZDC), complemented by a “Quartz Blade”, a Cherenkov counter. Both detectors are placed upstream of the beam dump, on the beam axis.

While the ZDC is sensitive to the total energy deposited, the Quartz Blade signal is proportional to the sum of the squares of the charges of the particles passing through. This allows to identify the cases where several nuclear fragments, resulting from a peripheral interaction in the target, deposit the same energy as the single beam ion.

The ZDC is made of four towers of quartz fibres immersed in a Tantalum absorber,

placed around the beam line and read by independent photo-multipliers, so that the centroid of the beam can be measured, burst by burst. The ZDC, besides measuring the forward hadronic energy for each collision, provides a good measurement of the integrated beam intensity, burst by burst, and provides “minimum-bias” triggers, where no dimuon is required. Figure 2.16 shows the E_{ZDC} distribution measured during the 2003 Indium run, for a small sample of the collected data, for beam and dimuon triggers, compared with the spectrum given by the Venus Monte-Carlo generator.

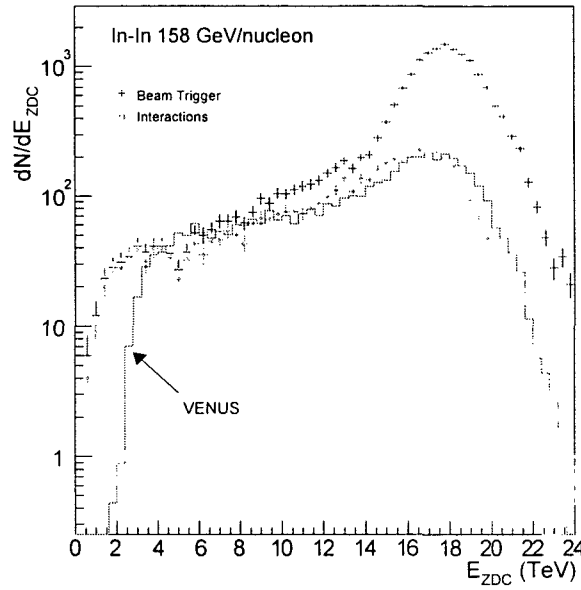


Figure 2.16: Comparison between the measured (using beam triggers) and simulated E_{ZDC} spectrum corresponding to 158 GeV/nucleon In-In collisions.

Figure 2.17 shows the distribution of the signal measured by the Quartz Blade, for beam triggers. The events with a signal below 1500 correspond to collisions in the target region.

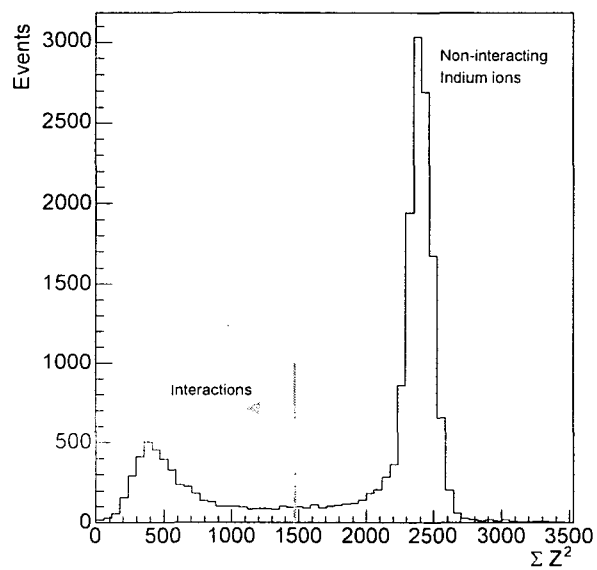


Figure 2.17: Distribution measured (using beam triggers) by the Quartz Blade, which allows us to identify events with interactions in the target region.

Chapter 3

The NA60 Microstrip Telescope

In Section 2.7.1 we have motivated the need for a vertex tracking telescope, which in proton runs is based on Silicon microstrip technology. After a brief introduction to semiconductor detectors in general, this chapter describes the microstrip sensor and the first part of the read-out chain, relevant for the raw data analysis. It also reports on its assembly and mechanical integration into the NA60 detector system.

3.1 Silicon Semiconductor Detectors

Silicon semiconductor sensors which in high-energy physics experiments are used for the purpose of particle tracking are made of a p-n junction, where p and n stands for p-doped and n-doped Silicon, respectively. One of the sides usually is finely segmented, which allows to have many individual sensing elements in one physical detector.

At the junction where the n-type Silicon is brought into contact with the p-type, a concentration gradient establishes through the presence of donor and acceptor atoms. Due to this concentration gradient the electrons diffuse from the n-type to the p-type Silicon, where they recombine with the holes of the acceptor atoms. Similarly, holes diffuse from the p-type into the n-type region, where they capture electrons from the donor atoms. At the junction, hence, a region free of charge carriers builds up, which is called the “depletion zone”. Through the recombination process the initially neutral Silicon becomes positively charged in the n-type region and negatively charged in the p-type region. The resulting electric field gradient across the junction eventually halts the diffusion process. The potential difference, in which the p-n junction is in equilibrium is called the diffusion voltage or “built-in” voltage, V_{bi} . It is typically of the order of $V_{bi} \sim 0.5$ V, depending on the donor and acceptor concentrations and the temperature at which the detector is operated.

In this depleted region charge carriers can be produced through the excitation or ionisation of the atomic electrons via thermal excitation or by the passage of an energetic charged particle. By collecting these newly created charge carriers the passing particle can be detected. In order to increase this natural depletion region over a larger zone, and thereby increasing the active area of the sensor, usually a

positive voltage is applied to the n-side of the diode. The applied voltage leads to an increased electric field across the diode and the detector becomes “reverse-biased”. By increasing the voltage, the depletion zone can be effectively extended over the whole detector thickness, since the depletion width, d , increases proportionally to the square root of the bias voltage, V_B ,

$$d = \sqrt{2 \cdot \epsilon \cdot \rho_n \cdot \mu_e \cdot V_B} \quad . \quad (3.1)$$

In this formula the built-in voltage was neglected since it is usually much smaller than the bias voltage ($V_B \approx 50 - 300$ V). Substituting material constants — the dielectric constant of Silicon is $\epsilon_{Si} = 1.06 \cdot 10^{-12}$ F/cm and the electron mobility at 300 K (for electric fields with $E < 10^3$ V/cm) is $\mu_e = v_e/E = 1350$ cm²/Vs — we obtain $d = 0.53 \cdot \sqrt{\rho_n \cdot V_B}$ μm for n-type Silicon with ρ_n in $\Omega\text{-cm}$ and V_B in Volts. The resistivity of the n-type material, ρ_n , is determined by the concentration of donor atoms, N_D ,

$$\rho_n = \frac{1}{e \cdot N_D \cdot \mu_e} \quad . \quad (3.2)$$

From these two formulae it can be seen that using an n-type Silicon with a small donor concentration, N_D , the sensor can be fully depleted while keeping the bias voltage to a minimum. For this reason, usually one side is heavily doped (in our case the p-side) so that the junction consists of p⁺-n Silicon, the “+” sign indicating the high acceptor concentration. In this way, the depletion region of the sensor extends now deep into the lightly doped junction side.

The bias voltage, which introduces the electric field, is applied to the diode via an ohmic contact either to the so-called “backplane”, which is the unsegmented side of the detector, or to the segmented side. Since in NA60 we use the former scheme for applying the bias voltage, we constrain the further discussion to this type of detector. The ohmic contact cannot be achieved by directly depositing the metal on the semiconductor surface. Such a contact would act as a junction with a depletion zone extending into the semiconductor material. To avoid this, a heavily doped n⁺ layer is introduced between the semiconductor and the metallic backplane. The use of a high doping concentration leads to a very thin depletion region. For very high N_D the depletion width is essentially zero and the leakage current at the metal-semiconductor junction is suppressed. Figure 3.1 illustrates a typical semiconductor detector.

In a depleted sensor an incident charged particle will create electron and hole pairs. These charge carriers will follow the electric field with a certain drift velocity. In addition, they diffuse uniformly outward from their point of creation, where the width of diffusion, σ_x , is given by the drift time, t_{drift} , and the diffusion constant, D ,

$$\sigma_x = \sqrt{2 \cdot D \cdot t_{\text{drift}}} \quad . \quad (3.3)$$

The diffusion constant is related to the mobility via the absolute temperature, T , given by the so-called “Einstein relation”, initially derived for ideal gases,

$$D/\mu = kT/e \quad . \quad (3.4)$$

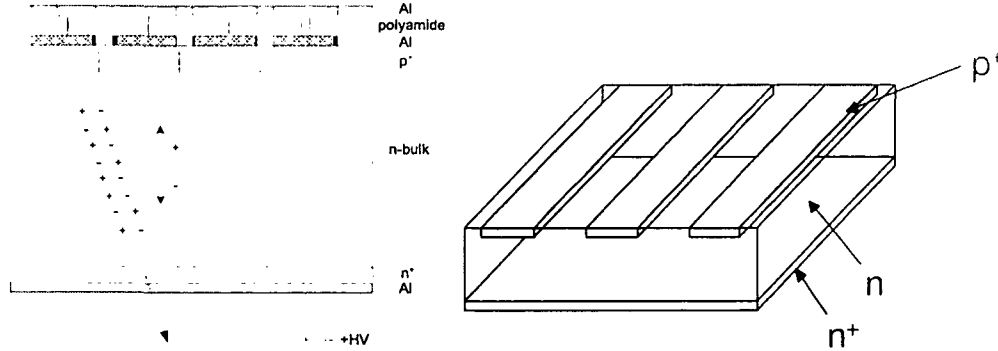


Figure 3.1: Cross-section of a double-metal layer semiconductor particle detector (left) and 3D view of a single sided segmented strip sensor (right).

For practical purposes we can estimate the drift time by assuming that the charge carriers were produced in the half thickness of the detector and by approximating the electric field by an average value, $E = V_B/d$. Using Eq. (3.1) and (3.2) we obtain

$$t_{\text{drift}} \approx \frac{d/2}{\mu_p V_B/d} = \frac{d^2}{2\mu_p V_B} = \frac{\epsilon}{\mu_p e N_D} \quad (3.5)$$

Note that in the configuration where the detector is read out on the p^+ doped side the charge carriers are the holes, denoted by the index “p”. The width of the diffusion cloud can, therefore, be estimated as

$$\sigma_x = \sqrt{2 \cdot D \cdot t_{\text{drift}}} = \sqrt{2 \frac{kT}{e} \mu_p t_{\text{drift}}} \approx \sqrt{\frac{kT}{e} \frac{2\epsilon}{e N_D}} \quad (3.6)$$

3.1.1 Energy-loss Distribution

The major process causing the energy-loss of a charged particle is the interaction with atomic electrons via their electromagnetic field. In *soft* electromagnetic interaction processes the energy is just sufficient to raise an atomic electron into the higher energy level (excitation), while in a *hard* collision the energy transfer is high enough to remove an electron from the atom (ionisation). In Silicon the energy gap and, hence, the energy to create an electron-hole pair is 1.1 eV at 300 K. However, a significant amount of the deposited energy goes into lattice vibrations, so that the effective (average) energy to create an electron-hole pair in Silicon is 3.6 eV at 300 K. The number of electron-hole pairs generated in these interactions and, therefore, the signal measured at the diode electrodes is proportional to the energy-loss of the incident particle. The number of interactions causing energy-loss per unit length and the amount of energy transferred in one single collision are statistical in nature. The energy-loss process is therefore described by a probability distribution function. For a *thick* absorber material the number of interactions in the absorber material is

very large and the energy-loss is Gaussian distributed, with a mean value which is the *average* energy-loss calculated by the Bethe-Bloch equation [20]. The energy-loss, $-dE/dx$, depends mainly on the velocity of the particle. It decreases as $1/\beta^2$ ($\beta = v/c$) for increasing particle velocity until a minimum is reached at $\beta\gamma = 3 - 4$. Particles with energies in this range are called “minimum ionising particles” (MIP’s). For muons this is the case if their momenta are higher than 300 MeV/c.

In a *thin* absorber the probability for a very large energy transfer in a single interaction is smaller, resulting in an asymmetric energy-loss probability distribution, characterised by a narrow peak with a long tail towards the rare, high energy transfers. Because of this tail, the mean energy-loss given by the Bethe-Bloch formula does not correspond to the peak of the distribution anymore. The position of the peak determines the *most probable* energy-loss instead, and the probability distribution is described by the Landau distribution.

The energy registered in a detector is, in general, smaller than the energy lost by the traversing particle. Very large energy transfers can produce secondary electrons, which themselves can excite or ionise the semiconductor atoms. These high-energetic electrons, also termed δ -electrons, often emitted under large angles with respect to the incoming particle’s direction, can traverse the detector without further interaction and can, hence, be lost for detection.

In a 300 μm thick Silicon sensor the most probable deposited energy results in the creation of $\sim 22\,000$ electron-hole pairs, or equivalently to a charge of 3.5 fC.

For a basic introduction to the working principles and the technology of semiconductor detectors the reader is referred e.g. to Refs. [21] and [22].

3.2 The NA60 Microstrip Sensor

3.2.1 Sensor Technology

The detectors used in the NA60 experiment are made of n-type high resistivity ($> 4\,\text{k}\Omega\cdot\text{cm}$) Si wafers of 100 mm diameter and 300 μm thickness [23]. The detector structure is Al/n⁺/n/p⁺/Al with the strip segmentation on the p⁺ side. The biasing of the detector is performed by applying the bias positive voltage to the aluminised backplane. The full depletion voltage, V_{depl} , for our 300 μm thick sensor can be calculated by solving Eq. (3.1) for V_{B} . With $\rho_n > 4\,\text{k}\Omega\cdot\text{cm}$ we obtain $V_{\text{B}} < 80\,\text{V}$. Around the active sensor area are five inner and five outer guard rings to prevent the flow of surface leakage current from the beam hole and the outer sensor edges, respectively, into the active area and to avoid breakdown at high voltages.

NA60 uses directly coupled sensors (“dc coupling”) without additional capacitors (“ac coupling”) between the p⁺ implant and the metallic contact. The use of additional capacitors would require an additional processing step in the fabrication of the sensors, in which the capacitors are realised by means of the deposition of e.g. a thin oxide layer (SiO₂). The advantage of an “ac coupled” sensor is that the electronics would be shielded from the leakage current of the sensor. The NA60 sensors, however, are read out by the SCTA128VG chip (see below), which easily withstands high levels

of leakage current, so that there is no need for the more costly fabrication of an “ac coupled” sensor.

3.2.2 Tracking Requirements

Each sensor provides the positions of the hits in one dimension. In order to obtain one space point, each microstrip *station* consists of two microstrip sensors (*planes*) assembled back to back, which have an inclination angle of $\pm 25^\circ$ with respect to the vertical axis, y . This inclination angle was obtained by considering two aspects for an optimal particle tracking:

- Without a magnetic field, particle trajectories are straight lines. To track the particles, the offset (x, y) of the interaction point from the beam axis and the track’s slope, given by the particle’s momentum ($\tan \alpha_x = p_x/p_z$ and $\tan \alpha_y = p_y/p_z$), have to be determined. To have the same resolution in the x and y directions, the strips of the two sensors in a given station, should be oriented orthogonal to one another (a relative inclination angle of 90°).
- Inside a magnetic field, particle tracks have a given curvature, whose radius is given by $r = p/(0.3B)$. To have an optimal curvature (C) measurement in the dipole field of PT7, whose magnetic field is directed along the vertical axis, y , and hence deflects the particles in the $x - z$ plane, *all* strips should be oriented in the vertical direction (the inclination should be 0°).

The optimisation criterion was, hence, chosen to minimise the following χ^2 :

$$\chi^2 = \left(\frac{\sigma_x}{\sigma_y} \right)^2 + \left(\frac{\sigma_y}{\sigma_x} \right)^2 + \left(\frac{\sigma(\alpha_x)}{\sigma(\alpha_y)} \right)^2 + \left(\frac{\sigma(\alpha_y)}{\sigma(\alpha_x)} \right)^2 + \frac{\sigma(C)}{\sigma_{\text{ideal}}(C)}. \quad (3.7)$$

The selected value of the inclination angle provides a $\sigma(C)$ only 5 % higher than $\sigma_{\text{ideal}}(C)$ and similar offset and slope resolutions in the x and y directions.

3.2.3 Strip Segmentation

Apart from fulfilling the geometrical requirement of matching the muon spectrometer’s angular acceptance, the sensors were designed such that their occupancy should be roughly constant across the whole active area and should be below 3% even in p-Pb interactions. The hit density in a fixed target experiment is highest close to the beam-axis. In an area $dS = 2r\pi dr$ it is given by the pseudorapidity density $dN/d\eta(r)$ and the radius r ,

$$\frac{dN}{dS} = -\frac{dN}{d\eta} \frac{1}{2\pi r^2}. \quad (3.8)$$

Figure 3.2 shows the hit density as obtained from a VENUS Monte-Carlo simulation for the z position of the first tracking plane.

To accomodate this inhomogeneous particle density the sensor has a finer granularity close to the beam hole than at larger distances from the beam axis. The

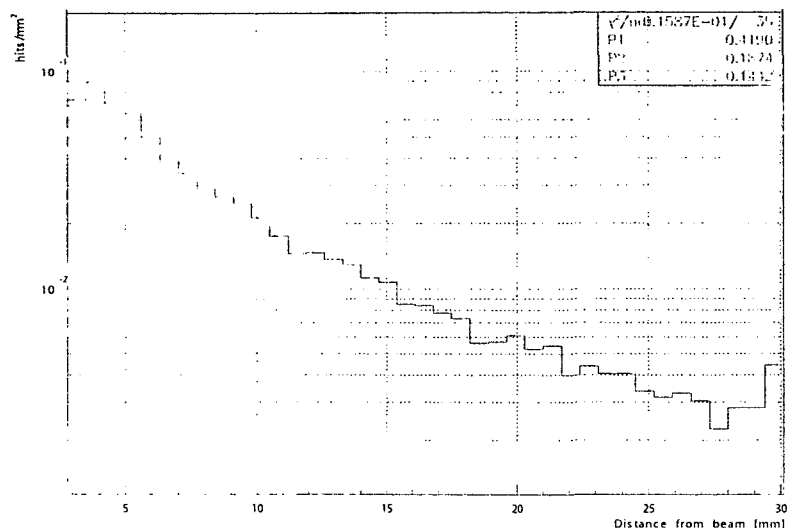


Figure 3.2: Hit density (hits per mm^2) expected in p-Pb interactions in the first tracking plane, as a function of the transverse distance from the beam. The simulation, performed using Venus and Geant, includes secondary charged tracks (due to pair creation, hadronic interactions, etc.).

sensor's active area is divided into an “inner” region with short strips and small strip pitches and an “outer” region with less granularity. The inner region covers $3 < r < 17$ mm; the outer region $17 < r < 35 - 45$ mm, giving a total sensitive area of about 50 cm^2 . The number of strips per sensor is constrained by the number of readout chips and the number of readout channels per chip. The SCTA128VG [24] chip (see below) reads out 128 strips. By using two hybrids per sensor, one on the left and one on the right side, which can accommodate up to 6 chips each, the sensor was designed to have a total number of $12 \times 128 = 1536$ strips. Given the number of strips and the requirement to keep the occupancy per sensor below 3%, both regions are furthermore divided into zones with varying pitch, ranging from 60 to $227 \mu\text{m}$. Figure 3.3 shows the design of the sensor.

Note that the sensor is designed symmetrically, with the symmetry axis inclined by 25° with respect to the y -axis, as explained above. The lengths of the strips vary mainly in the outer regions due to this rotation. On the top and bottom sides the sensors are cut to fit into the magnet's gap. The central hole of 3.6 mm diameter lets the non-interacting beam particles pass through. The dimensions and pitches of the strips of a given region are summarised in Table 3.1. In the regions where the strip length varies the length of the shortest and of the longest strips are given. The Table also summarises the grouping according to different common mode (CM) regions as will be explained in Section 4.4. The numbers given in parentheses correspond to the total number of strips in the given CM-region.

The pitch of the readout lines is $80 \mu\text{m}$. Each of them ends in two bonding pads, each with a size of $300 \times 110 \mu\text{m}^2$, separated by $700 \mu\text{m}$. The external bond pads of the even and odd strips are staggered by $500 \mu\text{m}$, see Fig. 3.4.

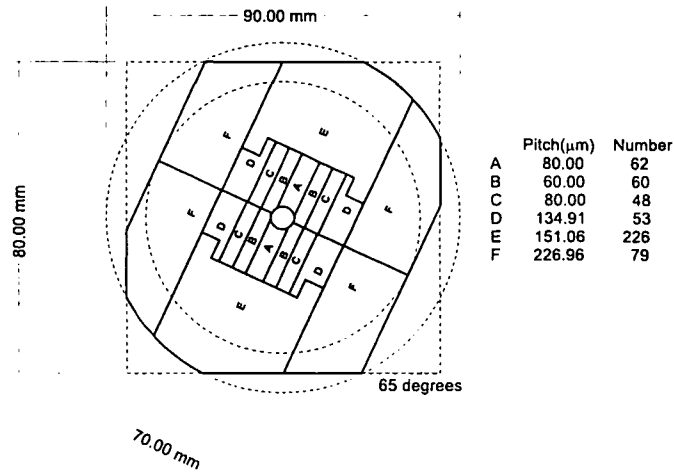


Figure 3.3: Sensor geometry, showing the different strip regions.

Given the underlying complex geometry of the NA60 sensor, a second metal layer is placed on top of a $\sim 3 \mu\text{m}$ thin polyamide layer, to route the signals from the strips

	#strip	region	length [cm]	pitch [μm]	CM-region	number
1	0 – 47	E3	2.3719 – 2.7030	151	1	48
	48 – 127	E2	2.6298 – 2.7890	151	2	80
chip 2	128 – 160	E2	2.9659 – 3.1256	151	3	33
	161 – 191	A3	1.4070 – 1.5325	80	4	31
	192 – 222	A2	1.4070 – 1.5325	80	5	31
	223 – 255	B2	1.5427 – 1.7070	80	6	33
chip 3	256 – 282	B2	1.7070	60	7	27
	283 – 330	C2	1.7070	80	8	48
	331 – 383	D2	1.7070 – 1.2070	135	9(16), 10(37)	53
4	384 – 457	F2	2.2267 – 4.1590	227	11	74
	458 – 511	B1	1.5427 – 1.7070	60	12	54
chip 5	512 – 517	B1	1.7070	60	13	6
	518 – 561	C1	1.7070	80	13	44
	562 – 566	F2	1.9833 – 2.1780	227	14	5
	567 – 598	D1	1.2070	135	15	32
	599 – 604	F1	2.7867 – 2.8396	227	16	6
	605 – 609	D1	1.2070	135	17	5
	610 – 613	C1	1.7070	80	17	4
	614 – 629	D1	1.7070	135	17	16
	630 – 639	F1	2.8502 – 2.9455	227	18	10
6	640 – 702	F1	2.9560 – 3.6122	227	19	63
	703 – 767	E1	2.1465 – 2.6394	151	20(33), 21(32)	65

Table 3.1: Characteristic strip properties for the 768 strips of half a microstrip sensor.

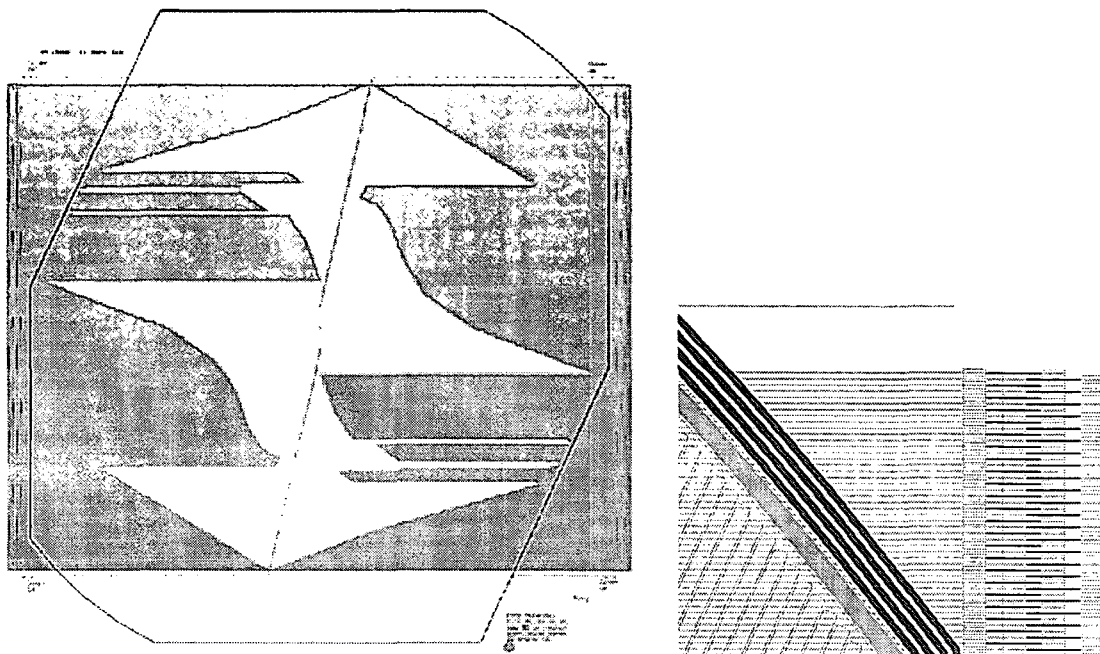


Figure 3.4: Left: Layer with the horizontal read-out lines, which bring the signal to the bonding pads on the left and right sides. The black surrounding line indicates the sensor's active area. Right: Zoom of the bond pads in the top right corner.

to the readout chips. The mask of these readout lines can also be seen in Fig. 3.4.

3.3 Read-out

3.3.1 Analogue versus Binary Read Out

The NA60 sensors use analogue read-out, where the pulse height information of each channel is preserved. Analogue read-out has several advantages as compared to a binary read-out, but it generally leads to more complex system aspects. In the following we list and briefly describe the advantages of analogue read-out and confront them with a list of drawbacks.

A crossing particle deposits a certain amount of energy in the sensor. In order to register the particle in a binary system, the discriminator threshold has to be carefully set. It should neither be too low, in which case too many “fake” hits would be recorded nor too high as to lose a real hit. The setting of the discriminator threshold has to be set *prior* to the data taking. Cases in which this threshold was not set in an appropriate way can not be corrected afterwards. In an analogue readout system no such threshold is required and the cuts for an optimal hit-extraction can be studied *after* the data have been taken.

In an analogue read-out system, if the detector and readout system are affected by a significant amount of correlated noise (i.e. common mode), the noise level can

be improved by subtracting that kind of noise.

The intrinsic position resolution of a strip is given by the distribution of hits across its pitch. Since in most cases the particles are distributed equally across the strip's pitch, the position resolution is given by

$$\sigma_x = \sqrt{\frac{1}{p} \int_{-p/2}^{p/2} x^2 \cdot dx} = \frac{p}{\sqrt{12}}. \quad (3.9)$$

where p is the pitch of the strip. In cases where the collected charge carriers arrive at the read-out electrode with a spatial spread comparable to the strip pitch the position measurement can be improved with respect to the intrinsic space resolution, σ_x , due to the fact that the generated charge becomes shared between adjacent strips. This spread can be due to track inclination of the passing particle (as schematically shown in Fig. 3.1), to diffusion of the produced charge carriers (see Eq. (3.6)) or due to a lateral drift of the charge carriers if the detector is operated in a magnetic field, in cases where the field lines are orthogonal to the charge carrier's initial velocity. Instead of taking the *centre* of the strip, the extracted hit position would now be assigned to a point between the two adjacent strips. The optimal space resolution for a binary read-out sensor, hence, can be reached if in 50% of all the cases the cluster size is two (i.e. two adjacent strips were hit) and if the remaining 50% are single-hit clusters. The theoretical position resolution would then be half of the intrinsic resolution, Eq. (3.9). In case the cluster size is larger than 1, in an analogue read-out sensor, the position resolution can still be further improved, since the relative signal amplitudes of the two adjacent strips are measured. The hit position can be obtained, e.g., by extracting the weighted average of the strip coordinates or by using special algorithms such as the so-called " η -method" [25]. In a binary read-out system it is not only the lack of amplitude measurement which does not allow this further improvement, but also the fact that the threshold for the strip with the lower charge collected cannot be adjusted independently and hence the deposited energy in the second strip could be below the detection threshold. The latter argument also holds for an analogue read out detector, but a careful study of the signal deposited in the neighbouring strip can maximise its detection probability.

The same argument holds if the charge is not only distributed in space, but also in time. In the case of NA60 four time samples of 25 ns each are collected whenever a trigger is received. By performing a weighted average of the signal in the different time slots or by fitting a functional shape to the four measured values, the time of the particle's passage within the readout gate can be determined. This time information could be used, for instance, to recognise "pile-up" events, within the accuracy of the read-out clock.

These advantages come together with a number of drawbacks. To record the analogue signal it has to be digitised and hence, the read-out electronics must comprise Analogue-to-Digital Converters (ADC's). In order to avoid distortions of the signal during data transmission, high quality cables are needed and the transmission path has to be minimised. Recording not only a "yes/no" information but rather the digitised signal amplitudes also leads to an increased data size, which in many cases

induces the need of data compression. The larger the data size, the longer the data transmission and recording, which increases the dead time of the detector system. All these additional requirements make the system more complex and increase the overall costs.

3.3.2 Overview of the Read-out Chain

The Silicon sensors are wire-bonded to and read out by 6 readout chips on both sides. The chips are placed on ceramic hybrids. The hybrids are connected to the so-called “buffer” or “service” cards. One of the tasks of the buffer cards is to amplify the outputs of the read-out chips and to convert these single-ended analogue outputs to fully differential analogue signals in order to cancel any noise picked up during transmission to the ADC cards. Furthermore, the buffer card interfaces the read-out chips with respect to power, command, clock input and trigger signal, and provides the bias-voltage for the sensor.

Behind concrete shielding to ensure a radiation safe environment, 5 metres away from the target region, these differential analogue signals are digitised in the ADC cards, where the data are compressed and formatted (for the compression algorithm see Ref. [26]). This distance is small enough to ensure a stable signal transmission in shielded twisted pair cables (“Category 6”) without losses and distortions due to the parasitic capacitance and resistance of the cables.

The whole system is fully synchronous at a clock speed of 40 MHz. This clock is generated in the ADC Central Control Board (ADC CCB). Also in the ADC CCB, the trigger signal from the experiment gets delayed and then broadcasted to all ADC cards and all SCTA readout chips (through the SCTA CCB). It is also the task of the CCBs to configure the ADC cards and the SCTA chips. For a detailed description of the whole readout chain, including the distribution of the NA60 trigger, the configuration commands for the read-out chips and the distribution of the 40 MHz clock to the readout chips and ADC cards, see Ref. [27].

3.3.3 The Hybrid

The hybrid carries the 6 readout chips. Wire bonds convey the signals from the sensor to the chips, through a pitch adapter zone, while on the other side a solid connector joins the hybrid to the buffer card.

Figure 3.5 shows the design and the realisation of the hybrid. The hybrid furthermore provides the bias-voltage for the sensor and conveys the command, power and clock from the buffer-card to the chips. The bias line ends on a golden circular pad on the right side of the hybrid. A thin wire glued to this pad brings then the high voltage to the backplane of the sensor. The hybrid consists of a 630 μm thick ceramic substrate on which 4 metal layers of 10 μm thickness are placed, interspaced by 4 isolating layers of 35 μm each.

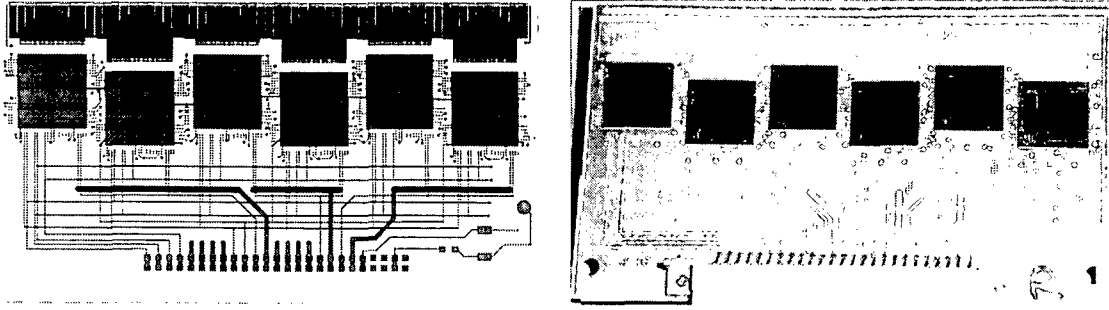


Figure 3.5: Design and realisation of the hybrid used in NA60.

3.3.4 The SCTA128VG Readout Chip

The sensors are read out by the radiation hard SCTA128VG chip [24], developed for the ATLAS SemiConductor Tracker (SCT). Figure 3.6 shows a photograph of the chip, glued onto the hybrid and wire-bonded to the pitch-adaptor on the left side. One can also see the wire bonds from the pitch-adaptor to the sensor.

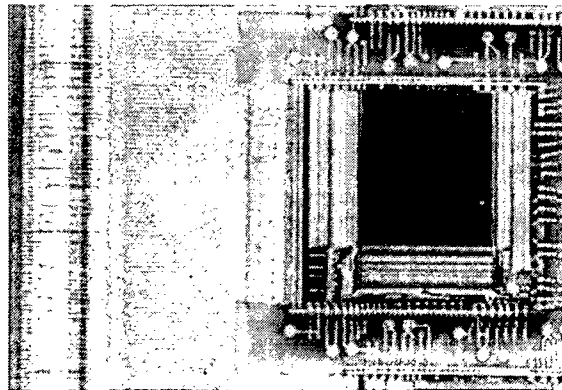


Figure 3.6: The read-out chip bonded to the pitch-adaptor on the left side.

The passage of a charged particle through the sensor excites or ionises the medium. The resulting charge carriers will enter the front-end electronics of the readout chip, which has the task to *amplify* and to *shape* the signal keeping a linear relation between the collected charge and its output voltage. This can be achieved by using a *charge sensitive* pre-amplifier, which consists of elements as depicted in Fig. 3.7 (left).

In such a circuit, where the incoming charge becomes collected at C_f , the output voltage V_0 is only proportional to the incoming charge, $V_0 \simeq -Q/C_f$ (for a given C_f) and is independent on the detector's capacitance, C_d . This is particularly important, since C_d is directly proportional to the electronic noise, as we will see in the next chapter. The gain of the SCTA128VG front-end amplifier, which is the output voltage per incoming charge, is about 50 mV/fC. Figure 3.7 (right) shows the extraction of the gain for a given channel by measuring the response of the chip to injected test pulses of varying heights.

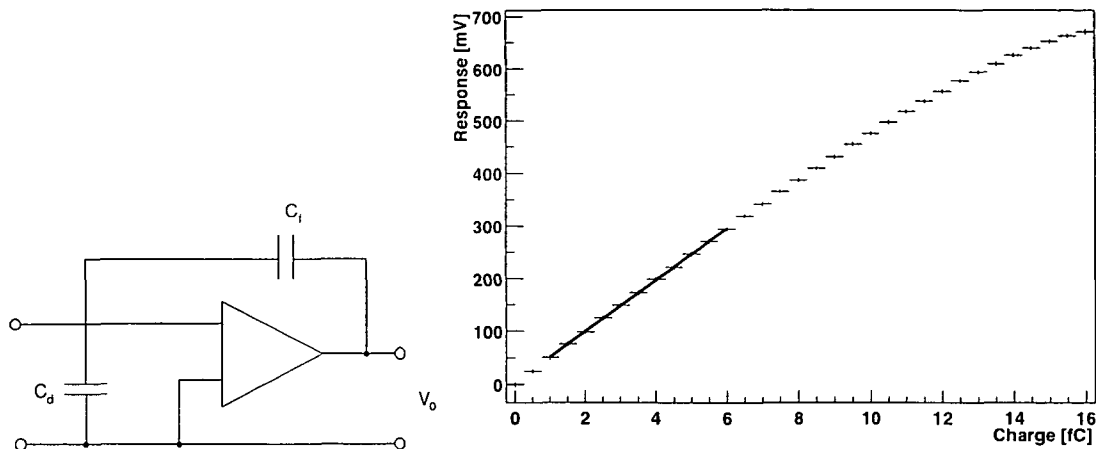


Figure 3.7: Left: Schematic diagram of a charge-sensitive pre-amplifier. Right: The gain for each individual channel can be extracted from a scan of the chip's response to injected test pulses of varying charge.

The linearity of the response of the chip was tested with calibration pulses in the range of 0–16 fC and is guaranteed in the range 0–12 fC. The given dynamic range of the pre-amplifier was optimised for charged particle detection, taking into account that a MIP deposits an average charge of 3.5 fC in the 300 μm thick Silicon sensor. The linearity in this range was tested to be guaranteed over all possible process variations (from batch to batch), temperature variations, $\pm 10\%$ variations in the power supply, before and after irradiation.

The amplified signal enters the semi-gaussian pulse shaper, which gives the signal a convenient form for further processing and optimises the *signal to noise ratio* (S/N). The shaper of the SCTA128VG chip consists of a series of CR and RC circuits (CR-RC³), which act as a bandpass filter centred on the signal's bandwidth. This suppresses the out-of-band noise and improves the signal to noise ratio.

The obtained pulse has a peaking time of 20–25 ns. This shaped signal is then sampled at 40 MHz rate and stored in a 128-cell analogue data buffer (ADB). Upon arrival of a trigger command, the SCTA chip can output 1, 2, 4 or 8 consecutive samples for each of its 128 channels. For the usage within the NA60 experiment the chip has been set to output 4 consecutive samples. In the offline analysis these four time samples are used to reconstruct the characteristic pulse shape and to identify the hit strips by applying certain threshold cuts on the extracted pulse height.

An analogue signal package from one chip consists of a seven bit header, followed by the 128 analogue channels with the physical data from the strips and a 9 bit trailer. Two chips are read out in a master-slave fashion so that the second chip has to wait until the first chip has transmitted its data stream. This sequence is the same for all the four time samples, so that the complete output of two chips follows the pattern [chip1sample1][chip2sample1]...[chip1sample4][chip2sample4], which lasts $2 \times 4 \times (7 + 128 + 9) \times 25 \text{ ns} = 28.8 \mu\text{s}$. Figure 3.8 illustrates this sequence. The low levels represent the raw data of the 128 channels of the master (M) and slave (S)

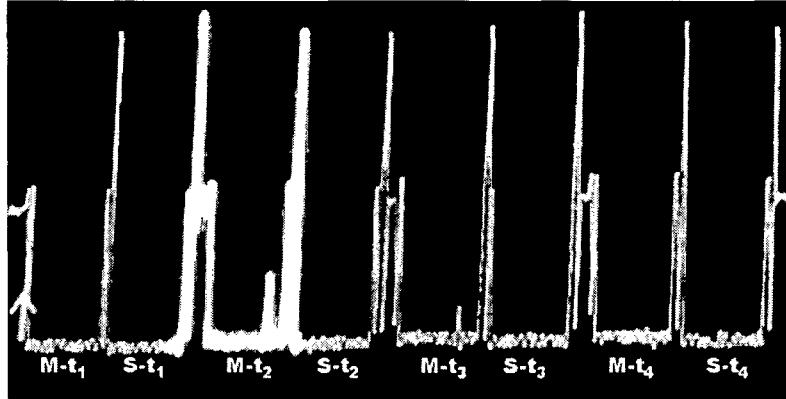


Figure 3.8: Output of two SCTA128VG readout chips, each consisting of 128 channels, in 4 time samples of the Master (M) and Slave (S) chips.

chips and for the four time samples. The “spikes” in between signal the header and trailer of the output sequence. While most of the channels show only the so-called pedestal level, we can clearly identify one hit strip in the master chip manifesting itself in a peak in the second and third time sample.

In this way, the data from the 6 chips on one hybrid are packed into 3 readout channels which enter the ADC cards. Note, however, that in the design of the NA60 hybrid each chip can be configured as the master or the slave to allow a flexible read-out sequence.

3.4 Mechanical Support and Installation

Each sensor with its two hybrids and buffer cards is held by an Aluminium frame, see Fig. 3.9.

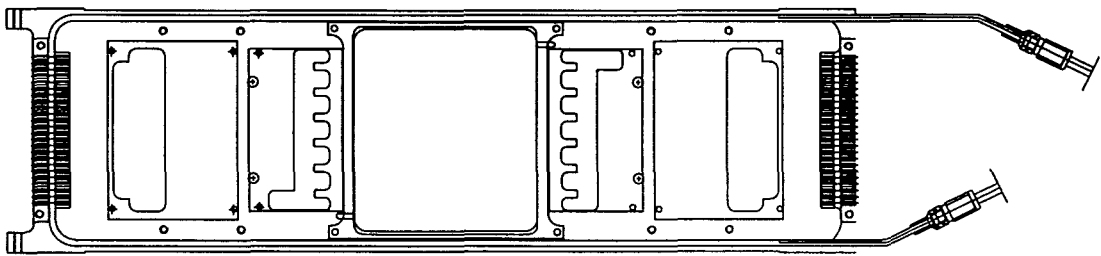


Figure 3.9: The design of one microstrip module.

The Aluminium plate has a central hole, where the sensor is positioned over a ceramic frame. This guarantees that in the acceptance of the NA60 detector the produced particles will only cross the 300 μm thick Silicon sensors, thereby minimising their multiple scattering.

To obtain one space point two sensors are placed back-to-back, interspaced by the shortest possible distance. For mechanical stability each frame is made of a 1 mm thick Aluminium alloy. Including the thicknesses of the ceramic frame and the Kapton strip, this gives a sensor interspacing of ~ 3 mm in each tracking station.

The electronic cards (hybrid and buffer card) have electronic components (resistors and capacitors) which stick out on the bottom. At these places, the Aluminium frame has holes to keep the thickness of the module to a minimum. This also allows a good thermal contact between the cooled Aluminium frame and the cards dissipating heat.

Figure 3.10 shows one finished module. We can also see that the individual stations are held by a support structure which fits in the gap of the PT7 magnet. This support allows to slide in the modules from the Jura side, at fixed z-positions.

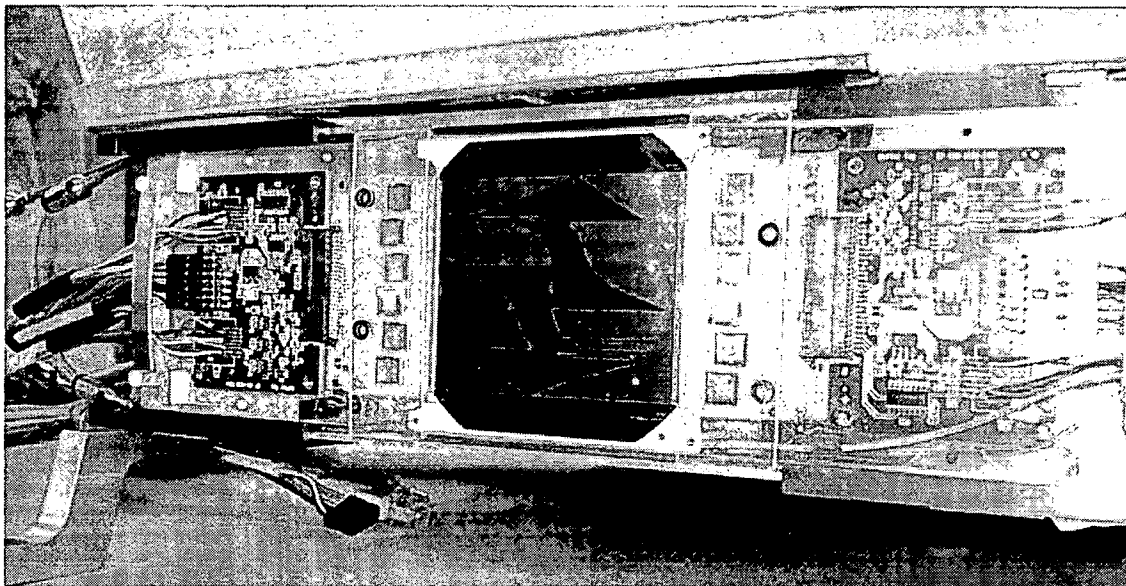


Figure 3.10: One microstrip module, in the supporting box.

Each of the 12 SCTA chips in a module dissipates 550 mW. Due to the direct contact of the hybrid with the Aluminium frame, the produced heat warms up the frame and, therefore, the sensor, in spite of the insulating ceramic and Kapton layers. In order to operate the sensor at a low temperature, thereby minimising its leakage current, the Aluminium frame is cooled with water at a temperature of around 15°C , circulating in a Copper cooling pipe running along the edges of the frame. The temperature on the hybrid and on the ceramic close to the sensor is monitored via two Platinum resistance thermometers (PT100's).

The total thickness of one module is determined by the thickness of the connector between the hybrid and the buffer card and amounts to 6 mm. Thus, the minimal interspacing between two consecutive tracking stations is 1.2 cm.

For an optimal tracking, the stations closer to the target should be placed with a small interspacing. Hence, some stations are placed touching one another. In these cases the rather thick RJ45 connectors of the shielded twisted pair cables, which are

connected to the buffer cards, cannot be used and the power and data cables are directly soldered to the buffer cards, as can be seen in Fig. 3.10.

The overall support structure holding the individual modules can be seen in Fig. 3.11, between the target and the BeO hadron absorber. This box can accom-

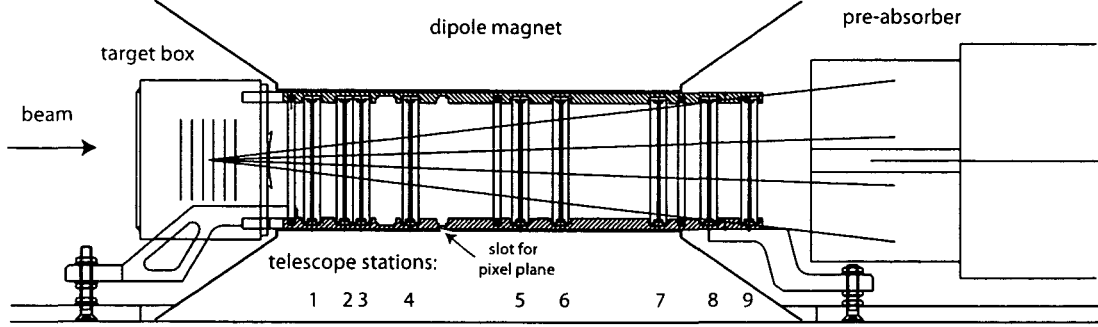


Figure 3.11: Design of the microstrip telescope to be placed between the pole shoes of the PT7 magnet. The beam comes from the left and hits one of the sub-targets indicated by 6 vertical lines. The muon spectrometer's acceptance (of 35 – 120 mrad) is shown by the four lines extending from the centre of the target system.

modate up to 9 tracking stations, located at the following distances from the target centre: $z = 7.6, 10.0, 11.2, 14.8, 23.0, 26.0, 34.0, 37.0$ and 40.0 cm. A small pixel plane was located at $z = 17.2$ cm.

3.5 Power Distribution

The low and high voltages for the microstrip telescope are provided by a SY1527 CAEN Multichannel Power Supply [28], which can be remotely controlled. The three low voltages, needed for the operation of the hybrid and of the buffer card are grouped into one thick cable to facilitate the connection. The CAEN crate is situated 5 m away from the sensors. In order to compensate the resulting voltage drop due to parasitic resistances in the cables, the low voltage cables are equipped with so-called “sense-wires”, which allow the power supply to deliver the programmed voltage at the far end of the cables.

3.6 Cooling Aspects

One of the sources of detector noise is the thermal excitation of electrons into the conduction band. The resulting current, termed *leakage current* I_{leak} , is a function of the temperature,

$$I_{\text{leak}}(T) \propto T^2 \cdot \exp\left(-\frac{E_g}{2k_B T}\right), \quad (3.10)$$

where E_g is the energy gap ($E_g(\text{Si}) = 1.1$ eV) and k_B the Boltzmann constant. The leakage current doubles if the temperature of the sensor increases by 7 °C. Thus, the

heat produced by the readout electronics (chips and buffer card) must be efficiently removed. By being placed in the gap of the PT7 magnet, the telescope is furthermore exposed to an ambient temperature of around 25 °C.

Previous to the data taking period elaborate tests on an optimal cooling system were carried out, see Ref. [29]. The working temperature of 20 °C, being significantly above the dew point, given the observed low humidity levels in the experimental zone, was identified as a value that ensures proper operation of the sensor while keeping the system aspects relatively simple (no problems with condensation, no need for vacuum, ...).

To achieve such temperatures, each module is equipped with a Copper pipe, with an inner diameter of 1.5 mm, in which water circulates with a temperature of around 15 degrees. The cooling of the water for all modules of the telescope is provided by a refrigerator which delivers cooled water with a pressure of up to 3 atm. This device needs no external water supply since it recycles the used water. The main cooling pipe, coming from the refrigerator, is split into smaller pipes to supply each module individually. The water enters the module from the bottom and exits on the top. Should, despite of a nominal operation *above* the dewpoint, condensation occur on the entrance of the cooling pipes, the water will not drop onto the cables or electronic cards.

3.7 Assembly Tests Prior to the Data Taking

After the selection of good read-out chips with almost no noisy channels, they were glued and bonded onto the hybrids. Then the chips went through a series of quality checks. In case of negative results, they were unbonded and exchanged with new ones. Chips which had one or at most two noisy channels were used in regions where the strips were outside of the detector's geometrical acceptance (we will see in Chapter 5 that for the first three tracking stations the "outer" regions are not used in the tracking).

Figure 3.12 shows such a quality check for two chips (the master and the slave chip) mounted on a given hybrid. These quality checks required uniformity of the gain in all the channels and measured noise values below a certain value. We can clearly see one strip which has twice the average strip noise.

Once the hybrids passed the tests, they were bonded to the sensor, previously glued onto the Aluminium. During the test of the first assembled modules we found that the microstrip sensors systematically had very high levels of "leakage current", which prevented their proper biasing. After a lengthy debugging phase we realised that these currents resulted from a resistive contact between the back side of the Silicon wafer and the end of the top most readout lines. The sensor mask was designed to cover the largest possible area within the 4 inch diameter wafers. While the active strips were always well within the Silicon, in many sensors the readout lines which end up in the top corner of the sensor were too close to the physical edge of the wafer, due to a small misalignment during the metal deposition phase. Once the problem was understood, the contacts between those extreme readout lines and the

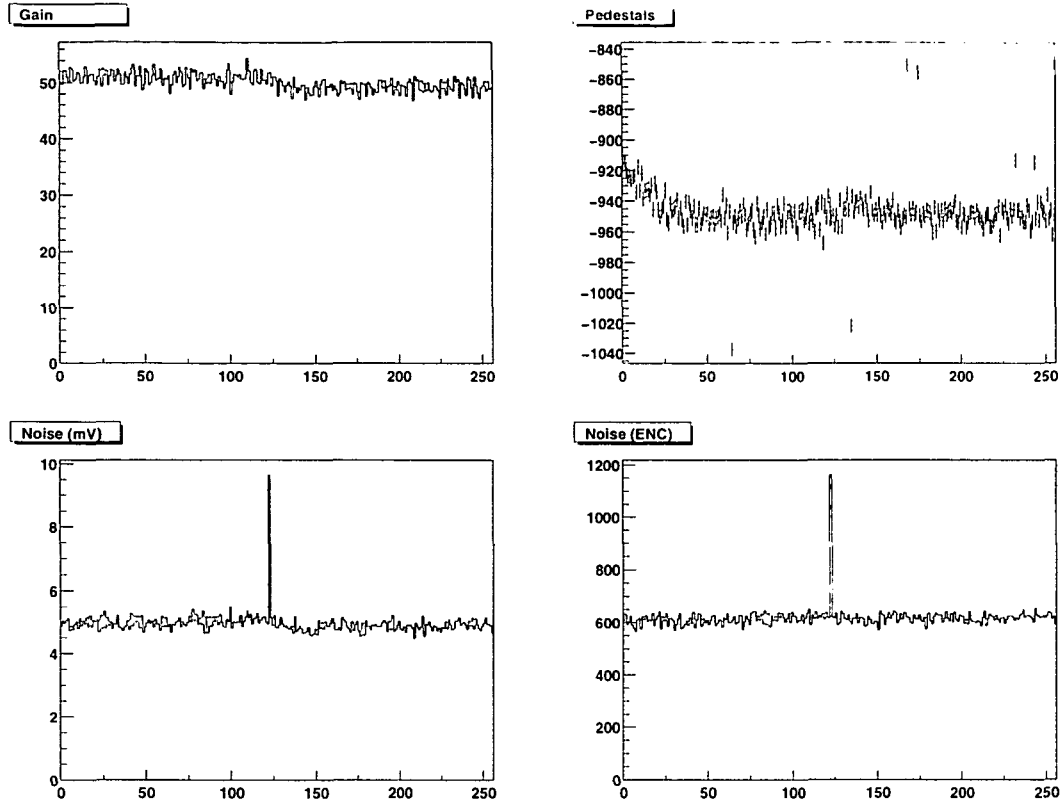


Figure 3.12: Extracted gain (in mV/fC), pedestal (in mV) and noise levels (in mV and ENC) for each of the strips from two chips. The pedestals will be addressed in the next chapter.

back side of the sensor were cut away, immediately decreasing the “leakage” current from hundreds of μA to just a few μA , in most of the sensors. Only one out of 18 sensors did not recover, and could not be used. Finally, 16 modules could be produced and installed in the telescope box.

Chapter 4

Raw Data Analysis of the Microstrip Sensors

The analysis of the raw data from the microstrip sensors proceeds in several steps. For each strip in the telescope the pedestals have to be subtracted from the raw data and the total noise evaluated. Due to electronic pick-up in a given event the pedestal values of several consecutive strips can take on higher or lower values than the average values, which is known as *common mode* (or correlated noise). Once the pedestal values and the common modes are subtracted from the raw data, the hit extraction of the sensors can be performed. From the obtained noise and occupancy levels we can mask the noisy and “absent” strips. In the following sections these steps will be outlined. The performance of the telescope as used in the June 2002 run will then be extensively discussed.

Let’s first explain certain expressions that we will use very often in the next pages. In the period of data taking a “run” is defined as an ensemble of collected events which were taken under the same conditions. This includes the beam intensity, the currents of the two magnets and the number of detectors acquiring data. Each triggered event gets assigned to a certain burst, a well defined time window with beam (in the proton run: 4.8 s), followed by a period with no beam. Each run consists, therefore, of a certain number of bursts, which themselves consist of a number of triggered events. A run typically lasts between half an hour and several hours.

We say that a strip was “hit” when its signal (after pedestal and common mode subtraction) exceeds a certain threshold, defined on the basis of the uncorrelated noise of the strip. A hit should signal the passage of a charged particle, but it can also be due to exceptionally high noise produced by the sensor or by the associated read-out electronics channel.

4.1 Strips Numbering Convention

The numbering of the strips which is given by the read-out sequence, can be seen in Fig. 4.1: strip number “0” is situated on the left side of the sensor on the lower edge in chip “L1”. The counting continues over all strips in the subsequent chips

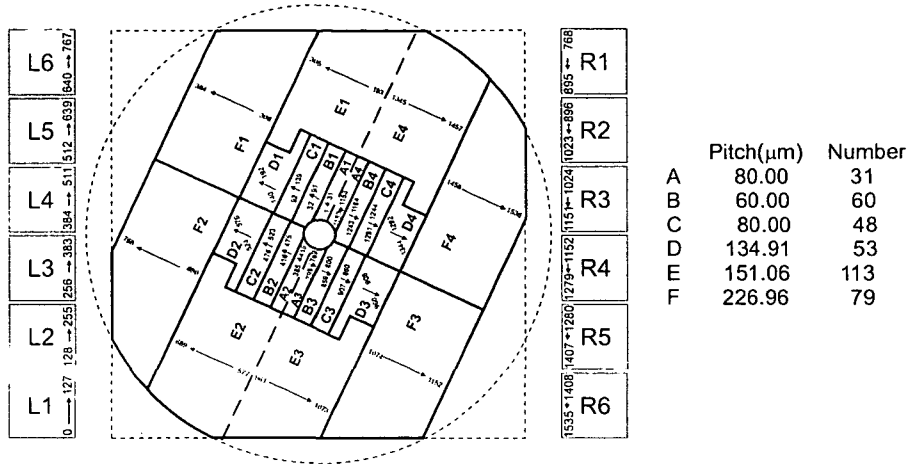


Figure 4.1: Strip numbering convention.

up to strip 767 in chip “L6”. In order to read out the sensor’s symmetric strips in the same sequence, the reading out of the second side starts on the top most chip, “R1” and ends with the last strip in chip “R6”. The numbers given in each region of the sensor refer to the numbering used internally in the NA60root framework for the clusterisation of the hit strips.

Note that NA60 uses a standard right handed coordinate system, in which the positive x -axis points to the right. This implies that the positive z axis points into the upstream direction. The chips “R1” to “R6”, hence, read out the “Jura” side, while the left chips “L1” to “L6” read out the chips on the “Salève” side.

4.2 The Pedestals

In the ADC cards the analogue signals are digitised by transforming the continuous values from mV into discrete ADC units. It is this output which we call the “raw data values”. By averaging the output of the ADC cards of each strip over many events — excluding events where a particle deposited a certain amount of charge and which will have a much higher ADC value — one can calculate the “base” level of each strip, which is called the “pedestal”.

For each strip, four raw data values corresponding to the 40 MHz sampled pulse shape are recorded. Due to a transient effect, when the readout chip starts to transmit data, the pedestal values for the first time sample are slightly higher than for the subsequent samples. Figure 4.2 shows the two sets of pedestal values for each strip of a given sensor (due to the symmetry reasons outlined in the previous chapter, we constrain the discussion from now onwards to the strips of one half of the sensor). Within each chip the pedestal values are roughly constant as a function of the strip number, except for the first few strips, which have slightly higher pedestals, also due to a transient effect.

We can see that the pedestal values range from ~ 15 to ~ 30 ADC counts. The

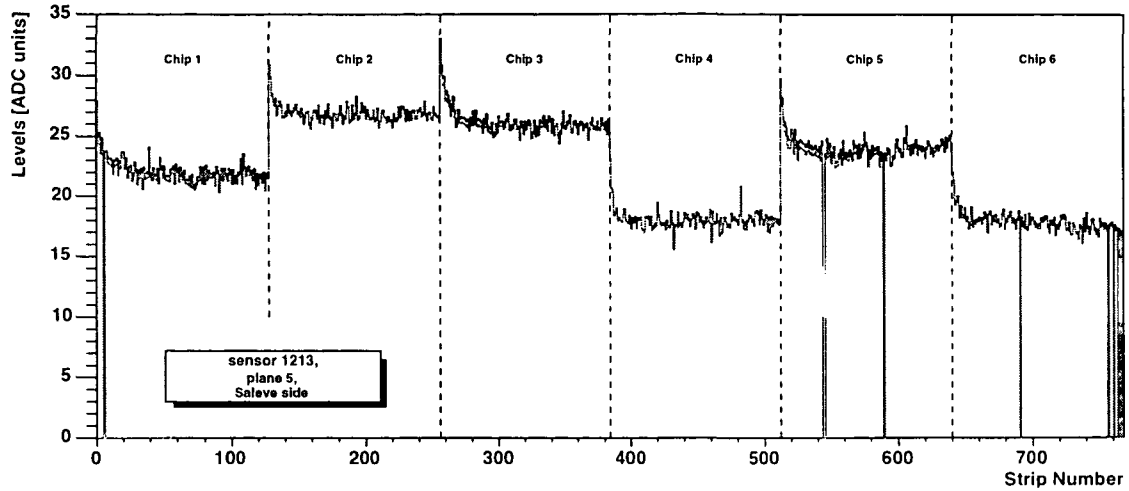


Figure 4.2: Pedestals for the strips of half a sensor. The slightly higher pedestal curve (black) is obtained from the first time sample, while the lower curve (red) was obtained by averaging over time samples 2, 3 and 4. The strips 6, 545, 546, 590 and 691 have been masked, as will be explained later.

levels are mainly determined by the individual chips' operating voltages. It is of no importance where this level sits, provided it is well above zero. The ADC cards cannot output negative ADC units; too large deviations from their mean value could lead to an “underflow” and to a loss in resolution since the underflow is coded as 0 ADC units. Figure 4.2 shows, furthermore, that in this particular sensor every second strip of the very last few strips was not wire-bonded, due to the problems described in Section 3.7 (the reason that only every second strip is affected is due to the fact that the bonding pads of the odd strips are further away from the sensor edge).

4.3 The Noise

Noise is defined as the RMS fluctuations of the raw data values around their mean (i.e. pedestal) values. After having verified that the noise levels are the same for all four time samples, we decided to calculate one single noise pattern from an average of all four samples.

In semiconductor detectors two types of noise sources are distinguished: the detector's intrinsic noise and the noise generated by the read-out electronics. The former is given by the Landau fluctuations in the generation of electron-hole pairs by an incident particle when depositing energy through ionisation and excitation. The electronics noise is usually characterised by the *total equivalent noise charge (ENC)* in order to compare this electronics noise directly to the “detector noise” and the signal, which are given in units of the elementary charge e^- . The ENC is defined as the ratio of the noise at the output of the front-end electronics to the signal ampli-

tude due to one electron charge, e . The electronics noise is understood to consist of several independent noise sources [30], to be added quadratically. We will first list the electronics noise sources which are independent of the sensor's geometry (i.e. strip length, strip pitch, detector thickness, etc.) and which will contribute to the noise pattern in a constant way, for each chip. In the remaining part of this section we will then discuss the impact of the individual strips on the observed noise pattern.

- In case of a pre-amplifier using bipolar transistors we can begin by considering the following three independent contributions: ENC_{leak} , ENC_{bc} and ENC_{fr} . The ENC_{leak} is the “shot noise”¹ of the detector's leakage current, created in the detector's bulk and surface, $ENC_{\text{leak}}^2 \propto I_{\text{leak}}^d$. The leakage current in the bulk comes from minority carrier diffusion across the pn-junction and the thermal generation of e/h pairs within the depletion zone. In order to reduce the leakage current from the surface, which is due to the existence of relatively high voltage gradients, Silicon detectors usually contain guard-rings, as briefly described in Section 3.2.1. The leakage current I_{leak}^d of a given strip is usually less than 1 nA. ENC_{bc} is the shot noise of the base current of the pre-amplifier, $ENC_{\text{bc}}^2 \propto I_b$, which is of the order 1 μA . ENC_{fr} is the shot noise of the current in the feedback path and is inversely proportional to the feedback resistor, R_f : $ENC_{\text{fr}} \sim 2V_{\text{th}}/R_f$, with the thermal voltage, $V_{\text{th}} = kT/q = 25 \text{ mV}$. The SCTA128VG pre-amplifier's feedback resistance is of the order of 100 k Ω , so that ENC_{fr} is $\sim 0.5 \mu\text{A}$. Out of these three contributions the latter two, ENC_{bc} and ENC_{fr} , are the dominating ones and the noise, which comes through the detector's leakage current, ENC_{leak} , is usually very small.

The so-called “flicker” noise, $ENC_{1/f}^2$, is found in most active components of the read-out chain. Because its noise spectrum is inversely proportional to the frequency it is often referred to as $1/f$ – noise. The amplifiers of the SCTA128VG read-out chip have a very narrow bandpass characteristic at high frequencies ($\sim 40 \text{ MHz}$), so that the contribution of this source of electronic noise is negligible.

- ENC_{preAmp}^2 is due to random (thermal) motion of electrons in resistors and due to the shot noise of collector currents in amplifiers and is, hence proportional to the temperature, T . More importantly, this noise is directly proportional to the capacitances present in the system, which are usually dominated by the detector's own capacitance. In order to minimise the overall noise, the detector capacitance should be kept to a minimum.

We will now extensively discuss the influence of the detector capacitance of the NA60 sensors on the total noise. By considering the sensor's geometrical aspects, we can distinguish three components of strip capacitance.

¹An electronic component through which a “constant” current $I = Q/t$ flows is subjected to variations in the current, ΔI , termed “shot” noise, due to the statistical fluctuations in the (quantised) number of charge carriers, $\Delta Q = \Delta N \cdot q$. The smaller the number of charge carriers through the device, the larger the resulting shot noise.

- The *inter-strip capacitance* is proportional to the strip length and inversely proportional to the distance between two neighbouring strips, which roughly increases with the strip pitch.
- The *capacitance to the backplane* is given by the area A of a given strip and is inversely proportional to the depletion depth d ,

$$C = \epsilon \frac{A}{d} \quad . \quad (4.1)$$

Thus, in order to minimise the noise resulting from this contribution, the detector should always be operated in fully depleted mode.

- The *overlap capacitance* exists only in double-metal layer technology where the second metal layer, the read-out lines, serves to convey the strip signals to the edges of the sensor. The contribution to the noise should be given by the overlap area of these two metal layers.

An elaborate study [31] was performed to fit all possible combinations of these geometric parameters to the noise pattern measured as a function of strip number. The following formula explains reasonably well the observed noise for a given strip i ,

$$\text{noise}(i) = p_1 + p_2 \cdot A_{\text{strip}}(i) + p_3 \cdot l_{\text{ro}}(i) + p_4 \cdot A_{\text{overlap}}(i), \quad (4.2)$$

where A_{strip} is the strip area (obtained by multiplying the pitch with the strip length), l_{ro} is the length of the read-out line which reads strip i , and A_{overlap} the overlap area of a given strip with all its crossing read-out lines. The strip length, strip area, the length of the read-out lines and how often a given strip is crossed by the read-out lines can be seen in Figs. 4.3–4.6, as a function of the strip number, for half a sensor. The width of the readout lines is 30 μm .

Figure 4.7 shows the noise pattern measured for the right side of sensor 1217, fitted with the above formula. The different contributions are also shown. The dashed line represents the contribution of the strip area, the dotted line the length of the read-out line, the dash-dotted line the crossing area and the solid line represents the constant term, specific of each chip, representing the electronic noise independent of the sensor's geometry. This contribution is also present if the strip is not bonded at all. Since each chip has its own individual noise level, the parameter p_1 is slightly different for each chip. Table 4.1 lists the obtained fit parameters.

From Fig. 4.7 we see that the chip-specific electronic noise is significant and contributes more than 50% of the noise of the strips with small area. In the testing phase of the sensors and of the read-out chain we measured the noise pattern of a sensor with two series of strips not bonded, see Fig. 4.8. The noise of the first 27 strips of chip 5 (strips 513–540) and of 6 strips in chip 6 (strips 651–657) is ~ 0.6 and ~ 0.7 ADC units, respectively. These values are in excellent agreement with the numbers obtained from the fit (Table 4.1). Figure 4.7 also shows that the sensor specific noise is dominated by the contributions due to the second metal layer, i.e. the read-out lines and the overlap area between read-out lines and active strips.

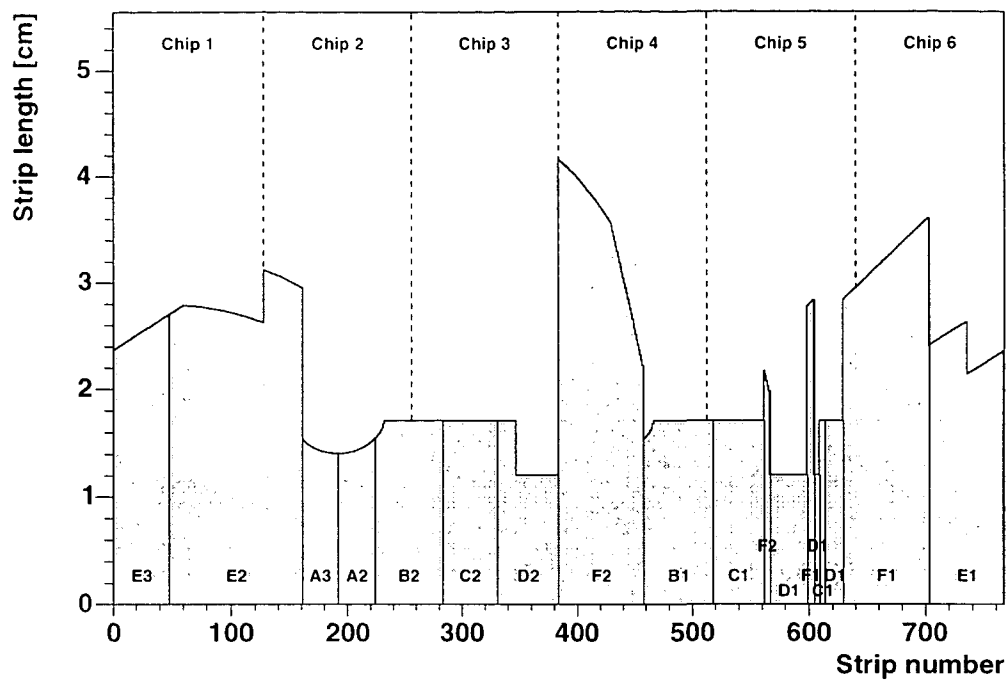


Figure 4.3: Length of each strip. The labels indicate the regions mentioned in Fig. 4.1.

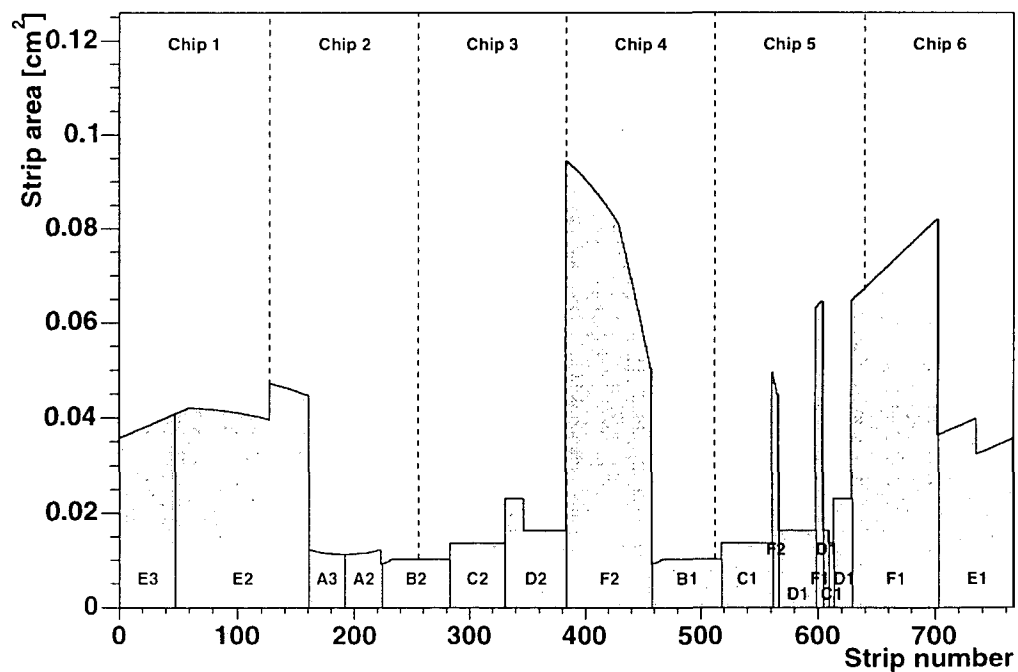


Figure 4.4: Area of each strip.

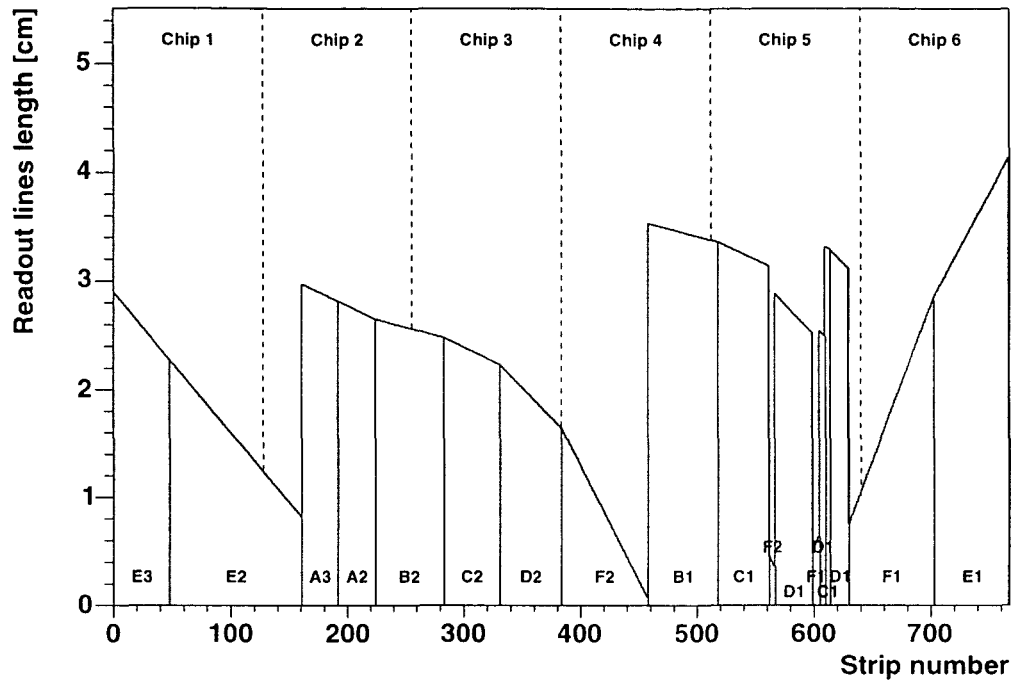


Figure 4.5: Length of the read-out lines which read each strip in the sensor, ignoring the differences of $500 \mu\text{m}$ due to the fact that the even and odd lines end on different columns of bonding pads.

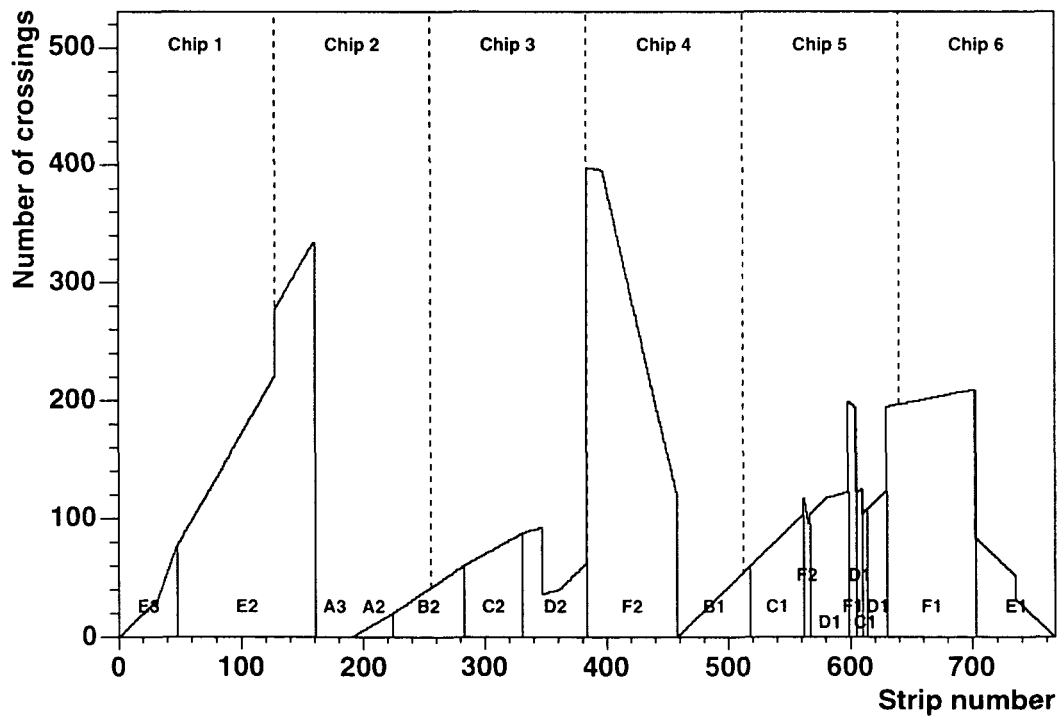


Figure 4.6: Number of read-out lines crossing the individual strips.

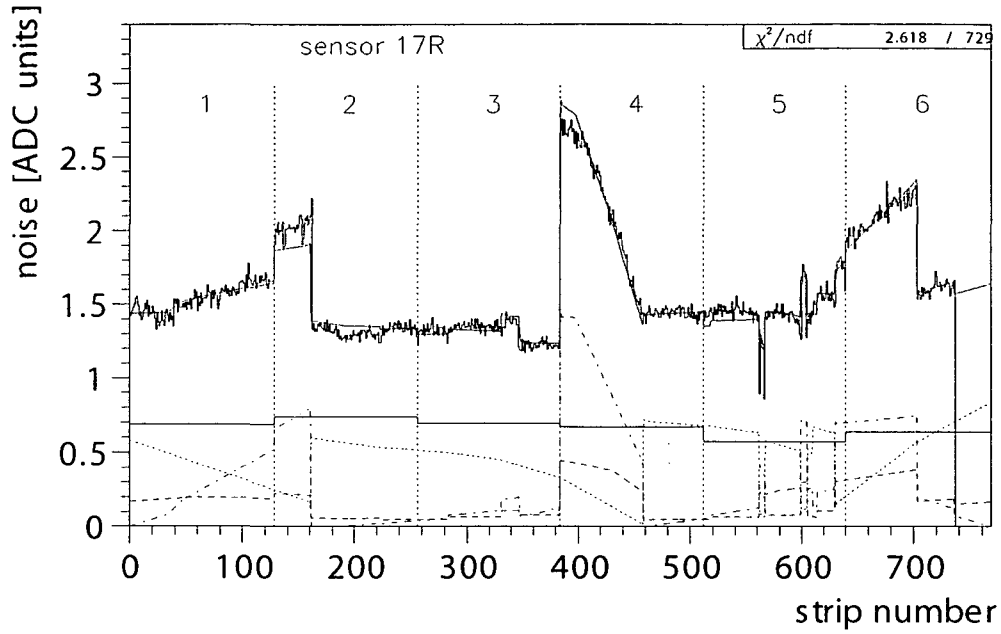


Figure 4.7: Measured noise pattern of the right side of sensor 1217, fitted with the function given in Eq. (4.2). The curves correspond to the chip-specific noise (solid), to the strip area (dashed), to the length of the read-out line (dotted) and to the overlap area of the strip with all the crossing read-out lines (dash-dotted).

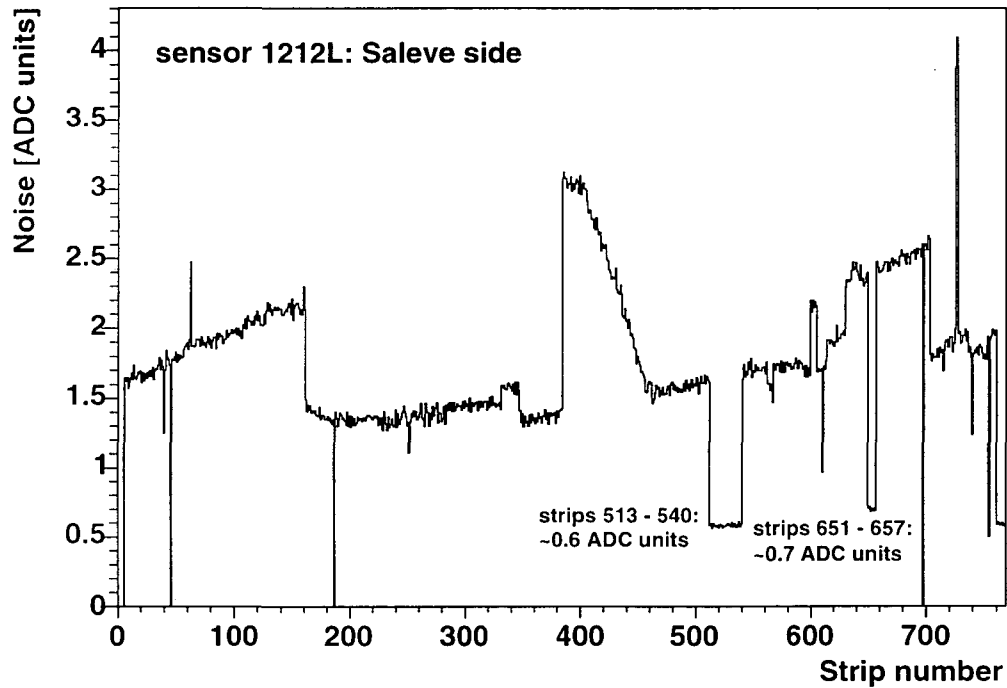


Figure 4.8: Unbonded strips have noise levels of the order of 0.6-0.7 ADC units.

p	value	units
p_{1a}	0.7 ± 0.3	ADC
p_{1b}	0.7 ± 0.3	ADC
p_{1c}	0.7 ± 0.3	ADC
p_{1d}	0.7 ± 0.4	ADC
p_{1e}	0.6 ± 0.3	ADC
p_{1f}	0.6 ± 0.4	ADC
p_2	4.7 (fixed)	ADC/cm ²
p_3	0.2 ± 0.1	ADC/cm
p_4	0.16 ± 0.05	ADC/(10 ³ cm ²)

Table 4.1: Fit parameters, as given in Eq. (4.2).

Prior to the wire-bonding of the sensors to the hybrids, the hybrids and the chips were tested, see Section 3.7. Their noise was measured in mV, which by measuring the gain of each channel can be directly converted into ENC units. From these measurements, shown in Fig. 3.12, we know that the constant electronic noise amounts to $\sim 600 e^-$ ENC. This allows us to convert the ADC units into ENC, one ADC unit corresponding to an ENC of $\sim 1000 e^-$. The total noise, which is between 1.5–3.0 ADC units for the individual strips, hence, amounts to about 1500–3000 e^- .

4.4 Common Mode

The common mode (CM) is an effect due to changes in the voltage, which -- through capacitive effects -- are translated into electric currents flowing into the read-out system, where they get amplified and registered. The common mode can be induced by electronic pick-up from the electronics chain, including voltage changes in the power supply, by capacitive effects within the cables or from the pre-amplifier, etc. Another source could be sudden local “discharges” from within the sensor, which lead to sudden changes of the bias-voltage, which cannot be compensated fast enough by the power supply.

Independently of the specific source of common mode, this kind of noise has the property that it affects several adjacent strips in a correlated fashion and must be evaluated on an event by event basis.

In the previous section we have seen how the strip’s capacitance influences the level of noise. Due to the fact that we have many strips with different lengths and pitches and hence different capacitances, we have evaluated the common mode separately in 21 independent regions. In Table 3.1 we list the strips which were grouped to extract the common mode.

After having subtracted the pedestals, the data of the neighbouring strips in a given CM region are fitted with a straight line, excluding the outliers coming from hit strips. This is done separately for each time sample. The outcome of this fit is then deduced from the pedestal-subtracted raw data of each strip. In this way, the average value of non-hit strips becomes zero. We have verified that a constant

or linear common mode subtraction along the whole chip still leaves unsubtracted noise in the sensor, while a linear common mode subtraction within each of the defined common mode regions further reduces the noise level. Figure 4.9 illustrates the procedure, with the curves in the upper and lower panels corresponding to the common mode uncorrected and corrected values, respectively, as a function of strip number. The black lines in the upper panels represent the outcome of the fit in each of the regions. In CM regions with only 5 or 6 strips a constant fit is performed for stability reasons.

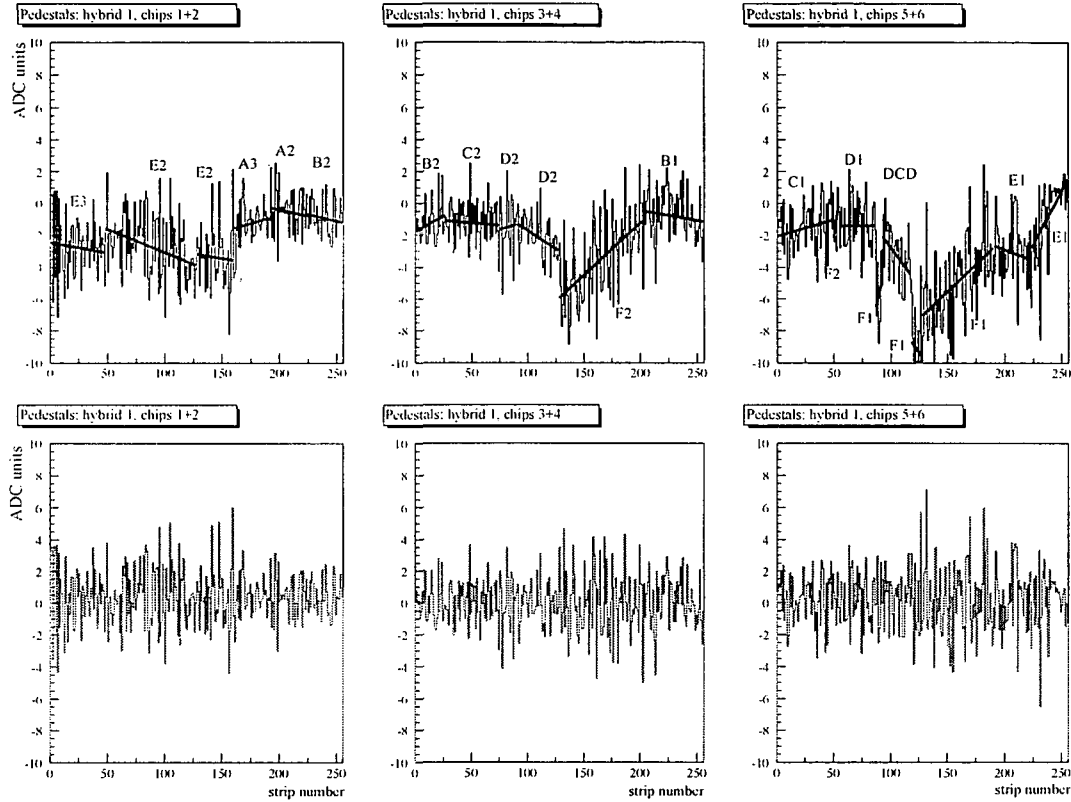


Figure 4.9: Pedestal subtracted raw data values, uncorrected (top panel) and corrected (bottom panel) for common mode as a function of the strip number. The black lines indicate the result of the fit.

4.5 Strip Masking and Calibration Files

Some of the strips have exceptionally high noise levels or could not be bonded, due to the reasons outlined in Section 3.7. These strips have to be masked, since their “random” response could lead to unwanted hits or they would disturb the correct common mode evaluation. The following list shows the steps used to identify these strips.

- For each sensor, the noise pattern is visually analysed to identify strips with an obviously different noise level than its immediate neighbouring strips, with the same geometrical characteristics. Such strips are permanently masked for all runs.
- For each run, strips with a noise higher than 5 ADC units or an average occupancy higher than 10% are also masked.
- Furthermore, and also for each run, to ensure a correct common mode evaluation, all the strips of a given common mode region were masked when more than 40% “inactive” strips were identified in that region.

Out of the 14 operated planes, 10 have less than 3.5% masked strips for most of the time, 2 planes around 6% masked strips, and the remaining two planes have slightly more than 50% masked strips, due to the fact that only half of the sensor was read out (see Section 4.7).

Due to slight performance variations in different data taking periods, we created one calibration file for each run, provided the run consisted of a sufficient number of collected triggers (more than 2000 events). A calibration file consists of the two pedestal values and the noise level for each strip and whether the strip was masked or not. The masking of each strip contains also the efficiency of each strip (see Sec. 4.7.2), which is used for the Monte Carlo simulations. Since the observed occupancy levels were small, as will be described in Section 4.7.4, there was no need to obtain the calibration files from so-called “pedestal runs”.

Since the subtraction of the common mode requires the knowledge of the noise and pedestal levels for each strip, the calibration files are obtained in several “refinement” steps. In a preliminary step the pedestals and the noise levels are calculated without correcting for common mode and assuming that no strips at all were hit. In the second iteration the common mode is calculated and subtracted from the overall noise and the preliminary noise is used to reject hit strips from these calculations. A third refinement step ensures then the best pedestal and noise evaluation, based on the previous knowledge. In the final step the masking of the strips is performed.

4.6 Digitisation

In the following we will explain three different methods to extract the hit strips, stating the advantages and drawbacks of each of these methods.

4.6.1 Fitting the Four Time Samples

For each collected charge, the read-out chip produces a well-shaped signal, which is sampled at 40 MHz. Figure 4.10 shows a typical example of these four time samples, already pedestal and common mode subtracted, produced as a response to a passing particle.

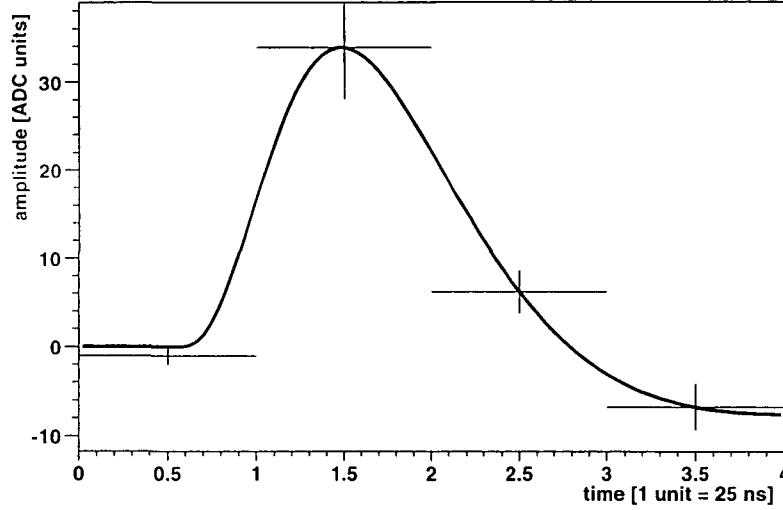


Figure 4.10: Fit of the four time samples of a given strip. The extracted pulse height would allow to measure the (relative) charge deposited by a passing particle, expressed in ADC units.

The shape of this pulse is given by the sequence of RC- and CR-circuits of the readout chip and can be described by a functional form (see Appendix B). This function has four parameters: the delay of the pulse, the pulse height, a parameter related to the undershoot of the pulse, and a parameter related to the peaking time of the pre-amplifier, which is around 20–25 ns. Since we cannot extract four parameters from the measurement of four time samples, the latter two parameters were fixed from scans in the laboratory with well defined calibration pulses and collecting *eight* time samples. To extract the signal, hence, the four time samples of each strip are fit, leaving only the pulse height and the delay as free parameters. To identify a hit strip the extracted pulse height (raw value minus pedestals and common mode) is then compared to a well defined threshold value (usually a few noise standard deviations). This method allows to extract not only the pulse height of the signal, which is a measure of the energy deposited in the given strip, but also to measure the time, within the 100 ns readout window, when the particle passed. Although the time resolution of such a measurement is not very good, it should allow to identify pile-up events to a certain extent.

This method was applied in the initial phase of the data analysis, since it allowed us to evaluate the behaviour of the strips by studying the obtained Landau distributed curves of the deposited energy, but was not used in the final reconstruction of the June 2002 data. The essential problem is that this method requires having measured all the four time samples. Due to problems in the compression algorithm of the raw data during the data taking, there is a fraction of events in which the data of one or several chips were corrupted in one of the four time samples. Hence, there are cases where only 3 time samples are available for a given strip.

4.6.2 Applying Simple Cuts to the Measured Values

An alternative method, much less time consuming, is to directly apply a cut to one or several consecutive time samples without the prior fit to the four samples to extract the peak height. This method is optionally implemented in NA60root, tagging a strip as hit, if 2 time samples are above 2σ or if 1 time sample is above 4σ , where σ is the uncorrelated noise of that given strip.

4.6.3 Applying a Probability Cut

To avoid the time consuming fit of the four time samples and to avoid having to assume any “knowledge” of the signal shape, a third method can be used, which only relies on statistics. Moreover, this method does not require the measurement of the 4 time samples. In fact, it could even be applied to strips only containing one time sample. This method, however, does not allow to extract any information about the amount of energy deposited. It simply gives the probability that the strip was hit or not.

By definition, pure random noise is Gaussian distributed. We can, hence, compare the χ^2 , calculated as $\chi^2 = 1/n \sum_i x_i^2 / \sigma_{\text{strip}}^2$, where n is the number of time samples and x_i are the pedestal and common mode subtracted raw data values, centered at zero for strips without a hit, to the mathematical distribution of a χ^2 distribution with n degrees of freedom,

$$\frac{dN}{d\chi^2} = \frac{(\chi^2)^{n/2-1} \cdot e^{-\chi^2/2} \cdot 2^{-n/2}}{\Gamma(n/2)} \quad (4.3)$$

For strips which are *not* hit, the probability of the χ^2 should be uniform over the whole interval from 0 to 1. Hit strips for which the signal is well above the noise level will lie in the tail of this Gaussian noise distribution and, therefore, have a rather low “noise probability”. Figure 4.11 shows the χ^2 probability obtained from the strips in the first plane.

While the non-hit strips are reasonably uniform across the interval from 0 to 1, the signal peaks sharply at very low probabilities. In the inset of the figure, we show the probability distribution below 0.2%. We can clearly see that by applying a cut at $P(\chi^2) < 0.1\%$ we keep all the hit strips, while rejecting all but 1 permill of the non-hit strips.

4.7 Performance in the June 2002 Run

4.7.1 Bias Voltage Scan

As mentioned in Section 3.2.1, we expect the bias voltage to be $V_B \lesssim 80$ V. Therefore, we performed a bias voltage scan ranging from 70 to 100 V. Figure 4.12 shows the Landau distribution of the pulse height from a fit to the four time samples for bias voltages of 70, 80, 90 and 100 V, revealing only a slight improvement of the extracted

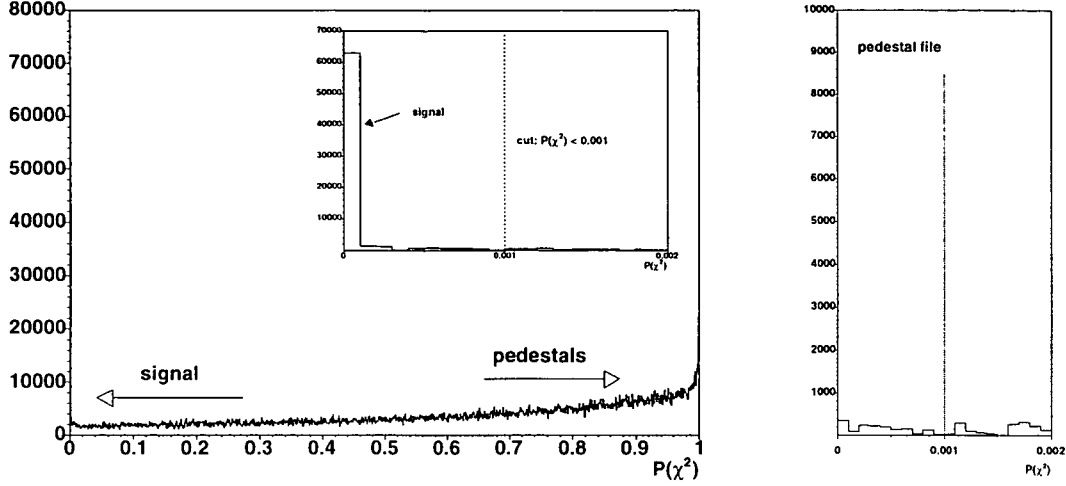


Figure 4.11: χ^2 probability of the strip values, which allows to distinguish between hit and non-hit strips. The inset shows a zoom on the window 0–0.2%. The right figure shows the absence of the signal peak in the pedestal runs.

peak height with increasing bias voltage. All the data were collected with a bias voltage of 70 V.

4.7.2 Strip Efficiency and Signal-To-Noise Ratio

The event sample selected for the efficiency studies consisted of a subsample of the reconstructed events where at least one muon track, reconstructed in the muon spectrometer, was matched to a track in the vertex telescope. Those events were reconstructed again with the same settings except for the absence of the plane for which the efficiencies were being evaluated. If the newly reconstructed event still contained a matched muon, an interpolation of the muon track to the plane under study was performed. The x and y coordinates were used to identify the expected position of a hit strip; this position established the *central* strip of a well defined region where we looked for hits. Whenever a hit was found within the limits of this region, the central strip was declared as efficient. This region was set large enough to account for the interpolation errors, the charge sharing among neighbouring strips and the drift of the electric charge carriers due to the magnetic field. Considering that the noise hit rate is around 1 per mill and the observed occupancies in the strip planes were smaller than 3%, as will be shown in Section 4.7.4, we have increased the search area beyond the minimum of 5 adjacent strips without noticing significant differences in the obtained efficiency values.

The efficiency of a strip is defined as the ratio between the number of hits found in the area around the strip and the number of interpolated muon tracks pointing to the strip. In Fig. 4.13 we show typical strip efficiencies as a function of strip number, obtained as an average over identical strips in several planes. The individual efficien-

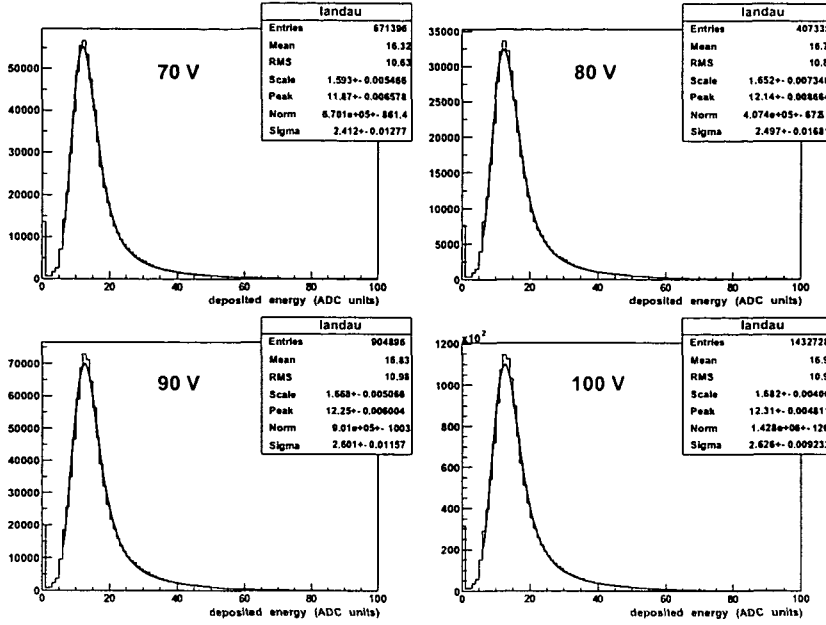


Figure 4.12: Landau peaks for different bias voltages.

cies for each strip in the whole vertex telescope are presented in the Appendix C. Note that we have used a different numbering convention as compared to the one given in Section 4.1, which will be described in the same Appendix. Superimposed to the average strip efficiencies in Fig. 4.13, we also show the average signal over noise ratios. The low efficiencies for some of the strips can be directly inferred from the low signal over noise values.

4.7.3 Detector Setup, Behaviour and Stability

The effective data taking period was from the 14th to the 19th of June 2002. The planes which could be successfully read out were the following: 4 stations at the beginning of the telescope at $z = 7.6, 10.0, 11.2$ and 14.8 cm and one station at $z = 40$ cm. In between there were 3 stations which had some kind of limitation. The station at $z = 26$ cm consisted of one operational plane and one plane which had such a high leakage current that it could not be depleted. At $z = 34$ cm one plane was missing and the other one was read out only on the “Jura”-side. The station at $z = 37$ cm also had the second plane read out only on the “Jura”-side.

In what concerns the raw data quality, it has been found that occasionally the data were corrupted due to problems in the compression algorithm of the ADC cards. This, however, happened at most in one of the four time samples in a given event, so that with the digitisation method used in the data analysis we did not lose any information, although the corruption always affected all 128 strips in the relevant chip.

At the end of the data taking period, the cooling of the PT7 magnet became inefficient, which led to an overall increase of the ambient temperature. This increase

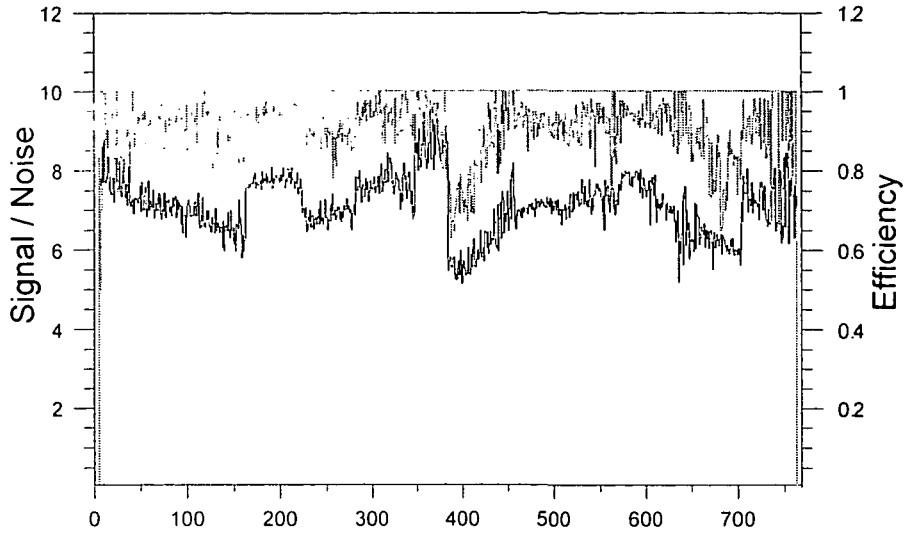


Figure 4.13: Signal to noise ratio and strip efficiency as a function of strip number.

in temperature of almost 10°C , measured on the ceramic close to the sensor, lead to an increase in the leakage current of more than a factor of 2. However, it did not affect the observed noise pattern, as is shown in Fig. 4.14.

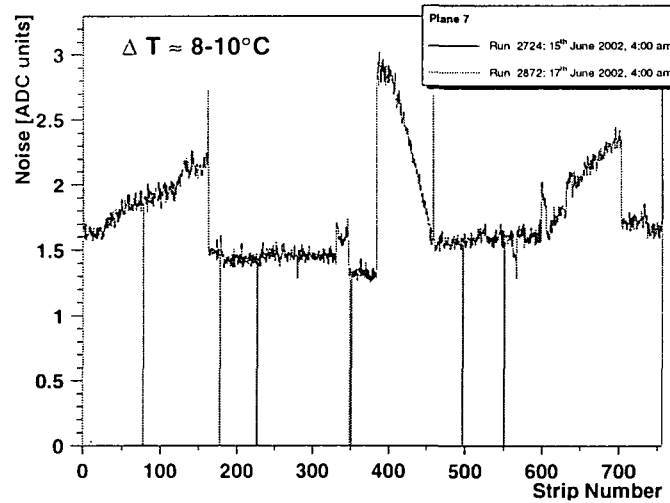


Figure 4.14: Noise pattern of a given sensor, obtained when operated at temperatures, differing by $\approx 9^{\circ}\text{C}$.

In Fig. 4.15 we compare the noise patterns observed at the beginning and at the end of the data taking period, for two different sensors. Comparing the noise levels of run 2568 to the ones of run 2968, we see changes in both directions — either towards higher or towards lower noise levels. These fluctuations cannot be attributed to a systematic change as a function of time.

We have also followed the time evolution of the behaviour of all the chips in

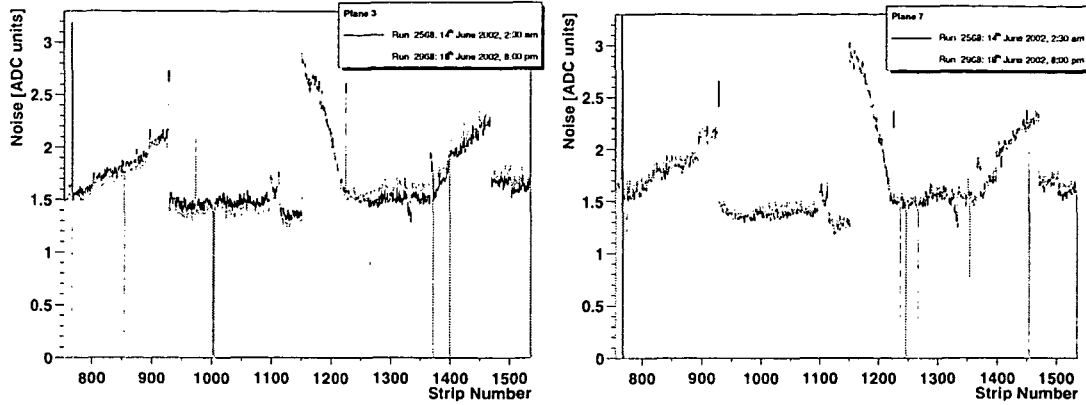


Figure 4.15: Comparison of the noise pattern of two sensors, as obtained at the beginning and at the end of the data taking period. The noise became slightly higher or lower, depending on the strips.

the full telescope by calculating an “average pedestal” and an “average noise” value for each burst, before applying any refined data processing (such as the common mode correction). These characteristic chip values were obtained by averaging the raw data values over all events in a given burst and over all 128 strips of the chip, regardless of their specific noise pattern. Figures 4.16 and 4.17 show these average pedestal and noise levels, respectively, for 6 chips in plane 6. These figures reveal fairly stable working conditions, confirming that we have not seen any deterioration of the detector’s performance due, e.g., to the induced radiation levels.

Individual chips, however, showed various kinds of problems during the period of data taking. Figure 4.18 shows a particularly striking example. Within runs 2722 – 2753 the raw data of chip 0 in plane 11 were not compressed correctly. On average, half of the output data were corrupted. The effect on the performance within these bursts can be seen by looking at the occupancy levels (lowest panel). While the occupancy level of this chip in other bursts is around 1.5%, in the very first bursts it was 0.5%. After run 2753 this problem was cured by connecting the read-out chips to properly working ADC channels. In the runs 2921 to 2939 the whole chip was masked since it did not acquire any data. We can see, furthermore, that in the runs 2778–2804, 2878 and 2968 this chip had anomalously high occupancy levels, which can be attributed to a malfunctioning of the read-out chain.

4.7.4 Occupancy Levels

As mentioned in Chapter 3, the detector was designed to have an average occupancy of less than 3% over the whole active area. Figure 4.19 shows that this was indeed the case in the first plane (the worst case).

The occupancies seen in the last station are much lower, as shown in Fig. 4.20. Of course, we cannot directly compare the occupancies of strips with different areas. This is why we used different colours to display the strips belonging to regions of significantly different areas. For the strips in region “A3+A2” and a few strips in

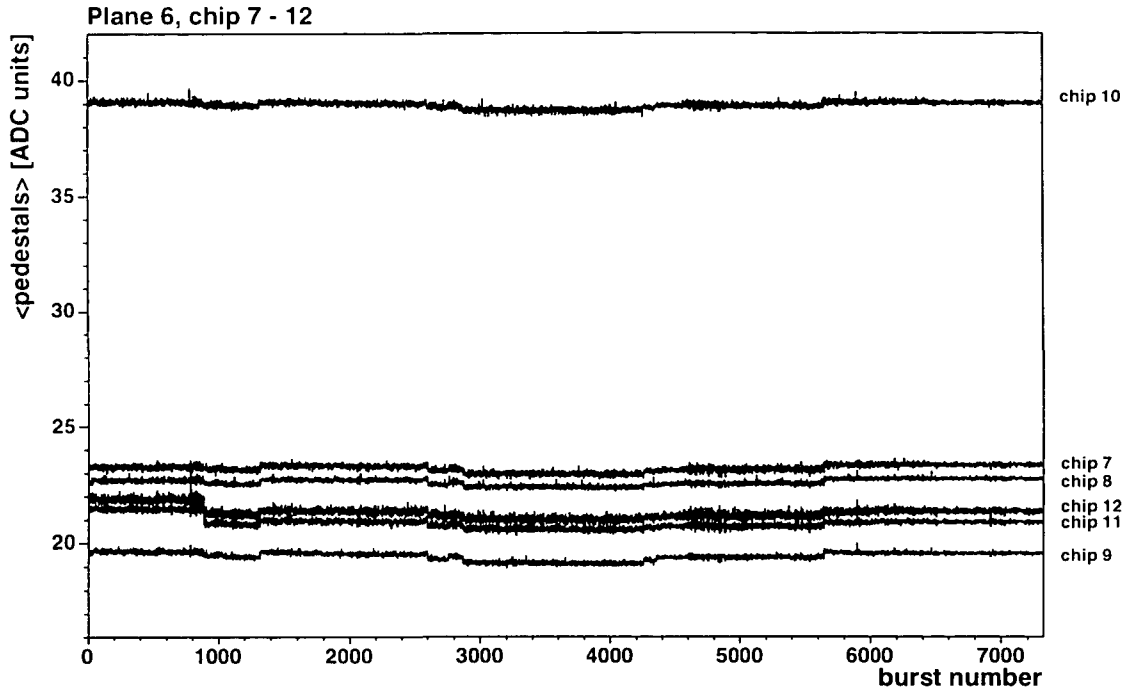


Figure 4.16: Time evolution of the average pedestal value of six chips in plane 6.

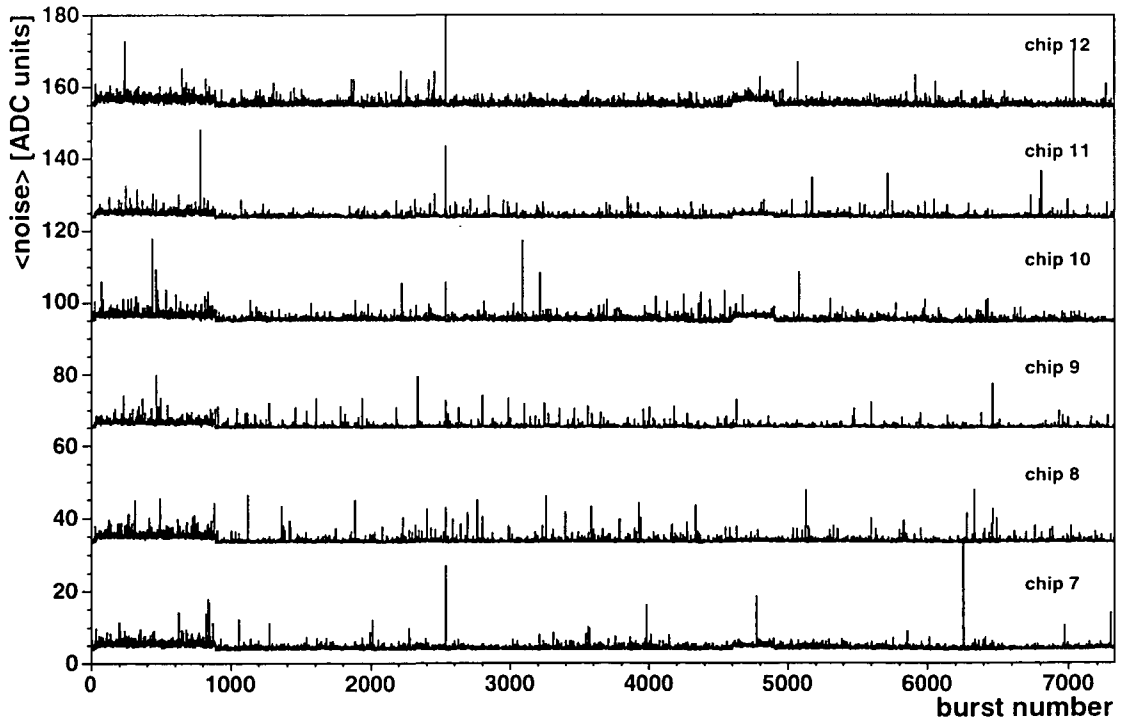


Figure 4.17: Time evolution of the average noise values of six chips in plane 6. The values of each chip were incremented by 30 with respect to the previous one, typical noise values being $\simeq 4 - 8$ for every chip.

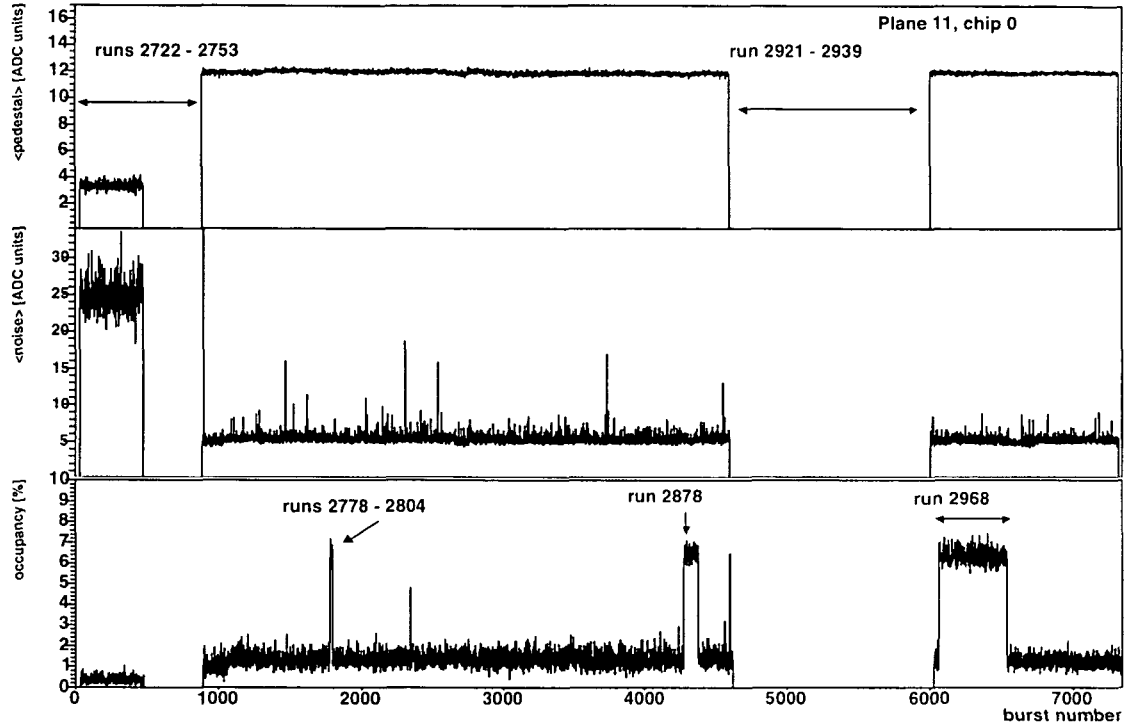


Figure 4.18: Pedestal, noise and occupancy levels of chip 0 in plane 11.

region “B2” the strip length varies slightly due to the presence of the beam hole. In this case, the area given in the legend refers to the average strip area. The decrease of occupancy within a given region reflects the $dN/d\eta \cdot 1/r^2$ dependence of the particle production. The observed occupancy levels are, hence, a convolution of the strip area with its radial position from the beam hole. To better appreciate their radial dependence, the hit occupancies are also shown normalised to the strip area, in the second panel. While the upper two panels show the occupancy levels calculated from the “digits”, the lower panels show the occupancy levels as obtained from the reconstructed tracks. Panels 3 and 4 show the obtained track density as a function of strip number and as a function of the average transverse distance from the beam axis, respectively. Panel 5 is the same as panel 4, but only for muon tracks.

By comparing the occupancy levels of the Salève and Jura sides of any given plane, see Fig. 4.21, we notice that before the beam intensity was raised from $\sim 1 \cdot 10^8$ protons/burst to $\sim (2 - 3) \cdot 10^8$ protons/burst (at around burst number 1100), the beam was not horizontally centered on the target, leading to decreased particle production and, hence, lower occupancies on the Salève side.

This hypothesis is confirmed by Fig. 4.22, which shows the reconstructed horizontal (top panel) and vertical (bottom panel) vertex coordinates of the collision, at the target. We can easily see a big change in the horizontal alignment of the beam at around burst 1100, while the vertical alignment remained much more stable during the full run.

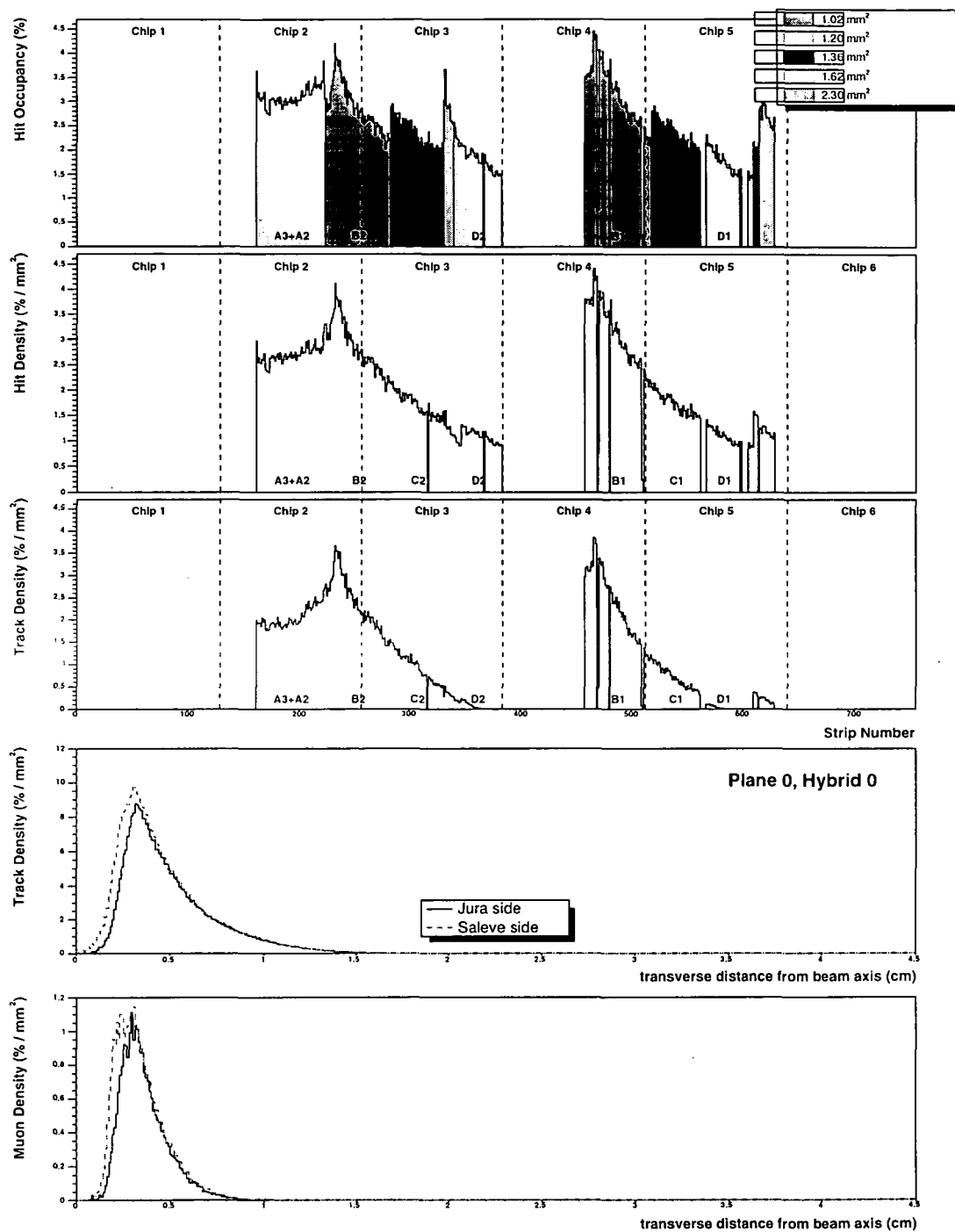


Figure 4.19: Occupancies for hits, all tracks and muon tracks, for the active strips in the first plane.

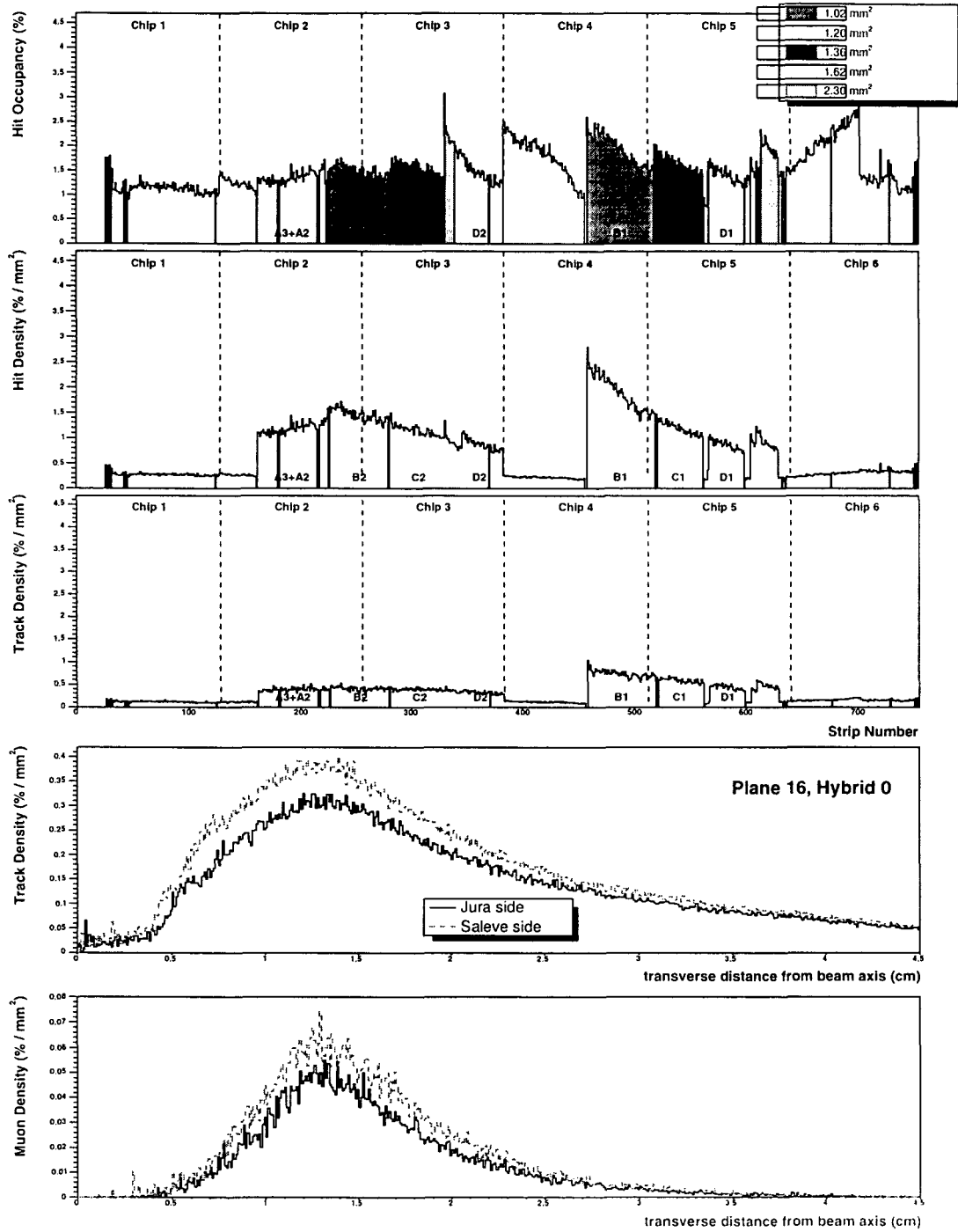


Figure 4.20: Occupancies for hits, all tracks and muon tracks, for the active strips in the last plane (of same orientation as in Fig. 4.19).

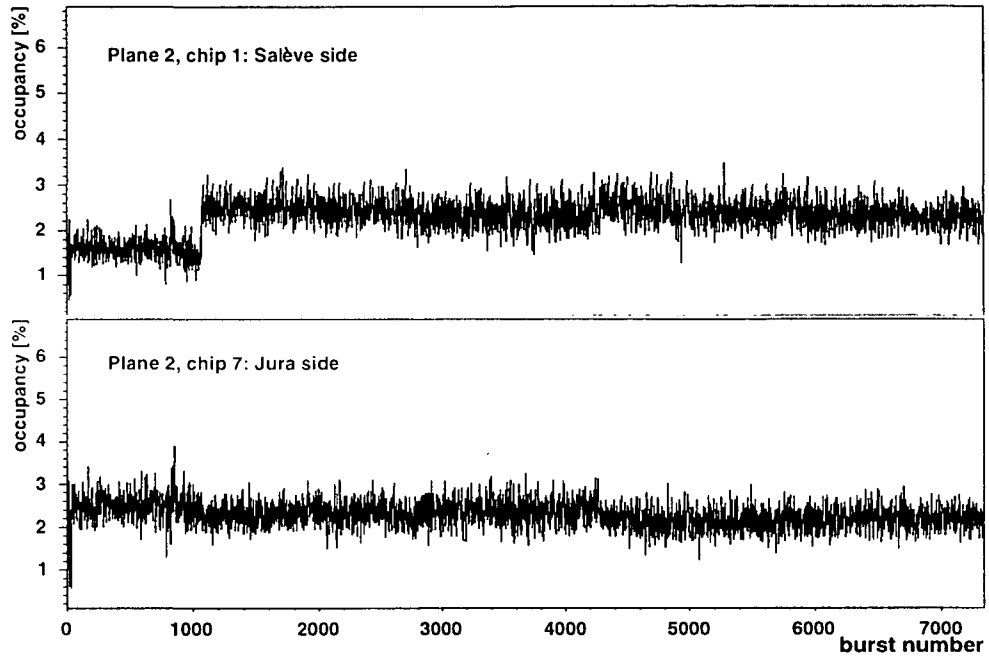


Figure 4.21: Occupancy levels of chips 1 and 7, which read out regions E, A and B. The latter two regions are situated close to the beam hole.

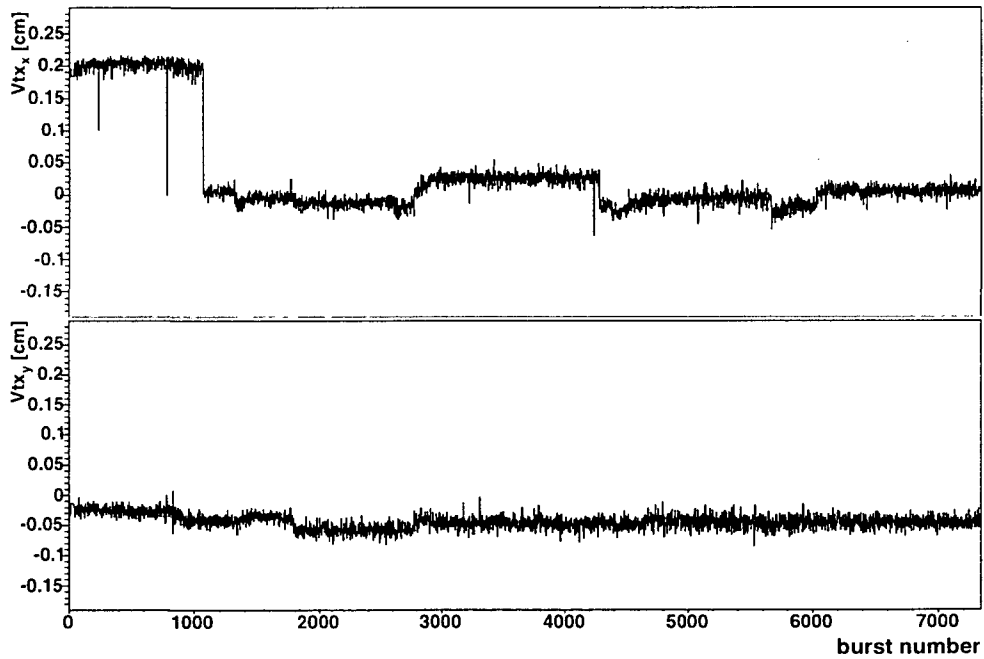


Figure 4.22: The reconstructed transverse vertex coordinates indicate that the beam intersected the targets slightly on the Jura side up to burst ~ 1100 .

4.7.5 Charge Sharing, Clusterisation

The secondary particles produced in the target region cross the tracking planes with a certain angle. Under a typical angle of 80 mrad, the particle will leave the 300 μm thick sensor with a shift in its radial coordinate of 25 μm , with respect to the position at the entrance of the sensors. This shift is not negligible with respect to the strip pitch of the inner region. Moreover, due to diffusion, the produced charge carriers will arrive at the read-out electrode with a given radial spread. From Eq. (3.6) we can derive that the width of the diffusion cloud should be $> 5 \mu\text{m}$ for our sensor. Since the telescope is operated inside a magnetic field, the Lorentz force will also act upon the produced charge carriers [32]. The resulting deflection angle, Θ_L , is given by the mobility of the charge carriers, μ , the Hall scattering factor, r_H , and the magnetic field strength, B ,

$$\tan \Theta_L = r_H \cdot \mu \cdot B \quad . \quad (4.4)$$

The Hall scattering factor for holes at room temperature is expected to be $r_H = 0.7$. For a magnetic field of 2 T we estimate that the charge carriers are deflected by up to 20 μm over the 300 μm thick sensor.

In cases where the Lorentz drift is oriented in the same direction as the transverse projection of the particle's track all these three effects add up, while if the two directions are opposite the effects can partially compensate one another. However, estimating the former case and combining these three factors we see that the deposited energy may be shared among two adjacent strips. Indeed, in $\sim 10\%$ of all events the energy is shared between two strips of the region A, B and C. Table 4.2 summarises the measured cluster sizes.

region	pitch [μm]	events with a double cluster [%]	$\langle \text{cluster size} \rangle$
A	80	10	1.16
B	60	11	1.17
C	80	9	1.13
D	135	6	1.09
E	150	5	1.08
F	227	5	1.09

Table 4.2: Fraction of events with a cluster size of 2 and corresponding average cluster sizes.

For regions of 60 – 80 μm pitch we have measured an average cluster size of 1.15. Note, however, that the *real* cluster size must be somewhat larger, due to the fact that the shared signal is sometimes too small to be detected in the second (or third) strip. Figure 4.23 shows graphically that not all the deposited energy is collected in a single strip with a small pitch. In regions where the strip pitch is large (see solid line) the registered signal is significantly larger than in regions with small pitch (the lower line shows the statistical error on the extracted signal height).

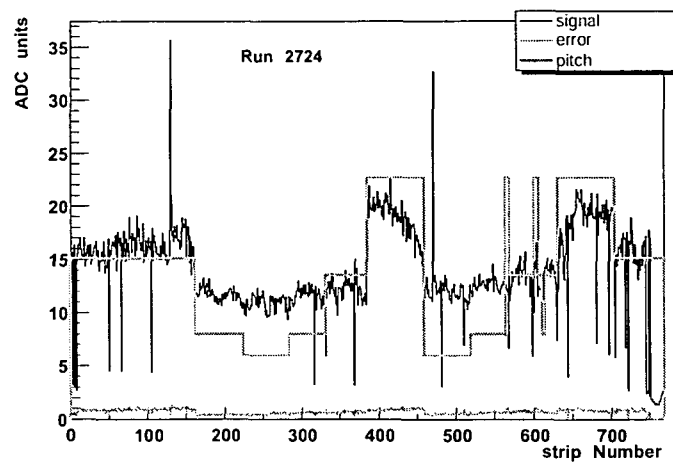


Figure 4.23: The energy deposited by a passing particle, expressed in ADC units, depends on the strip pitch (solid line).

Whenever adjacent strips were hit, the fired strips were, hence, used to build a so-called "cluster". It is these clusters, which are then used to reconstruct tracks in the vertex telescope.

Chapter 5

Data Reconstruction and Selection

5.1 Setup in the 400 GeV p-A 2002 Run

In this section we summarise and overview the detectors used in the 2002 proton run and relevant for the present analysis.

The data analysed in this thesis were taken during five days of the 400 GeV proton run in June 2002. We used three Argonia detectors, located upstream of the target system, to independently measure the beam intensity, burst by burst. The spill length over which the beam was delivered was 4.8 s within an SPS cycle of 16.8 s. The target system consisted of 6 sub-targets arranged in the following sequence: In, Be, Be, Be, Pb, Be, each with a thickness of 2 mm and an inter-spacing of 8 mm. The target system was followed by the microstrip vertex telescope, which consisted of 12 fully working micro-strip planes, and two planes which were read out only to 50%. Its arrangement can be seen in Fig. 5.1. After 3 “small” microstrip stations, consisting of 2 planes each, there was one large station, followed by a small pixel-plane. Only one plane was operational in each of the next two stations, situated at 26 and 34 cm downstream of the target. The latter of these was, moreover, only read out on one side. The last two stations consisted of two planes each, but one of these four planes was read out only on one side.

Downstream of the vertex telescope the main hadron absorber was located, made of BeO and Al₂O₃ blocks followed by graphite and ending with 20 cm of Iron. The muon spectrometer (including the trigger hodoscopes, the multi-wire proportional chambers and the ACM toroidal magnet) was operated with a plane switched off in the multi-wire proportional chamber number 6.

The two spectrometer magnets, PT7 and ACM, were operated with a current of ± 900 A and ± 4000 A, respectively. Runs to be used for the data analysis were taken with all possible combinations of the PT7 and ACM’s magnetic fields in order to cancel any (possible) systematic effects. Apart from collecting dimuons of opposite sign, we also collected like-sign muon pairs in order to derive the so-called “combinatorial background”, see Sec. 8.1.

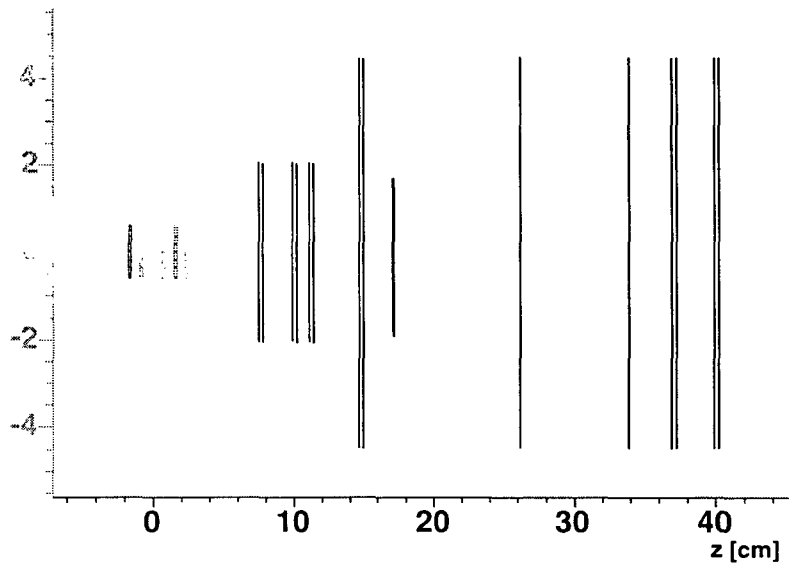


Figure 5.1: Sketch of the target system and the vertex telescope.

5.2 Data Reconstruction

The recorded raw data (analog or digital detector signals) are converted into a hit map of the individual sub-detector elements (strip planes, trigger hodoscopes, multi-wire proportional chambers, ...). The data reconstruction of the digitised and clustered data is then performed in several steps. Since the number of tracks *after* the hadron absorber is significantly smaller than in the vertex region, the tracks in the muon spectrometer are reconstructed first. Only if at least two muons were found, whose origin is in the target region, the track reconstruction in the vertex telescope is performed. If at least two tracks in the vertex telescope were found the event reconstruction proceeds via fitting the vertices of the found tracks. The matching of the muons coming from the muon spectrometer to candidate tracks in the vertex telescope proceeds by taking into account the multiple scattering and energy loss of the muons in the hadron absorber. In the following, we explain how these steps are performed. Where necessary, we also give the used cuts, which were applied to reconstruct the June 2002 data.

We will use several abbreviations which we explain here. The vertex telescope is often referred to as “VT”. We also use the expression “VT” tracks to refer to tracks reconstructed in the VT telescope. The muon spectrometer is named shortly “PC” telescope, PC standing for “proportional chambers”. “PC” muons and “PC” dimuons are reconstructed muons and dimuons, using the PC telescope’s information only. On the other hand, “VT” muons and “VT” dimuons are fully reconstructed muons and dimuons, which are first reconstructed in the PC telescope and then matched to reconstructed tracks in the VT telescope. Furthermore, “OS” dimuon stands for opposite-sign (+−) and “LS” for like-sign (++) and (−−) muon pairs.

5.2.1 Track Reconstruction

Track Reconstruction in the Muon Spectrometer

Before describing the reconstruction algorithm in the muon spectrometer, I remind that each multi-wire proportional chamber (MWPC) consists of 3 independent wire planes with a mutual rotation of 60° , called U, V and Y planes. The spectrometer consists of two sets of 4 stations, which are called the “forward” and the “backward” telescopes. The toroidal magnetic field bends charged particle tracks only within the magnet itself, so that in the telescopes the tracks to be reconstructed are straight lines.

The PC reconstruction algorithm was developed [33] within the NA50 experiment and starts by reconstructing tracks in the backward telescope due to the lower occupancy. It consists of the following main steps:

- **Building of the *projected tracks* in the backward telescope:** In a given subplane clusters are searched which should roughly lie in the same plane as in the other tracking stations, see Fig. 5.2. To build a projected track, hits in at least three MWPC’s out of four possible are requested. This is performed in each of the 3 projections separately.

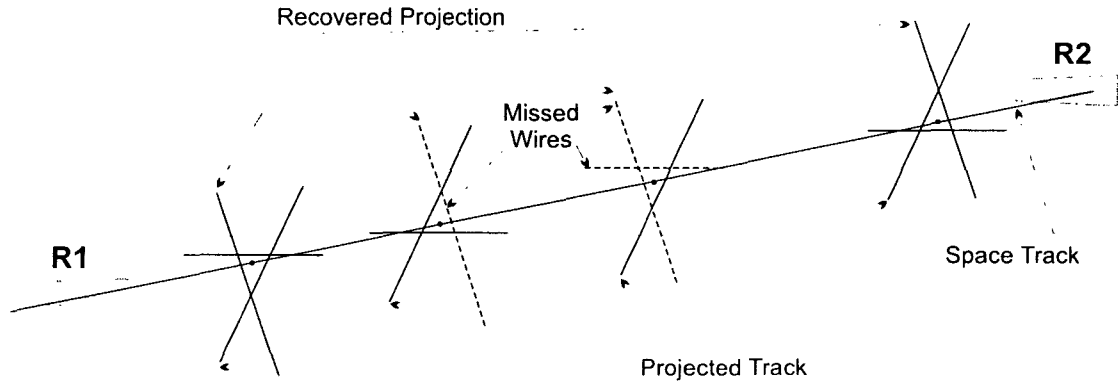


Figure 5.2: Visualisation of the building of a space track from the projected tracks.

- **Binding the backward telescope’s projected tracks into *space tracks*:** The intersection line of each pair of projected tracks (UV, UY or VY) is computed and the complementary Y, V or U projected track is sought, cutting on the distance between its plane and the obtained intersection line. The obtained space points, consisting each of at least one hit wire, are fitted by a straight line. If, by extrapolating back to the ACM magnet, the track would pass through the Iron sectors, the track is rejected (“iron cut”). Tracks which, furthermore, would miss hit slabs of the R3 and R4 hodoscopes, are also discarded.
- **Recovery of tracks with missing hits:** In cases where two projected tracks were identified but a third one could not be constructed due to missing hits in two stations, the list of hit wires which were not used in any space track is

searched for hits in the vicinity of the UV, UY or VY intersection point in each station. In case of positive result the missing projection gets completed. For an illustration of this method, see Fig. 5.2.

- **Reconstruction in the forward telescope:** The same algorithm of reconstruction is used in the forward telescope, rejecting tracks which do not cross any of the hit slabs in the R1 and R2 hodoscopes, or where the extrapolated track would go through the Iron sectors of the ACM magnet.
- **Forward and backward tracks' matching:** For each pair of forward/backward telescope tracks, reconstructed in the same sextant, the point of closest approach is evaluated. The forward/backward tracks are only matched if their mutual distance at the found z position of closest approach is sufficiently small and if the position of closest approach is sufficiently close to the bending plane.
- If after the space track binding stage two or more tracks share a common wire, we select the track with the best χ^2 for the binding and forward/backward association.
- **Applying further quality cuts:** For each coincidence of hit slabs in the R1 and R2 hodoscopes ("V"), which gives a rough measure of the track's polar angle in the forward telescope, the corresponding active slabs in R3 and R4 are verified. The "V" selects muons pointing back into the target region; since the R3/R4 combination measures the polar angle of the track in the backward telescope, the "V/R3/R4" coincidence cut selects furthermore muons which are deflected with a restricted bending angle. This hardware cut, which is implemented already on the trigger level, cuts random coincidences resulting from spurious hits. In the analysis these (hardware) cuts can be verified, but has not been done in the present analysis. We verified that through the reconstruction procedure we did not introduce "spurious" tracks, so that applying this cut did not change the reconstructed data sample.

By combining the reconstructed PC tracks with the hodoscopes' information we only keep tracks which crossed the detector within the read-out gate of the trigger hodoscopes (~ 20 ns), thereby rejecting muon tracks due to pile-up interactions during the chamber's read-out gate (~ 80 ns [34]). Events with more than two muons reconstructed in the muon spectrometer are very rare. The track reconstruction efficiency of the muon spectrometer has been carefully evaluated and is close to 100%.

The reconstruction algorithm rejects half of the collected triggers mainly because the trigger resulted from fake combinations of hodoscope hits and no (or only one) tracks could be reconstructed in the chambers, or because at least one reconstructed track went through the Iron poles of the toroidal magnet.

In Fig. 5.3 we see the z -vertex distribution of PC dimuons in the mass range $0.4 < M < 0.6$ GeV and for masses larger than 1.5 GeV. In both cases the distribution is asymmetric around $z = 0$, shifted towards positive z -values. If through

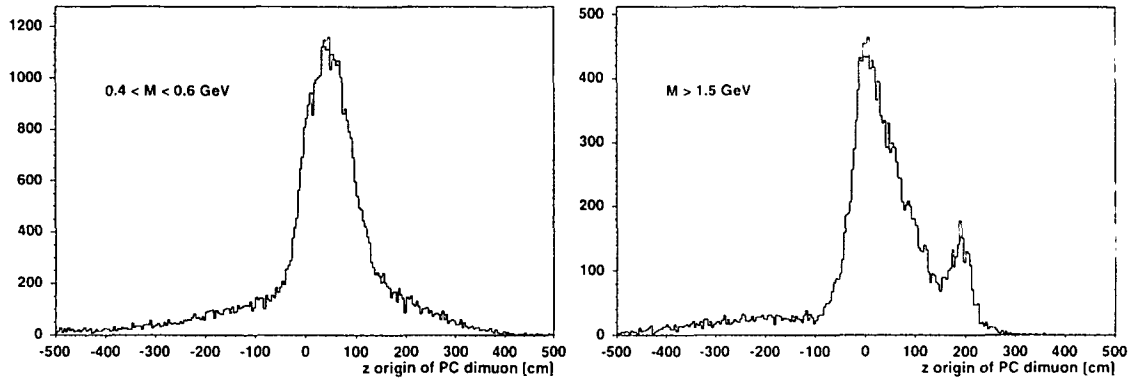


Figure 5.3: z -vertex distribution of PC dimuons.

multiple scattering in the hadron absorber the single muons increase their p_T , they will most likely be still accepted in the muon spectrometer, while if the scattering decreases their p_T they are most likely to pass through the inner inactive zone of the muon spectrometer and will be lost. By reconstructing the muon tracks of “outward scattered” muons and extrapolating them back to the target the apparently “increased” opening angle leads to an extrapolated dimuon origin which lies at more downstream z -values than the original production vertex.

We can see, furthermore, that the width of the distribution decreases for dimuons with larger masses. For PC dimuons with $M > 1.5$ GeV we can distinguish between dimuons produced in the target region and dimuons produced in the hadron absorber and beam dump.

Track Reconstruction in the Vertex Telescope

The reconstruction of tracks in the target region is done taking into account the magnetic field of the dipole magnet PT7. Since the measurement of curved tracks involves the extraction of 5 parameters, as outlined in Sec. 3.2.2, the measurement of at least 3 space points is required. We distinguish mandatory and optional planes in the track reconstruction. The pixel plane was declared optional, since it was not permanently read out and its angular acceptance was too small. The first 6 tracking planes have the outer region of their microstrip sensors outside of the angular acceptance of the muon spectrometer. Therefore, only their inner regions are used for the tracking.

The space coordinates of a cluster in a single plane are given by the centre of adjacent hit strips, having a large uncertainty due to the length of the strips (the strips are “one-dimensional” sensing elements). The term “cluster” should, hence, *not* be mistaken with the x, y coordinates measured in a given station. In order to have more flexibility in the reconstruction procedure and not to be dependent on the sensor’s inefficiencies, a “space point” can consist of x and y coordinates measured in planes of two *different* stations. It is, hence, the *single-plane clusters* of individual planes rather than the combined information of two planes in a given station, which are the tracking inputs.

Prior to the VT track reconstruction, the occupancies in all planes are checked. In case the occupancy of at least one plane is unphysically high (higher than 10%) the event is not processed. The algorithm starts by building a *track seed*.

- First, the space coordinates of two clusters, one in the most downstream and the other one in the most upstream planes, are logically combined. A straight line through these two clusters, which are chosen to come from planes of different angular orientation, is extrapolated back into the target region (note that there is no deflection of the tracks in the yz plane) and a relaxed cut is applied on whether this track points back to the target region or not.
- In the second step, an interpolation to a well-defined intermediate plane is performed by taking into account the magnetic field. A coarse “roadwidth” is defined by extrapolating a track with maximum (positive and negative) curvatures, defined by a charged particle of 1 GeV/c momentum. Within this defined interpolation zone a new cluster is searched for. As soon as a track seed consists of 3 (single plane) clusters, a first track fit is performed. At this preliminary step a rather relaxed quality check of this fit and a relaxed vertex cut are applied.
- If the track seed withstands these initial cuts, the construction of the whole track is done by adding clusters first from mandatory, then from optional planes. The search for new clusters is now limited to the roadwidth of the track seed, which is given by the χ^2 of the fit combined with the position resolution of the sensor.
- The position error of a given cluster takes into account that a cluster can consist of several strips. It furthermore takes into account the integrated multiple scattering at the given plane. This is done by calculating the multiple scattering in each of the 300 μm thick sensor planes for a “standard particle” of 10 GeV.
- A new cluster is added to the track seed only if it fulfills a set of requirements: (a) The χ^2 distance between the interpolated track seed and the position of the cluster should be reasonably small. (b) The quality of the renewed fit should be reasonably good and the extracted curvature should correspond to momenta above 1 GeV/c. (c) The χ^2 distance of the seed extrapolation to one of the sub-targets should be within defined limits. In case the cluster does not fulfill these requirements it is discarded and a new cluster of the same plane inspected.
- If, after checking all planes for new clusters, the number of successfully added clusters satisfies the minimum limit requested — including clusters from optional planes — the track is accepted and the clusters used are tagged. In the present reconstruction algorithm, tracks are finalised if they consist of at least 8 (single plane) clusters out of 12 fully and efficiently working planes.
- The final validation of the seed is done by comparing how many clusters it shares with already validated tracks. If this number is higher than the maximally

allowed number of shared clusters (i.e. 1 in our analysis), then the track with the larger number of clusters or with the smaller χ^2 is validated, while the other one is discarded.

- The outlined algorithm is only applied in a *second* iteration of the reconstruction procedure. The present algorithm, namely, tries to find tracks out of *all* clusters found in the whole telescope, which gives a large number of possible combinations. In order to limit this search, the track reconstruction tries in a *first* iteration to find tracks consisting of 11 clusters, which become masked and cannot be used for a further search in the second iteration. In this way, the number of possible combinations for new tracks (during the second iteration) becomes limited. Then, a more thorough search is performed using the remaining clusters, allowing for a few missing hits (only 8 clusters are requested to validate the track, as mentioned above).

5.2.2 Vertex Finding

The vertex finding algorithm is based on a robust¹ fitting method, which assigns a weight to each of the contributing tracks, as outlined in Ref. [35]. Only tracks which consist of at least 10 clusters and have a good fit quality ($\chi_{\text{fit}}^2 < 2$) are selected to contribute to the vertex fitting. The method is based on solving the following set of equations for the vertex position (x_v, y_v, z_v) in an iterative way,

$$\begin{aligned}\sum_i w_i^k \frac{1}{\sigma^2} e_i \frac{\partial e_i}{\partial x_v} &= 0, \\ \sum_i w_i^k \frac{1}{\sigma^2} e_i \frac{\partial e_i}{\partial y_v} &= 0, \\ \sum_i w_i^k \frac{1}{\sigma^2} e_i \frac{\partial e_i}{\partial z_v} &= 0,\end{aligned}\tag{5.1}$$

where i runs over the number of qualified tracks. The weights, w_i^k , in a given iteration step, k , are calculated from the residuals, e_i , the so-called Tukey constant, c_T , and the parameter σ , which is given by the weights and residuals of the previous iteration, $k-1$:

$$w_i^k = \begin{cases} \left(1 - \left(\frac{e_i^k}{c_T \cdot \sigma^{k-1}}\right)^2\right)^2 & , \text{ if } |e_i^k| \leq c_T \cdot \sigma^{k-1} \\ 0 & , \text{ otherwise} \end{cases}$$

with $\sigma^{k-1} = \sqrt{\frac{\sum w_i^{k-1} \cdot (e_i^{k-1})^2}{\sum w_i^{k-1}}}$.

(5.2)

The residual at the seed position z_v is defined as the difference between a “seed” vertex (x_v, y_v) and the transverse coordinates of the extrapolated track, taking into

¹Robust methods are methods which are not sensitive to outliers with small error bars.

account the magnetic field,

$$e_i^k = \sqrt{\Delta x^2 S_{xx}^{-1} + \Delta y^2 S_{yy}^{-1} + 2\Delta x \cdot \Delta y S_{xy}^{-1}}, \quad (5.3)$$

where S^{-1} is the inverse covariance matrix.

In view of optimising the z -vertex resolution, the Tukey constant was varied around the value used in Ref. [35], $c_T \sim 3.0$. The results were insensitive to the exact value of the Tukey constant, if it is within the range 2.5–3.0. We have used the value 2.7 for the present reconstruction.

The iteration stops if the difference with respect to the previous z -vertex position is smaller than $100 \mu\text{m}$. In the reconstruction of the proton data typically ~ 20 iterations were needed. Tracks whose residuals are too large, are not assigned to the identified vertex. As long as the remaining number of qualified tracks is larger than 1, the search for a new vertex is started. In the final step of the vertex finding — after all vertices have been identified — also the tracks which did not qualify for the vertex finding are attached, if possible, to one of the found vertices. The number of reconstructed vertices per event, hence, can be larger than 1. In roughly 30% of all events, we reconstruct 2 vertices, and the frequency of 3 reconstructed vertices is about 5%.

Vertices reconstructed between a -3σ distance from the first target and a $+3\sigma$ distance from the last target are assigned to one of the 6 sub-targets according to Table 5.1.

Target	z [cm]	Δz [cm]
In	-1.66	-2.000 — -1.255
Be 1	-0.85	-1.255 — -0.455
Be 2	-0.07	-0.455 — +0.345
Be 3	0.74	+0.345 — +1.150
Pb	1.53	+1.150 — +1.930
Be 4	2.32	+1.930 — +2.600

Table 5.1: Target positions (after alignment) and the z -ranges over which we identify the individual targets.

These specific values were obtained from the final z -vertex distribution, shown at the bottom of Fig. 5.4. This figure shows the effects of certain quality cuts, which were used in the vertexing algorithm.

The first panel shows the z -vertex distribution obtained without having applied any cuts. From fitting the individual peaks (with a Gaussian) and the continuum between two targets (with a Polynomial of 2^{nd} order) and integrating the resulting curves in the ranges given in Table 5.1 we obtain the number of “real” and “background” vertices given in the figure. The second panel shows the effect of applying a cut on the quality of the fitted vertex by requiring that the χ^2 of the fit should be less than 40. The third panel shows the distribution selected by requiring that the variable σ , as described above, is smaller than 5. Comparing panel two and three we

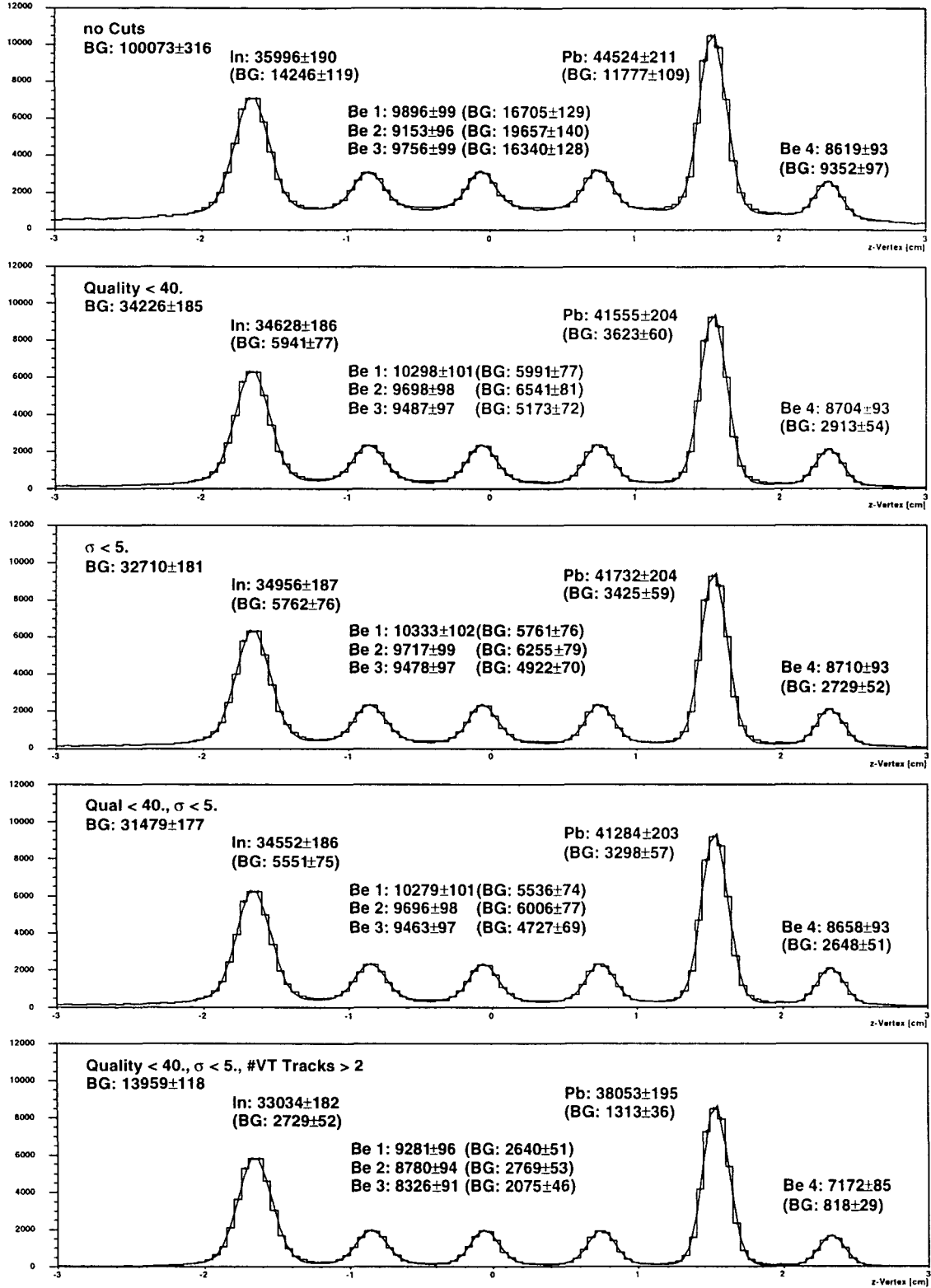


Figure 5.4: Applying certain quality cuts during the vertexing procedure to clean the z -vertex distribution.

see that these cuts, applied individually, have a very similar effect. They both cut mostly events which have the vertex between two targets, while keeping most of the vertices reconstructed under the peaks. Panel 4 then shows the combined effect of these two cuts. We also evaluated the effect of requiring a minimum of three tracks attached to the vertex. To keep as many p-Be events as possible, we have not applied this selection criterion in the final data analysis.

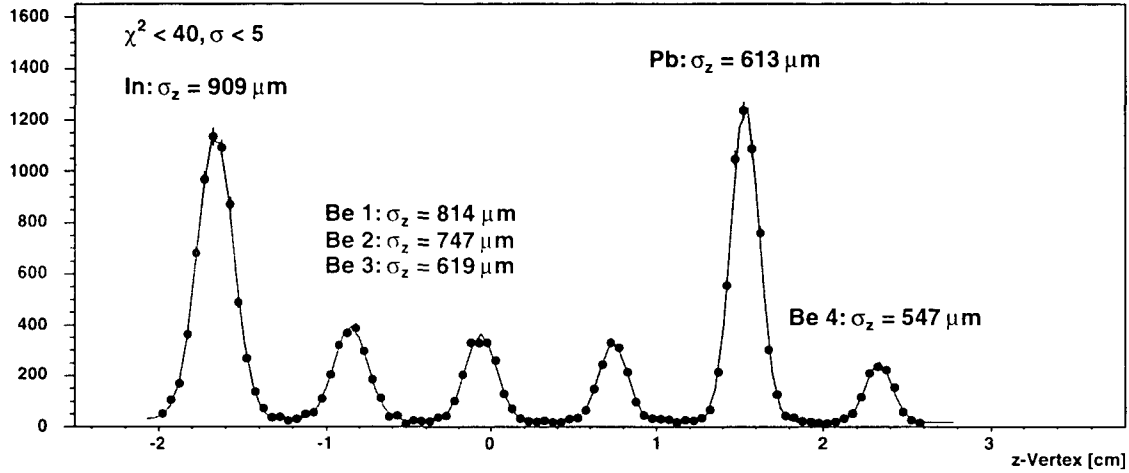


Figure 5.5: z -vertex distribution and resolutions for the 6 sub-targets, in the matched dimuon event sample.

Figure 5.5 shows the z -vertex distribution and resolutions for the selected events with a dimuon matched. The values for the z -vertex resolution were obtained by deconvoluting the target thicknesses from the measured resolutions. They lie between 600 and 900 μm , and improve for the more downstream targets, mainly due to the fact that the reconstructed tracks are extrapolated over a smaller distance. Note that the tracks from more downstream targets also undergo less multiple scattering.

The z -vertex resolution depends on the number of tracks attached to the vertex. The more tracks contribute to identify the interaction vertex the better the resolution. The numbers given in Fig. 5.5 were integrated over all vertices, regardless of the number of tracks attached. Figure 5.6 shows the dependence of the z -vertex resolution on the number of tracks. For vertices consisting of more than ~ 10 tracks the resolution in the Lead target is around 400 μm .

The fact that the z -vertex resolution starts to saturate for more than ~ 7 tracks is due to the wrong attachment of tracks coming from other vertices (either from re-interactions or from interaction pile-up vertices). When fitting the dependence on the number of tracks of the z -vertex resolution, this effect has been taken into account by adding a term proportional to $\sqrt{N_{\text{tracks}}}$ to the usual parameterisation $1/\sqrt{N_{\text{tracks}} - 1}$. The results of such fits are also shown in Fig. 5.6, for the Indium and Lead targets.

Figure 5.7 shows the distribution of VT tracks attached to the identified vertices. The upper panel compares the distributions for the three different target materials, taking together the statistics from all Be targets. Since the individual sub-targets

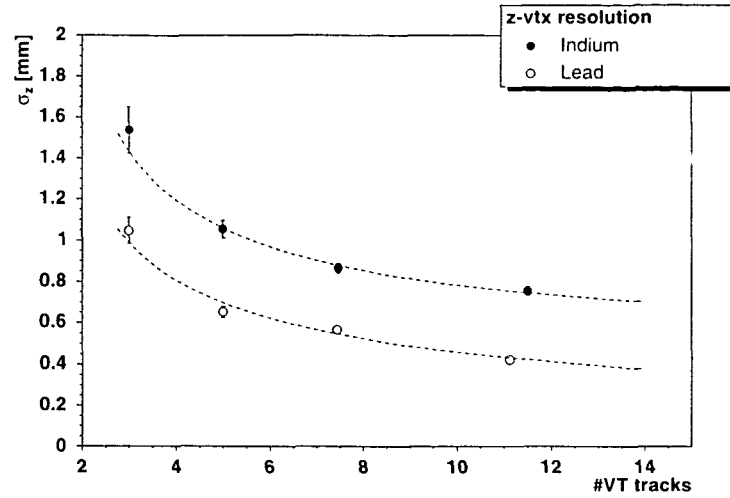


Figure 5.6: Dependence of the z-vertex resolution on the number of tracks attached to the vertex.

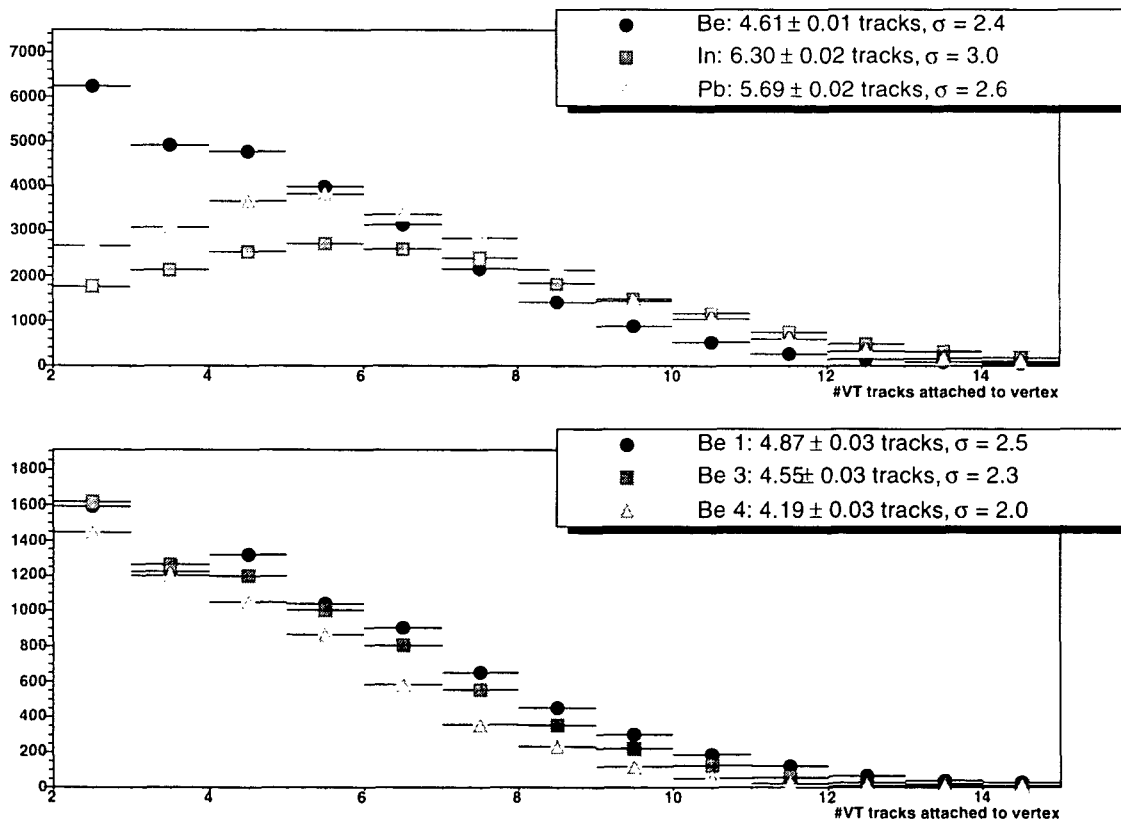


Figure 5.7: Number of VT tracks attached to the interaction vertex.

have different acceptances, depending on their z-position, the lower panel compares the distribution of VT tracks for three of the four Be targets. Table 5.2 summarises

the average number of reconstructed tracks in the individual sub-targets, and the spread of the distribution.

Target	Average	r.m.s.
In	6.30 ± 0.02	3.0
Be 1	4.87 ± 0.03	2.5
Be 2	4.70 ± 0.03	2.4
Be 3	4.55 ± 0.03	2.3
Pb	5.69 ± 0.02	2.6
Be 4	4.19 ± 0.03	2.0

Table 5.2: Average number of tracks attached to the reconstructed vertices.

5.2.3 Dimuon Track Matching

The matching of a reconstructed dimuon from the muon spectrometer to two track candidates in the vertex telescope proceeds in the following way. For each PC muon, the matching VT track is sought. Only VT tracks with the same charge as the PC muon and with roughly the same kinematics are considered as matching candidates. This requirement implies that the slopes (k_x and k_y) and the curvatures (C) of the VT track and of the PC muon, corrected for multiple scattering and energy loss in the hadron absorber, should be similar. A cut on the following matching χ^2_{match} is performed.

$$\chi^2_{\text{match}} = \left(\frac{\Delta k_x}{\sigma_{k_x}} \right)^2 + \left(\frac{\Delta k_y}{\sigma_{k_y}} \right)^2 + \left(\frac{\Delta C}{\sigma_C} \right)^2, \quad \text{where} \quad (5.4)$$

$$\sigma_i^2 = (\sigma_i^{\text{PC}})^2 + (\sigma_i^{\text{VT}})^2; \quad i = k_x, k_y, C \quad (5.5)$$

The errors of the PC muon and of the matching candidate are added in quadrature. Selected candidates are refitted loosely constrained by the momentum (curvature) of the PC muon. Up to 4 candidates per PC muon are stored for further processing.

If both muons of the PC dimuon have at least one match candidate in the vertex telescope, we perform a joint fit of the vertex telescope dimuon candidate with a common vertex. If there are several VT track candidates for the PC muons, we select the VT dimuon candidate which gives the best matching χ^2 .

In Fig. 5.8 we can see the highly improved z-vertex resolution for fully reconstructed dimuons (c.f. Fig. 5.3). The left figure shows the z-vertex distribution for opposite sign dimuons in the mass region of the ϕ meson. The right figure shows the extracted dimuon z-vertex resolution as a function of mass.

5.2.4 A Typical Reconstructed Event

In Fig. 5.9 we see a typical reconstructed event in the vertex telescope. The incoming proton causes an interaction in the Pb target, which produces 13 secondary particles.

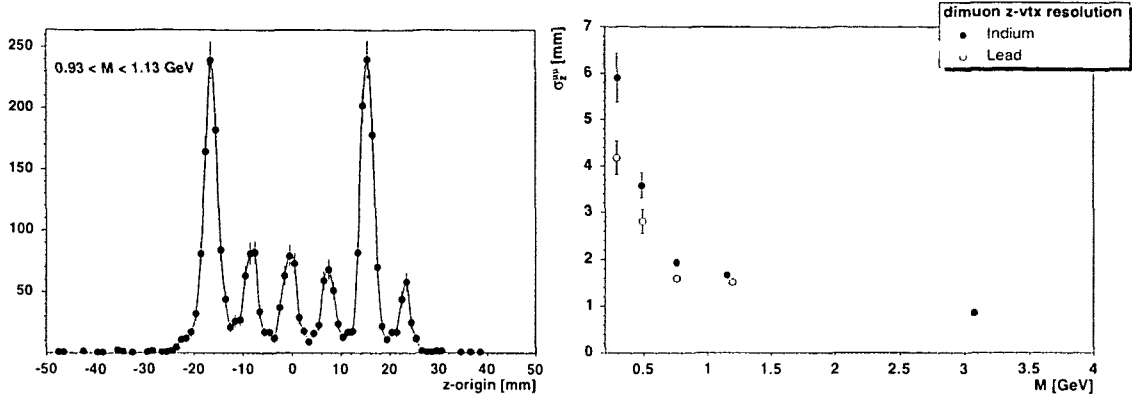


Figure 5.8: Left: Distribution of the z-origin of VT dimuons for the mass range of the ϕ meson. Right: Mass dependent z-vertex resolution for matched dimuons.

After track reconstruction and muon matching we have identified the two muons, shown in thick (red) lines and the reconstructed mass of the ϕ meson improved from 0.91 to 1.02 GeV.

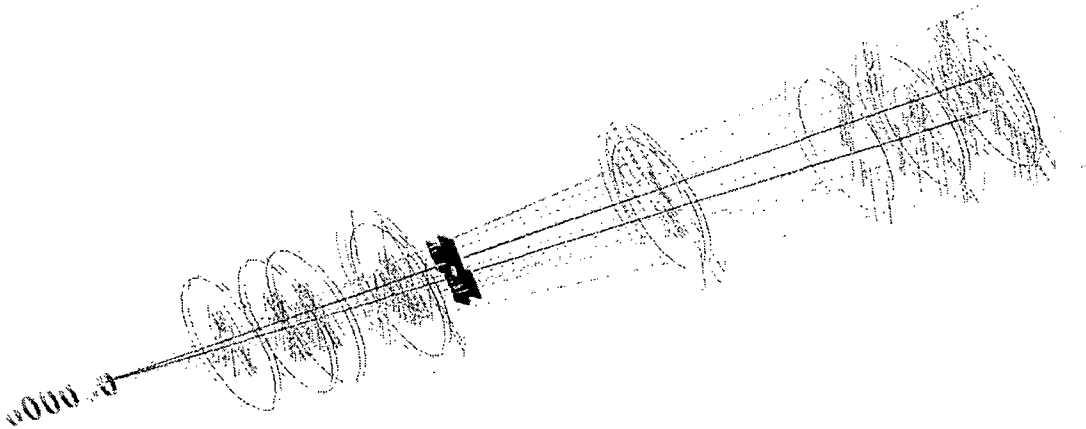


Figure 5.9: Event display in the vertex telescope with a matched ϕ meson, shown as thick (red) lines. Run 2770, burst 2, event 33. The individual strip planes are drawn as discs, showing the fired strips.

5.3 Data Selection and Luminosity Evaluation

5.3.1 Run and Burst Selection

For the physics analysis we have considered runs which fulfilled the following list of requirements:

- All efficient microstrip planes of the vertex telescope must have acquired data. These comprise 12 fully working planes and two planes where only 50% of the strips were read out. The pixel plane was not mandatory for the track reconstruction in the vertex telescope.
- Only runs in which both magnets were switched on were used for the physics data analysis.
- Only dimuon triggers were analysed.
- Each run had to contain more than four collected bursts.

These requirements lead to 50 selected runs, which in total contain ~ 8100 bursts. Each burst contains of the order of 50 to 100 dimuon triggers. The stability of data taking during these bursts was carefully evaluated by scanning a series of variables, burst by burst. These include the number of collected triggers, the number of reconstructed dimuons in the muon spectrometer and the number of matched dimuons in the vertex telescope. These variables can be seen in Figs. 5.10 and 5.11.

These figures also show the output of the Argonia detectors, which is proportional to the number of incoming protons per burst, and are used for the luminosity calculation, see Sec. 5.3.2. The first panel of these two figures shows the information from the Argonia-3, where we can see the increase in beam intensity after around 1100 selected bursts. The second panel shows the relative behaviour of the three Argonia. Within 1% accuracy they show the same number of incoming protons over all bursts. The vertical lines indicate the beginning of a new run. The numbers correspond to the run number and are shown only for runs with a reasonable amount of bursts. The runs whose number is plotted in *red* (faint letters) correspond to runs where the pixel plane was also read out. The third panel shows the number of collected triggers, normalised to the beam intensity, integrated over the burst. Ideally, this number should be constant as a function of time. Deviations from its usual value reveal problems during the data taking. In the first ~ 4000 bursts we can see four deviations. In the very first run the number of collected triggers was significantly smaller. The average momentum of the secondary particles in the vertex telescope (shown in the last panel) reveals the problem: the magnetic field of the PT7 magnet was not switched on — contrary to what was written in the “logbook”. During run 2828 the number of collected triggers in each burst was set to 20 in order to perform some tests for the data acquisition system. Around burst ~ 3300 the number of collected triggers was smaller than usual, due to problems in the trigger system. After having verified that the extracted dimuon mass spectrum differed from the one obtained in “good” bursts, we have discarded these bursts (< 100 bursts). Finally, around burst ~ 3150 the number of reconstructed dimuons is zero since there was a problem in the read-out chain of the microstrip telescope, which caused three microstrip planes to not being read out. During the second ~ 4000 bursts, shown in Fig. 5.11, a few bursts (roughly bursts 4700–4800) show a significantly different trigger over beam intensity ratio, due to problems in the trigger system. During bursts 5050–5350 the PT7 magnet stopped working, presumably due to problems with the cooling of the magnet’s coils. During

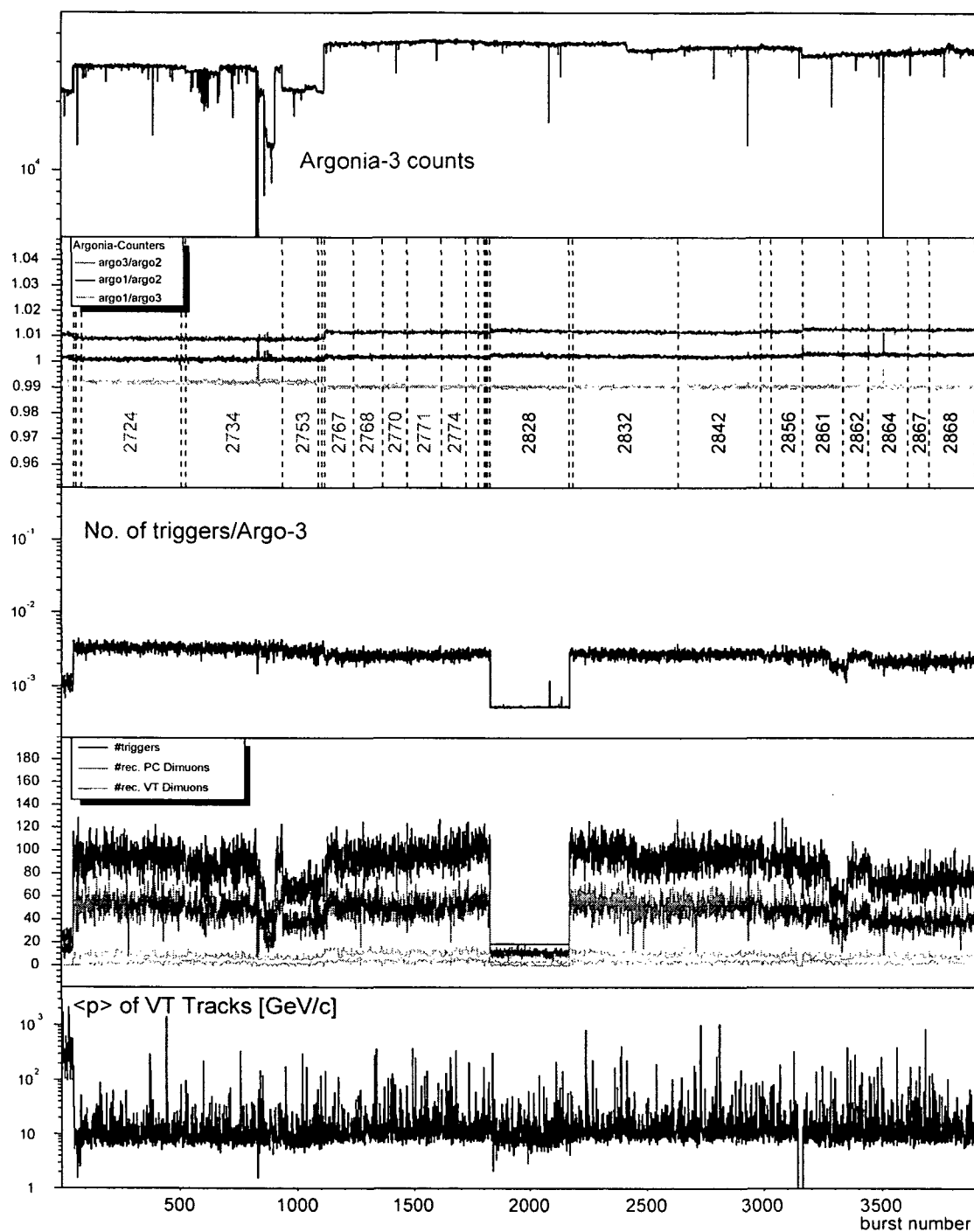


Figure 5.10: Burst by burst monitoring of certain variables, within the first half of the pre-selected runs.

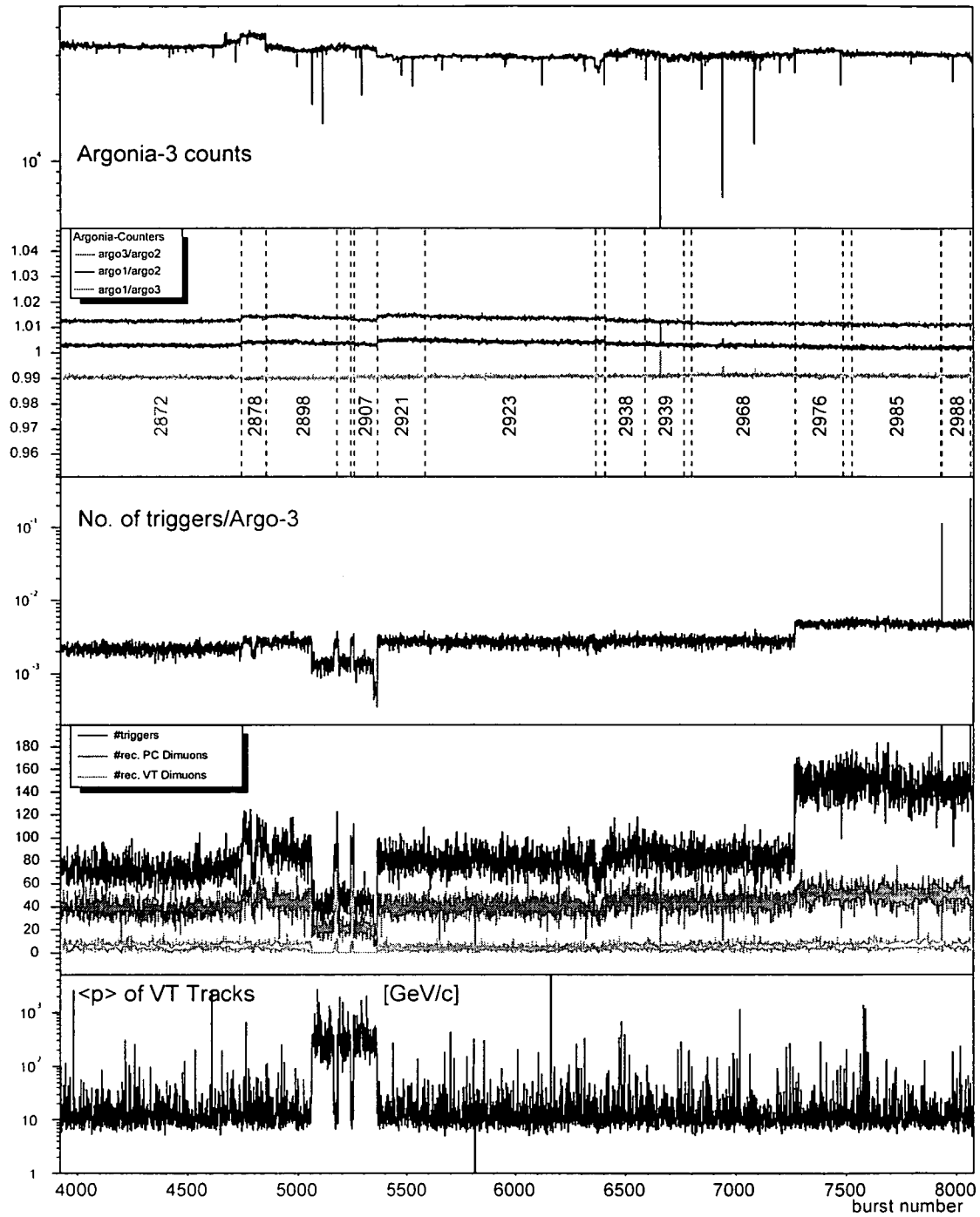


Figure 5.11: Burst by burst monitoring of certain variables, within the second half of the pre-selected runs.

the last ~ 800 bursts we observed a higher trigger rate, which did not lead to an increased number of reconstructed dimuon events. We noticed that four sextants of trigger hodoscope R3 were constantly giving a signal, leading to many accidental triggers. This, however, did not affect the quality of the reconstructed dimuons.

We have also noted that, in bursts without beam, the DAQ system writes to tape a copy of the last event of the previous burst, still present in the memory buffer. Of course, such “empty bursts” were eliminated from our analysis.

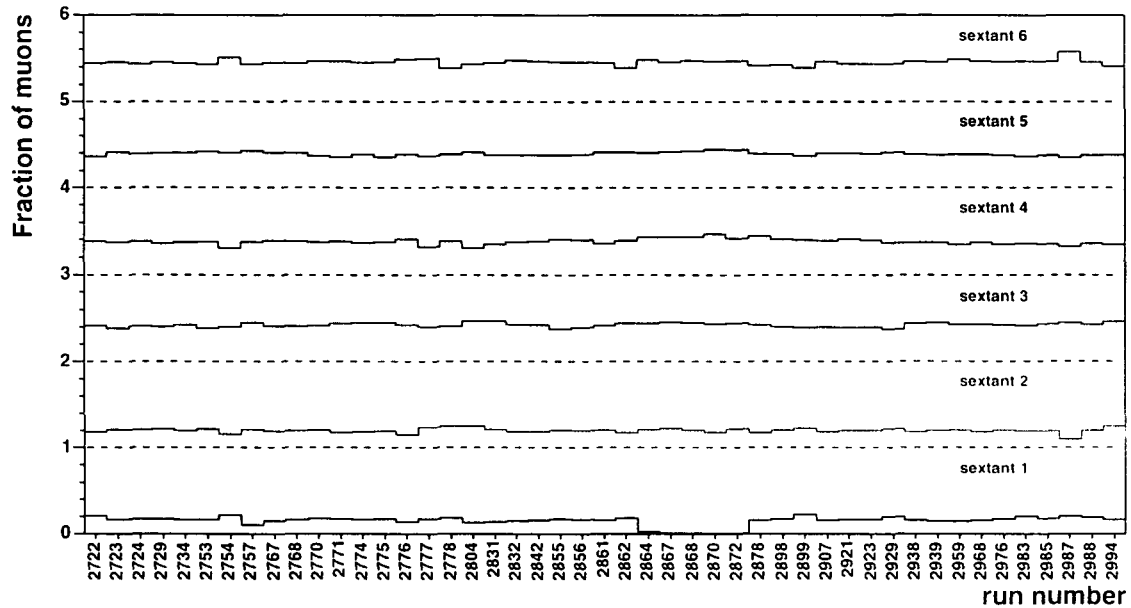


Figure 5.12: Fraction of muons passing through the individual sextants, as a function of the run number.

Finally, we performed quality checks for the muon spectrometer. In particular we looked at the fraction of muons passing through each individual sextant, as a function of time. Usually, sextants 1 and 2 (bottom and top sextants, see Fig. 2.6), see less muons, due to the fact that the vertex magnet bends the muons in the horizontal plane to the Jura and Salève sides. Figure 5.12 shows the fraction of reconstructed PC muons passing through the individual sextants. In order to separate the 6 curves we have added an offset of 1 to each of them, increasing with the sextant index. While usually the fraction of muons passing through sextants 3–6 is around 40%, it is half that value for sextants 1 and 2. During runs 2864 to 2872 there was a problem in the sextant 1 of the “R1” hodoscope, so that muons passing through this sextant did not contribute to the trigger decision. This affected 20% of the hitherto selected statistics. After having verified that the mass distribution in these runs does not differ in a significant way from the remaining period of data taking, see Fig. 5.13, we have not excluded these runs from the data analysis.

Tables 5.3 and 5.4 list the pre-selected runs with the corresponding number of collected and selected bursts and corresponding observations (comments are placed in parentheses).

Run No.	selected/total bursts	PT7/ACM polarity	Problems and observations
(2688)	0/52	0/+	PT7 off
2804	13/19	+/-	ok
(2828)	0/347	+/-	20 triggers/burst fixed by the DAQ; luminosity information not useable
2831	18/19	+/-	ok
2832	448/460	+/-	bursts 0-9: reconstructed data not readable
2842	352/374	+/-	(no beam on the last 13 bursts)
2855	48/51	-/-	ok
2856	110/132	-/-	bursts 111-132: one LDC was missing
2861	114/175	+/-	bursts 116-174: problems in one sextant
2862	89/109	-/-	bursts 1-19: problems in one sextant
2864	170/176	-/-	(problems in trigger hodoscope R1)
2867	94/95	-/-	(problems in trigger hodoscope R1)
2868	197/198	-/-	(problems in trigger hodoscope R1)
2870	23/24	-/-	(problems in trigger hodoscope R1)
2878	100/117	-/-	(bursts 50-64: smaller amount of triggers, while Argonia showed usual values)
2898	220/325	-/-	bursts 208-309: problems with PT7
2899	7/66	-/-	bursts 8-64: problems with PT7
2907	17/19	-/-	ok
(2909)	0/108	0/-	PT7 not working
2921	223/242	-/-	ok
2923	780/1190	-/-	ok
2929	42/44	-/-	ok
2938	183/184	+/-	ok
2939	179/282	+/-	ok
2959	35/37	+/-	ok
2968	472/777	+/-	(bursts 293-484 and 582-590: no beam)
2976	219/225	+/-	ok
2983	41/43	+/-	(first burst not decoded)
2985	402/407	+/-	reconstructed events 13682-13828 not readable
2987	7/9	+/-	the last burst had 3342 triggers (!)
2988	128/131	+/-	the last burst had 7833 triggers (!)
2994	13/15	+/-	ok

Table 5.3: The pre-selected runs not containing the pixel plane. The second column gives the number of selected and collected bursts. The last column summarises problems and observations. Runs in parentheses were discarded.

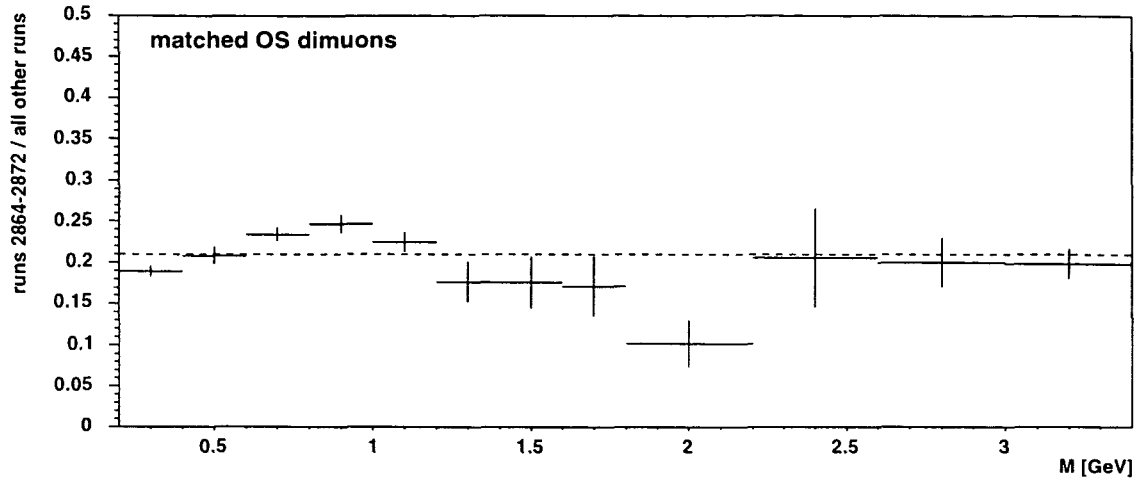


Figure 5.13: Ratio of the matched opposite sign (OS) dimuon mass spectrum of runs 2864–2872 to the spectrum obtained during the other selected runs.

Run No.	# of selected/total	PT7/ACM	Problems and observations
2722	11/18	-/+	ok
(2723)	0/25	-/+	unusual ratio #VT/#PC dimuons
2724	425/448	-/+	reconstructed events 712–753 not readable
2729	19/26	-/+	ok
2734	412/646	-/+	(many bursts with almost no beam)
2753	151/159	-/+	(lower beam intensity than before)
2754	17/22	-/+	ok
2757	11/13	-/+	ok
2767	125/126	-/+	(beam intensity raised)
2768	127/127	-/+	ok
2770	107/109	+/+	ok
2771	150/154	+/+	ok
2774	106/109	+/+	ok
2775	55/56	+/-	ok
2776	28/35	+/-	ok
2777	9/10	+/-	ok
2778	4/8	+/-	ok
2872	819/837	-/-	(problems in trigger hodoscope R1)

Table 5.4: List of pre-selected runs where the pixel plane was also operated. The second column gives the number of selected and collected number of bursts. The last column summarises problems and observations.

Runs which are placed in parentheses were discarded from the event analysis. Discarding all bursts where problems were found leaves 7170 bursts, collected during 46 runs, for the physics data analysis. The fraction of the selected bursts taken with the polarities $+/+$, $-/+$, $+/-$ and $-/-$ for the PT7 and ACM magnets, were

5%, 18%, 37% and 40%, respectively. Bursts where the Argonia information is either missing or ambiguous (run 2828) were excluded. Their number is very small, representing $\simeq 1\%$ of the total collected statistics.

The number of dimuons reconstructed by the muon spectrometer, integrated over the selected bursts, is 320 000, out of which one third was taken including the pixel plane. The corresponding number of collected triggers is almost two times higher due to accidental (“fake”) triggers or events with at least one of the muons not surviving the iron and fiducial cuts.

5.3.2 Luminosity Evaluation

For the selected bursts, we have evaluated the integrated luminosity, \mathcal{L} , according to

$$\mathcal{L} = N_{\text{inc}} \cdot N_{\text{tgt}}, \quad (5.6)$$

where N_{inc} is the number of incident protons and N_{tgt} is the number of nucleons in the individual targets. N_{tgt} is given by the target material’s properties: the mass number, A , the density, ρ , the interaction length, λ_I , and the target thickness, L ,

$$\begin{aligned} N_{\text{tgt}} &= \frac{N_A \cdot \rho \cdot l_{\text{eff}}}{A}, \quad \text{with} \\ l_{\text{eff}} &= \lambda_I \left[1 - e^{-\frac{L}{\lambda_I}} \right]. \end{aligned} \quad (5.7)$$

N_A is the Avogadro constant, $6.022 \cdot 10^{23} \text{ mol}^{-1}$. In the calculation of N_{tgt} we have used the material properties as given in the Particle Data Group tables [20], except for the interaction length of Indium, which was derived from neighbouring elements, $\lambda_I (\text{In}) = 22.9 \text{ cm}$. The target thicknesses, measured with $20 \text{ } \mu\text{m}$ precision, are 1.97 mm for the Indium and 1.95 mm for the Beryllium and the Lead targets. The resulting values for N_{tgt} are 0.0246, 0.0075 and 0.0067 b^{-1} for the Be, In and Pb targets, respectively.

The number of incident protons is “counted” by the three Argonia detectors, burst by burst, simply multiplying their signal by numerical calibration factors: 7000, 7660 and 7720 for the Argonia detectors 1, 2 and 3, respectively, with a precision of 5% [36]. The integrated number of protons for the selected bursts is $1.74 \cdot 10^{12}$ protons. Since the targets had a diameter of 1.2 cm and the beam profile is a Gaussian with a width of around $300 \text{ } \mu\text{m}$, we are sure that the beam is fully intercepted by the targets.

Each of the Argonia detectors registers the total number of protons in a given burst (“burst gated”), and the number of incident protons during the time when the DAQ system is not busy (“trigger gated”). These two numbers allow us to calculate the lifetime of the NA60 detector. After having received a trigger, the detector system needs a certain time to read out the data and is not capable of processing a new event during this “dead time”. Since the number of triggers per burst was relatively low and the amount of data to be read out per event was not exceedingly high, the dead-time of the experiment was only 1% for most of the selected runs, see Fig. 5.14.

In the last 5 runs, however, the dead-time increased to 4% due to problems with one of the trigger hodoscopes. These dead-times have been taken into account when

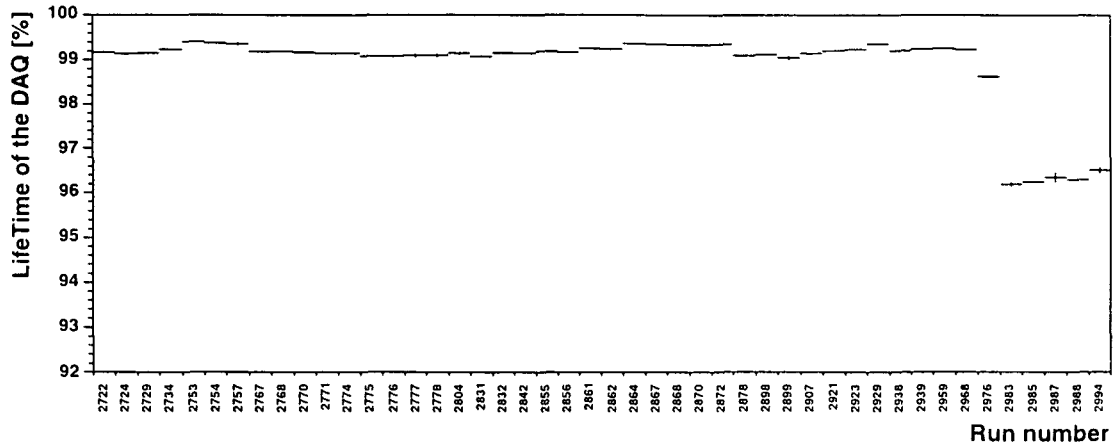


Figure 5.14: Lifetime of the detector system, for the selected runs.

calculating the overall luminosities. Moreover, the fact that a small fraction of the beam becomes absorbed when passing through the sub-targets has also been taken into account. The beam intensity corrected for dead time is shown in Fig. 5.15 for the selected bursts. The integrated luminosities, for each target, are listed in Table 5.5.

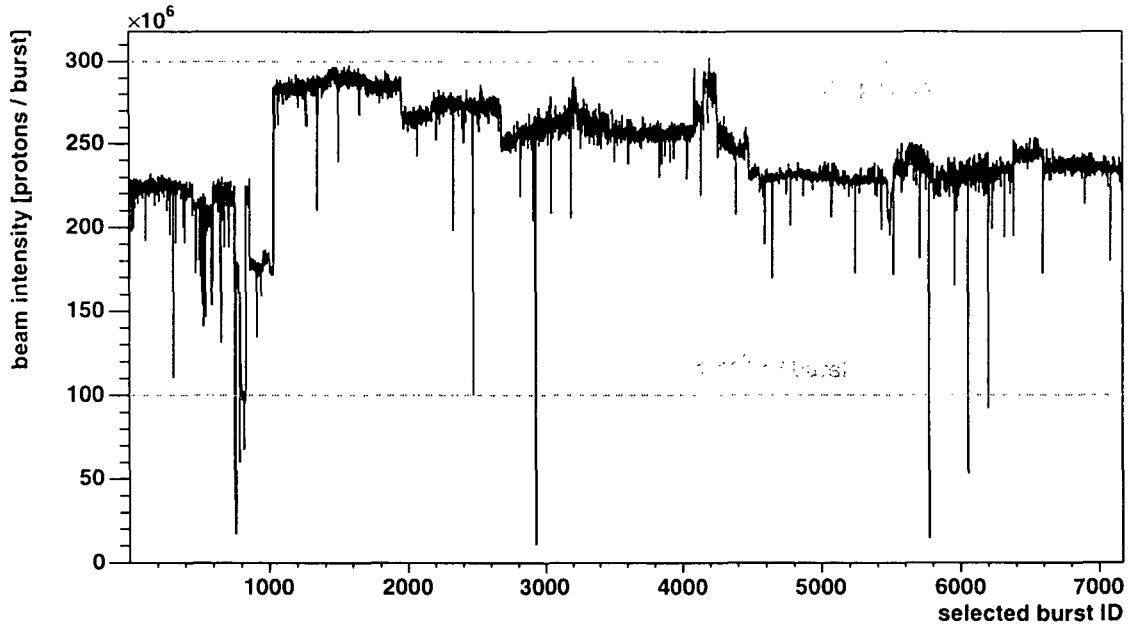


Figure 5.15: Measured beam intensity for the selected bursts.

5.3.3 Selecting Dimuons from the Target Region

Within the selected bursts we not only have “interesting” physics events but also events, where the trigger dimuon was produced outside of the target region, in par-

Target	N_{tgt} [b ⁻¹]	$\exp(-a_i)$	$\int \mathcal{L} \cdot dt$ [nb ⁻¹]
In	0.0075	1	13.1
Be	0.0246	0.991	43.1
Be	0.0246	0.986	42.9
Be	0.0246	0.982	42.7
Pb	0.0067	0.977	11.4
Be	0.0246	0.966	42.0

Table 5.5: Integrated luminosities for the selected bursts, target by target.

ticular in the hadron absorber and beam dump. Of course, in such events we would not be able to match the two muons from the muon spectrometer to tracks in the vertex telescope and they would be naturally discarded from the final event selection. However, in order to study and understand the matching efficiency, we have to discard such events *before* the matching.

As we have seen, the vertex resolution of the PC dimuons is insufficient to determine whether the two muons were produced in the target region or not. If the (single) muon tracks are backwards extrapolated into the target region, they have an “offset” (dx , dy) in the transverse plane at the centre of the target, $z = 0$, whose magnitude is given by the multiple scattering they suffered while crossing the hadron absorber. Since the multiple scattering angle ($\theta_{\text{MS}} \propto dx$) is inversely proportional to the muon’s momentum the products $p \cdot dx$ and $p \cdot dy$ are constant, if we neglect that the momentum resolution changes with momentum. The distribution of these two variables will be Gaussian, provided the muons are produced in the target region. For muons coming from elsewhere along the beam line, we expect an additional offset, as depicted in Fig. 5.16, giving rise to a Gaussian distribution with a larger width. Since we do not know the origin of the muons, we will measure the convolution of

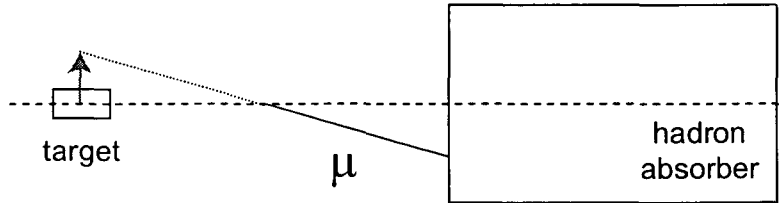


Figure 5.16: Offset in transverse plane at $z = 0$ for muons produced downstream of the target system.

both distributions, from which the widths can be extracted. We can then calculate the probability of the following χ^2 distribution,

$$\chi^2 = \left(\frac{pdx}{\sigma(pdx)} \right)^2 + \left(\frac{pdy}{\sigma(pdy)} \right)^2, \quad (5.8)$$

where σ is the width of the distribution for muons coming from the target region. In this probability distribution muons belonging to the distribution with the larger

width will manifest themselves at low probability values. We can, hence, filter out events where one or both muons do not come from the target, by simply applying a cut on the obtained probability distribution, typically of the order of a few percent. Within our collaboration this single muon cut is often referred to as the " $p * D_{\text{target}}$ " cut.

Chapter 6

Expected Dimuon Sources

The dimuon mass spectrum is a rich superposition of various sources resulting in a continuously falling spectrum, decorated with several distinct resonances. The continuous processes are the Drell–Yan dimuons, which are dominating at large dimuon masses (i.e. above ~ 3.5 GeV) and the semi-muonic simultaneous decays from two D mesons. The latter dimuon source is called “open charm”. Its contribution is strongest at around 0.8 GeV. At the lower end of the dimuon mass spectrum the electromagnetic decays of the light pseudo-scalar and vector mesons (η , η' , ρ , ω and ϕ) are the dominating processes, adding to the continuous spectrum via their Dalitz decays and/or giving rise to distinct peaks via their 2-body decays. We call their superposition the “hadronic decay cocktail”. At higher masses we see the J/ψ , and the ψ' . The more massive bottomonium states cannot easily be produced at SPS energies, since their cross-sections are very small.

The hadronic decay cocktail was simulated with the Monte Carlo generator “Genesis”, which was first developed within the framework of the NA45/CERES experiment. The code was adjusted for NA60 needs, changing electrons into muons and adding the J/ψ among other improvements. The Drell–Yan and open charm processes were generated with the Pythia event generator.

All simulated processes were tracked through the NA60 apparatus, using GEANT. Events in which a dimuon gave rise to a trigger were reconstructed as the collected data, using the same reconstruction settings. In this way, we reproduce the effects imposed by the detector, such as the finite acceptance window, the energy loss, and the smearing of the kinematic variables through multiple scattering or due to the finite resolution of the apparatus.

6.1 Light Meson Decays

Mesons consist of a quark and an antiquark. For spin-1/2 quarks and antiquarks we can form spin triplet states ($\uparrow\uparrow$) with $J = 1$ and spin singlet states ($\uparrow\downarrow$) with $J = 0$. Fermions and antifermions have intrinsic opposite parity so that the $f\bar{f}$ pair carries parity $P = -1$. If they have orbital angular momentum, L , their parity is given by $P_{f\bar{f}} = (-1)^{L+1}$. Thus, the $J = 0$ states in the ground state $L = 0$ have the quantum

numbers $J^P = 0^-$, which are called “pseudo-scalars” and the $J = 1$ states with $L = 0$ have $J^P = 1^-$ and are called “vector mesons”. For three quark flavours, we expect families of mesons containing $3^2 = 9$ states, or “nonets”. The (u, d, s) pseudo-scalar and vector nonets decompose into a singlet and an octet state, each.

The pseudo-scalar octet contains an iso-vector triplet, namely the three pions, $\pi^+(u\bar{d})$, $\pi^0(1/\sqrt{2}(u\bar{u} - d\bar{d}))$, $\pi^-(\bar{u}d)$, and two iso-doublets, the $K^+(u\bar{s})$, $K^0(d\bar{s})$, $K^-(\bar{u}s)$ and the $\bar{K}^0(\bar{d}s)$. The last member of the octet and the singlet consist of an iso-scalar each, the $\eta_8 = 1/\sqrt{6}(u\bar{u} + d\bar{d} - 2s\bar{s})$ and the $\eta_0 = 1/\sqrt{3}(u\bar{u} + d\bar{d} + s\bar{s})$. The actual states η and η' observed in nature are not the pure states mentioned; they are rather a linear combination of the above wave functions:

$$\eta = \left(\frac{\cos \theta_P}{\sqrt{6}} - \frac{\sin \theta_P}{\sqrt{3}}\right)u\bar{u} + \left(\frac{\cos \theta_P}{\sqrt{6}} - \frac{\sin \theta_P}{\sqrt{3}}\right)d\bar{d} - \left(\frac{\cos \theta_P}{\sqrt{6}/2} + \frac{\sin \theta_P}{\sqrt{3}}\right)s\bar{s} \quad (6.1)$$

$$\eta' = \left(\frac{\sin \theta_P}{\sqrt{6}} + \frac{\cos \theta_P}{\sqrt{3}}\right)u\bar{u} + \left(\frac{\sin \theta_P}{\sqrt{6}} + \frac{\cos \theta_P}{\sqrt{3}}\right)d\bar{d} - \left(\frac{\sin \theta_P}{\sqrt{6}/2} - \frac{\cos \theta_P}{\sqrt{3}}\right)s\bar{s} \quad (6.2)$$

The pseudo-scalar mixing angle, θ_P , is thought to be $\approx -10^\circ$, with a large uncertainty [20].

The (quark) structure of the vector nonet is identical to the one of the pseudo-scalars. The $J = 1$ analog of the pions are the ρ 's with the same quark contents. The vector counterparts of the η and η' are the ϕ and the ω , respectively. The observed ϕ and ω states are again mixtures of the pure states. The measured angle $\theta_V \approx 35^\circ$ is much larger than θ_P and is compatible with the ideal mixing angle for which the ϕ becomes a pure $s\bar{s}$ state:

$$\omega = \frac{1}{\sqrt{2}}(u\bar{u} + d\bar{d}) \quad (6.3)$$

$$\phi = s\bar{s} \quad (6.4)$$

The properties of the pseudo-scalar and vector mesons which contribute significantly to the dimuon mass spectrum either through a decay into two muons or via a Dalitz decay are summarised in Table 6.1.

Resonance	Mass [MeV]	Γ [MeV]	J^{PC}	Quark-content
η	547.30 ± 0.12	$(1.18 \pm 0.11) \cdot 10^{-3}$	0^{-+}	see Eq. (6.1)
ρ	771.1 ± 0.9	149.2 ± 0.7	1^{--}	$1/\sqrt{2}(u\bar{u} - d\bar{d})$
ω	782.57 ± 0.12	8.44 ± 0.09	1^{--}	$1/\sqrt{2}(u\bar{u} + d\bar{d})$
η'	957.78 ± 0.14	0.202 ± 0.016	0^{-+}	see Eq. (6.2)
ϕ	1019.456 ± 0.020	4.26 ± 0.05	1^{--}	$s\bar{s}$

Table 6.1: Properties of the light pseudo-scalar and vector mesons contributing to the dimuon mass spectrum, values taken from Ref. [20].

6.1.1 The Pseudo-scalar Mesons, η and η'

Figure 6.1 shows the Dalitz and 2-body decays of the η and the η' pseudo-scalar mesons. The (Single) Dalitz decay is a 2γ decay, in which one of the photons is

virtual and converts into a lepton pair, $PS \rightarrow \gamma^* \gamma \rightarrow \mu^+ \mu^- \gamma$. There is also a Double Dalitz decay, in which both γ 's are virtual photons and convert into a lepton pair, but with a much smaller branching ratio. The decay of the η into two muons is a 4^{th} order electromagnetic process, where the μ^+ coming from one γ^* and the μ^- coming from the other γ^* are contracted.

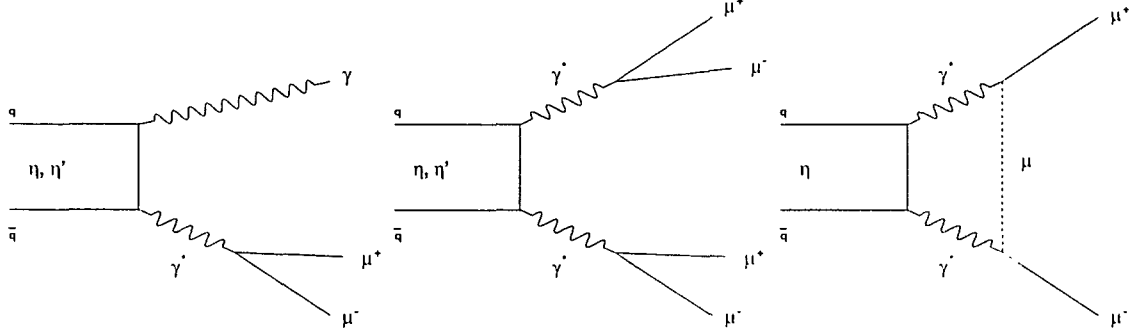


Figure 6.1: Single, Double Dalitz and two body decays of the pseudo-scalar mesons η and η' .

The branching ratio into two muons has a lower limit [37] given by the radiative decay channel,

$$BR(PS \rightarrow l^+ l^-) \geq BR(PS \rightarrow \gamma\gamma) \cdot 2\alpha^2 \left(\frac{m_l}{m_{PS}} \right)^2 \sqrt{1 - 4 \left(\frac{m_l}{m_{PS}} \right)^2} . \quad (6.5)$$

From this equation we can see that the electronic branching ratio is suppressed with respect to the muonic branching ratio, by the ratio $(m_e/m_\mu)^2$. For the η the following lower limits were deduced [37]:

$$\begin{aligned} BR(\eta \rightarrow \mu^+ \mu^-) &\geq 4.0 \cdot 10^{-6}, \\ BR(\eta \rightarrow e^+ e^-) &\geq 1.7 \cdot 10^{-9} . \end{aligned}$$

Indeed, only the muonic branching ratio is measured by now. Its value, taken from Ref. [38], is $BR(\eta \rightarrow \mu^+ \mu^-) = (5.8 \pm 0.8) \cdot 10^{-6}$.

For the η' 2-body decay channels there are also such theoretical lower limits. Experimentally, however, not even an upper limit is published in the PDG tables so that we can safely neglect its contribution to the dimuon mass spectrum. Its (Single) Dalitz decay channel is comparable to the one of the η , so that we must consider this process. Unfortunately, the production cross-section of the η' was never measured. In Ref. [39] the η'/π^0 ratio is given for high p_T . Based on this measurement, in Ref. [40] the η' cross-section was extracted by fitting the observed p_T spectra of the η' and of the π^0 with the Bourquin-Gaillard parameterisation [41]. A similar analysis was performed for the η , from which the ratio $\eta'/\eta = 1/3$ was extracted (with rather large uncertainties). In Ref. [42] a value of $\eta'/\eta < 0.2$ was found at 95% confidence level. Following the analyses performed in Refs. [8] and [6], we have assumed $\eta'/\eta = 0.15$.

6.1.2 The Light Vector Mesons: ρ , ω and ϕ

The vector mesons ρ , ω and ϕ mainly contribute to the dimuon mass spectrum via their di-muonic decay mode. The electromagnetic decay of the vector mesons ρ , ω and ϕ into two muons proceeds via a virtual photon, $V \rightarrow \gamma^* \rightarrow \mu^+ \mu^-$. The ω possesses, furthermore, a Dalitz decay mode, in which the lepton pair is accompanied by a π^0 , $\omega \rightarrow \gamma^* \pi^0 \rightarrow \mu^+ \mu^- \pi^0$. See Fig. 6.2 for the corresponding diagrams.

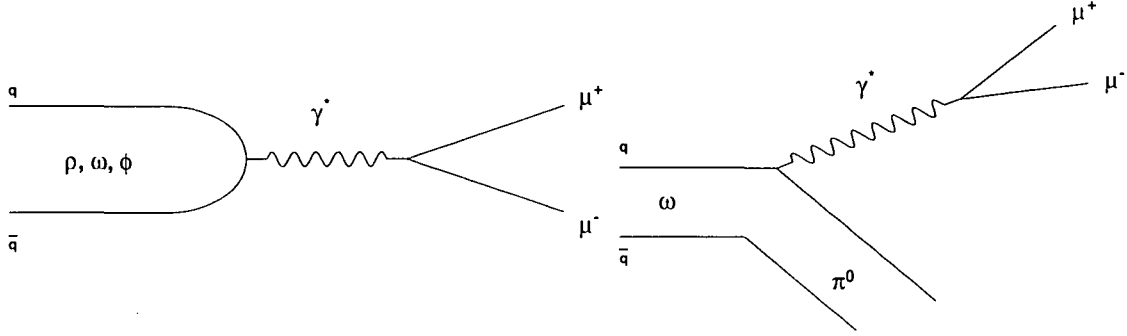


Figure 6.2: Dimuonic decay of the vector mesons ρ , ω and ϕ (left) and the ω Dalitz decay (right).

6.1.3 The Vector Dominance Model

The Vector Dominance Model (VDM) is a phenomenological model which describes the resonance interaction between photons and hadrons. A virtual photon can interact with a hadron not only directly but also after a transition into a virtual vector meson state. This is possible since vector mesons (like the ρ , ω and the ϕ) have the same quantum numbers as the photon, $J^P = 1^-$. This mechanism is especially pronounced when the transferred momentum squared, q^2 , approaches the squared mass of the vector meson. The VDM model provides a framework to describe e.g. the ρ resonance and the form factors of the η , η' and ω Dalitz decays. This “realisation” of a virtual intermediate particle results in a strong enhancement of the form factor, as will be described below.

6.1.4 Branching Ratios

Table 6.2 summarises the processes contributing to the hadronic cocktail and gives their branching ratios, taken from the Particle Data Group tables [38].

Note that we used the electronic branching ratio for the ω 2-body decay, since it is known with much better accuracy than the muonic value. We have done this assuming lepton universality, which states that the weak force couples to all leptons with the same strength. It hence follows that the leptonic branching ratios should be the same, apart from phase space considerations, which are negligible here. Indeed, the electronic and muonic branching ratios, listed in the PDG tables, agree within their error bars, $BR(\omega \rightarrow e^+ e^-) = (7.14 \pm 0.15) \cdot 10^{-5}$, $BR(\omega \rightarrow \mu^+ \mu^-) = (9.0 \pm 3.1) \cdot 10^{-5}$.

Particle		Decay	BR
Dalitz	η	$\mu^+\mu^-\gamma$	$(3.1 \pm 0.4) \cdot 10^{-4}$
	η'	$\mu^+\mu^-\gamma$	$(1.04 \pm 0.26) \cdot 10^{-4}$
	ω	$\mu^+\mu^-\pi^0$	$(9.6 \pm 2.3) \cdot 10^{-5}$
2-body	η	$\mu^+\mu^-$	$(5.8 \pm 0.8) \cdot 10^{-6}$
	ρ	$\mu^+\mu^-$	$(4.55 \pm 0.28) \cdot 10^{-5}$
	ω	$\mu^+\mu^-$	$(7.14 \pm 0.15) \cdot 10^{-5}$
	ϕ	$\mu^+\mu^-$	$(2.85 \pm 0.19) \cdot 10^{-4}$

Table 6.2: Processes included in the hadronic decay cocktail and the branching ratios considered in our study.

6.1.5 Nuclear Dependence of the Production Cross-Sections

While the Drell-Yan and open charm production cross-sections in p-A collisions are known to scale linearly with the number of target nucleons, A , this is not the case for light meson production. It has been a usual procedure to express the nuclear dependence of particle production as a power law,

$$\sigma_{pA} = \sigma_0 \cdot A^\alpha \quad . \quad (6.6)$$

Several experiments used this parameterisation, and some values are compiled in Table 6.3.

	Experiment		p_{lab} [GeV/c]	Targets	α	Phase Space p_{lab}, p_T in GeV/c
ρ/ω	FNAL CP (76)	[43]	p 225	C, Sn	0.69 ± 0.02	$x_F > 0.15$
	E358 (76)	[44]	n ~ 300	Be, Al, Cu, Pb	0.62 ± 0.03	$p_{\text{lab}} > 75$
	FNAL CP (76)	[43]	π^+ 225	C, Sn	0.72 ± 0.03	$x_F > 0.15$
	E672/E706 (92)	[45]	π^- 530	Be, Cu	0.77 ± 0.02	$0.1 < x_F < 0.8$
ϕ	IHEP BIS-2 (90)	[43]	n 30–70	C, Al, Cu	0.81 ± 0.06	$x_F > 0, p_T < 1$
	NA11 (84)	[46]	p 120	Be, Ta	0.86 ± 0.02	$0 < x_F < 0.3, p_T < 1$
	FNAL CP (76)	[43]	p 225	C, Sn	0.76 ± 0.03	$x_F > 0.15$
	E358 (76)	[43]	n ~ 300	Be, Al, Cu, Pb	0.68 ± 0.03	$p_{\text{lab}} > 75$
	HERA-B (04)	[47]	p 920	C, Ti, W	1.01 ± 0.01 ± 0.06	$2.95 < y < 4.20,$ $0.5 < p_T < 12.1$
	NA11 (84)	[46]	π^- 120	Be, Ta	0.90 ± 0.02	$0 < x_F < 0.3, p_T < 1$
	FNAL CP (77)	[43]	π^+ 225	C, Sn	0.77 ± 0.04	$x_F > 0.15$
	E672/E706 (92)	[45]	π^- 530	Be, Cu	0.81 ± 0.04	$0.1 < x_F < 0.8$

Table 6.3: Available α measurements for the ρ/ω and ϕ resonances. Several of these lines were taken from Ref. [43].

At first sight, from these values, we would derive that the α parameter ranges approximately from 0.62 to 0.77 for the ω and from 0.68 to 1.01 for the ϕ . We would also conclude that the quoted error bars have been largely underestimated. However, we should not rush into such conclusions. On one hand, we cannot easily compare the different quoted values to one another, since they were obtained with different beam particles and in different phase space windows. It is well known that α , whatever the

process, varies as a function of x_F (or rapidity) and as a function of p_T , as can be seen, e.g., in Figs. 6.3 (and 6.13). In particular, the value of α decreases for large x_F and increases with p_T (the “Cronin effect”).

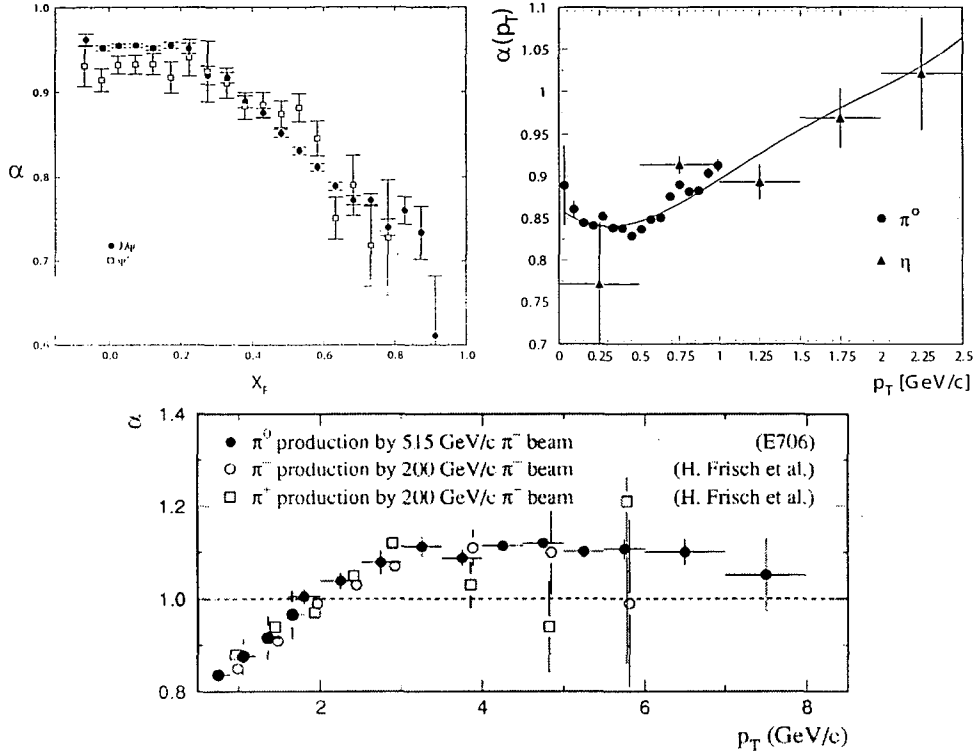


Figure 6.3: Top left: α of J/ψ and ψ' as a function of x_F , as measured by E866 in 800 GeV protons incident on Be, Fe and W [48]. Top right and bottom: α of π and η mesons as a function of p_T . Top right: CERES compared p-Au to p-Be collisions at 450 GeV [42]. Bottom: E258 compared π^- incident on H, Be, Cu and W targets at 200 GeV [49]; E706 compared π^- incident on H, Be, Cu at 515 GeV [50].

On the other hand, the nuclear dependence cannot be properly determined from only two nuclear targets, especially if we use the very simplistic A^α function, and if the two targets are relatively light, as is the case of several measurements quoted in this table. Therefore, the values previously measured can hardly be used as reference to our own measurements, except to indicate that the ϕ meson seems to have a steeper nuclear dependence than the ρ/ω mesons.

6.1.6 Transverse Momentum Distributions

The CERES Collaboration reproduced [6] the measured p_T distributions from π^0 , η and ω mesons, see Fig. 6.4, with a functional form consisting of a Boltzman term complemented by a power law term, to better account for the hard tail.

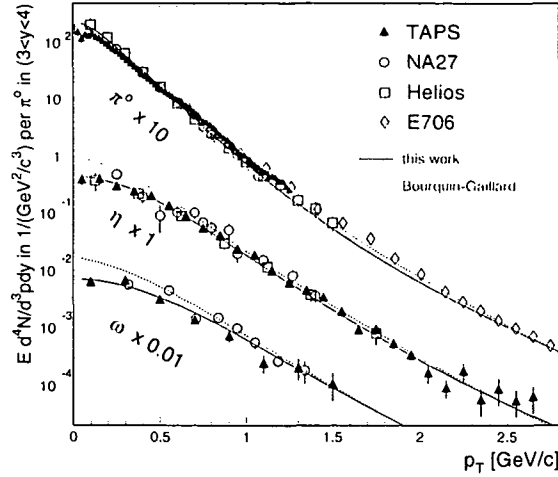


Figure 6.4: p_T distributions of π^0 , η and ω mesons, measured by CERES-TAPS, NA27, HELIOS-1 and E706, as included in Ref. [6].

$$\frac{1}{p_T} \frac{dN}{dp_T} = \beta \exp(-m_T/T) + \alpha \frac{(1 - 2m_T/\sqrt{s})^\gamma}{(1 + m_T^2)^4}, \quad (6.7)$$

where all variables (p_T , m_T , T and \sqrt{s}) are expressed in GeV. In our simulations we have kept the parameters used by CERES and NA38/NA50: $\beta = 0.15 \text{ GeV}^{-2}$, $\gamma = 7.9$ and the α parameter is 0.011 GeV^6 for the η , η' and ϕ , and 0.02 GeV^6 for the ρ and ω . We have also generated p_T distributions according to the form

$$\frac{1}{m_T} \frac{dN}{dm_T} = \frac{1}{p_T} \frac{dN}{dp_T} = m_T \cdot K_1\left(\frac{m_T}{T}\right), \quad (6.8)$$

with the “inverse slope” parameter, T , taken to be 180 MeV for all resonances between the η and the ϕ masses.

6.1.7 Rapidity Distributions

The rapidity distributions were generated according to the expression $1/\cosh^2(ay)$, similar to a Gaussian of $\sigma = 0.75/a$.

The width of the pion rapidity distribution was estimated using Landau’s expression $\sqrt{\log \gamma_{\text{proj}}}$. The width of the rapidity distribution for heavier mesons is decreased proportionally to the maximum rapidity (in the c.m.s. frame, y^*) with which such a meson can be produced for a given \sqrt{s} : $\sigma_{\text{part}} = \sigma_\pi \cdot y_{\text{max}}^*(m_{\text{part}})/y_{\text{max}}^*(m_\pi)$, with $y_{\text{max}}^* = \log(\sqrt{s}/m_{\text{part}})$. Table 6.4 summarises the width parameters of the rapidity distributions for the particles relevant for the Genesis event generator, including the π^0 , at $E_{\text{lab}} = 400 \text{ GeV}$. Figure 6.5 illustrates the width of the rapidity distributions for a 400 GeV proton beam as a function of mass.

This simple parameterisation has been used by several experiments, since it describes reasonably well existing measurements. The rapidity widths measured by

particle	mass [GeV]	σ_y	a_y
π^0	0.135	1.84	0.41
η	0.547	1.35	0.56
ρ	0.771	1.23	0.61
ω	0.783	1.23	0.61
η'	0.958	1.16	0.65
ϕ	1.019	1.14	0.66
J/ψ	3.097	0.75	1.00

Table 6.4: Parameters of the rapidity distributions of particles with different masses, for a beam energy of $E_{\text{lab}} = 400$ GeV.

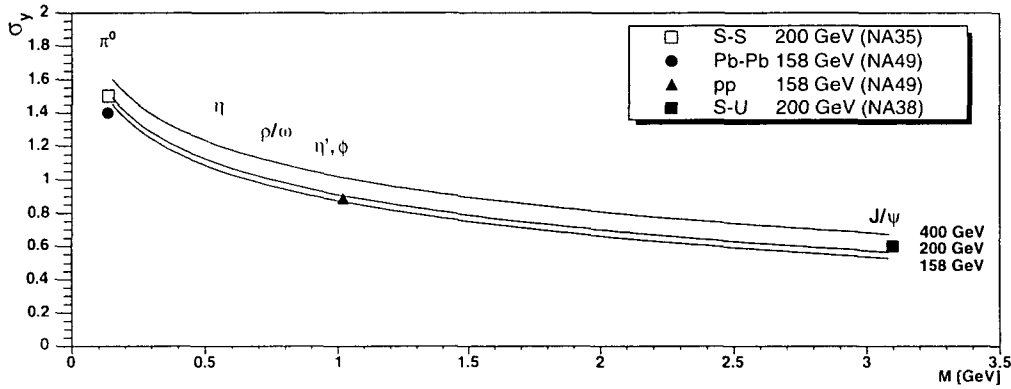


Figure 6.5: Widths of the rapidity distributions in p-A collisions at 158, 200 and 400 GeV, as a function of the particle's mass.

the NA49 Collaboration in pp collisions at $E_{\text{lab}} = 158$ GeV [51], for the ϕ and π^0 mesons, for instance, are $\sigma_y(\phi) = 0.89 \pm 0.06$ and $\sigma_y(\pi) = 1.5$, respectively, and the width of the J/ψ meson measured by the NA38 Collaboration [10] in S-U collisions at $E_{\text{lab}} = 200$ GeV is 0.6. NA35 measured rapidity distributions for negatively charged hadrons in S-S collisions at $E_{\text{lab}} = 200$ GeV [52].

Note that in the current implementation of Genesis no $y - p_T$ correlations were included to conserve energy and momentum. This should be a good approximation, since our acceptance window is restricted to a small range around mid-rapidity.

6.1.8 Resonance Mass Line Shapes

For the mass line shapes of the narrow resonances η , ω and ϕ , we have used a modified relativistic Breit-Wigner parameterisation, first proposed by G.J. Gounaris and J.J. Sakurai [53], with the widths and masses taken from the PDG tables. The

formula,

$$\frac{dN}{dM} = \frac{\sqrt{1 - \frac{4m_\mu^2}{M^2}}(1 + 2\frac{m_\mu^2}{M^2})}{(m_{\text{res}}^2 - M^2)^2 + \left[m_{\text{res}} \left(\frac{\Gamma_{\text{res}}}{M} \frac{(M^2/4 - m_\mu^2)^{3/2}}{(m_{\text{res}}^2/4 - m_\mu^2)^{3/2}} \right) \right]^2} \quad , \quad (6.9)$$

where m_{res} and Γ are the resonance's pole-mass and total decay width, and m_μ is the muon mass, ensures a lower mass cut-off at twice the muon mass.

The ρ predominantly decays in the two pion channel, $BR(\rho \rightarrow \pi^+\pi^-) \approx 100\%$. Particles decaying via the strong interaction are characterised by lifetimes of the order of $\tau \sim 10^{-22} - 10^{-24}$ s, resulting in decay widths, $\Gamma \equiv 1/\tau$, of around 100 MeV. The ρ , hence, is a “broad” resonance with a decay width of ~ 150 MeV. Due to its broadness the shape of the ρ is highly influenced by phase space effects and by the production mechanism. Figure 6.6 shows the diagram by which the ρ contributes to the dimuon mass spectrum.

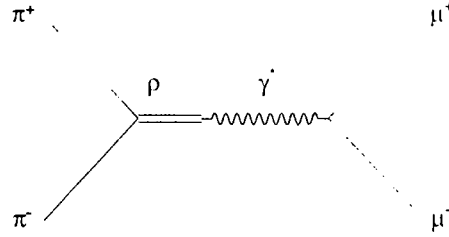


Figure 6.6: Production of the ρ resonance and its subsequent muonic decay, as described by the Vector Dominance Model.

Its differential rate can be expressed as

$$\frac{d^4R}{dq^4} = \int d\Phi \cdot f(p_\pi^+) f(p_\pi^-) \cdot |\mathcal{M}|^2 \cdot F_{12}, \quad (6.10)$$

where Φ is the momentum (phase) space and $f(p_\pi^\pm)$ are the occupation probabilities of the available momentum space. The distribution of the incoming pions is approximated by the Boltzmann distribution, $f(p) \approx \exp(-E/T)$. The matrix element squared, $|\mathcal{M}|^2$, for the given process, $\sigma_{\pi^+\pi^- \rightarrow \mu^+\mu^-}(q^2)$, depends on the transferred momentum squared, which defines the invariant mass squared of the produced dimuon, $q^2 \equiv M^2$. The factor F_{12} is the flux of incoming particles.

The ρ propagator is dressed by momentum dependent $\pi\pi$ loops, see Fig. 6.7. For

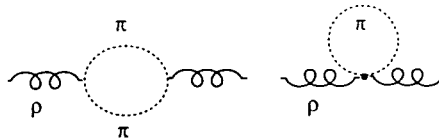


Figure 6.7: First order diagrams of the vacuum fluctuations of the ρ propagator [54].

this reason the constant decay width Γ_ρ in the “Breit-Wigner” expression, which describes the resonance, has to be replaced by a mass dependent width [54], $\Gamma_\rho(M)$.

The rate, Eq. (6.10), can be calculated within the framework of the VDM. A detailed calculation can be found in Ref. [55]; here, we only summarise the result. The differential rate of the given process has the form

$$\frac{d^4 R(M)}{dM d\mathbf{q}} = \frac{2\pi\alpha^2 m_\rho^4}{3(2\pi)^5} \frac{\left(1 - \frac{4m_\pi^2}{M^2}\right)^{3/2} \sqrt{1 - \frac{4m_\mu^2}{M^2}} \left(1 + \frac{2m_\mu^2}{M^2}\right)}{(M^2 - m_\rho^2)^2 + M^2 \Gamma_{\text{tot}}^2} \frac{M}{\sqrt{M^2 + \mathbf{q}^2}} e^{-\frac{\sqrt{M^2 + \mathbf{q}^2}}{T}}, \quad (6.11)$$

where the last two terms come from the momentum dependent phase space. T is a “temperature” parameter related to hadronisation. Its value, 170 MeV [56], was deduced from pion p_T distributions in elementary reactions and nuclear collisions at SPS energies.

To obtain the single differential rate, dR/dM , we have to integrate over the 3-momentum. We obtain for the dimuon mass distribution of the ρ resonance,

$$\frac{dR(M)}{dM} = \frac{\alpha^2 m_\rho^4}{3(2\pi)^4} \frac{\left(1 - \frac{4m_\pi^2}{M^2}\right)^{3/2} \sqrt{1 - \frac{4m_\mu^2}{M^2}} \left(1 + \frac{2m_\mu^2}{M^2}\right)}{(M^2 - m_\rho^2)^2 + M^2 \Gamma_{\text{tot}}^2} (2\pi MT)^{3/2} e^{-M/T}. \quad (6.12)$$

The result of this derivation was introduced as an update [57] to the previous version of the Genesis code, which did not include the momentum dependent phase space corrections. In Fig. 6.8 this new line shape is compared to the previous version and to a simple and a relativistic Breit-Wigner parameterisation.

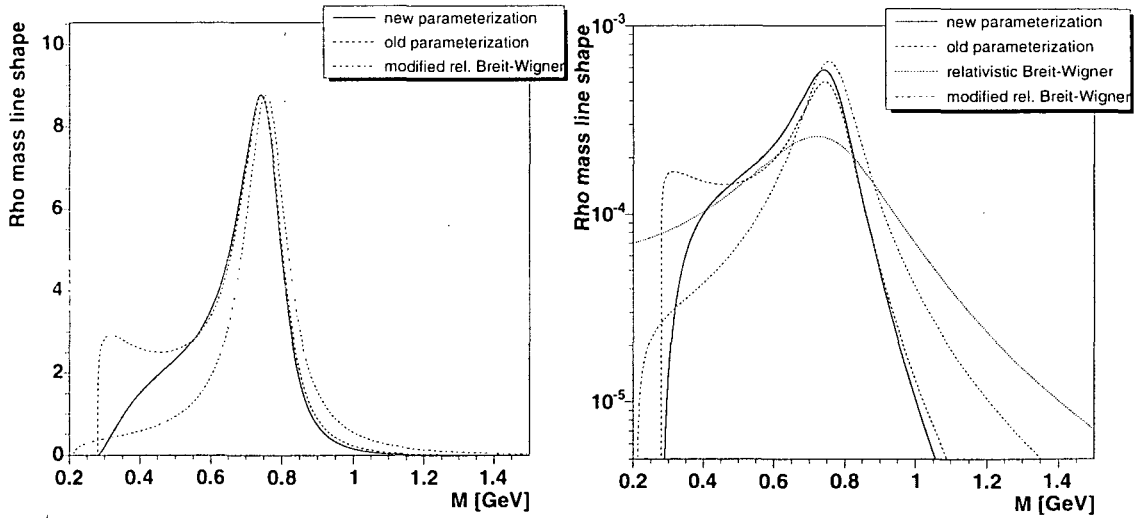


Figure 6.8: Comparison of different ρ line shapes in linear (left) and logarithmic (right) scales. The shape implemented in NA60root is represented by the solid line.

The new mass line shape falls off more steeply with mass at high momentum transfer and has a less pronounced “left shoulder”, due to the last two terms in Eq. (6.12).

6.1.9 Dimuon Mass Distribution for the Dalitz Decays

The lepton pair mass distribution in conversion decays involving a photon was derived by N. Kroll and W. Wada [58],

$$\frac{dN}{dM} = \frac{1}{M} \left(1 + 2 \frac{m_\mu^2}{M^2}\right) \left(1 - \frac{M^2}{m_{\text{res}}^2}\right)^3 \sqrt{1 - \frac{4m_\mu^2}{M^2}} \quad (6.13)$$

The expression for the ω Dalitz conversion decay is different because the accompanying π^0 is not massless,

$$\frac{dN}{dM} = \frac{1}{M} \left(1 + 2 \frac{m_\mu^2}{M^2}\right) \left[\left(1 + \frac{M^2}{m_\omega^2 - m_{\pi^0}^2}\right)^2 - \frac{4m_\omega^2 M^2}{(m_\omega^2 - m_{\pi^0}^2)^2} \right]^{3/2} \sqrt{1 - \frac{4m_\mu^2}{M^2}} \quad (6.14)$$

The measured dimuon mass spectrum for the Dalitz conversion decays deviates from the expressions (6.13) and (6.14) by the so-called electromagnetic transition form factors, $|F(q^2)|^2$. Reference [37] gives an introduction to this topic and shows a comprehensive compilation of the measurements on the transition form factors available.

In the VDM the Dalitz conversion decays are described by the diagrams depicted in Fig. 6.9. The Dalitz decay of the η , η' and ω mesons can proceed via the conversion into any of the three vector mesons (ρ , ω , ϕ) and the form factor $F(q^2)$ is calculated as a sum of the three diagrams,

$$|F(q^2)|^2 = \left| \sum_{V=\rho,\omega,\phi} w_V \left(\frac{m_V^2}{(m_V^2 - q^2) + im_V \Gamma_V} \right) \right|^2 \quad (6.15)$$

In practical terms, however, only the diagram involving the ρ meson is of importance, since its weight, w_ρ , which enters quadratically in $|F(q^2)|^2$, is larger than the ones of the ω and ϕ .

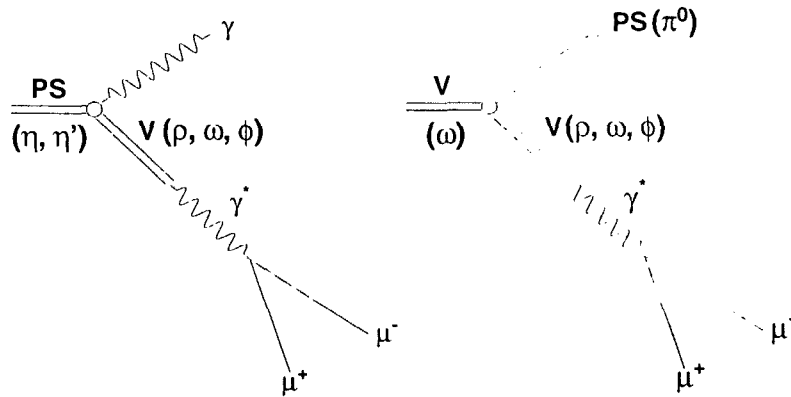


Figure 6.9: Dalitz decays of the η , η' and ω , as described by the VDM.

The Vector Dominance Model predicts a growth of the transition form factors with increasing dilepton mass. Its influence is, hence, more important for heavier

decaying mesons (such as the η' meson). The calculations for the η and η' mesons compare well to the Lepton-G measurements¹, as shown in Fig. 6.10.

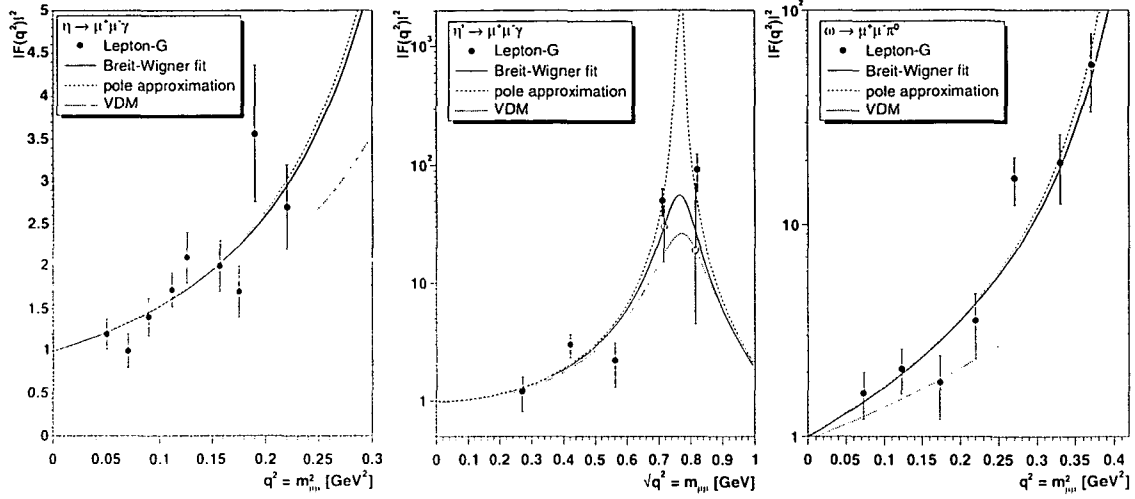


Figure 6.10: Electromagnetic transition form factors for the η , η' and ω Dalitz decays, as given in the review of Landsberg [37].

For the ω meson, however, the VDM predictions differ significantly from the Lepton-G data for $q^2 > 0.25 \text{ GeV}^2$. For this reason, a fit to the Lepton-G data has been used as form factor of the ω Dalitz decay. The Lepton-G data for the transition form factor were originally parameterised in the pole approximation as $|F(q^2)|^2 = 1/(1 - q^2/\Lambda_{\text{part}}^2)$, as can be seen in Fig. 6.10. Here, q is the 4-momentum of the virtual photon, hence, q^2 is the invariant dimuon mass squared; Λ_{part}^2 is the characteristic mass for the respective decaying meson. The parameters obtained by the Lepton-G Collaboration are $\Lambda_\eta = (0.72 \pm 0.09) \text{ GeV}$, $\Lambda_{\eta'} = (1.7 \pm 0.4)^{-1/2} \text{ GeV}$ and $\Lambda_\omega = (0.65 \pm 0.03) \text{ GeV}$. While this parameterisation was adopted for the form factor of the η , we have used a different fit to the η' and ω Lepton-G data, properly describing the resonant behaviour, by means of a Breit-Wigner functional form, $|F(q^2)|^2 = a^4/[(a^2 - q^2)^2 + a^2 b^2]$. The parameters obtained were $a = 0.764 \text{ GeV}$, $b = 0.102 \text{ GeV}$ for the η' and $a = 0.6519 \text{ GeV}$, $b = 0.04198 \text{ GeV}$ for the ω form factor.

6.1.10 Distribution of the Decay Angles

The azimuthal angle, ϕ , is generated isotropic for all decay modes.

For the polar decay angle we have used two possible distributions in the case of the 2-body decays: uniform and $1 + \cos^2 \theta$. In the Dalitz decays, the two muons are accompanied by a third decay partner. In case of the pseudo-scalar η and η' , the third partner, a real photon, carries spin 1. In order to conserve angular momentum, the

¹“Lepton-G” is the name of a magnetic spectrometer used by several experiments at the Serpukhov (IHEP) accelerator, near Moscow. The measurements to which these comparisons refer were conducted between 1978 and 1980 and are summarised in the review of Landsberg [37], in which all the corresponding references can be found.

spins of the real and virtual photons must be anti-parallel. Since for the real photon the helicity zero does not exist, the virtual photon cannot have helicity zero either. Instead, a $1 + \cos^2 \theta$ distribution is expected. For the ω Dalitz the third partner is a π^0 , which has spin 0. Hence, the two muons are not emitted under a preferred angle, and we have generated a uniform distribution for the polar angle. The polar decay angle is calculated in the rest frame of the decaying virtual photon between the positive muon and the third decay partner, see Fig. 6.11 (left).

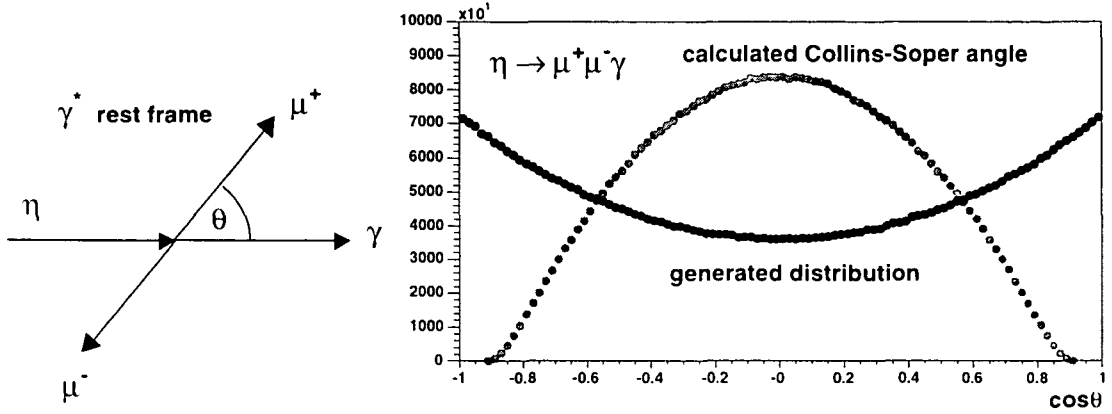


Figure 6.11: Left: The polar decay angle of dimuons coming from the Dalitz decays is defined in the rest frame of the decaying γ^* . Right: Comparison of the generated distributions of the cosine of the polar decay angle to the one calculated in the Collins-Soper frame.

The decay angles are *generated* in the rest frame of the decaying particle, i.e. in the meson's rest frame in case of the 2-body decays or in the rest frame of the virtual photon in case of the Dalitz decays. When re-calculating the decay angle from the two reconstructed muons, we have to specify a certain frame in which the angle should be given since angles are not Lorentz invariant. The most convenient frame is the so-called Collins-Soper frame. The Collins-Soper angle is defined in the elementary nucleon-nucleon collision's centre-of-mass (c.m.s.) frame as the angle between the positive muon and the beam-axis. With this specific definition [59] the angle is invariant under z -boosts, so that the angle can be calculated from laboratory as well as from c.m.s. coordinates (see Appendix A). However, due to the fact that a given angular distribution is generated in the *decaying particle's* rest frame and the Collins-Soper angle is calculated in the c.m.s. frame, the two distributions usually look quite different, which is illustrated in Fig. 6.11 (right) for the case of the η -Dalitz decay.

For the Dalitz decays the generated single muon kinematics (p_x, p_y, p_z, θ , etc.) first have to be Lorentz-boosted from the rest frame of the virtual photon into the rest frame of the decaying meson (η, η' or ω). Only then can their kinematics, analog to what is done for the 2-body decays, be boosted into the lab-frame, where the experiment is carried out and all energies and momenta are measured.

6.2 Open Charm and Drell–Yan

The continuum of the dimuon mass spectrum between the ϕ and the J/ψ mesons consists of the Drell–Yan process (DY) and of the simultaneous semi-muonic decay of pairs of D mesons. For the generation of these two processes we have used the Pythia event generator [60], version 6.208.

6.2.1 The Drell–Yan process, DY

Drell–Yan is an electromagnetic process occurring in hadron-hadron interactions in which a lepton pair (e^+e^- , $\mu^+\mu^-$) is produced, in leading order, from quark-antiquark annihilation, $q\bar{q} \rightarrow \gamma^* \rightarrow \mu^+\mu^-$, see Fig. 6.12.

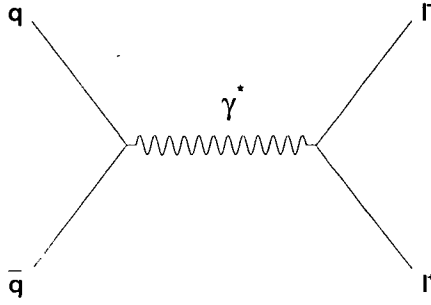


Figure 6.12: The Drell–Yan process, at leading order.

The elementary QED cross-section, σ , is given by the fine structure constant α and the propagator of the virtual photon, $1/M^2$,

$$\sigma_i(q_i\bar{q}_i \rightarrow \mu^+\mu^-) = \frac{4\pi\alpha^2}{3M^2}e_i^2, \quad (6.16)$$

where e is the electric charge ($e_u = +2/3$, $e_d = -1/3$, ...). The quark and the antiquark can only annihilate if they are of the same flavour. In order to obtain the elementary QED cross-section, we have to average over all possible colours, by multiplying with a factor $1/3$. The probability to find a quark or an antiquark with a given momentum fraction, $x_i = p_{\text{parton}_i}/p_{\text{nucleon}}$, inside colliding hadrons A and B, is given by the *parton distribution functions*, PDFs. Convoluting the elementary cross-section (at leading order) with the parton distribution functions, $f_i^A(x_1)$ and $\bar{f}_i^B(x_2)$, we obtain the differential DY cross-section

$$\frac{d^2\sigma}{dx_1 dx_2} = \frac{4\pi\alpha^2}{3M^2} \frac{1}{3} \sum_i e_i^2 [f_i^A(x_1)\bar{f}_i^B(x_2) + \bar{f}_i^A(x_1)f_i^B(x_2)] \quad (6.17)$$

In the above formula the sum runs over all constituent quarks of the parent hadrons. Re-expressing this formula in terms of measurable dilepton parameters, M and x_F , gives

$$\frac{d^2\sigma}{dM^2 dx_F} = \frac{4\pi\alpha^2}{3M^4} \frac{1}{3} \left(\frac{x_1 x_2}{x_1 + x_2} \right) \sum_i e_i^2 [f_i^A(x_1)\bar{f}_i^B(x_2) + \bar{f}_i^A(x_1)f_i^B(x_2)], \quad (6.18)$$

with

$$x_1 = \frac{1}{2} \left[\sqrt{x_F^2 + 4\tau} + x_F \right] \quad (6.19)$$

$$x_2 = \frac{1}{2} \left[\sqrt{x_F^2 + 4\tau} - x_F \right] \quad (6.20)$$

$$\tau = M^2/s = x_1 x_2 \quad (6.21)$$

The $1/M^4$ term in this expression leads to a rapid fall of the production cross-section with increasing lepton mass.

For the generation of DY we used the “MRS (A) low Q^2 ” parton distribution functions [61], which allows to generate dimuons down to masses of around 1 GeV (its Q_{\min}^2 is 0.625 GeV). This leading order cross-section underestimates the observed production cross-section, requiring a scaling K-factor of the order of 2. For a compilation of DY cross-sections, see e.g. Ref. [62].

The mass of the lepton pair is given by the momentum fractions of the colliding partons, x_1 and x_2 , and by the squared centre-of-mass energy, s .

$$M^2 = Q^2 = x_1 x_2 s \quad (6.22)$$

The polar angular distribution of the leptons in the rest frame of the decaying γ^* is predicted to be $(1 + \lambda \cdot \cos^2 \theta)$, with $\lambda = +1$, in the basic Drell–Yan model of spin-1/2 parton annihilation, reflecting the transverse polarisation of the decaying virtual photon. The E772 Collaboration measured the angular distribution of Drell–Yan dimuons [63], in p-Cu interactions at 800 GeV, with an event sample of $\sim 50\,000$ dimuons with masses in the range $11 < M_{\mu\mu} < 17$ GeV with $-0.3 \leq x_F \leq 0.8$ and $p_T \leq 6$ GeV/c. They extracted $\lambda = 0.96 \pm 0.04 \pm 0.06$.

Since the production cross-section depends on the charge of the interacting quarks and the nucleons have different quark contents, we have to generate both types of elementary interactions: pn and pp interactions. The Drell–Yan process is a hard process, which is not affected by the surrounding nuclear matter. In much the same way as the cross-section in pp collisions is the sum of the one of the constituent quarks, σ_{pA} is the sum of the elementary nucleon-nucleon cross-sections. Hence, σ_{pA}^{DY} should be obtained by scaling the elementary production cross-sections *linearly* with the number of nucleons in the nucleus, $\sigma_{pA} = \sigma_{pp} \cdot Z + \sigma_{pn} \cdot (A - Z)$, A being the mass number and Z the atomic number. Table 6.5 lists integrated measurements on the dependence of the Drell–Yan production cross-section on the mass number A , taken with proton beams at around 400 GeV, parameterised according to Eq. (6.6).

Experiment	Beam	p_{lab} [GeV/c]	Targets	α	$M_{\mu^+\mu^-}$ [GeV]
NA3(79) [64]	p	200	H, Pt	1.03 ± 0.03	4 – 8.5
E288(81) [65]	p	400	Be, Cu, Pb	$1.007 \pm 0.018 \pm 0.028$	5 – 11
NA50(03) [66]	p	450	Be, Al, Cu, Ag, W	$0.995 \pm 0.016 \pm 0.019$	2.9 – 4.5

Table 6.5: α measurements for the DY process.

There is a more recent measurement, performed by the E772 Collaboration [67], which gives the α parameter as a function of mass, p_T , and x_F . As already observed for other processes, the value for α rises with increasing p_T and decreases for large x_F values, see Fig. 6.13 (left). On the right hand side of this figure we show the recent NA50 measurement of the α extracted from 5 different targets.

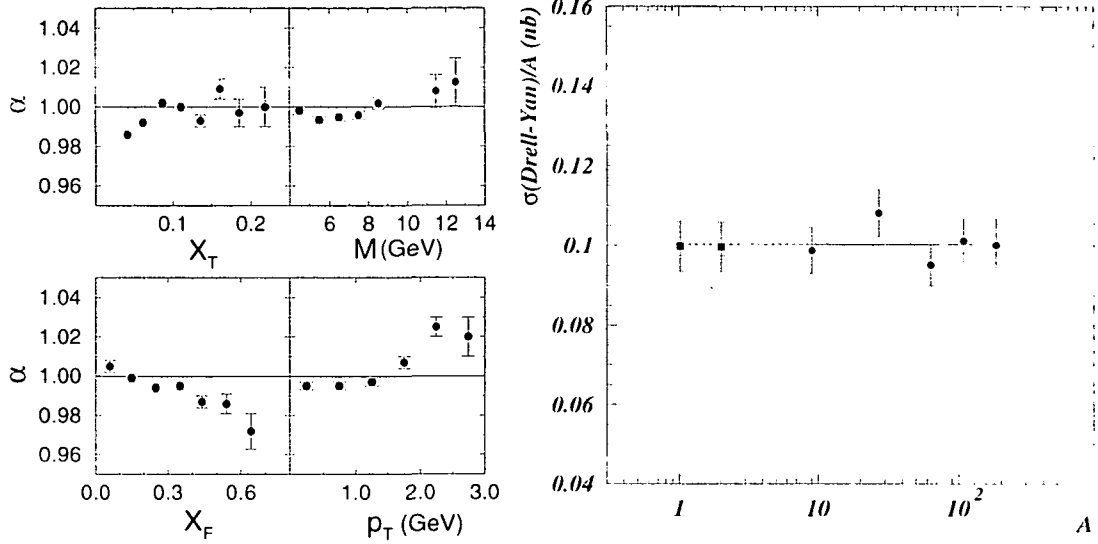


Figure 6.13: Left: α_{DY} as a function of $x_T = 2p_T/\sqrt{s}$, M , x_F and p_T , as measured by the E772 Collaboration. Right: The α_{DY} measurement of NA50, extracted from 5 targets.

We have neglected the nuclear effects on the *quark* and *antiquark* distribution functions, which are expected to be small, as will be discussed below. In Ref. [10] the Pythia calculations (using version 5.7) were compared to the DY data from the NA3 Collaboration [68], which were collected in p-Pt collisions at 400 GeV/c. The calculations, performed with the GRV-LO (1992) sets of PDFs required a K-factor of 2.1 ± 0.3 . By scaling the Pythia LO calculation with this K-factor, we obtain the elementary pp and pn cross-sections: $\sigma_{\text{pp}}^{\text{DY}} = 16.7$ nb and $\sigma_{\text{pn}}^{\text{DY}} = 14.7$ nb.

6.2.2 Open Charm

D mesons are formed via the creation of a $c\bar{c}$ pair and the subsequent hadronisation (“fragmentation”) of the charmed quarks, when each of them binds with a u , d or s quark (or antiquark), to form the D mesons. If both charmed hadrons then decay semi-muonically they may contribute to the dimuon mass spectrum, if the two muons are accepted and reconstructed. Since the energy of the muons depends on the decay kinematics the formed muon pair will have a continuum spectrum of invariant masses.

Charm production at SPS energies proceeds through gluon fusion in 80% of the cases and through quark-antiquark annihilation in the other 20%. The corresponding first order diagrams can be seen in Fig. 6.14.

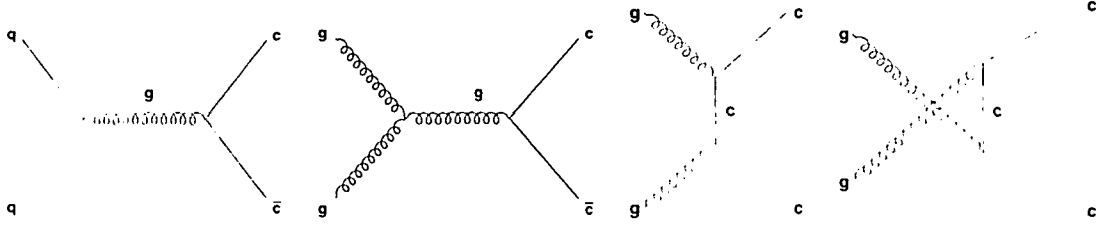


Figure 6.14: Production mechanisms for $c\bar{c}$ production in first order perturbation theory.

The cross-section to produce a $c\bar{c}$ pair in a proton-proton collision, $\sigma_{c\bar{c}}^{\text{pp}}$, is obtained by convoluting the perturbatively calculated partonic cross-section, $\hat{\sigma}_{ij}$, with the (non-perturbative) parton distribution functions of the interacting hadrons, $f_{i,j}^p(x, \mu^2)$,

$$\sigma_{c\bar{c}}^{\text{pp}} = \sum_{ij=q\bar{q}, gg} \int dx_1 \cdot dx_2 \cdot f_i^p(x_1, \mu^2) \cdot f_j^p(x_2, \mu^2) \cdot \hat{\sigma}_{ij} \quad . \quad (6.23)$$

The partonic cross-section depends on the available energy, on the mass of the heavy quark, m_Q , and on the strong coupling constant, α_s , evaluated at a scale μ .

$$\hat{\sigma}_{ij}^{LO} = \frac{\alpha_s^2(\mu)}{m_Q^2} \cdot f_{ij}^{0,0} \quad . \quad (6.24)$$

In this equation, $f_{ij}^{0,0}$ is a dimensionless scaling function which depends on \hat{s} and m_Q^2 , with \hat{s} being the squared partonic centre of mass energy, $\hat{s} = x_1 x_2 s$. The indices represent the interacting partons ($q\bar{q}$ or gg).

This leading order calculation needs to be scaled up by a K-factor. In Ref. [69] an extensive review of measured D meson cross-sections was performed and compared to LO calculations performed with Pythia, having varied Pythia's input parameters, like the mass of the c quark, which is not directly accessible to experimental measurements, or the set of parton distribution functions. From the measurements of D meson production, the total $c\bar{c}$ cross-section was plotted as a function of the collision energy, as shown in Fig. 6.15. The Pythia calculations were then scaled up in order to describe the existing data. From this procedure, the full phase space pp cross-section was derived to be around $20 \mu\text{b}$ at $E_{\text{lab}} = 400 \text{ GeV}$.

In order to generate “open charm”, we have used Pythia with its standard settings, except that the mass of the charm quark was set to $m_c = 1.35 \text{ GeV}$ and the primordial momentum of the interacting partons was generated according to a Gaussian distribution of variance $k_T^2 = 0.8 \text{ (GeV/c)}^2$. As parton distribution functions we have used the “CTEQ6L” [70] set. We have generated all final state charmed hadrons with a semi-muonic decay, D^+ , D^0 , D_s^+ , Λ_c^+ , Ξ_c^0 , Ξ_c^+ , Ω_c^0 and their corresponding anti-particles with the relative particle abundances given by Pythia, which uses the Lund string fragmentation model. In order to accelerate the generation process, we have set the corresponding branching ratios into muons to 100%. In the final event analysis each event contributed then with a weight which is the product of the

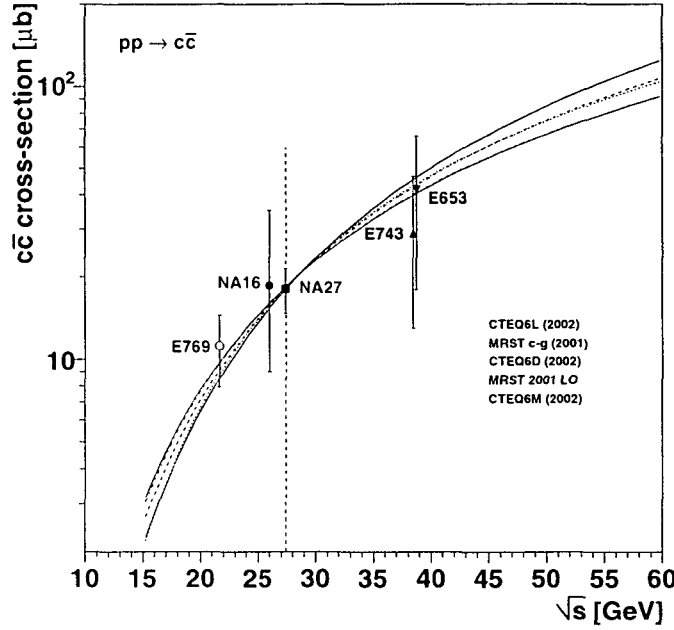


Figure 6.15: Full phase space $c\bar{c}$ production cross-section as a function of energy, showing the available measurements and Pythia calculations using different sets of PDFs.

branching ratios of the two decaying charmed hadrons, thereby correctly accounting for the individual branching ratios, which were taken from the Particle Data Group tables [38].

Contrary to what has been observed for “hidden charm”, i.e. J/ψ and excited charmonia states, open charm seems to scale linearly with the mass number A , apart from the nuclear modifications of the PDFs. The few available experiments, mostly performed with pion beams, see Table 6.6, are all consistent with A^1 , but their error bars are quite large.

Therefore, we used a linear scaling with the mass number, A , only taking into account the small effect of the nuclear modifications of the PDFs, discussed below. The obtained $c\bar{c}$ cross-sections are 167 μb , 2.25 mb, and 4.14 mb, for p-Be, p-In and p-Pb interactions, respectively.

6.2.3 Nuclear Effects on the PDFs

If the protons are inside nuclei, their partons have modified distributions. These nuclear effects are expressed as the ratio of the PDFs observed in a proton of a nucleus with respect to the ones in a “free” proton,

$$R_i^A(x, Q^2) = f_i^A(x, Q^2)/f_i^p(x, Q^2) \quad . \quad (6.25)$$

These “nuclear weight functions”, calculated with the EKS 98 [76] model, are shown in the left panel of Fig. 6.16. According to these curves, which are independent of

Exp.	E _{lab}	target	α	observed D mesons
p-A collisions				
E789 [71]	800	Be, Au	$\alpha(D^0)=1.02\pm0.03\pm0.02$	Be: $D^0=1360$ Au: $D^0=1040$
π^- -A collisions				
WA82 [72]	340	Si, Cu, W	$\alpha(D^0+D^+)=0.92\pm0.06$ $\alpha(D^0 \rightarrow K^- \pi^+)=1.03\pm0.11$ $\alpha(D^0 \rightarrow K^- \pi^+ \pi^- \pi^+)=0.93\pm0.11$ $\alpha(D^+ \rightarrow K^- \pi^+ \pi^-)=0.84\pm0.08$	Si: $D^0+D^+=102$ Cu: $D^0+D^+=528$ W: $D^0+D^+=1017$
E769 [73]	250	Be, Al, Cu, W	$\alpha(D^0+D^+)=1.00\pm0.05$ $\alpha(D^0)=1.05\pm0.15$ $\alpha(D^+)=0.95\pm0.06$	all targets: $D^0=650$ $D^+=776$
WA92 [74]	350	Cu, W	$\alpha(D^0+D^+)=0.93\pm0.05\pm0.03$ $\alpha(D^0)=0.92\pm0.07\pm0.02$ $\alpha(D^+)=0.95\pm0.07\pm0.03$	Cu: W: $D^0=3245, D^0=628$ $D^+=2753, D^+=546$
E706 [75]	515	Be, Cu	$\alpha(D^+)=1.28\pm0.33$	Be+Cu: $D^+=110$

Table 6.6: Nuclear target dependence of charm production in proton and pion induced collisions. Note that D^0 and D^+ mean $D^0 + \bar{D}^0$ and $D^+ + D^-$, respectively.

the PDF sets used, the charm experiments carried out at SPS energies are in the anti-shadowing region, where $R_i^A(x, Q^2) > 1$. Therefore, as shown in the right panel of this figure higher charm cross-sections are expected, for our energies, in p-A (and A-A) collisions, with respect to a linear scaling from pp collisions.

For the DY process, which is due to quark-antiquark annihilation, we do not expect visible changes on the production cross-sections in p-A collisions, as compared to a linear scaling from pp collisions, since the modifications on the quark and anti-quark parton distributions, at our energies, are very small and of opposite sign, see Fig. 6.16.

6.3 The Generated Dimuon Mass Spectrum

In Fig. 6.17 we can see the dimuon mass spectrum generated with the hadronic decay cocktail, open charm and DY, in pp collisions at 400 GeV.

The mass spectrum shown here has been smeared such that the ω and ϕ resonances have a mass resolution close to the one seen in the measured data. Note that we have only selected events generated in the NA60 phase space domain, which will be described and defined in Chapter 7. For illustration purposes we have normalised the individual curves using particle ratios based on those given in Ref. [6, 8]. The open charm and DY curves were normalised as outlined above. The shaded areas represent the uncertainties corresponding to cross-sections and branching ratios. For the ω 2-body decay, for which we took the electronic branching ratio, we have used

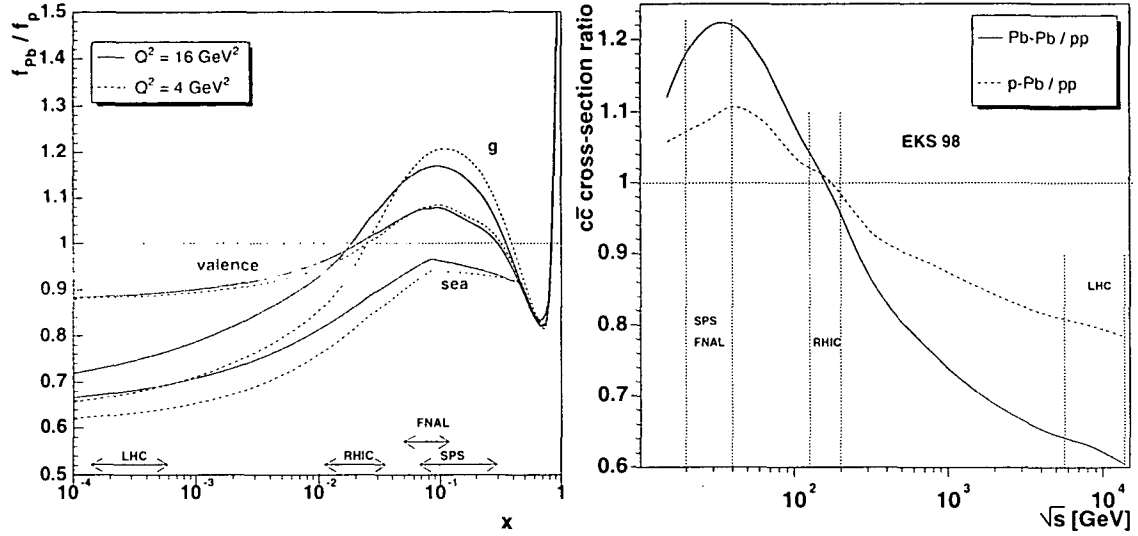


Figure 6.16: Left: Nuclear effects on the PDFs. Right: Effect of the nuclear modifications of the PDFs on the $c\bar{c}$ production cross-section, relative to a linear scaling from pp collisions, versus collision energy.

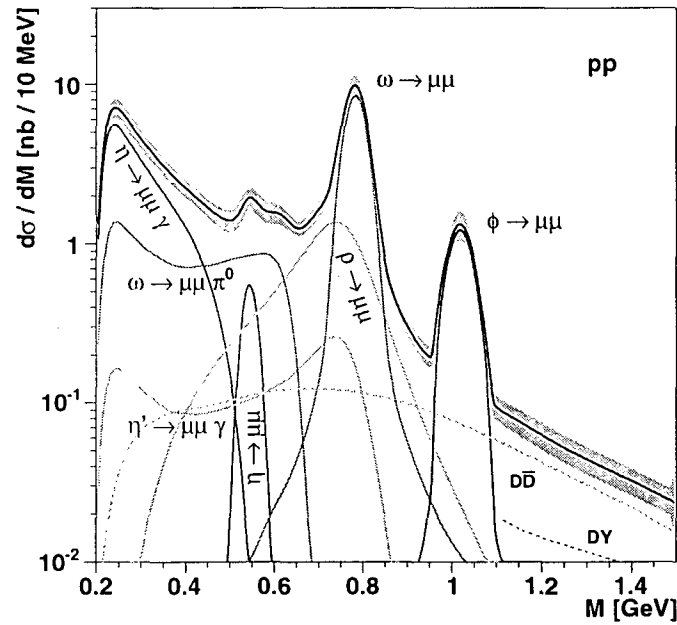


Figure 6.17: Generated dimuon mass spectrum for pp collisions at 400 GeV, including artificial smearing.

an uncertainty of 10%. The uncertainties on the DY and $c\bar{c}$ cross-sections were taken to be 20%. The weighted average of the uncertainties of the D mesons' semi-muonic branching ratios amounts to 18.5% and was added quadratically to the error band of the charm cross-section.

Chapter 7

Acceptances, Phase Space Window and Efficiencies

7.1 Reconstruction of the Monte Carlo events

The generated and triggered events are subjected to the same reconstruction procedure as the real data, described in Chapter 5. In a realistic proton-nucleus collision, together with the two triggered muons many other particles are produced. Those which are produced in the angular acceptance window of the muon spectrometer must be reconstructed, to find suitable match candidates for the two tracks seen in the muon spectrometer. Besides, we also need to reconstruct as many tracks as possible to identify the target where the interaction took place. Clearly, the number of clusters and the number of reconstructed tracks in the vertex telescope influences the vertexing, reconstruction and matching efficiencies. In order to have a MC simulation as realistic as possible, a full underlying hadronic event has to be simulated together with the two muons. In order to correctly describe the particle multiplicities and kinematic distributions of p-A collisions, we have used the VENUS event generator [77], version 4.12, an event generator widely used by heavy ion experiments at SPS energies (see, e.g., Ref. [78]).

In a first step, a muon pair is generated in one of the 6 sub-targets, with a relative probability given by the target thicknesses, in terms of interaction length, and by the relative beam intensity reaching each target. Only events in which the dimuon satisfies the trigger conditions are kept for further processing. At the vertex of the dimuon, a hadronic event is then generated with VENUS and the output stored together with the output of the dimuon event generator. To make the MC simulation as realistic as possible, the generated tracks leave a signal in a given microstrip detector plane with a probability proportional to the strip efficiencies. By triggering on and by reconstructing the dimuons in the outlined way, the detector acceptance, the correct detector smearing effects and the reconstruction inefficiencies are applied to the simulated events in a way expected to mimic the real detector's effects.

7.2 Acceptances and the Phase Space Window

In much the same way as most fixed-target experiments, the NA60 detector does not have 4π coverage. The aperture of the ACM magnet, in particular, determines the angular coverage of the muon spectrometer, which can easily be translated into an acceptance window in dimuon rapidity. The existence of the hadron absorber, on the other hand, imposes a minimum threshold in the energy of the measured muons, which is also a limiting factor in the phase space window probed by the experiment.

Naturally, any physics result must be reported together with the phase space window where the measurements were done. In the previous experiments using the same muon spectrometer, NA38 and NA50, the probed phase space window was quoted in terms of dimuon variables, such as $3.0 < y < 4.0$, $|\cos\theta_{CS}| < 0.5$ and $m_T > 2 \cdot (y - 3.5)^2 + 0.9$ GeV (see Ref. [8]). With respect to this window, the studies done in NA60 are affected by the presence of the dipole field and of the Silicon tracking telescope in the target region. Therefore, we must tune the values previously quoted and, if needed, add some further event selection criteria, to ensure that our physics results will be obtained with a minimum of acceptance corrections and model-dependent assumptions.

In the next sections we will explain in detail how the final analysis event sample has been defined, on the basis of the calculated differential acceptances and of comparisons between the measured data and the reconstructed MC events. We will see that NA60 has a much better coverage of low (transverse) mass dimuons than the previous experiments because of the presence of the dipole field, which, on the other hand, shifts the probed rapidity window (for low mass dimuons) to slightly more forward values. This is essentially due to the fact that the magnetic field increases the opposite-sign dimuon opening angle, so that both muons are bent into the acceptance of the muon spectrometer, rather than being lost in the “beam dump”. In the very low mass region, where this effect plays a role, we see a pronounced m_T - y correlation in the collected data, see Fig. 7.1.

We will also see that the beam hole of the silicon sensors reduces in a visible way the angular coverage of the (low p_T) muons produced in the most downstream targets. Muons with forward angles can be tracked, or not, in the vertex telescope depending on the target in which they are produced. For the extraction of the nuclear dependence of the ω and ϕ mesons, we cannot compare the forward rapidity ϕ mesons produced in the Indium target with the backward rapidity ϕ mesons produced in the last Beryllium target. For this reason, we have to apply a cut on the muon’s angle, or pseudo-rapidity.

7.2.1 Dimuon Rapidity and $\cos\theta_{CS}$

In Fig. 7.2 we compare the rapidity and $\cos\theta_{CS}$ distributions of the measured opposite-sign (OS) and like-sign (LS) dimuons with the corresponding simulated distributions, in the mass region 0.65–1.15 GeV, which is dominated by the ρ , ω and ϕ mesons. Since the dimuon phase space cuts are applied on the PC dimuon level, these distributions are compared before using the information of the vertex telescope. On this level

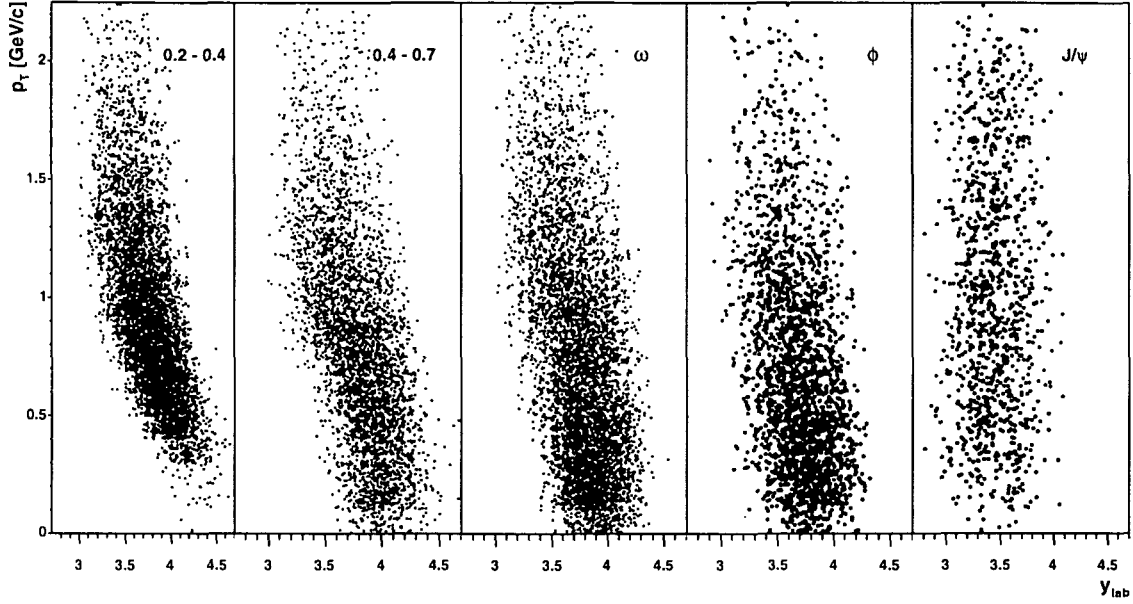


Figure 7.1: p_T versus rapidity for various mass windows (collected data).

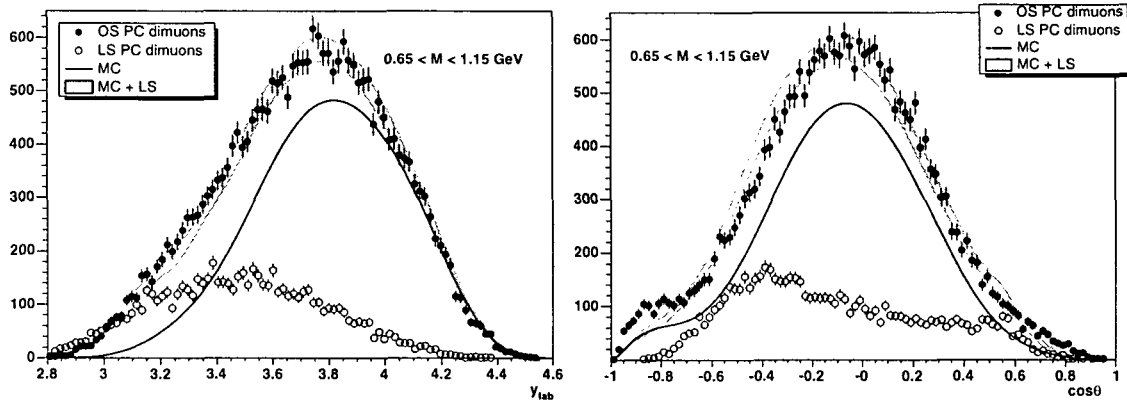


Figure 7.2: Raw data and Monte Carlo rapidity and $\cos\theta_{CS}$ distributions of PC dimuons in the mass region $0.65 < M < 1.15$ GeV, which is dominated by the ρ , ω and ϕ resonances.

the background contamination is not negligible — it is of the order of 30% — and we cannot directly compare the measured opposite-sign dimuons to the Monte Carlo simulation. Adding the like-sign dimuons to the Monte Carlo distributions we get a reasonable description of the observed OS spectra.

Figure 7.3 shows the rapidity and $\cos\theta_{CS}$ differential acceptances for the ω and ϕ mesons. By only selecting events with dimuon rapidity in the range from 3.3 to 4.3 and $\cos\theta_{CS}$ between -0.5 and 0.5 , we ensure that the acceptances do not vary by more than a factor 10 among two events studied in the final analysis. In this way we minimise the risk of introducing distortions in the analysis, due to imperfections in the way our Monte Carlo simulations describe the detector effects.

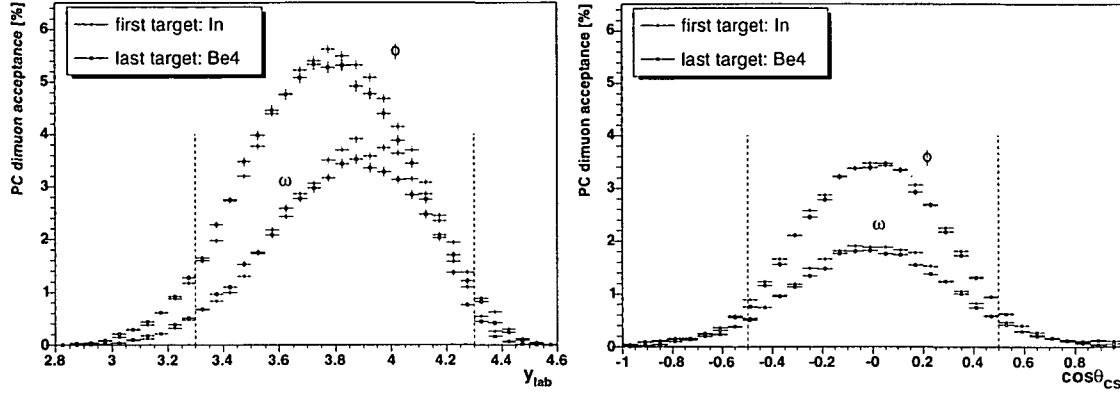


Figure 7.3: Rapidity and $\cos\theta_{CS}$ differential acceptances for the ω and ϕ mesons, calculated with Genesis.

7.2.2 Single Muon Pseudo-Rapidity, η

The η distribution of the measured single muons is also fairly well described by our MC simulations, see Fig. 7.4.

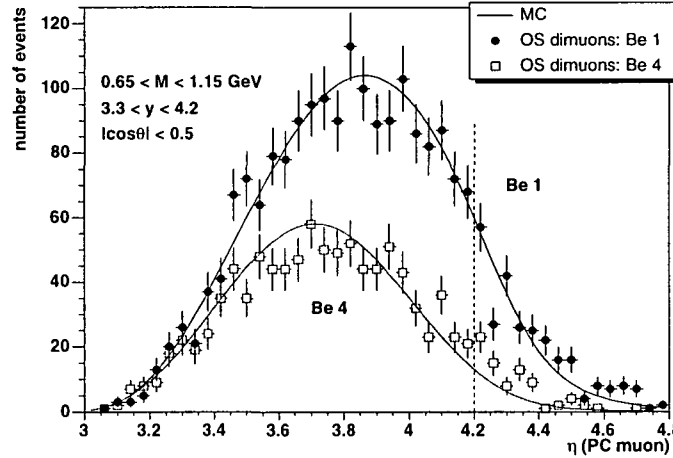


Figure 7.4: Pseudo-rapidity distributions of fully reconstructed single muons for the first and fourth Beryllium target.

The shift of the peak of the η distributions measured for the first and last Be targets, from ~ 3.9 to ~ 3.7 , is due to the fact that muons emitted from the last target are mostly accepted under larger angles. Furthermore, we can see that the more downstream targets have a significantly smaller acceptance at least for low mass dimuons. In Fig. 7.5 we see the fraction of muons reconstructable in the vertex telescope, from those which have been already reconstructed within the muon spectrometer's phase space window, as a function of the muon's pseudo-rapidity (a track is "reconstructable" in the vertex telescope, if it passes through a minimum amount of mandatory detector planes). As expected, the "VT single muon acceptance" is 100% for muons emitted at large angles, i.e. small pseudo-rapidities, but

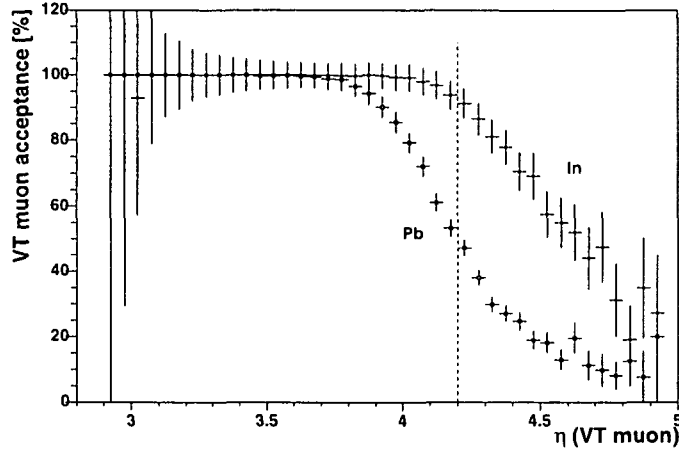


Figure 7.5: Pseudo-rapidity dependence of the probability that a muon in the muon spectrometer's phase space window is reconstructable in the vertex telescope.

degrades significantly for forward angles. The effect is very pronounced for the last target, where the acceptance drops already for $\eta > 3.7$. We have chosen to place a cut at $\eta = 4.2$, to have more than $\sim 50\%$ acceptance for muons coming from the Pb target. Since the single muon (pseudo-)rapidity is highly correlated with the dimuon rapidity, rejecting events with $\eta > 4.2$ effectively removes most of the events with dimuon rapidity above 4.2. Therefore, we have adapted the rapidity dimuon window to $3.3 < y_{\text{lab}} < 4.2$.

We should now see how many PC dimuons reconstructed within the chosen phase space window have both muons passing through the active area of the vertex telescope, such that they could leave a hit in the mandatory detector planes. The fractions are 97%, 96%, 92%, 88%, 79% and 69% from the most upstream to the most downstream targets. In Fig. 7.6 we show these fractions as a function of dimuon mass. We can see that the loss in acceptance induced by the beam-hole of the Silicon sensors is particularly significant for dimuons of masses around 300–700 MeV.

7.2.3 Dimuon m_T - y Correlation

In Fig. 7.7 (left) we compare the m_T distributions obtained from the MC simulations with the measured OS and LS spectra for 5 different rapidity bins. The agreement is fairly good.

From the m_T versus rapidity 2-D correlation plot, shown on the right hand side of this figure, we define a rapidity dependent m_T cut, $m_T > c \cdot (y_{\text{lab}} - y_{\text{lab}}^{\text{max}})^2 + m_T^{\text{min}}$, where $y_{\text{lab}}^{\text{max}} = 4.2$. The constants c and m_T^{min} were fixed by ensuring that the lower edge of the observed m_T distributions, shown on the left panel, does not have an acceptance below 10% of the maximum value. In this way, we obtained $c = 0.7 \text{ GeV}$ and $m_T^{\text{min}} = 0.4 \text{ GeV}$.

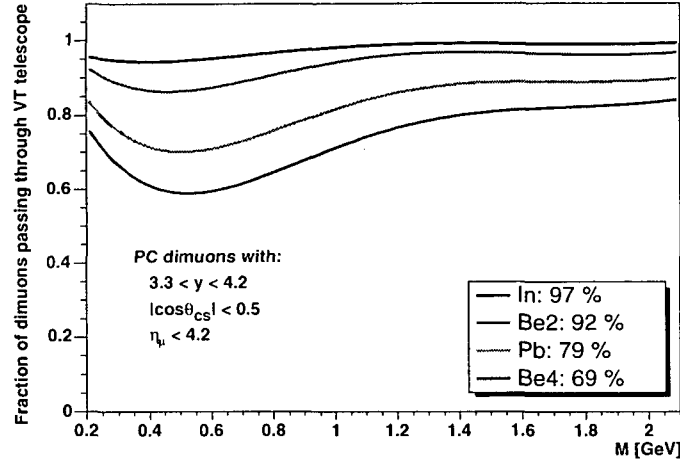


Figure 7.6: Expected fraction of reconstructed PC dimuons, in the chosen phase space window, whose single muons pass through the active area of the vertex telescope, as a function of dimuon mass.

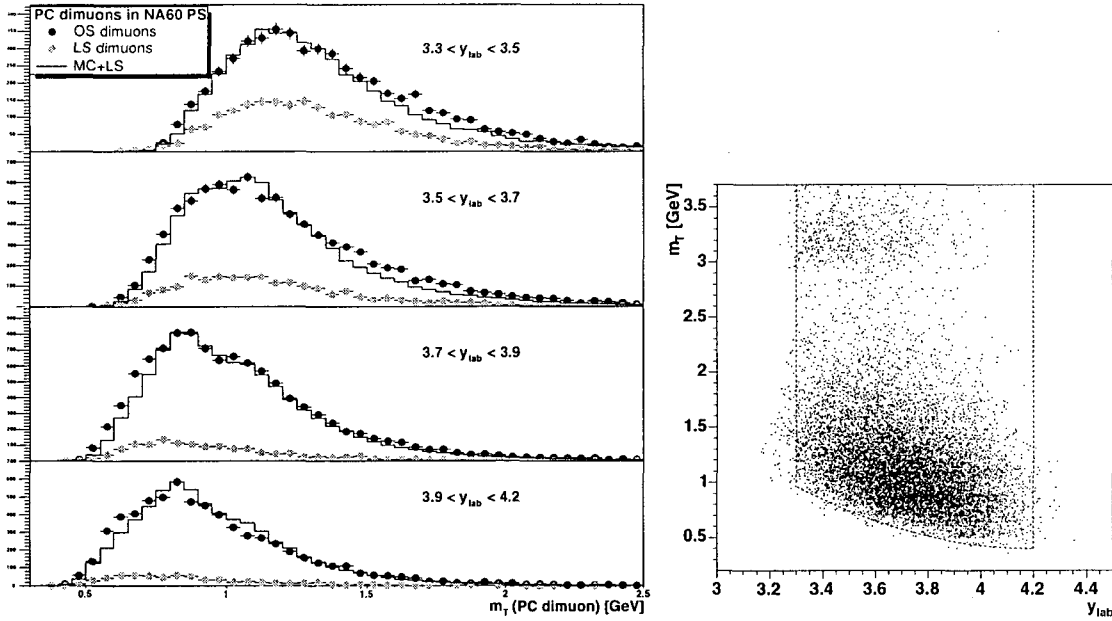


Figure 7.7: Left: m_T distributions for 5 different rapidity intervals, comparing the measured OS events to the sum of the LS and Monte Carlo spectra. Right: m_T - y correlation (reconstructed data).

7.2.4 Acceptances

The NA60 phase space window for the present analysis, which focusses on the ω and ϕ resonances, is summarised by the selection criteria given in Table 7.1.

Within this well-defined phase space window we may now evaluate the processes' integrated acceptances. Mainly because of the hadron absorber, but also due to the

$$\begin{aligned}
& 3.3 < y_{\text{lab}}^{\mu\mu} < 4.2 \\
& |\cos \theta_{\text{CS}}| < 0.5 \\
& \eta_{\mu} < 4.2 \\
& m_{\text{T}} > 0.7 \cdot (y_{\text{lab}} - 4.2)^2 + 0.4 \text{ GeV}
\end{aligned}$$

Table 7.1: Phase space window defined for the present analysis.

trigger condition, which requires the two muons to pass through different sextants, the acceptances are highly dependent on the dimuon mass. As already mentioned, the presence of the vertex magnet largely increases the acceptance for opposite sign low mass dimuons. Figure 7.8 shows the p_{T} differential acceptances for different mass windows *without* (left) and *with* (right) magnetic field.

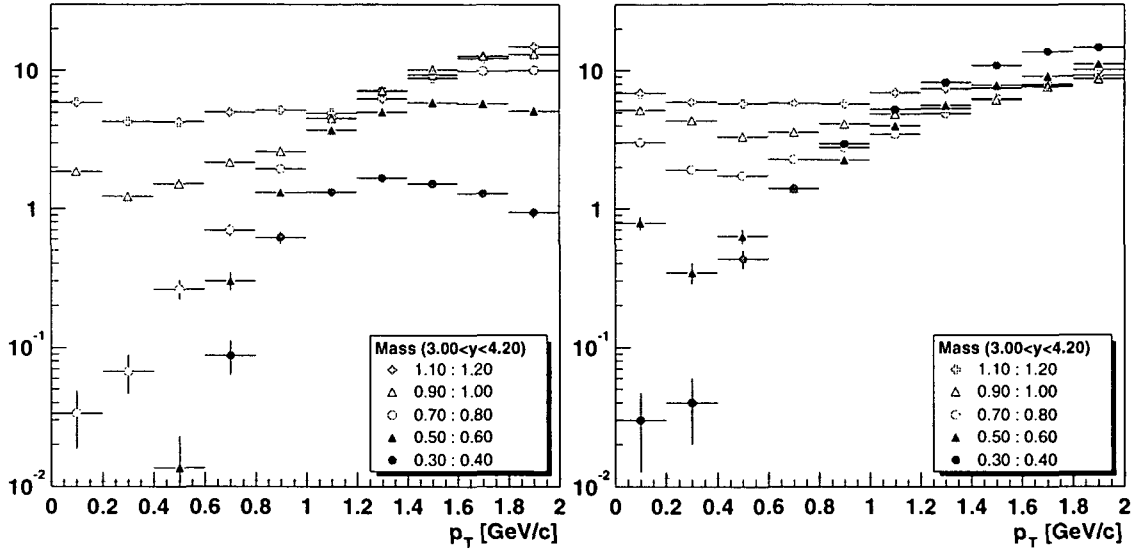


Figure 7.8: Dimuon acceptances, in %, as a function of p_{T} , shown for different mass windows without (left) and with (right) the 2.5 T dipole field. The acceptances here were evaluated for $3.0 < y_{\text{lab}} < 4.2$ and $|\cos \theta_{\text{CS}}| < 0.5$.

For dimuons with a mass smaller than the ϕ meson and with low p_{T} the improvement in acceptance can be as large as two orders of magnitude. Since the acceptances depend slightly on the polarity of the magnetic fields, our MC simulations were performed for all four possible combinations of the PT7 and ACM polarities, and the final acceptances were obtained from their average.

In Table 7.2 we give the detection acceptances of our detector, for each of the physics processes under study. The first line gives the values evaluated for the dimuons reconstructed in the muon spectrometer only. We then give the corresponding values when requiring that the muons should also be accepted in the vertex telescope, which significantly depend on the target where they were produced. We also give the extrapolation factors (“F”) to go from a cross-section measured in our phase space window to the full phase space, which do not depend on the target.

	η -D	η' -D	ω -D	η	ρ	ω	ϕ	$D\bar{D}$	DY
PC	2.08	2.78	2.31	2.44	3.62	4.06	7.31	15.4	14.4
In	1.97	2.67	2.18	2.30	3.51	3.96	7.20	15.3	14.3
Be	1.89	2.51	2.05	2.20	3.46	3.88	7.12	14.6	13.9
Be	1.79	2.44	1.97	2.08	3.39	3.76	7.04	14.1	14.0
Be	1.70	2.27	1.85	1.96	3.17	3.48	6.81	13.3	13.8
Pb	1.45	2.00	1.56	1.65	2.86	3.16	6.13	12.3	13.0
F	30.0	14.2	21.4	18.0	13.5	11.0	9.1	—	—

Table 7.2: Process acceptances, in %, for dimuons accepted in the muon spectrometer (“PC”), and also accepted in the vertex telescope, target by target, with respect to the NA60 phase space window. We also give the factor to extrapolate the production cross-sections of the low mass processes to full phase space (“F”). The acceptances for the continuum processes $D\bar{D}$ and DY were calculated in the mass range $1.5 < M < 2.5$ GeV.

7.3 Signal Detection Efficiencies

We use the vertex telescope to improve the dimuon mass resolution and the signal over background ratio, besides the identification of the interaction vertex. The drawback is that we loose a certain fraction of events, because of the limited detector acceptance and because the reconstruction algorithm cannot be 100% efficient. If we want to understand in which step the PC dimuons are lost, we have to separately study the following aspects:

- the VT dimuon acceptance,
- the VT track reconstruction efficiency and
- the single muon matching efficiency.

The first issue was already discussed in Sec. 7.2.2. In this section we will study the latter two factors, by using Monte Carlo simulations. This is the only way to isolate the individual terms. In the next section, where the final data analysis event selection will be described, we will see how our calculations compare to the real data.

7.3.1 VT Track Reconstruction Efficiency

The track reconstruction algorithm of the vertex telescope combines all possible clusters from the first plane with the last plane and, after performing some rough checks on whether this track seed points back to one of the targets, adds suitable clusters from planes in between. If a cluster is discarded, the previously established track seed is re-used and a new, more suitable cluster is searched for. This gives a large number of possible combinations of clusters to be checked. In a high multiplicity event where many clusters are deposited in the telescope, the procedure not only becomes CPU intensive but starts to reconstruct “fake” tracks. With Monte Carlo simulations we

know the exact trajectories of the generated particles and where they left a hit and we can, hence, study the rate of fake reconstructed tracks.

Since the angular coverage of the vertex telescope is limited, we have to select a sample of tracks which pass through the active area of at least the mandatory detector planes. Furthermore, we require that the tracks have $\eta < 4.2$. Such tracks are then simulated with GEANT, leaving a signal in the strip detectors convoluted with the measured strip efficiencies, and are subjected to the reconstruction algorithm. The extracted reconstruction efficiencies, hence, include also the detection efficiencies of the strip planes. For each target, we have calculated the track reconstruction efficiencies as the ratio of the number of reconstructed tracks to the number of initially selected “reconstructable” tracks. A generated track is not always reconstructed with only the clusters which it deposited in the telescope; there are cases where the reconstructed track contains clusters due to other tracks. Therefore, we have evaluated the reconstruction efficiency for tracks with $< 20\%$, $20\text{--}50\%$ and with $> 50\%$ wrong clusters, as a function of the number of deposited clusters in the whole telescope, see Fig. 7.9 (left).

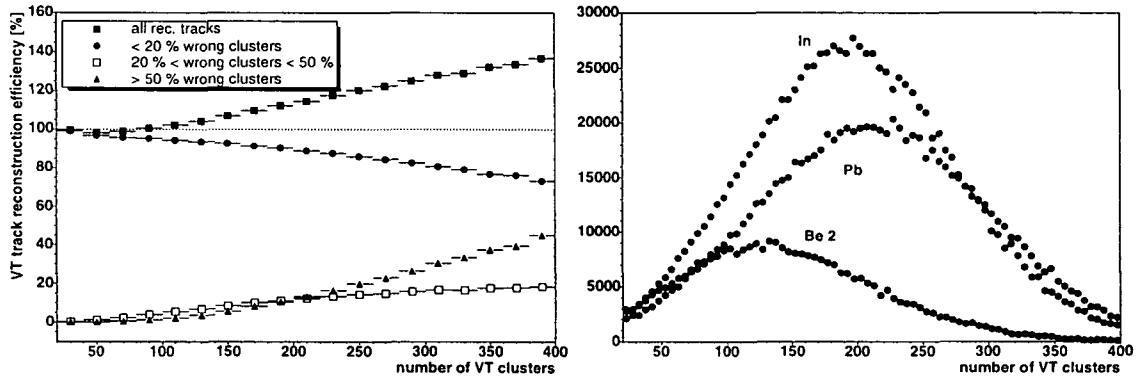


Figure 7.9: Left: Track reconstruction efficiency as a function of deposited clusters in the telescope for different reconstruction “qualities”. Right: MC distribution of the number of clusters, for several targets.

As expected, in events where many clusters are deposited, the total number of reconstructed tracks is larger than 100%, since the fake match rate increases. On the other hand, the number of “correctly” reconstructed tracks (i.e. with less than 20% wrong clusters) decreases as a function of the number of clusters. These efficiencies have to be convoluted with the distribution of deposited hits, which depends on the target in which the interaction took place and can be seen on the right panel of Fig. 7.9.

In this evaluation we have used not only the muon tracks (generated with Genesis), but also π , K and other secondary particle tracks from Venus. In Fig. 7.10 we show the reconstruction efficiencies for muon tracks only, which, in general, have higher momenta. The rate of “fake” tracks is significantly smaller, even for events with ~ 400 deposited clusters. When both generated muons fall in the acceptance of the vertex telescope, as ensured here, the dimuon track reconstruction efficiency is the

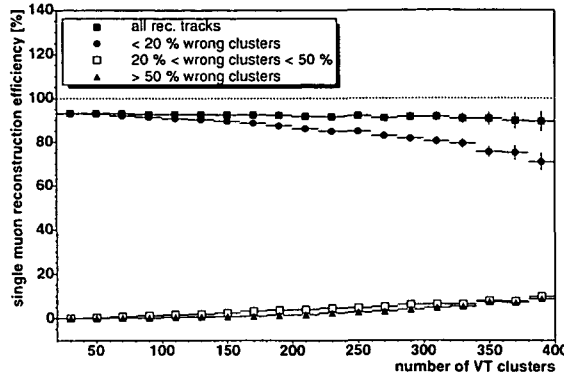


Figure 7.10: Single muon reconstruction efficiencies as a function of the number of clusters in the vertex telescope.

product of the single muon reconstruction efficiencies.

7.3.2 Matching Efficiency

We have studied the single muon matching efficiency using two classes of simulated events. The first class is composed of events where the generated muon has been correctly reconstructed, i.e. the number of wrongly assigned clusters is less than 20%. The study of this class of events gives access to the intrinsic efficiency of the track matching algorithm. The second class is composed of all events, irrespective of the number of clusters wrongly assigned to the muon track. The study of this event sample, where we do not use the Monte Carlo information which we would not have from the measured data, gives us the efficiency which we must use in the physics studies. In both cases, we have ensured that the muons are within the phase space window defined in the previous section. A priori, we would expect that the fraction of “fake” matches increases with the number of candidate tracks. However, for muons with less than 20% wrong clusters, the matching efficiency is 98%, independently of the number of reconstructed tracks, see Fig. 7.11 (left). This is due to the fact that the matching is performed not only in angular but also in momentum space, and because the number of “high” momentum tracks in p-A collisions is small, even if the total particle multiplicity is high. Moreover, this result shows that the matching algorithm works well and that the matching χ^2 was well tuned. On the right side of Fig. 7.11 we show the matching efficiency without a reconstruction quality cut. The single muon matching efficiency is still quite high, more than 90% even for events with ~ 25 reconstructed tracks. In the remaining 10% we rather *miss* to match the muon than to fakely match it. The reason is that the adding of “wrong” clusters distorts the fit of the track and results in a wrong momentum measurement.

Again, since both muons must be within the detector acceptance, the dimuon matching efficiency is the product of the single muon matching efficiencies. In Fig. 7.12 we show the convolution of the single muon reconstruction and matching efficiencies as a function of the number of clusters, for the Indium and Lead targets.

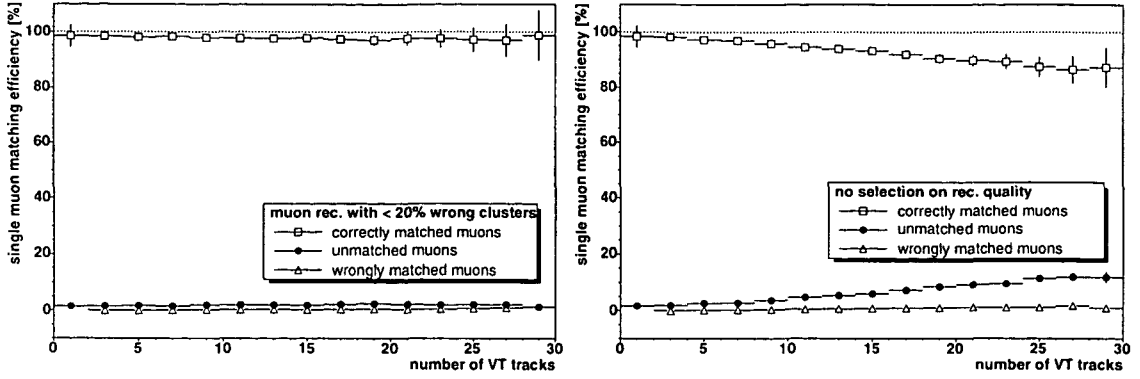


Figure 7.11: Single muon matching efficiencies for “correctly” (left) and all (right) reconstructed muon tracks.

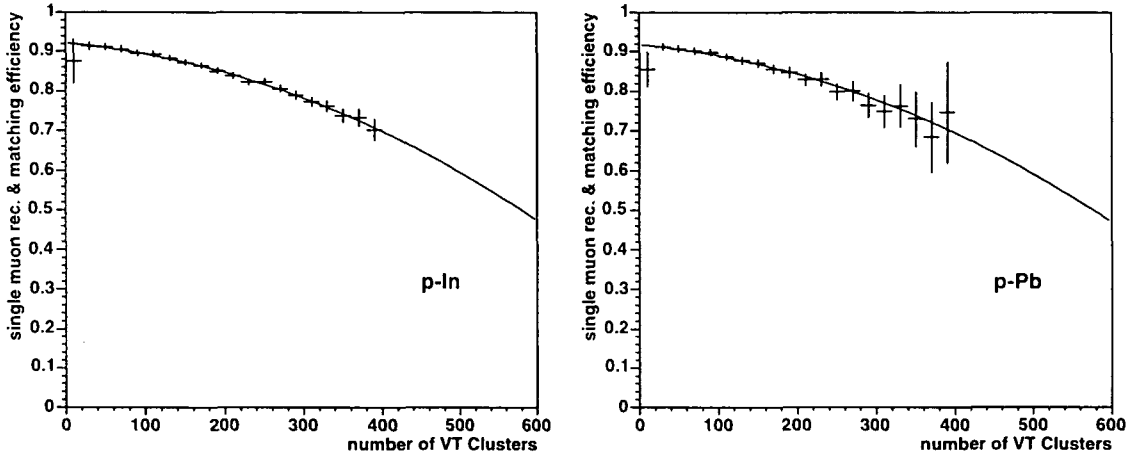


Figure 7.12: Single muon reconstruction and matching efficiency as a function of the number of clusters, for the In and the Pb target.

7.3.3 Vertexing Efficiency

A vertex must consist of at least two reconstructed tracks with sufficient fit quality. In particular, those tracks must have been reconstructed with at least 10 clusters. Of course, the more reconstructed tracks participate in the vertexing, the more accurate the vertex determination. Therefore, we expect higher vertexing efficiencies for the In and Pb targets, which give higher multiplicity events, on average. This is confirmed by the Monte Carlo simulations, as shown in the left panel of Fig. 7.13.

The drop in efficiency from the upstream to the downstream Be targets is due to the loss of tracks which go through the beam-hole of the first Silicon sensors.

In this figure, we show both the fraction of vertices reconstructed in the same target as the generated vertex (“correctly rec. vertices”) and the total fraction of reconstructed vertices. Their difference is fairly small, indicating that we hardly assign any events to the wrong target. In the right panel of Fig. 7.13 we show the reconstructed target ID versus the generated target ID.

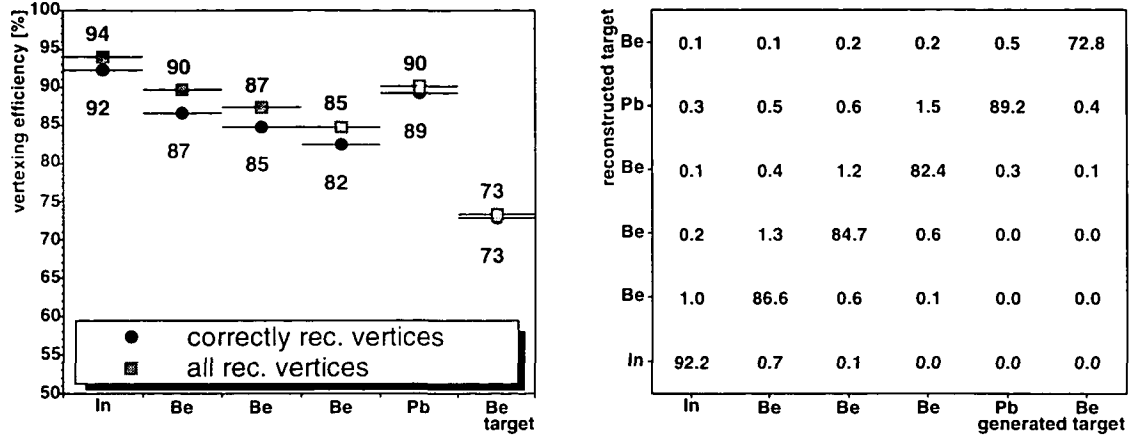


Figure 7.13: Left: Vertexing efficiency for the individual targets. Right: Pattern of reconstructed target ID for each generated target position.

The vertex is reconstructed in a more downstream (upstream) target in $\sim 2\%$ (1%) of the events. The difference to 100% are events where the algorithm could not reconstruct any vertex. In summary, the fraction of events assigned to a wrong target should be very small.

However, even if only one primary vertex was generated, in around 8% of all events we reconstruct 2 vertices, see Fig. 7.14 (left), because of inefficiencies of the vertexing procedure and of interactions of secondary particles in downstream targets.

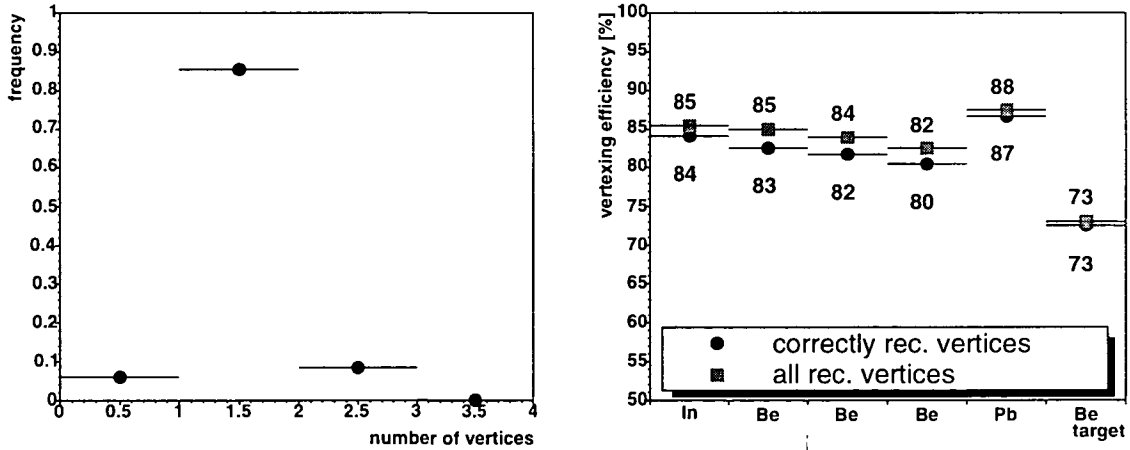


Figure 7.14: Left: Number of reconstructed vertices per event. Right: “Vertexing efficiencies”, including the target identification cuts.

We will see in Section 7.4 that we reject from the physics analysis event sample the events where more than one vertex is reconstructed, to minimise the contamination from interaction pile-up. By integrating this requirement into the target identification we obtain the vertexing efficiencies shown on the right panel of Fig. 7.14.

7.3.4 Integrated Efficiencies

In the previous sections we have seen the track reconstruction efficiency as a function of number of clusters and the matching efficiency as a function of the number of reconstructed VT tracks. By convoluting these differential efficiencies with the respective distributions we get the integrated efficiencies. In Fig. 7.15 we show the distributions of the number of clusters in the full VT telescope, for the matched dimuon sample, and for three targets.

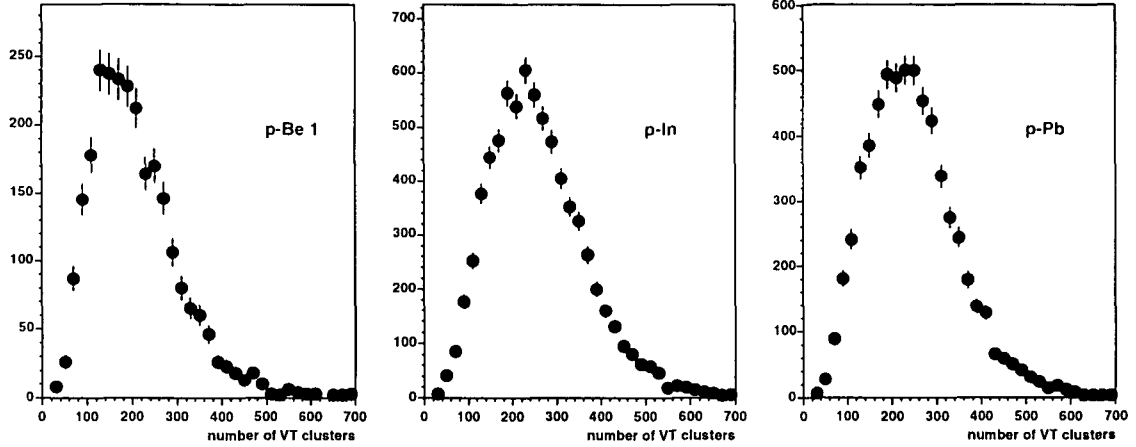


Figure 7.15: Distribution of the number of VT clusters seen in the measured data, in three different targets.

Convoluting the differential *single muon* reconstruction and matching efficiencies with the measured cluster distributions we obtain the integrated single muon efficiencies. The corresponding *dimuon* efficiencies are collected in Table 7.3 for each target, together with the vertexing efficiencies.

Target	$\epsilon_{\text{rec\&match}}^{\mu\mu}$ [%]	ϵ_{vtx} [%]
In	62	84
Be	67	83
Be	66	82
Be	64	81
Pb	51	87
Be	59	73

Table 7.3: Dimuon reconstruction and matching efficiency and vertexing efficiency, for each target.

The loss of dimuons because of the track matching is largely compensated by the improved dimuon mass resolution, which allows us to perform a proper study of the low mass resonances.

7.4 Final Analysis Event Sample

From the reconstructed data we have to define a subsample of events of sufficient quality to extract robust physics results. First, we want to ensure that the dimuon was produced in the target region and not in the hadron absorber or beam dump, so that we only try to match muons which had a chance to cross the vertex telescope. This is done by applying the single muon “ $p \cdot D_{\text{target}}$ ” cut, described in Section 5.3.3. We then ensure that there was indeed a proton interacting in one of the sub-targets by requiring one (and only one) reconstructed vertex within the target region. Then, we apply the phase space cuts, which were tuned to optimise the acceptance of the ω and ϕ mesons. Requiring that both PC muons must have $\eta < 4.2$ ensures that almost all dimuons should be within the detector’s acceptance, whatever the target where they were produced. As we have seen in the previous section, the most downstream targets will suffer acceptance losses of around 20–30%.

Note that the same selection procedure has been applied to the Monte Carlo simulations. We will now discuss the individual selections, and show their specific effect on the dimuon mass spectrum by building the ratio between the “surviving” sample and the events selected up to the *previous* step.

A $p \cdot D_{\text{target}}$ cut of 1% probability was applied on the PC muons. Integrated over all dimuon masses this reduced the OS sample by 22% and the LS sample by 37%, as can be seen in Fig. 7.16.

We have verified that practically all events of the *matched* dimuon sample survive this cut: out of the rejected dimuons only 2.5% of the OS sample and 0.8% of the LS sample had both muons matched to reconstructed tracks in the vertex telescope. In Fig. 7.17 we compare the PC dimuon’s z -vertex distribution before and after applying this cut, for $M > 1.5$ GeV. Events in which the dimuon came from the hadron absorber are clearly rejected, together with some dimuons from upstream of the target region.

To study certain physics variables as a function of the mass number A of the target nucleus, we have to know in which target the muon pair was produced. In $\sim 55\%$ of all events we do not find any vertex within the target region (i.e. between -2.0 and $+2.6$ cm). The reasons for that are threefold. Firstly, in around 22% of all events the vertex is reconstructed either up- or downstream of the target region, see Fig. 7.18, mostly in the second Silicon station of the Beam Tracker (at $z = -10$ cm) or in the stainless steel window of the cryostat vacuum box (at $z = -5$ cm). Secondly, the vertexing efficiency is $\sim 80\text{--}90\%$ (see Section 7.3.3), and should be much lower for collisions away from $z \simeq 0$, so that the *real* number of collisions in the target region is surely less than 78%.

Finally, due to the fact that the beam was not always centered with respect to the telescope’s beam axis, see Fig. 4.22, it is very likely that the beam halo interacted with the periphery of the microstrip sensors, sometimes producing a dimuon and secondary particles, which will not give a vertex in the target region.

In this run the beam intensities were such that we had up to 20% pile-up interactions within the 4×25 ns read-out gate of the microstrip telescope. Since in our

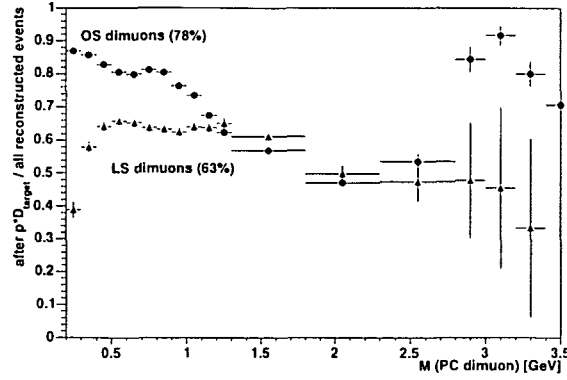


Figure 7.16: Fraction of events surviving the p^*D_{target} cut, as a function of dimuon mass.

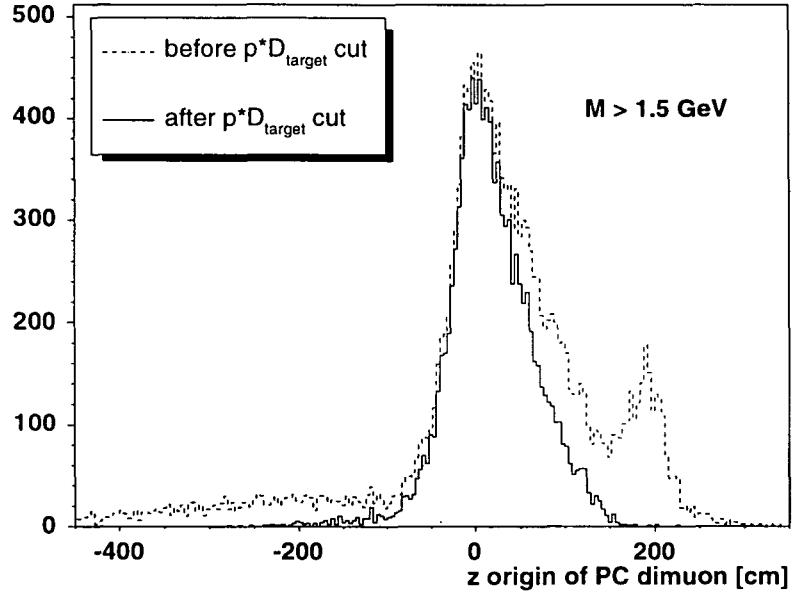


Figure 7.17: z origin of OS PC dimuons of $M > 1.5$ GeV before and after applying the p^*D_{target} cut.

physics studies we neither want to include events with a pile-up interaction nor events with re-interactions of energetic secondary particles in more downstream targets, we rejected all events which more than two vertices reconstructed. This includes events where one vertex was reconstructed outside of the target region and another one in the target region. The amount of events with 2 or more reconstructed vertices is around 5%. In this way, we keep $\sim 40\%$ of the pre-selected events, see Fig. 7.19 (left).

We have evaluated the effect of the phase space cuts on the dimuon and single muon levels separately. Requiring that the dimuon should verify $3.3 < y < 4.2$ and $|\cos \theta_{\text{CS}}| < 0.5$ selects $\sim 45\text{--}75\%$ of the OS events, depending on the dimuon mass, as shown in Fig. 7.19 (right). From the Monte Carlo simulations (pure “signal”) we

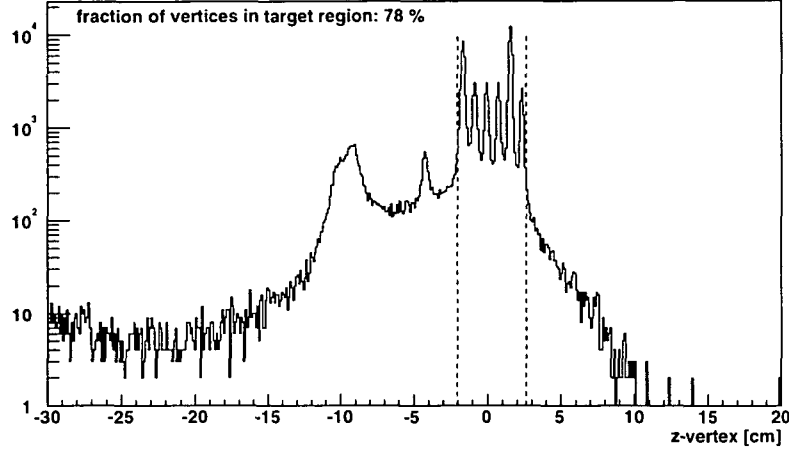


Figure 7.18: z -vertex distribution of the reconstructed vertices.

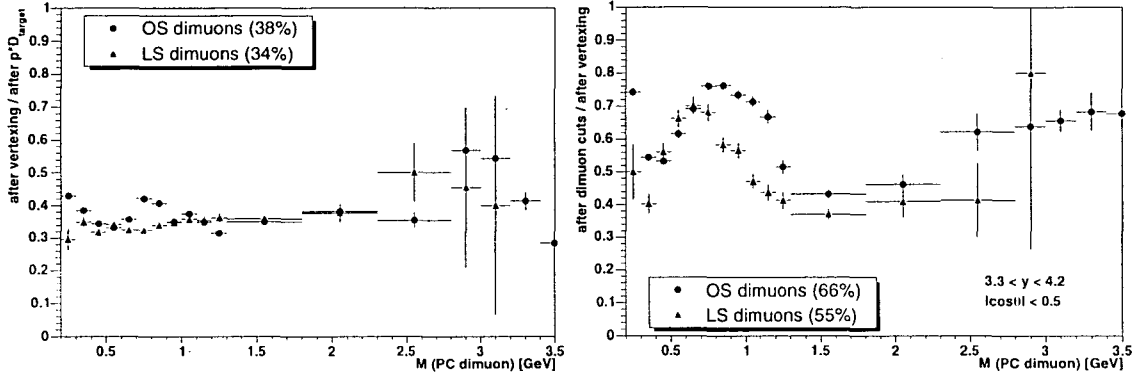


Figure 7.19: Fraction of events with a sufficiently good vertex (left) and after additionally requiring that the PC dimuons are within the defined phase space (right), as a function of dimuon mass.

expect to keep around 85% of the ω and ϕ resonances. The other 10% of OS dimuons in the ρ/ω and ϕ mass window which are rejected are most likely background.

Requiring that both muons have $\eta < 4.2$ rejects around 30% of the previously selected events. The expected mass dependence from the Monte Carlo simulations (Fig. 7.6) is seen in the data, displayed on Fig. 7.20 (left). The shape of this figure, with its minimum at $M \approx 0.5$ GeV, comes from the specific average p_T value of single muons from dimuons of a given mass, convoluted with the p_T differential acceptance, as was shown in Fig. 7.8.

The m_T cut, requiring that $m_T > 0.7 \cdot (y_{\text{lab}} - 4.2)^2 + 0.4$ GeV is only relevant for dimuon masses close to threshold. Its effect on the collected data can be seen on the right hand side of Fig. 7.20. The parameters of this cut are such that only events really on the edge of the phase space window are removed.

With the first two selection cuts (p^*D_{target} cut and identification of the target) we have tried to only pre-select dimuons from the target region. We have then

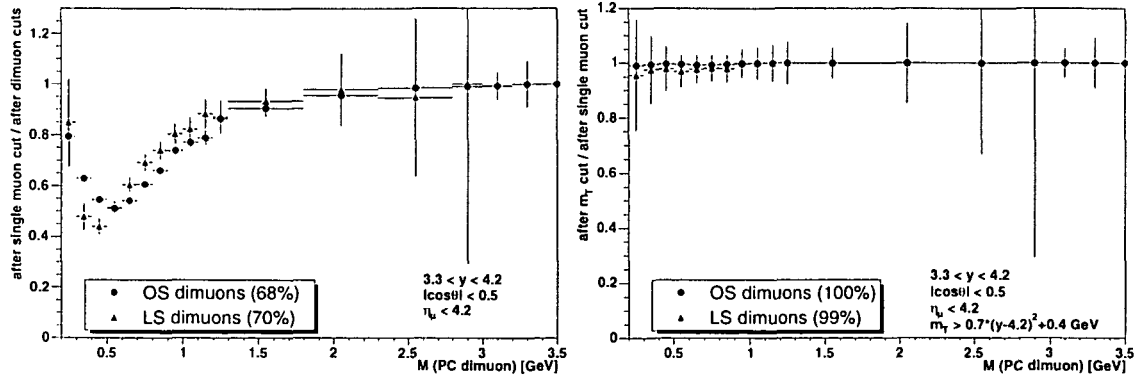


Figure 7.20: Fraction of events after the single muon η cut (left) and after applying the m_T cut (right), as a function of dimuon mass.

required that the reconstructed muons are emitted under such angles that they have a reasonable chance of passing through the vertex telescope. Now we can ask the question: out of these selected dimuons, how many have both muons matched in the vertex telescope? Figure 7.21 answers this question, for the In and Pb targets, as a function of the dimuon mass.

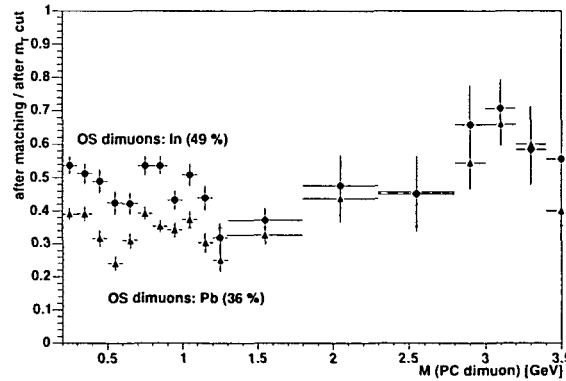


Figure 7.21: Fraction of dimuons surviving the matching procedure, as a function of dimuon mass.

As discussed in Section 7.3, the ratio “#VT dimuons/#PC dimuons” comprises the ratio between the VT and PC dimuon acceptances and the dimuon reconstruction and matching efficiencies. From the Tables 7.2 and 7.3 we expect that the product of these factors is $0.97 \times 0.62 = 60\%$ for the Indium target and $0.79 \times 0.51 = 40\%$ for the Lead target. On the other hand, the ratio “# VT dimuons/# PC dimuons” for LS dimuons is only 25%, which must also be true for the combinatorial background in the OS sample. Knowing that the background level is 30% before the matching, we expect the fraction of matched signal events from the *opposite sign* sample to be $70\% \times 60\% + 30\% \times 25\% = 50\%$ for the Indium target and $70\% \times 40\% + 30\% \times 25\% = 35\%$ for the Lead target. These values are in good agreement with what we see in Fig. 7.21. By doing the matching we have, hence, also rejected a significant fraction

of the combinatorial background.

In Table 7.4 we summarise the rate of matches for different mass windows and for each of the 6 targets.

Mass [GeV]	all	0.20–0.45	0.45–0.65	0.65–0.95	0.95–1.20	1.20–2.7	M>2.7
In	49±1	53±2	45±2	50±2	45±2	38±3	66±6
Be 1	46±1	52±3	40±3	48±2	39±3	33±4	71±10
Be 2	43±1	46±3	38±3	44±2	39±3	29±4	70±10
Be 3	39±1	42±3	33±3	42±2	35±3	24±3	62±10
Pb	36±1	38±1	28±2	35±1	34±1	33±2	62±4
Be 4	35±1	40±3	30±3	33±2	30±3	33±5	53±8

Table 7.4: Fraction of events with an OS dimuon remaining after the matching, expressed in %, for different mass windows and the 6 targets.

In Fig. 7.22 we show the PC dimuon mass distribution, for OS and LS muon pairs, after each step of the event selection procedure.

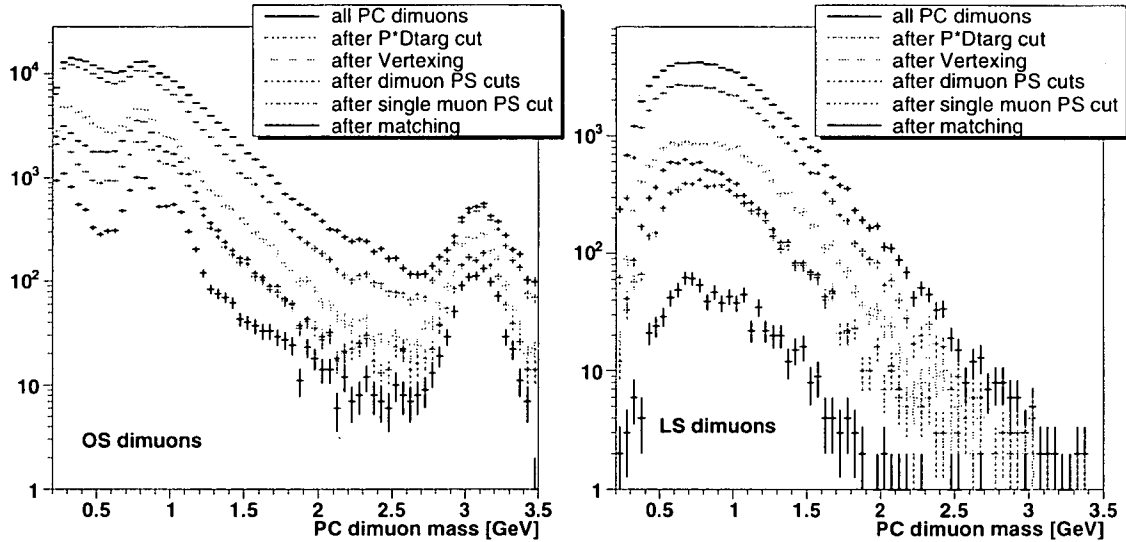


Figure 7.22: PC dimuon mass distributions after each event selection step.

In Table 7.5 we have summarised the fraction of events remaining after applying the individual selection criteria, where the successive lines integrate the effect of all previous cuts. In this table we also give the number of surviving dimuons for the mass windows indicated in Fig. 7.23. Note that in the last row, which shows the fraction of matched muons, the quoted numbers refer to the Indium target only.

After this event selection procedure we have evaluated, for each process and target, the integrated acceptances convoluted with the overall efficiencies. These values were obtained dividing the number of reconstructed events surviving the event selection procedure by the number of generated events in our well defined phase space

Mass [GeV]	all		0.20–0.45		0.45–0.65		0.65–0.95		0.95–1.2		1.2–2.7		M>2.7	
Selection	OS	LS	OS	LS	OS	LS	OS	LS	OS	LS	OS	LS	OS	LS
—	250k	75k	61k	7k	57k	17k	80k	28k	52k	21k	32k	14k	5k	65
pD_{target}	78	63	86	57	81	65	80	64	72	64	57	61	83	32
vertexing	29	22	34	19	28	21	31	21	26	23	20	22	42	12
$y, \cos\theta_{\text{CS}}$	19	12	21	9	16	14	23	14	18	11	9	9	27	8
η	13	8	14	5	9	7	15	10	14	9	8	8	27	8
matching	6	1	8	1	4	1	7	2	6	1	3	1	18	

Table 7.5: Fraction of events remaining after each selection step. Numbers are given in %, except for the first row, which shows the total number of reconstructed dimuons. The last row refers to the In target.

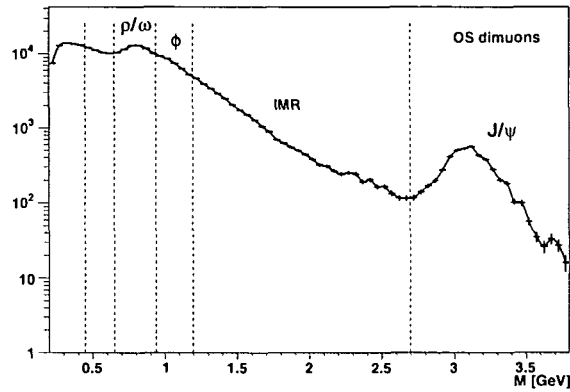


Figure 7.23: PC dimuon mass distribution of *all* reconstructed events (before event selection).

window. The resulting numbers can be seen in Table 7.6. The product of the acceptances, given in Table 7.2, by the overall efficiencies, given in Table 7.3, is smaller because the individual efficiencies are not independent from one another. In case the generated muons are emitted under such angles that they pass through the active area of the vertex telescope, they usually give rise to “high quality” reconstructed tracks, since their momenta are usually higher than the momenta of other secondary particles (π , K, ...). Since the vertexing algorithm requires at least two tracks with sufficient quality, events where the muons were reconstructed will most likely contain a successfully reconstructed vertex. Moreover, we have seen in Section 7.3.2 that, provided the muons are reconstructed with sufficient quality, the matching efficiency is close to 100%.

	Acceptance \times Efficiency [%]								
	η -D	η' -D	ω -D	η	ρ	ω	ϕ	D \bar{D}	DY
In	1.25	1.75	1.40	1.50	2.37	2.69	4.96	7.4	10.0
Be	1.33	1.80	1.47	1.59	2.56	2.85	5.36	9.3	10.7
Be	1.28	1.75	1.42	1.50	2.50	2.73	5.21	8.0	10.1
Be	1.16	1.57	1.29	1.38	2.24	2.41	4.95	8.0	9.7
Pb	0.89	1.25	0.96	1.04	1.82	2.01	4.04	6.5	9.0
Be	0.77	0.96	0.76	0.89	1.53	1.64	3.49	6.6	8.2

Table 7.6: Integrated acceptances convoluted with the efficiencies for all processes and for each of the 6 targets.

Chapter 8

Dimuon Analysis, Results and Discussion

In this chapter we will extract and present the physics results from our data analysis, including the nuclear dependence of the production cross-sections of the ω and ϕ mesons.

8.1 Background

8.1.1 Introduction

Any experiment measuring dimuon production needs to take into account that a significant fraction of the measured opposite-sign muon pairs are not due to *dimuons*, i.e. $\mu^+\mu^-$ pairs produced together, by a virtual photon (from $q\bar{q}$ annihilation) or by the $\mu^+\mu^-$ decay of a resonance (e.g., ρ , ω , ϕ , J/ψ , ψ' , etc.). There are many other sources of opposite-sign muon pairs, which we can separate in two main groups, depending on whether those mechanisms also lead to like-sign pairs or they only lead to opposite-sign pairs.

The first group is mostly composed of muon pairs due to the in-flight decays of pions and kaons, but there are also some events where one of the muons comes from the decay of a resonance, such as a ϕ or a J/ψ , and the other comes from a pion decay, for instance. In any case, these events can equally well lead to opposite-sign and to like-sign muon pairs and are, therefore, called the “combinatorial background”.

The second group is part of the *signal* dimuon sources and includes, in particular, the Dalitz decays of the light vector mesons and the open charm decays. Why are the muon pairs from decays of D mesons taken to be a “signal contribution” rather than being considered in the same way as the decays of the pions and kaons? The reason is simple: at SPS energies charm production is a rare process and we never have more than one pair of charmed mesons produced in the collisions we are studying. From a $D\bar{D}$ pair we cannot get two positive (or two negative) muons. This is why we cannot use the measured like-sign muon pairs to estimate the fraction of opposite-sign dimuons due to charm decays; we must compute them as a “signal” source, using

Monte Carlo event generators, as we have seen in Chapter 6. This will no longer be the case at LHC energies, where so many charmed hadrons will be produced that they will also contribute to the “combinatorial background”.

There are other processes which only lead to opposite-sign muon pairs. For instance, there are events where a single string fragments into a pair of high- p_T pions, necessarily of opposite charge. Such events cannot be estimated from the measurement of the like-sign muon pairs. The same is true for the events where a ρ decays into a $\pi^+\pi^-$ pair, followed by the simultaneous decay of both pions into muons [40]. In our analysis, we have neglected these two “signal” sources of muon pairs from pion decays.

The most frequent origin of “combinatorial background” muon pairs is the simultaneous decay of pions and/or kaons. Yet, the probability that a pion decays into a muon which is accepted in the muon spectrometer is rather low, around 10^{-3} . The shorter decay length of the kaons partially compensates for their lower production yields, leading to almost equal numbers of muons from pion or kaon decays.

The probability that a certain pion decays before being stopped by the hadron absorber is completely independent of the probability that another pion will also decay. Therefore, from the numbers of like-sign muon pairs, N^{++} and N^{--} , we can determine the *corresponding* number of opposite-sign muon pairs, $N^{+-} = 2 \cdot \sqrt{N^{++} \cdot N^{--}}$. The derivation of this equation is not as trivial as it may seem at first sight, but has been given often enough (see, e.g., Ref. [33]), and will be skipped here. However, this relation does *not* account for possible correlations between the two muons, either present at the production level or induced by the experimental conditions, which we describe in the next paragraphs.

8.1.2 Correlations at the Production Level

In general, the pions and kaons are produced with intrinsic correlations, the most important being imposed by the conservation of electrical charge. Such charge correlations are particularly important in the case of (low energy) pp collisions, when the total multiplicity of charged particles is particularly small. It is clear that, in these events, charge conservation cannot be neglected and, therefore, it is more likely to produce opposite-sign than like-sign muon pairs. Traditionally, the ratio between the opposite-sign “combinatorial background” and the expression $2 \cdot \sqrt{N^{++} \cdot N^{--}}$, which only accounts for the *uncorrelated* muon pairs, is named the R_{Bg} factor, often simply written as R . In fact, this factor is a function of the dimuon mass, rapidity and transverse momentum, and must be estimated through Monte Carlo simulations, using event generators such as Venus. However, such calculations are affected by a multitude of uncertainties and cannot be taken as much more than crude estimates.

In the case of high multiplicity collisions, such as high-energy heavy-ion collisions, it is clear that the very high number of produced pions and kaons smears out completely any charge correlation that may exist at the production level. In such collisions, hence, the R factor must be unity, except in the most peripheral collisions, where a value slightly higher than 1 can be understood. This expected behaviour has been reproduced by Monte Carlo simulations in the framework of the NA50 analysis

of the intermediate mass dimuons [4]. In the case of p-A collisions, the effects of charge correlations are expected to be more important and should depend on the specific target nuclei under consideration. The exact value of R will also depend on the interaction rate or, for a given target system, on the intensity of the beam. Indeed, for very high beam intensities (in NA50 values in excess of 10^9 protons per second have been used) and thick targets, the interaction rate can be so high that we will have two muons from *different* interactions crossing the spectrometer within the 20 ns gate of the trigger electronics, and giving a “dimuon” trigger. These two muons are uncorrelated and will reduce the low-multiplicity charge correlation effect, effectively reducing R to values close to 1. It should be clear, from this discussion, that a Monte Carlo calculation of R for p-A collisions will always remain quite uncertain. On the other hand, the absolute levels of combinatorial background are usually much lower in p-A collisions, making the exact knowledge of R less important than in heavy-ion interactions.

Fortunately, the exact value of R can be experimentally measured. The basic idea behind such a measurement is the following: while the *signal* processes produce muons in the vicinity of the target (resonance decays, Drell-Yan, open charm), the “in-flight” decays of the pions and kaons happen much further down-stream and are significantly affected by the placement (or not) of a good hadron absorber very close to the target. In the scope of the NA38 experiment [10], two data samples were collected, of p-W collisions at 200 GeV and at relatively low beam intensities, the only difference between the two being the extension of the hadron “pre-absorber”: in one of the setups the pions and kaons traversed a significantly longer distance in air, before reaching the absorber. Comparing the opposite-sign dimuon mass distributions of the two data sets and imposing that the *signal* component, by definition, is the same in both spectra, apart from the global luminosity scale, it was possible to extract the value of R for this collision system, 1.19 ± 0.04 . It is a good idea to perform such a measurement, for instance, by simply moving away from the beam line the hadron “pre-absorber”. In the case of heavy-ion collisions, however, the absolute background level is already very high with the pre-absorber in place, so that the data collected in the two “different” configurations would not be different enough to accurately establish by how much the value of R exceeds unity. During the 2002 proton run we had no time to make such a measurement and, therefore, we must estimate the values of R , for each of our target materials, starting from the evaluation made by NA38.

Our estimations were done under the following assumptions: the value by which R exceeds unity is inversely proportional to the charged particle multiplicity of the p-A collisions under consideration; the charged particle multiplicity in p-A collisions scales with the mass number of the target nucleus as $A^{0.2}$; and it increases with the collision energy as $\log \sqrt{s}$. The last assumption is needed to convert the value measured by NA38 with 200 GeV protons to the corresponding value at 400 GeV. Following this procedure we derived the following R values for our collision systems: 1.31, 1.21 and 1.17, for p-Be, p-In and p-Pb, respectively.

8.1.3 Correlations Induced by the Detector Conditions

So far, we have only mentioned that the two muons may be correlated at the production level. However, even when the charged particle multiplicities are very high, the two *measured* muons can easily have strong correlations, leading to an *effective* R factor different from unity. Indeed, in order to derive the yield of background opposite-sign muon pairs included in our measured sample from the, also measured, like-sign yields, the R factor must incorporate the ratio between opposite-sign and like-sign muon-pair acceptances:

$$R_{\text{effective}} = R_{\text{production}} \times \frac{A^{+-}}{\sqrt{A^{++} \cdot A^{--}}} .$$

In the NA38 and NA50 experiments, this ratio of acceptances (which include the effect of the trigger conditions) was forced to be unity by the use of the so-called “image cut”: each of the measured events would only be kept for further analysis if the muon pair would still comply to the acceptance and trigger conditions when any of the muons would have its charge reversed. This selection cut reduces the data sample to the fraction of events verifying $A^{+-} = A^{++} = A^{--}$, thereby simplifying the background subtraction procedure at the expense of significantly reducing the available statistics (especially for low mass dimuons). The HELIOS-3 experiment, for instance, could not apply such a selection cut and, therefore, had an effective R factor of 1.57 ± 0.10 in p-W collisions [79], clearly dominated by correlations induced by the detector effects. Indeed, HELIOS-3 had a dipole magnet in the target region and a trigger condition which required one of the muons above the beam line and the other below. Given the orientation of the dipole field lines, it was much easier to fulfill this condition when the pair of muons had opposite charge: one would be deflected upwards, the other downwards. It is clear that the R factor must be much higher in such a case, to compensate for the much lower trigger/acceptance probabilities of the like-sign muon pairs. By now it should be obvious why this R factor is a *function* of the kinematical variables of the dimuon. In certain “corners of phase space” the ratio between opposite-sign and like-sign detection acceptances may be completely different from other regions, so that we cannot approximate this ratio by a single constant factor.

The NA60 experiment also has a dipole magnet in the target region and a trigger condition which imposes that the two muons must be in different sextants of the scintillator hodoscopes. Therefore, the muon-pair acceptances are influenced by “geometrical” effects which can be rather different for opposite-sign and like-sign pairs, and which are very difficult to incorporate in a (multidimensional) R function. The procedure we have followed in NA60 is quite different: we evaluate the opposite-sign background through a “mixed event technique”. This means that we combine a single muon of a like-sign muon pair with single muons of other like-sign events, thereby building “mixed-event” ++, -- and +- data samples. Of course, each formed muon pair must satisfy the trigger conditions. This way we can check that the built and measured like-sign event samples have compatible shapes, before using the generated +- sample to estimate the combinatorial background in the measured

opposite-sign spectra. Furthermore, this procedure results in background *shapes*, of any kinematical variable, which are much less influenced by statistical fluctuations.

There is, however, one more important point that needs to be addressed. The “pools” of positive and negative single muons used for the event mixing were obtained from *dimuon* triggers and, therefore, are *biased* by the dimuon trigger condition that requires the two muons to be in different sextants. If we had built these “pools” from single muon triggers, not affected by the dimuon trigger condition, we could have directly proceeded with the event mixing, selecting each muon with the same probability as any other muon. The bias introduced by the dimuon trigger condition is particularly important in NA60, since the dipole field in the target region imposes sizeable asymmetries on the azimuthal angle distributions of the positive and negative muons. In particular, the ratio of $++$ to $--$ muon pairs changes quite significantly from one sextant to another. This means that the single muons used for the event mixing must be selected with probabilities which depend on the sextant (and on the muon charge). These probability factors depend on the ACM and PT7 polarities and, hence, are evaluated for each of the four field polarity combinations separately.

Let’s reiterate this problem, and its solution, to ensure that they are clearly understood. We want to evaluate the kinematical distributions of the combinatorial background $+-$ muon pairs by mixing uncorrelated positive and negative single muons (collected in different events). However, we cannot simply combine all the measured single muons with each other, because their distributions among the six sextants are biased by the dimuon trigger condition, and this bias distorts in different ways the $+-$, $++$ and $--$ muon pairs, mostly because of the PT7 field. Before mixing the single muons in muon pairs, we must calculate what would be their distribution among the six sextants if we had no trigger condition rejecting events with both muons in the same sextant.

In the absence of single muon triggers, we must find a way to extract these values from the measured distribution of like-sign muon pairs, in the several sextant combinations, N_{ij}^{++} and N_{ij}^{--} , with $i, j = 1, 2, \dots, 6$. A detailed discussion of this problem is available in Ref. [80], which we briefly summarise in the next lines. The probabilities for a *single muon* to be detected in sextant i , p_i^\pm , with $i = 1, 2, \dots, 6$, would be easy to obtain, apart from a trivial normalisation factor, from the number of dimuon events with both muons on the same sextant: $\sqrt{N_{ii}^{++}}$ and $\sqrt{N_{ii}^{--}}$. This assumes that, apart from the trigger condition, the detection probabilities of each muon are independent, $N_{ij}^{ab} \sim p_i^a \cdot p_j^b$, where a and b stand for $+$ and/or $-$. Such events are absent from our collected data sample, because of the trigger condition, but we can infer these values from the distribution of events in the other sextants,

$$N_{ii}^{++} = \frac{N_{ij}^{++} \times N_{jk}^{++}}{N_{jk}^{++}} ,$$

where $i \neq j \neq k$. An analogous expression can be written for the negative muons. See also Ref. [80] for the derivation of the statistical uncertainties of these probabilities. The numerical values of the single muon probabilities used in our data analysis are given in Tab. 8.1, for the four field polarity combinations.

PT7/ACM		sextant 1	sextant 2	sextant 3	sextant 4	sextant 5	sextant 6
+-	p ⁺	7.2±0.8	7.1±0.8	36.1±2.8	2.2±0.4	2.3±0.4	45.0±3.5
	p ⁻	6.4±1.1	9.7±1.4	5.1±1.0	44.5±4.9	31.6±3.6	2.8±0.7
-+	p ⁺	9.8±1.6	11.1±1.7	3.0±0.8	39.5±0.5	33.3±4.0	3.3±0.9
	p ⁻	5.7±1.3	8.9±1.7	31.3±4.7	2.8±0.9	1.9±0.7	49.5±7.3
--	p ⁺	3.7±0.7	10.2±1.3	3.3±0.7	44.5±4.6	35.6±3.7	2.7±0.6
	p ⁻	3.5±0.7	11.7±1.5	37.9±3.9	2.7±0.6	3.6±0.7	40.5±4.1
++	p ⁺	4.3±1.4	7.4±1.8	38.3±7.0	1.6±0.8	3.2±1.1	45.2±8.2
	p ⁻	9.6±3.7	9.6±3.7	1.3±1.1	33.5±9.8	45±13	1.3±1.2

Table 8.1: Probabilities, in %, for a positive (negative) muon to pass through each individual sextant, for the four different combinations of the PT7/ACM field polarities.

In Fig. 8.1 we see that the obtained (by event mixing) mass spectra reproduce reasonably well the measured distributions of the ++ (left) and -- (right) muon pairs. All field polarities have been included.

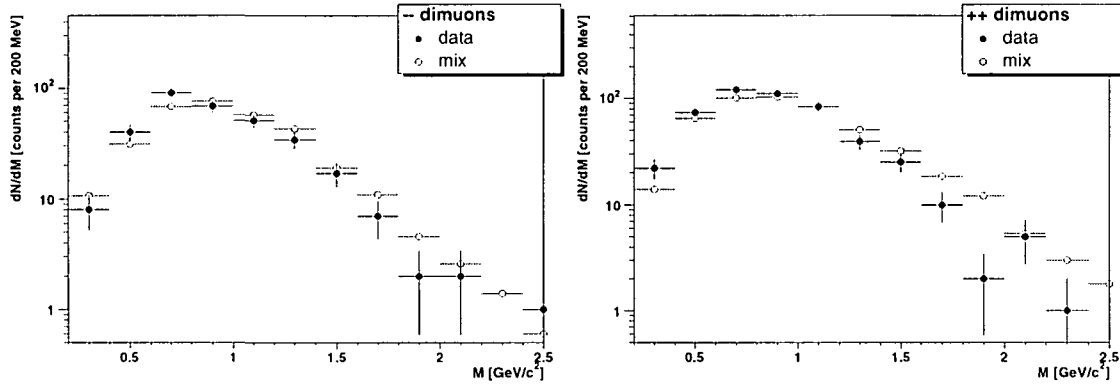


Figure 8.1: Comparison between the measured like-sign dimuon mass distributions and the corresponding distributions obtained with the “mixed event technique”.

8.1.4 Impact of the Muon Track Matching

Before concluding this section we should say a few words on the impact of the muon track matching on the background levels. Clearly, the muon track matching reduces significantly the population of muons from pion and kaon decays, either because the decay happens after the vertex telescope and the muon track does not match the parent track, or because the decay happens within the telescope, and the decay kink invalidates the track reconstruction. The ratio between the estimated combinatorial background and the measured opposite-sign dimuons drops from $\sim 30\%$ at the PC level to $\sim 10\%$ at the VT level, integrated over all dimuon masses.

A priori, we could consider wrongly matched dimuons as an additional background source. This contribution is reasonably small in proton-nucleus collisions, since the

average multiplicities are quite low (see Section 7.3.2 for a discussion on the expected rate of “fake” matches). Moreover, as explained in Section 5.2.3, when we found more than one match candidate for a given PC muon (which happens in less than 10 % of all events), we selected only one of them. The few cases where accidentally the “wrong” track was taken will, hence, lead at most to a degraded mass resolution for the ρ/ω and ϕ resonances, but will not give rise to an increased dimuon yield.

8.2 Dimuon Kinematical Distributions

In the previous chapters we have discussed the reconstruction and selection of the measured data, the several expected “signal” dimuon sources, and the detector acceptances and efficiencies, which influence the way we measure those physics processes. In the preceeding section of this chapter we have discussed the combinatorial background present in our opposite-sign dimuon data and the way we calculate its contribution. We are now ready to compare the measured data to a superposition of the several expected dimuon sources, and extract some information concerning the production of low mass dimuons. In this study, it is clear that the most interesting step is the analysis of the dimuon mass distributions measured in each target. However, before we enter that part of the data analysis, we should look at a few more basic issues, to ensure that we can trust our Monte Carlo simulations, in terms of detector effects and of kinematical generation functions. We will also shortly address the improvement in mass resolution due to the muon track matching.

8.2.1 Dimuon Mass Resolution

Through the muon track matching we have achieved important improvements in the dimuon mass resolution and in the ratio signal to background. These two improvements can be appreciated by comparing the two panels of Fig. 8.2, which show the combinatorial background and opposite sign dimuon mass distributions for all selected events *before* the matching and for the final analysis event sample *after* the matching. While before the matching the background level is $\sim 30\%$, it is only 10% after the matching. Before the matching the ϕ only appears as a shoulder on the ρ/ω peak; after the matching they are measured with a mass resolution of 29 ± 1 and 32 ± 1 MeV, respectively. Since the mass resolution for high mass dimuons is not dominated by angular resolution, the improvement in the mass resolution of the J/ψ is less important, being 96 ± 3 MeV after the matching.

In Fig. 8.3 we show the low mass dimuon mass distribution in a linear scale, showing a hint of an η peak.

To ensure a correct comparison between the measured and simulated dimuon mass distributions, it is important to verify that the smearing effects present in our Monte Carlo program reproduce the mass resolution seen in the real data. In previous experiments, such as NA38 and NA50, this was not the case and the simulated distributions had to be artificially smeared by ad-hoc factors, before the measured distributions could be analysed.

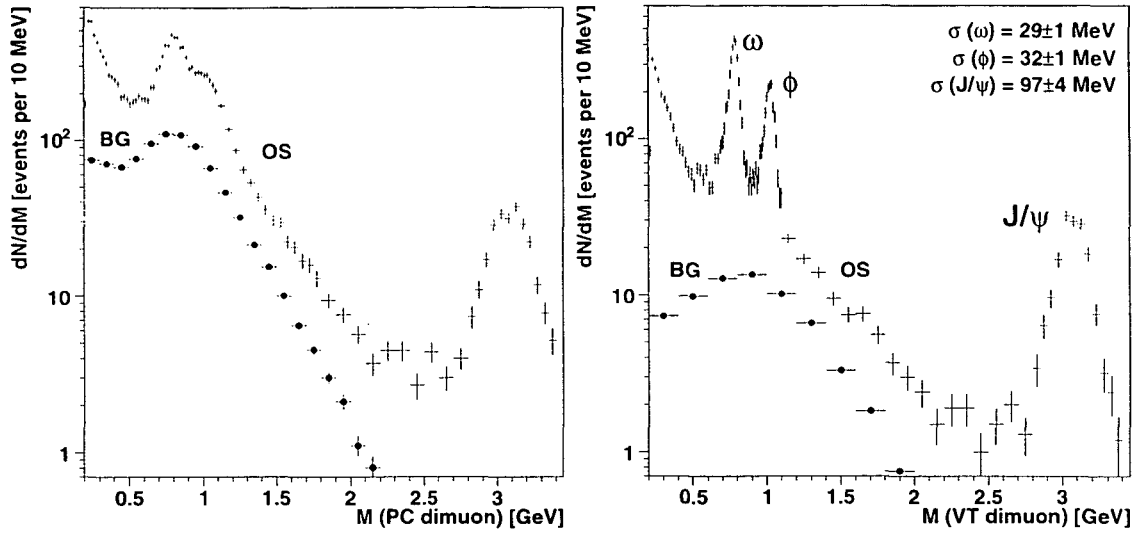


Figure 8.2: OS dimuon and combinatorial background mass distributions before (left) and after (right) muon track matching (sum of all targets).

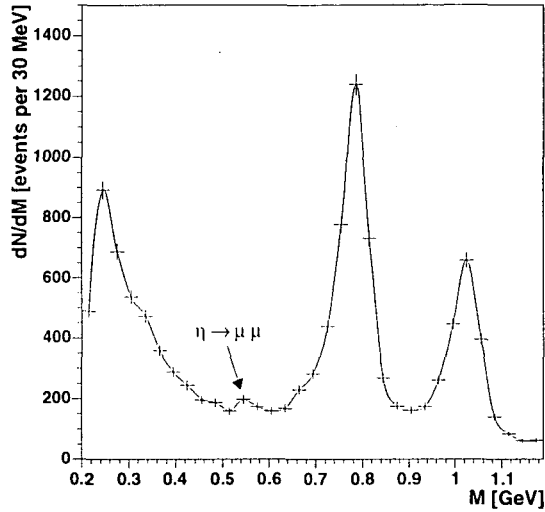


Figure 8.3: Low mass dimuon mass distribution in a linear scale, adding all six targets.

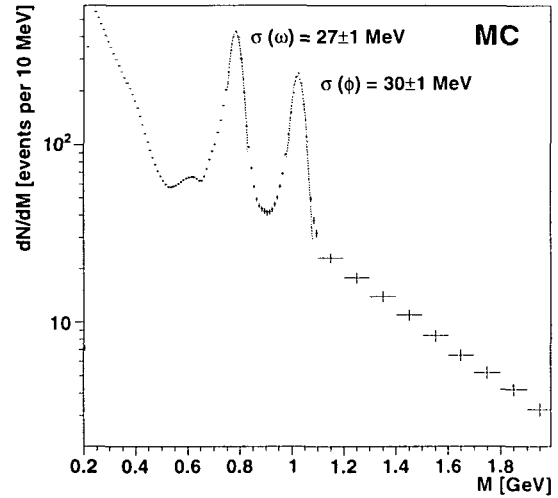


Figure 8.4: Reconstructed Monte Carlo dimuon mass distribution (all targets), showing the ω and ϕ mass resolutions.

Figure 8.4 shows the reconstructed Monte Carlo dimuon mass spectrum, after adding all the six targets. By fitting the peaks in the same region as was done in Fig. 8.2 we obtain the following mass resolutions: $\sigma_{MC}^{\omega} = 27 \pm 1$ and $\sigma_{MC}^{\phi} = 30 \pm 1$ MeV. These values agree quite well with what we see in the measured data, showing that our Monte Carlo program properly describes the experimental setup, as well as the multiple scattering and energy loss mechanisms.

This agreement gives us confidence that we do not need to replace our Monte Carlo distributions by analytical parametrisations which would then be tuned to the

measured data. It may be worth recalling that such a procedure has been used by NA50 for the J/ψ suppression studies, for instance, with the J/ψ resonance in the reconstructed Monte Carlo being fitted to an empirical analytical function with around 10 free parameters, several of them being then refitted to the measured data. In our case, we can use the reconstructed Monte Carlo histograms directly in the analysis of the measured data, without passing through any intermediate empirical functions.

8.2.2 Kinematical Distributions: Overview and $\cos \theta_{CS}$

We will now verify if we used reasonable kinematical distributions in the event generation. We can only do this verification for the ω and ϕ mesons, since they are easily identifiable through their pronounced peaks in the mass spectra, and in the kinematical ranges where we have sufficient statistics. We are only concerned with the three most important distributions for the generation of dimuons: the rapidity, the p_T and the $\cos \theta_{CS}$ decay variable.

For the studies presented in the remaining of this section, we will identify as “ ω ” and “ ϕ ” the opposite-sign muon pairs in the mass windows 0.70–0.85 and 0.93–1.07 GeV, respectively. In the first window, the ρ and ω mesons are expected to contribute around 23 and 63 %, respectively (fractions deduced from the studies described in the next section of this chapter). Since the y and p_T distributions of the ω and ρ mesons are expected to be almost identical, there are only 12 % of events from other sources in this selection. In the case of the “ ϕ ” mass window, we estimate that the dimuons from the ϕ decays represent 78 % of the total, with 10 % of the events being combinatorial background.

In spite of its relevance for the event generation, we cannot verify if the $\cos \theta$ decay variable has been simulated in the best way, given the fact that our acceptance in this variable is so narrowly concentrated around zero that we are unable to distinguish in our data between uniform and $(1 + \cos^2 \theta)$ distributions. Following the analysis previously done by the HELIOS-1 experiment, which we will discuss at the end of this Chapter, we will present our results using $(1 + \cos^2 \theta)$ distributions for the ρ , ω and ϕ mesons. We will also mention, nevertheless, the values obtained if we would use uniform distributions.

Figure 8.5 compares the $\cos \theta_{CS}$ distributions of the measured opposite-sign muon pairs with those of the reconstructed Monte Carlo (added to the small contribution of like-sign muon pairs), for the ω and ϕ events produced in each of the six targets. At this “reconstructed level”, we see a remarkable agreement between the simulated Monte Carlo and the measured data. A more detailed study, only for the y and p_T variables, is presented in the next two sections.

8.2.3 ω and ϕ Rapidity Distributions

Figure 8.6 shows the rapidity distributions measured in the In and Pb targets for the ω and ϕ dimuons, at the raw data level. We can easily see that the forward rapidity dimuons produced in the Pb target, placed very close to the first tracking planes of the

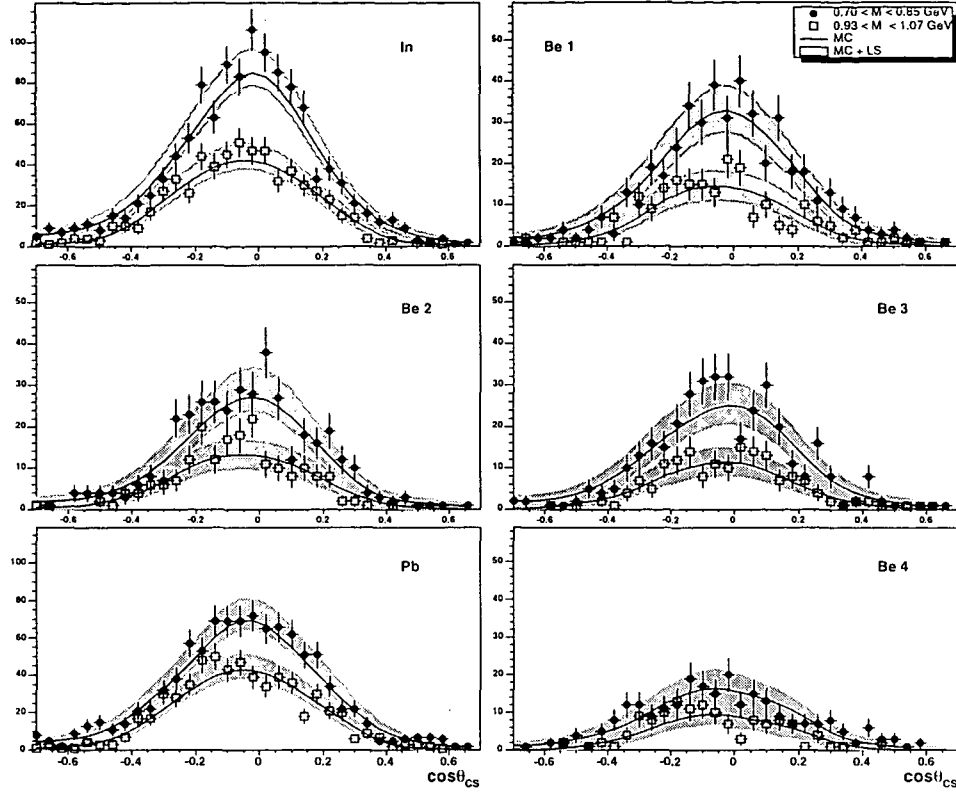


Figure 8.5: $\cos \theta_{CS}$ distributions of the reconstructed Monte Carlo and of the measured opposite-sign dimuon data, for the ω and ϕ events in each of the six targets.

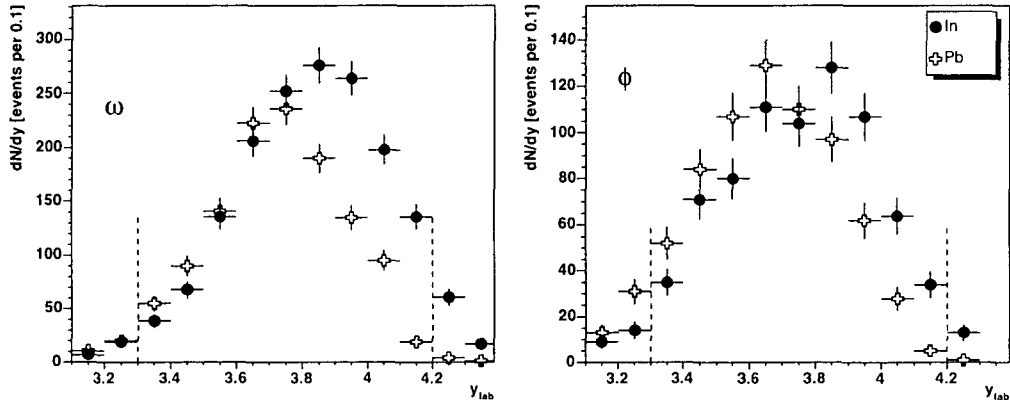


Figure 8.6: Rapidity distributions measured in the In and Pb targets for the ω and ϕ dimuons. The vertical lines indicate our selected y phase space window.

vertex telescope, are much less present in our data than the corresponding dimuons produced in the most upstream In target. This very pronounced acceptance difference is seen in Fig. 8.7, which shows the differential rapidity acceptances, convoluted with the reconstruction, matching and vertexing efficiencies, for each target. The In and

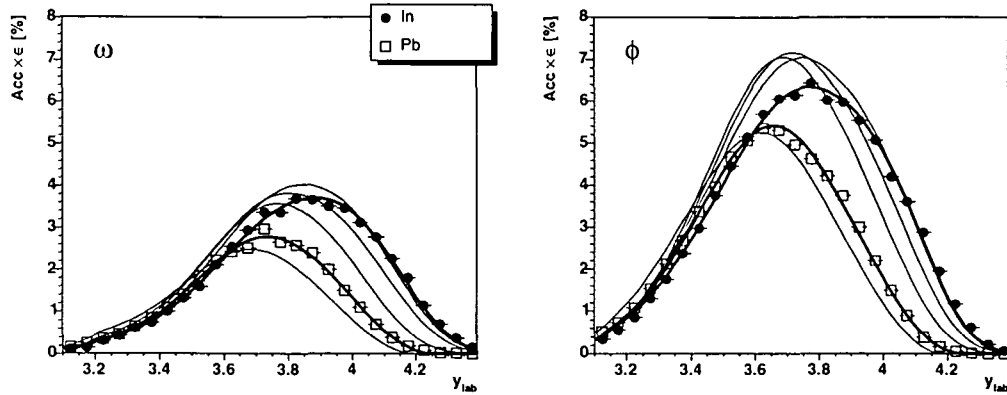


Figure 8.7: ω and ϕ differential rapidity acceptances, convoluted with the reconstruction, matching and vertexing efficiencies, for each target.

Pb parametrised curves are displayed in thicker lines and compared to the points directly extracted from the Monte Carlo simulations, which are affected by statistical fluctuations. The other lines correspond to the Be targets.

Unfortunately, it is not simple to correct the measured rapidity distributions for acceptance effects, since there are very strong correlations between the y and p_T acceptances, as shown in Appendix D. For instance, the more forward the rapidity, the higher the acceptance of low p_T dimuons. Given the relatively low statistics of our data samples and the narrow range of our rapidity window, it is not worth making a big effort to obtain acceptance-corrected y distributions. We would not be able, anyway, to make a detailed study of the existence or not of backward rapidity shifts from p-Be to p-Pb collisions. It is much more reasonable to stay at the level of the measured data, and compare their spectra to the reconstructed Monte Carlo events, equally affected by acceptances and efficiencies (including their correlations). This is what we do in Fig. 8.8, which shows, for the ω and ϕ events in each of the six targets, the comparison between the reconstructed Monte Carlo (plus a rather small number of like-sign muon pairs) and the measured opposite-sign dimuon data. Within the statistical accuracy of the measured data, we can say that the agreement is quite remarkable, for both resonances and for all the targets. This confirms that the rapidity distributions we used for the event generation provide a good description of our measurements.

8.2.4 ω and ϕ Transverse Momentum Distributions

Before we go into the details of our own transverse momentum measurements, it is interesting to compare the p_T spectra of two low mass dimuon windows, 200–450 and 450–700 MeV, to what could be done by the NA38 experiment, in the higher of these two windows. This comparison can be seen in Fig. 8.9, where we see the dramatic improvement of NA60 in low- p_T acceptance for low mass dimuons, mostly due to the presence of the magnetic field in the vertex region. The dipole field of PT7 opens the angle of low- p_T opposite-sign muon pairs, deflecting them into the angular region

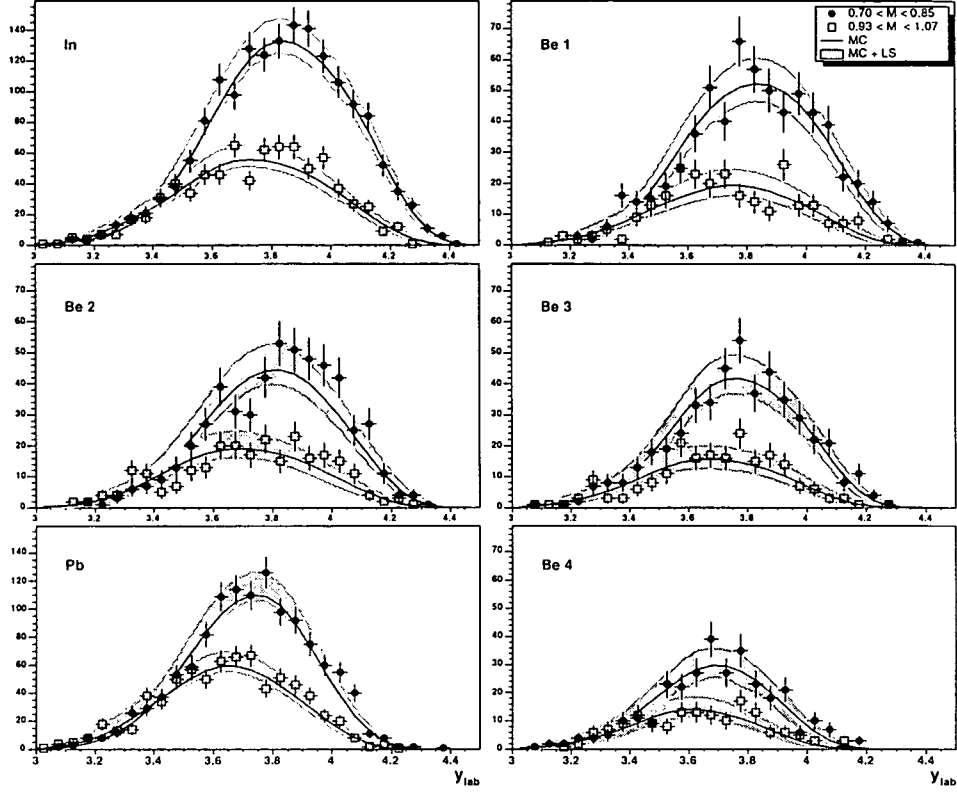


Figure 8.8: y distributions of the reconstructed Monte Carlo and the measured opposite-sign dimuon data, for the ω and ϕ events in each of the six targets.

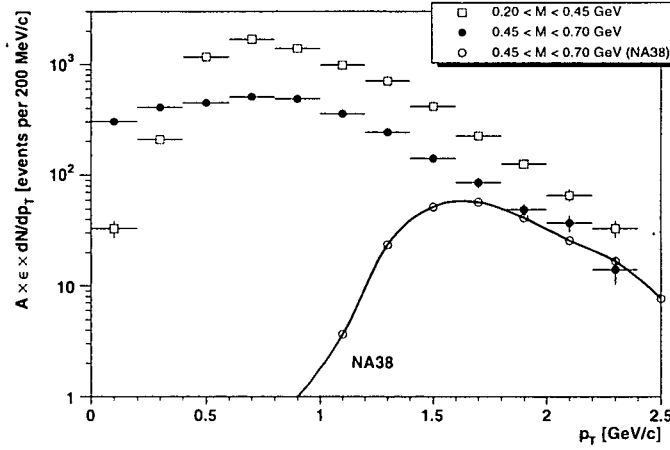


Figure 8.9: p_T distributions of reconstructed dimuons in three different mass windows, compared to the ones of NA38.

covered by the experiment (but remaining at forward rapidities).

Figure 8.10 shows the p_T distributions of the ω and ϕ dimuons, measured for each of the six targets, compared to the corresponding distributions from the reconstructed

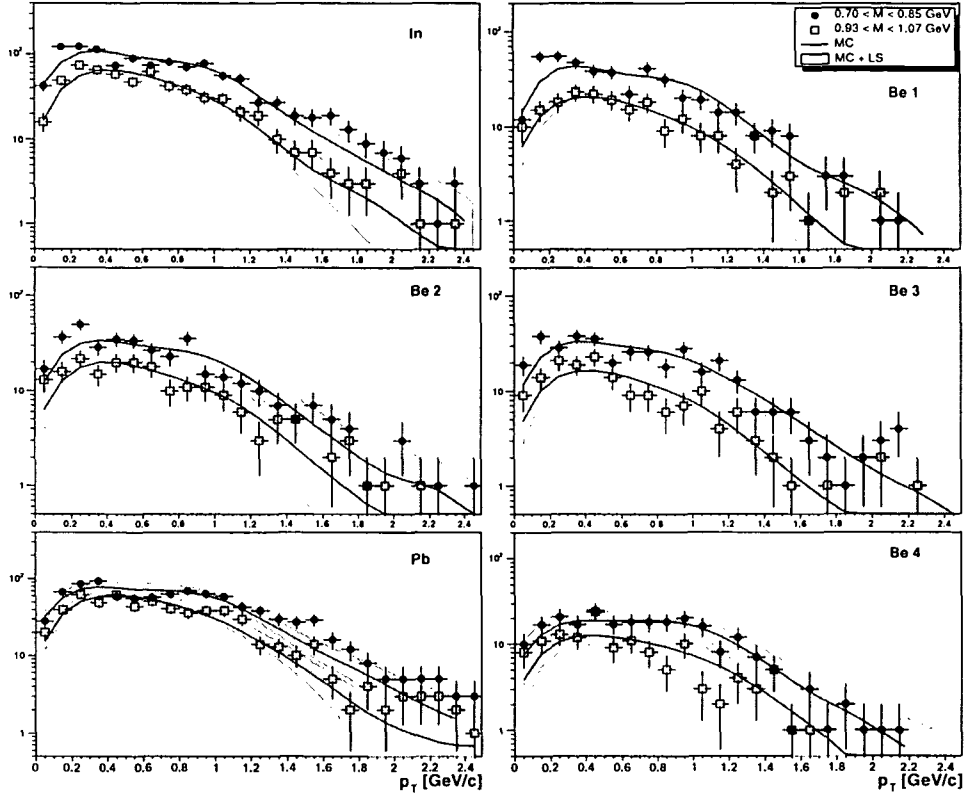


Figure 8.10: p_T distributions of the reconstructed Monte Carlo and of the measured opposite-sign dimuon data, for the ω and ϕ events in each of the six targets.

Monte Carlo. A careful look reveals that the data points seem to be somewhat flatter than the Monte Carlo bands, at least in the case of the In and Pb targets. This indicates that the generated p_T distributions may not provide the best description of the measured data.

To improve this situation, we varied the value of T in the generation function, $dN/dp_T = p_T \cdot m_T \cdot K_1(m_T/T)$, and calculated, for each step, the $\chi^2/\text{n.d.f}$ for the comparison between the corresponding reconstructed Monte Carlo histograms and the measured data. In each step, we obtained the new reconstructed Monte Carlo histogram from the original one, weighted bin by bin with the ratio between the new generation function and the one we used to really generate the events, where the value of T was set to 180 MeV for all resonances and targets. We have seen that the best agreement between the simulated and measured distributions is obtained for the following T values: $T^\omega = 167 \pm 3$ and $T^\phi = 164 \pm 8$ MeV for the Be target; $T^\omega = 186 \pm 4$ and $T^\phi = 188 \pm 7$ MeV for the In target; $T^\omega = 198 \pm 4$ and $T^\phi = 196 \pm 6$ MeV for the Pb target. Figure 8.11 compares the $1/p_T \cdot dN/dp_T$ distributions measured for the ω and ϕ dimuons, in each of the three nuclear targets, with the improved reconstructed Monte Carlo distributions. For illustration purposes, the panels include dotted lines representing the error bars in the distributions due to the error of T . While we have significant evidence that the value of T increases from Be to Pb, we do not see any

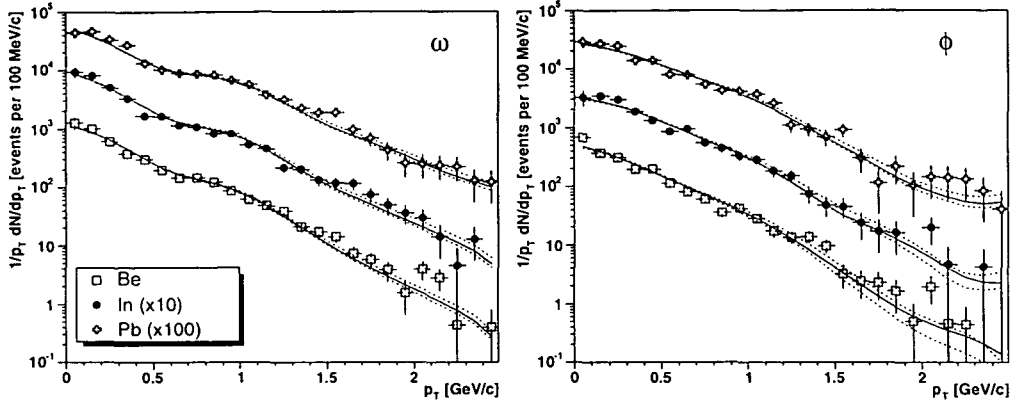


Figure 8.11: $1/p_T \cdot dN/dp_T$ distributions of the ω and ϕ dimuons, for each of the three nuclear targets: Be, In and Pb. See the text for details.

difference between T^ω and T^ϕ .

Given the relatively flat shape of the differential acceptance curves in p_T , and given the fact that the values of T extracted from the data are quite close to those used in our original simulations, we believe that the integrated acceptances we have previously calculated are very close to the values we would obtain using new T values, tuned to the data. Nevertheless, we have calculated by how much the acceptances of the ω and ϕ dimuons change, using the new values of T and assuming common values of T for both resonances: 166, 187 and 197 MeV, respectively for the Be, In and Pb nuclei. We should underline that the *differential* p_T acceptances remain the same, and we simply calculate a new integrated acceptance, as

$$A^\omega = \frac{\int dp_T A^\omega(p_T) G^\omega(p_T)}{\int dp_T G^\omega(p_T)}, \quad (8.1)$$

and analogously for the ϕ , where $G^\omega(p_T)$ is the new p_T generation function, with the tuned T values. Table 8.2 shows by how much the new acceptances differ with respect to the old values.

	In	Be 1	Be 2	Be 3	Pb	Be 4
ω	1.002	0.996	0.993	0.990	1.020	0.976
ϕ	0.998	1.002	1.001	1.001	1.003	0.995

Table 8.2: Acceptance correction factors for the ω and ϕ due to the updated T parameters in the p_T distribution.

We see that the variation with respect to the previously calculated integrated acceptances is, indeed, very small. Using the acceptances calculated with $T = 180$ MeV or with the tuned T values will not change, in any significant way, the final result which we will present in the next section. Nevertheless, we have taken the slightly improved values in our analysis, also using the same value of T for the η and ρ resonances. We neglect this small correction in the case of the Dalitz decays, since the

change of the dimuon p_T distribution cannot be easily obtained from the change in the parent's distributions, and a proper calculation would require redoing the full Monte Carlo event generation and reconstruction.

8.3 Analysis of Low Mass Dimuon Production

8.3.1 Nuclear Dependence of ω and ϕ Production

In this section we use the Be, In and Pb data to derive the nuclear dependence of the ω and ϕ production cross-sections, using the simple power law parametrisation $\sigma_{pA} = \sigma_0 \cdot A^\alpha$, where A is the mass number of the target nucleus and σ_0 can be qualitatively interpreted as a kind of “elementary nucleon-nucleon production cross-section”.

The product $B\sigma_{pA}$, where B stands for the branching ratio of the decay under consideration, in the target i , can be obtained by dividing the number of observed ω 's and ϕ 's, N_i , by the integrated luminosity, \mathcal{L}_i , the acceptance, A_i , and the overall efficiency, ϵ_i ,

$$B\sigma_{pA_i} = \frac{N_i}{\mathcal{L}_i \cdot A_i \cdot \epsilon_i} \quad . \quad (8.2)$$

The values of $B\sigma_0$ and α , for each of the two resonances, can be derived by comparing the dimuon mass distributions measured in the Be, In and Pb targets. Since we had all the targets simultaneously in the beam, the measurement of α is not affected by the uncertainties of the integrated luminosity.

The dimuon mass spectrum up to the J/ψ peak is expected to result from the superposition of 9 “signal” sources, as described in Chapter 6. We cannot simply integrate the mass spectrum in a given mass window around the ω and ϕ resonances to obtain the respective yields in the three target materials. We must consider the superposition of the simulated mass distributions of each individual signal source, after the reconstruction procedure, which convolutes the generated events with the detector acceptances, efficiencies and smearing effects.

The reconstructed Monte Carlo events (generated for all the field polarities) were subjected to the same event selection criteria as the real data, including the phase space window. The individual Monte Carlo reconstructed histograms, denoted by dN_i^j/dM , for each target, i , and each simulated “signal” process, j , were divided by the total number of generated events, in full phase space, such that their integral is equal to the product of the acceptance and efficiencies. It is important to underline that this normalisation is done with respect to full phase space and not with respect to the fraction of events generated inside our specific phase space window. The latter option would lead to a much more complicated analysis, given the fact that the phase space window is defined on the basis of *dimuon* and *single muon* selection cuts, not easy to extrapolate to the meson level, in particular in the case of Dalitz decays. On the other hand this implies trusting the generation functions, in y , $\cos\theta$, etc., outside of our phase space window. Since there is little knowledge on the distribution of the

$\cos\theta$ variable, we will use both, $1 + \cos^2\theta$ and uniform distributions, when quoting our results.

The opposite-sign dimuon mass distributions obtained from the p-Be, p-In and p-Pb data samples are *simultaneously* fitted to a function which is a superposition of several terms, one of them being the combinatorial background. This allows us to work directly with the distributions of measured (and selected) opposite-sign dimuon events. The combinatorial background contribution is determined (and remains completely fixed) by the procedure described in the first section of this chapter. The open charm contribution is obtained from the Monte Carlo simulation already properly normalised, apart from the luminosity factor, \mathcal{L}_i , which is specific of each target, i . We neglect the Drell-Yan contribution since our analysis is concentrated on the mass window below 1.1 GeV, where this process cannot be properly calculated and is expected to be negligible. The other seven terms correspond to the $\mu^+\mu^-$ and/or Dalitz decays of the mesons η , ρ , ω , η' and ϕ . Also these reconstructed Monte Carlo histograms are multiplied by the target-specific luminosity factors. Furthermore, they are multiplied by the appropriate branching ratios, B , summarised in Chapter 6, such that the only remaining factor to obtain the number of measured events in our data is the full phase space production cross-section of the parent meson, in p- A_i collisions, $\sigma_0^j A_i^{\alpha_j}$:

$$\sum_{i=Be,In,Pb} \frac{dN_i^{OS}}{dM} = \sum_{i=Be,In,Pb} \frac{dN_i^{BG}}{dM} + \mathcal{L}_i \left(\frac{d\sigma_{pA_i}^{D\bar{D}}}{dM} + \right. \quad (8.3)$$

$$B^{\eta_D} \sigma_0^\eta A_i^{\alpha_\eta} \frac{dN_i^{\eta_D}}{dM} + B^{\eta'_D} \sigma_0^{\eta'} A_i^{\alpha_{\eta'}} \frac{dN_i^{\eta'_D}}{dM} + B^{\omega_D} \sigma_0^\omega A_i^{\alpha_\omega} \frac{dN_i^{\omega_D}}{dM} +$$

$$\left. B^\eta \sigma_0^\eta A_i^{\alpha_\eta} \frac{dN_i^\eta}{dM} + B^\rho \sigma_0^\rho A_i^{\alpha_\rho} \frac{dN_i^\rho}{dM} + B^\omega \sigma_0^\omega A_i^{\alpha_\omega} \frac{dN_i^\omega}{dM} + B^\phi \sigma_0^\phi A_i^{\alpha_\phi} \frac{dN_i^\phi}{dM} \right)$$

Note that the four individual p-Be measurements are added. The superscripts of the branching ratio, B , and of the Monte Carlo mass distributions, dN/dM , have the following meaning: η_D , η'_D and ω_D stand for the Dalitz decay modes of the quoted mesons, while η , ρ , ω and ϕ stand for their leptonic 2-body decays.

In order to extract the nuclear dependence of the ω and ϕ mesons, we perform a fit to the dimuon mass distributions between 0.6 and 1.1 GeV. In the fit, we leave five parameters free: the σ_0 and α values of the ω and ϕ contributions, and the σ_0 of the ρ . We assume, and impose, that the η , η' and the ρ have the same α value as the ω . We have also fixed the normalisations of the η and η' with respect to those of the ω ($\eta/\omega = 0.815$ and $\eta'/\eta = 0.15$, values based on Ref. [6]). Anyway, given the fact that the fit starts at 0.6 GeV, the results are completely insensitive to the η and η' contributions.

The result of the fit is shown in Fig. 8.12 for the 3 target materials. In this figure we can see the individual contributions to the dimuon mass spectrum due to the combinatorial background ("BG"), open charm ("D \bar{D} ") and Drell-Yan ("DY") dimuons. The fitted contributions of the ρ , ω and ϕ are drawn on top of the sum of the former three processes, which is indicated by the dotted line. The sum of all

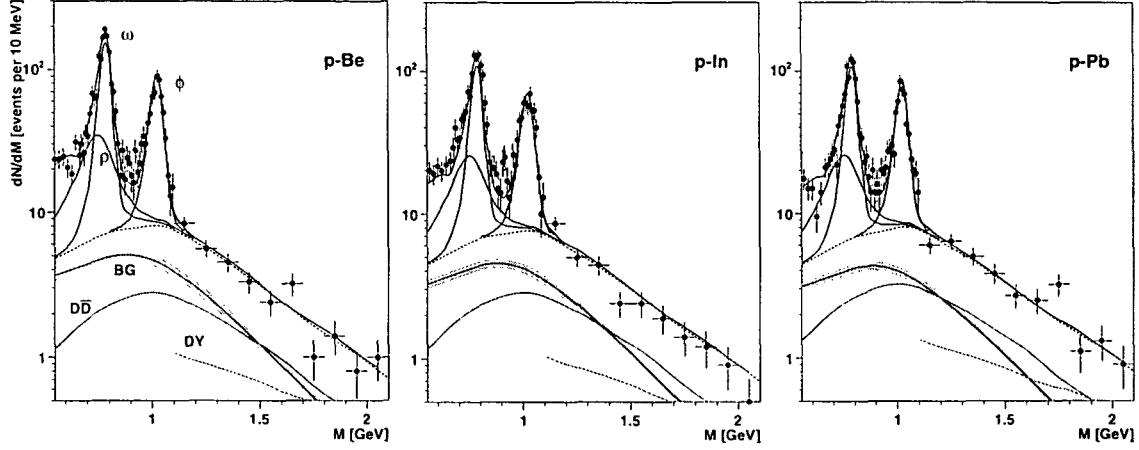


Figure 8.12: Simultaneous fit of the opposite-sign dimuon mass distributions measured in p-Be, p-In and p-Pb collisions.

contributions is shown as a solid line. From this fit (assuming the branching ratios given in Chapter 6), we obtain the following elementary full phase space cross-sections and values for the α : $\sigma_0^\rho = 11.5 \pm 1.0$, $\sigma_0^\omega = 10.1 \pm 0.6$ and $\sigma_0^\phi = 0.53 \pm 0.05$ mb, $\alpha^\omega = 0.83 \pm 0.01$ and $\alpha^\phi = 0.91 \pm 0.02$. The corresponding values if we use a uniform decay angle distribution for the ρ , ω and ϕ mesons are $\sigma_0^\rho = 9.4 \pm 0.8$, $\sigma_0^\omega = 7.6 \pm 0.4$, $\sigma_0^\phi = 0.40 \pm 0.03$ mb. The quoted errors refer to statistical uncertainties only. From these fits we derive the number of ω 's and ϕ 's present in our final data samples: $N^\omega = 966, 676$ and 660 , $N^\phi = 575, 464$ and 511 , for the Be, In and Pb targets, respectively.

8.3.2 Very Low Mass Dimuons

So far, we have restricted our analysis to the domain 0.6–1.1 GeV, dominated by the ρ/ω and ϕ peaks, standing on a smooth and relatively small “continuum”, composed essentially of combinatorial background and of open charm muon pairs. It is always quite robust to extract the production yields of narrow resonances, even when we are not certain of the specific composition of the underlying continuum. Now we would like to extend our analysis down to the lowest dimuon masses, where we no longer have pronounced resonances (maybe in the future also the η 2-body decay can be used to extract the η cross-section, provided it is distinct enough from the underlying continuum). A study of this continuum region, therefore, is intrinsically more difficult. Furthermore, we are also aware that the lower we go in mass, the more sensitive we are to an exact description of detector effects (acceptance and efficiencies) by our Monte Carlo simulation. Nevertheless, we will make an attempt to describe our low mass dimuon data as a superposition of the sources mentioned in Chapter 6, plus the combinatorial background. We start the fit from threshold, adding as new free parameters the σ_0^η and α^η , since the mass region below ~ 0.45 GeV is dominated by the η -Dalitz decay. Also the ω and η' Dalitz decays are present, but they are much smaller. As before, the ω -Dalitz contribution is fixed by the ω cross-section measured

through its 2-body decay, taking into account the different branching ratios, while the η' is fixed to the η . We have bound the α of the η' to the α of the η since these two mesons have similar quark content. The simultaneous fit of the 3 dimuon mass spectra was performed in the same way as before, but in the mass range 0.2–1.1 GeV. The outcome of the fit can be seen in Fig. 8.13.

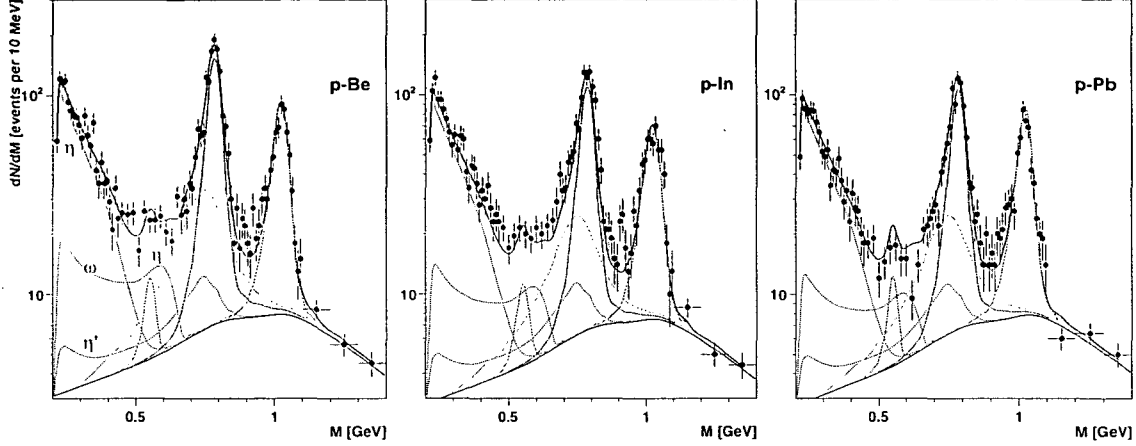


Figure 8.13: Simultaneous fit of the three measured dimuon mass distributions to the superposition of the expected sources, and the combinatorial background, within the mass range 0.2–1.1 GeV.

We have drawn the Dalitz decays of the η , η' and ω , and the 2-body decays of the η , ρ , ω and ϕ on top of the sum of the other processes. The line following the data shows the sum of all contributions, as given by the fit. The corresponding elementary production cross-sections and α values are summarised in Table 8.3. We see that

	$1 + \cos^2 \theta$	uniform
σ_0^η [mb]	9.5 ± 0.6	10.2 ± 0.6
σ_0^ρ [mb]	11.6 ± 1.0	8.9 ± 0.7
σ_0^ω [mb]	10.5 ± 0.6	8.0 ± 0.5
σ_0^ϕ [mb]	0.53 ± 0.05	0.40 ± 0.03
α^η	0.93 ± 0.02	
α^ω	0.82 ± 0.01	
α^ϕ	0.91 ± 0.02	

Table 8.3: Elementary full phase space production cross-sections, and their dependences on the mass number A , for the η , ρ , ω and ϕ mesons, as extracted from a simultaneous fit to the three dimuon mass spectra.

extending the fit to the full mass region does not influence the ρ , ω and ϕ results. This was expected, as outlined above, since the η does not contribute to the dimuon mass spectrum above 0.6 GeV.

From these values we derive the cross-section ratio $\sigma_\eta/(\sigma_\rho + \sigma_\omega)$. We obtain 0.43 ± 0.04 , if we assume a $1 + \cos^2 \theta$ decay angle distribution for the ρ and ω and

0.61 ± 0.05 if we take a uniform distribution.

8.4 Discussion and Conclusions

There are essentially three different issues, reported in the previous sections, which should be discussed: the nuclear dependence of the ω and ϕ production cross-sections, expressed by the α values; the ρ , ω and ϕ elementary production cross-sections, expressed by the σ_0 values; and the ratio between the η and $\rho + \omega$ production cross-sections that would best describe our low mass dimuon range, in the absence of any other physics contributions or detector effects we may have missed, $\sigma_0^\eta/(\sigma_0^\rho + \sigma_0^\omega)$.

In what concerns the nuclear dependence of the ω and ϕ production cross-sections, there are not many previous measurements with which we can compare our values. In the case of the ρ/ω , Table 6.3 shows that $\alpha = 0.69 \pm 0.02$ (for proton beam) but this is at forward x_F , where the α is expected to be smaller than at mid-rapidity. In the case of the ϕ , the same Table shows a measurement performed in a phase space window similar to ours, by NA11, with 120 GeV protons, giving $\alpha = 0.86 \pm 0.02$. At higher energies and p_T HERA-B measures $1.01 \pm 0.01 \pm 0.06$. The values we extracted from our data, $\alpha^{\rho/\omega} = 0.82 \pm 0.01$ and $\alpha^\phi = 0.91 \pm 0.02$, are not far from these previous measurements.

We should underline that we see the ϕ production cross-section increasing with the target's mass number significantly faster than the ω , an observation that may help explaining the “ ϕ enhancement” observed in heavy-ion collisions by NA38 and NA50 [81]. It is also interesting to note that the η seems to scale with the target's mass number in the same way as the ϕ . This might be due to the presence of a strange quark component in both mesons. This observation, if confirmed, would indicate that η production could also be “enhanced” in heavy-ion collisions, with respect to ω production in the same way as the ϕ .

We will now discuss the elementary (nucleon-nucleon) production cross-sections we deduce from our data for the ρ , ω and ϕ mesons. We start by recalling the values we have obtained: $\sigma_0^\rho = 11.6 \pm 1.0$, $\sigma_0^\omega = 10.5 \pm 0.6$ and $\sigma_0^\phi = 0.53 \pm 0.05$ mb if we assume $1 + \cos^2 \theta$ decay angle distributions; $\sigma_0^\rho = 8.9 \pm 0.7$, $\sigma_0^\omega = 8.0 \pm 0.5$ and $\sigma_0^\phi = 0.40 \pm 0.03$ mb if we assume uniform $\cos \theta$ distributions.

The NA27 experiment has also measured the absolute production cross-sections of these three particles, among many others, including the η , in pp collisions at 400 GeV [82]. The experimental setup included a bubble chamber, used as target and vertex detector, two gamma detectors for γ/π^0 detection, Cherenkov counters for particle identification, and a magnetic spectrometer for charged particle tracking. The particles of relevance to our study were observed in the following decay channels: $\eta \rightarrow \gamma\gamma$ and $\eta \rightarrow \pi^+\pi^-\pi^0$; $\rho \rightarrow \pi^+\pi^-$; $\omega \rightarrow \pi^+\pi^-\pi^0$; and $\phi \rightarrow K^+K^-$. The corresponding invariant mass distributions can be seen in Fig. 8.14. Extrapolating to full phase space their positive x_F measurements, NA27 obtained the following total production cross-sections: $\sigma^\eta = 9.8 \pm 0.6$, $\sigma^\rho = 12.6 \pm 0.6$, $\sigma^\omega = 12.8 \pm 0.8$ and $\sigma^\phi = 0.62 \pm 0.06$ mb.

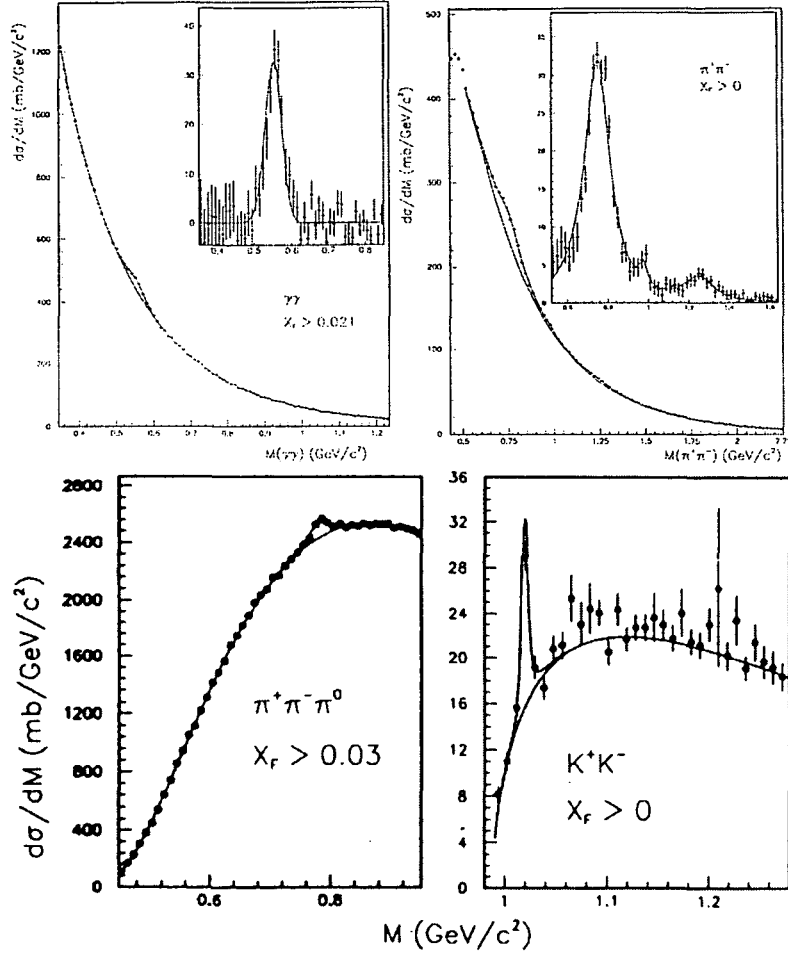


Figure 8.14: Invariant mass distributions from which NA27 obtained the η , ρ , ω and ϕ cross-sections in pp collisions at 400 GeV/c.

Before we compare the NA27 values to our own measurements, it is important to note that, given their similar masses, the ρ and the ω are likely to suffer interference effects when measured in the same decay channel. A detailed study was performed by the HELIOS-1 experiment (described below), which found a negative interference effect, leading to a measured “ $\sigma^{\rho/\omega}$ ” total production cross-section in the dilepton decay channel 15% smaller than the sum of the individual production cross-sections, $\sigma^\rho + \sigma^\omega$, as measured in independent decay channels.

Assuming that our dimuon data is affected by the same interference effect as derived by HELIOS-1, we deduce a total $\rho + \omega$ production cross-section, corrected for the interference, of $\sigma^\rho + \sigma^\omega = 25.4 \pm 1.3$ mb, to be compared with the NA27 value, 25.4 ± 2.0 mb. Given the remarkable coincidence of these two numbers, we can also take the alternative approach of starting from the NA27 value and derive the existence of a 15% negative interference effect. The ϕ values can be compared directly, since there are no interference effects to be taken into account. We see that there is a perfect agreement between the two experiments in what concerns the ρ/ω

resonances, while our ϕ value is $\sim 20\%$ lower than the one quoted by NA27.

This comparison was done using the values we obtained with the $1 + \cos^2 \theta$ decay angle distributions. If we would use those corresponding to uniform $\cos \theta$ distributions, $\sigma^\rho + \sigma^\omega = 19.4 \pm 1.0$ mb and $\sigma^\phi = 0.40 \pm 0.03$ mb, the agreement with NA27 would considerably degrade. This is an indirect indication that the $1 + \cos^2 \theta$ distributions provide a better description of the ρ , ω and ϕ dimuon decays.

Before we move to some comments on the η production yield that best describes our low mass dimuon spectra, we should briefly mention the HELIOS-1 experiment. HELIOS-1 studied di-electron *and* dimuon production in p-Be collisions at 450 GeV [7]. In order to better understand the contribution from the η Dalitz decay to the dilepton mass spectra, they fully reconstructed the $l^+ l^- \gamma$ decay by complementing the dilepton measurement with the data of an electromagnetic calorimeter. The performances of HELIOS-1 and NA60 are comparable in terms of dimuon mass resolution and phase space covered: $+0.25 < y^* < +1.50$, $-0.75 < \cos \theta < 0.75$, $m_T > 0.4$ GeV for $\mu\mu$ and $-0.25 < y^* < +1.25$, $-0.75 < \cos \theta < 0.75$, $m_T > 0.25$ GeV for ee . Their background contamination is larger, around 50 % away from the resonances. The $\mu\mu\gamma$, $\mu\mu$, $ee\gamma$, and ee invariant mass distributions measured by HELIOS-1 are shown in Fig. 8.15, where the individual contributions have been indicated.

HELIOS-1 also used a $1 + \cos^2 \theta$ decay angle distribution to extrapolate their ρ and ω measurements to full phase space, obtaining $\sigma^\eta/(\sigma^\rho + \sigma^\omega) = 0.54 \pm 0.05$ from the ee data and 0.52 ± 0.06 from the $\mu\mu$ data, before any correction for interference effects. It should be noted that the η cross-section measured in the $l^+ l^- \gamma$ mode provides an excellent description of the *dilepton* mass spectra. Before we compare the HELIOS-1 measurements to our result, we should extrapolate the HELIOS-1 measurement to pp collisions, assuming the α^η and $\alpha^\omega = \alpha^\rho$ extracted from our data. We deduce $\sigma_0^\eta/(\sigma_0^\rho + \sigma_0^\omega) = 0.43 \pm 0.04$ for the ee data and 0.41 ± 0.05 for the $\mu\mu$ data. These values compare quite well to our value, $\sigma_0^\eta/(\sigma_0^\rho + \sigma_0^\omega) = 0.43 \pm 0.04$. This comparison is especially valuable since it is not sensitive to the ρ/ω interference effects.

The corresponding NA27 measurement is lower, $\sigma^\eta/(\sigma^\rho + \sigma^\omega) = 0.39 \pm 0.04$, but cannot be directly compared to our measurements because it is not affected by the ρ/ω interference. Correcting our measurements for the 15 % factor measured by HELIOS-1 we derive the value 0.37 ± 0.03 , in better agreement with the NA27 measurements.

Also the CERES experiment measured the *photons* produced in p-Be and p-Au collisions at 450 GeV [42], in a special (high statistics) proton run together with the TAPS electromagnetic calorimeter. The η and ω were reconstructed from the $\eta \rightarrow \gamma\gamma$ and $\omega \rightarrow \pi^0 \gamma \rightarrow \gamma\gamma\gamma$ decay channels. Figure 8.16 shows the $\gamma\gamma$ and $\pi^0 \gamma$ invariant mass spectra, showing the η and ω peaks. The larger error bars on the ω are presumably due to the ω 's smaller acceptance, as compared to the η , and to the fact that a third photon had to be observed. The p_T differential cross-sections were measured down to 20 MeV/c, from which the differential ratio of the η to π^0 production cross-sections was extracted. The measurement was conducted in the rapidity window $3.1 < y < 3.7$ (i.e. $-0.33 < y^* < +0.27$). CERES-TAPS did not measure the production cross-section of the ρ . Therefore, they provided a value for the

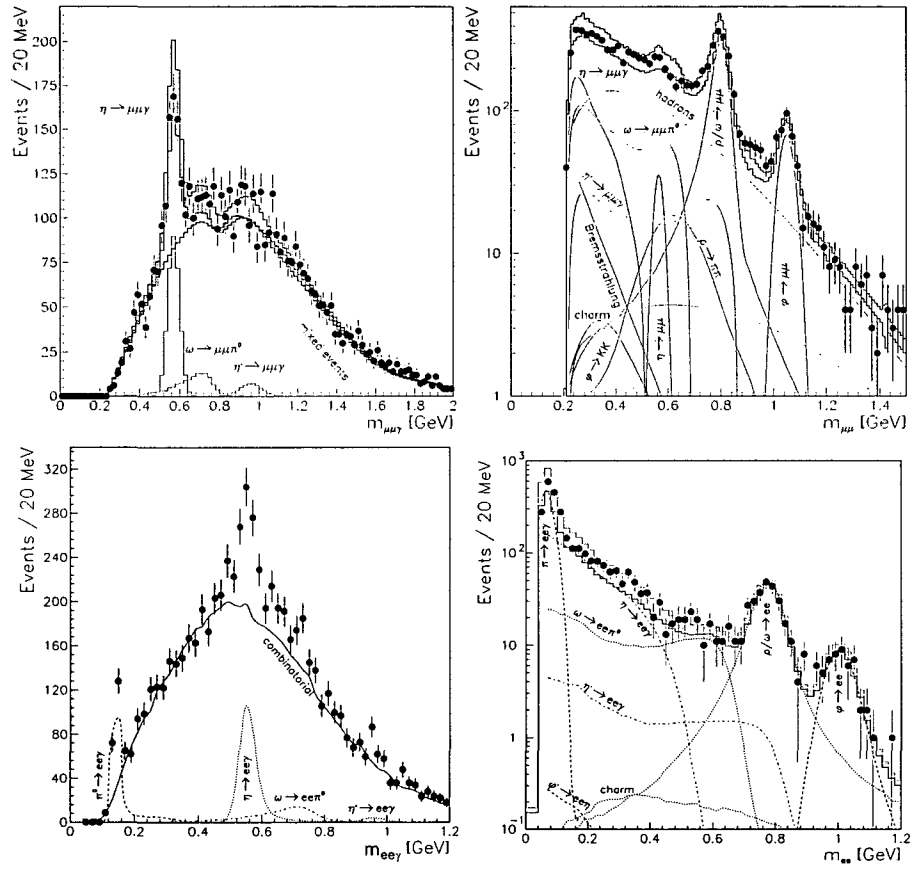


Figure 8.15: $\mu\mu\gamma$, $\mu\mu$, $ee\gamma$, and ee invariant mass spectra measured by HELIOS-1 in 450 GeV p-Be collisions.

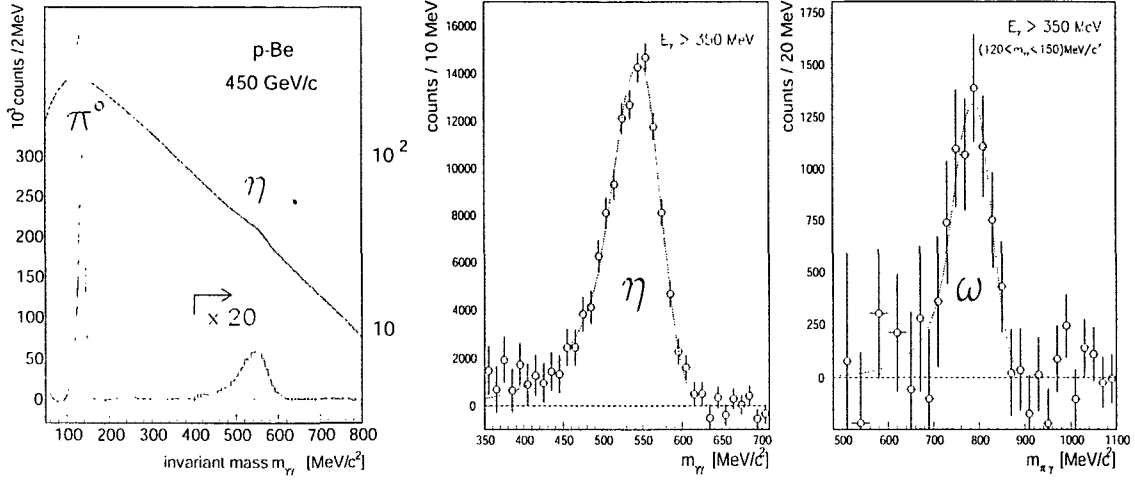


Figure 8.16: Invariant $\gamma\gamma$ (before and after background subtraction) and $\pi^0\gamma$ mass spectra measured by CERES-TAPS in 450 GeV p-Be collisions.

ratio $\sigma^\eta/(2 \cdot \sigma^\omega)$. In their phase space window, CERES-TAPS measured $\sigma^\eta/(2 \cdot \sigma^\omega) = 0.34 \pm 0.03$ in p-Be and 0.37 ± 0.04 in p-Au. Before comparing the CERES-TAPS values to the measurements of all other quoted experiments we should extrapolate this value to full phase space. This can be easily done with the extrapolation factors for the η/π^0 and ω/π^0 cross-section ratios given in Ref. [6]. The ratios $\sigma^\eta/(2 \cdot \sigma^\omega)$ in p-Be and p-Au increase by 13%. Furthermore, as was done for the HELIOS-1 measurement, these ratios should be extrapolated to elementary pp collisions, using α^η and α^ω from our measurement. These two extrapolations performed on the CERES-TAPS ratios provide two values for $\sigma_0^\eta/(2 \cdot \sigma_0^\omega)$: 0.31 ± 0.02 from p-Be and 0.23 ± 0.03 from p-Au.

Figure 8.17 compares the $\sigma_0^\eta/(\sigma_0^\rho + \sigma_0^\omega)$ extracted from our data to the values of the HELIOS-1, NA27 and CERES-TAPS experiments. The leptonic measurements (HELIOS-1 and NA60) were corrected for the ρ/ω interference observed by HELIOS-1 [7]. The values shown are given for full phase space, using the $1 + \cos^2\theta$ decay angle distribution to extrapolate the ρ and ω measurements of HELIOS-1 and NA60. The lower points of the HELIOS-1 measurements show the measured values, when extrapolated to elementary pp collisions. The open symbols of CERES-TAPS show the ratio measured within $3.1 < y < 3.7$ without any corrections. The closed symbols show the values after extrapolating the measurements to full phase space and to elementary pp collisions, as described above.

We conclude that the η yield which best describes our low mass dimuon data is in very reasonable agreement with the measurements of previous experiments.

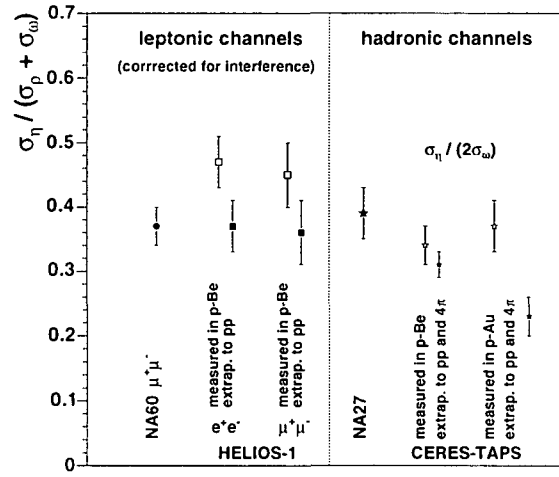


Figure 8.17: Comparison between the $\sigma_\eta / (\sigma_\rho + \sigma_\omega)$ values deduced from our data and those of previous experiments, made in leptonic and hadronic decay channels.

Appendices

A.) Dimuon Kinematics

The kinematic variables relevant for the present analysis are mainly the dimuon's rapidity, y , the transverse momentum, p_T , the transverse mass, m_T , and the polar decay angle, defined in the so-called "Collins-Soper" frame, θ_{CS} . The rapidity variable is defined as

$$y = \frac{1}{2} \ln \frac{E + p_z}{E - p_z}, \quad (8.4)$$

and relates the longitudinal momentum, p_z , with the energy, E . For momenta much larger than the rest energy, $p \gg m$, the rapidity can be approximated by the "pseudo-rapidity" variable, η , which only depends on the polar angle, θ :

$$\eta = -\ln \tan(\theta/2) \quad . \quad (8.5)$$

The transverse mass is defined as

$$m_T = \sqrt{m^2 + p_T^2} \quad . \quad (8.6)$$

The following two formulae relate the rapidity and the transverse mass to the energy and the longitudinal momentum, p_z , respectively,

$$E = m_T \cdot \cosh y, \quad (8.7)$$

$$p_z = m_T \cdot \sinh y \quad . \quad (8.8)$$

Angles are not Lorentz invariant. They, hence, have to be specified in a specific frame. For hard processes, in particular the Drell-Yan process, see Chapter 6, it is convenient to define the decay angles (θ , ϕ) in the Collins-Soper frame [59]. The polar Collins-Soper angle, θ_{CS} (usually given as $\cos \theta_{CS}$), is defined as the angle between the positive muon and the momentum vector of the interacting partons, approximated by the beam axis, z , in the centre-of-mass (c.m.s.) frame,

$$\cos \theta_{CS} = \frac{2}{m\sqrt{m^2 + p_T^2}} (l_{\mu_1}^+ l_{\mu_2}^- - l_{\mu_1}^- l_{\mu_2}^+) \quad , \quad (8.9)$$

where $l^\pm = 1/\sqrt{2}(l^0 \pm l^z)$ are the positive and negative light-cone variables. This angle has the advantage of being manifestly invariant under z -boosts so that the angle can be calculated from laboratory as well as from c.m.s. coordinates.

B.) Functional Form of the SCTA Output Signal

The output of the SCTA128VG chip is a semi-Gaussian pulse, which can be described by a functional form. In the following the *C* routine is given, with which the four time samples were fitted.

```
double vexp3(double *x, double *p){
    double t, v, alpha, beta, tp;
    double ff;
    t = *x - p[0];
    if( t < 0 ) return 0.;
    v = p[1];
    alpha = 3./p[3];
    beta = 1./p[2];
    if(alpha <= beta) return 99999.;
    tp = 3.*(1. - beta / (alpha - beta)) / alpha;
    ff = v*vexp3a(t,alpha,beta)/(vexp3a(tp,alpha,beta));
    return ff;
}

double vexp3(double *x, double *p){
    double mu, mt, m4, ff;
    mu = alpha - beta;
    mt = mu*t;
    m4 = mu*mu*mu*mu;
    ff = exp(-alpha*t) * (alpha*t*t*t/mu - 6.*beta*(exp(mt)-0.5*mt*mt - mt
-1.)/m4);
    return ff;
}
```

C.) Parameterisation of the Strip Efficiencies

Figures 8.18 to 8.20 show the measured and parameterised strip efficiencies for the microstrip planes used in the proton-nucleus 2002 run.

Note that we have used a different strip numbering convention as compared to the one given in Sec. 4.1. This numbering scheme is more convenient for the data reconstruction, where an increasing strip number for physically *neighbouring* strips is favoured. The numbering here is done quadrant by quadrant, and in each quadrant the strip number increases when going from region A to region F. In the first 3 stations (i.e. 6 detector planes) only the inner regions, A–D, are used for the tracking, so that there are no efficiencies available for the strips in the outer regions E and F. The fourth station, consisting of strip planes “06” and “07”, is already fully used for the tracking. However, very few triggered muons passed through the outer area, so that

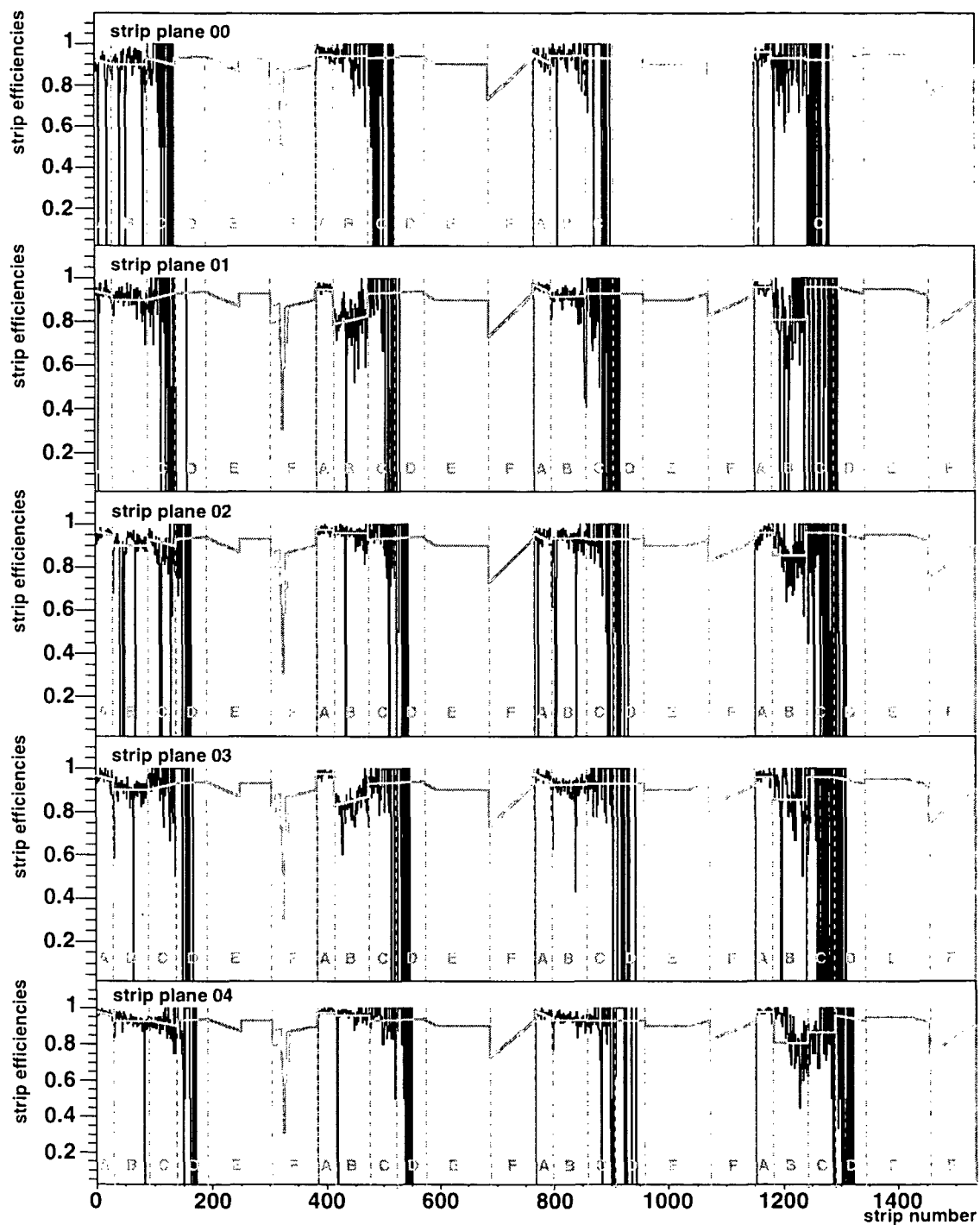


Figure 8.18: Measured and parameterised strip efficiencies for the first five detector planes.

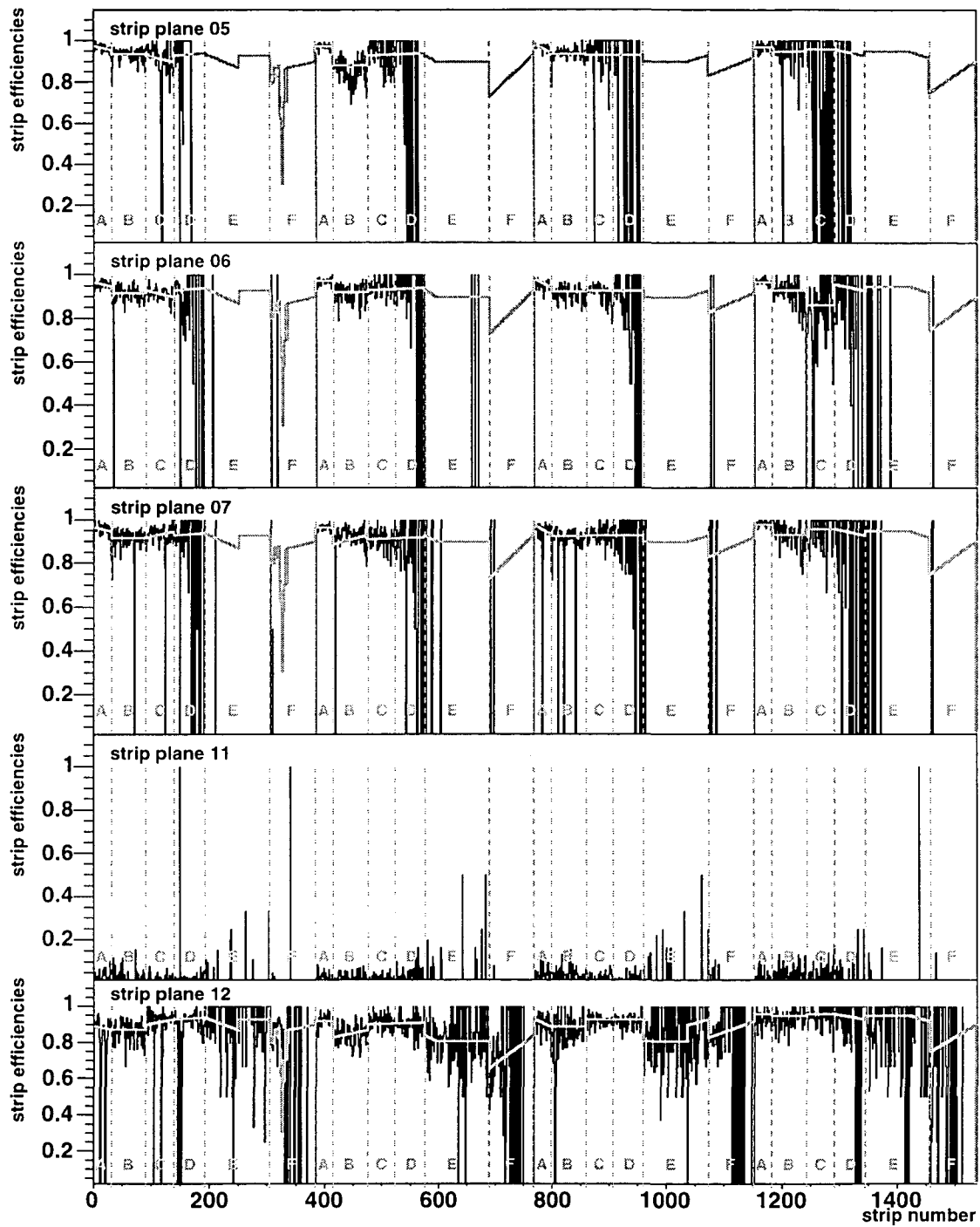


Figure 8.19: Measured and parameterised strip efficiencies for the small planes 5, 6 and 7 and for the first two large planes, 11 and 12.

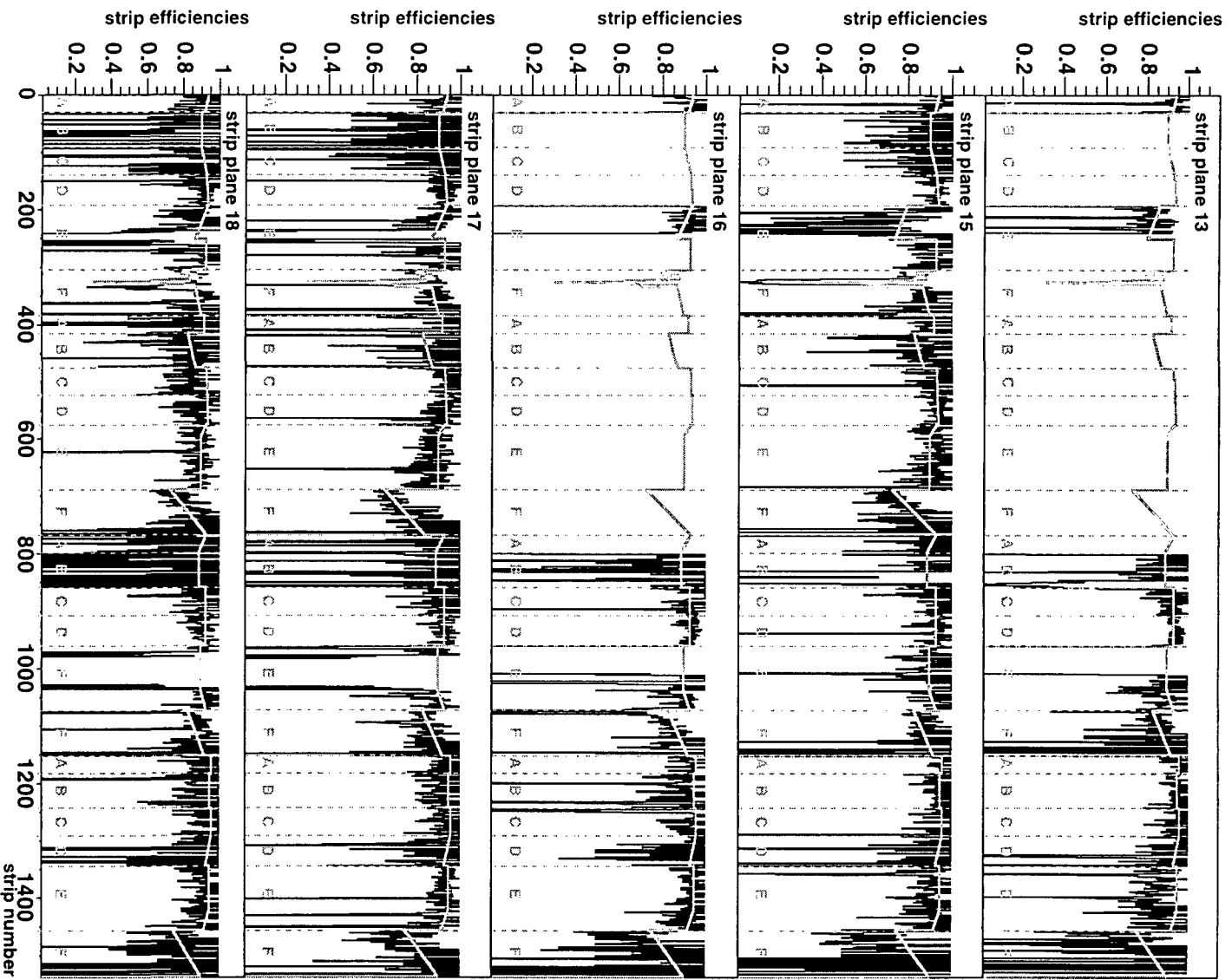


Figure 8.20: Measured and parameterised strip efficiencies for the last five detector planes.

this plane could not be included in the calculation of the “outer strip efficiencies”. Plane 11 had too high leakage current so that it could not be sufficiently depleted (it was operated with a voltage of ~ 10 V only). For this reason, its strip efficiencies are practically zero. Strip planes 13 and 16 were read out only on one side, so that the remaining strips could not be used to evaluate any efficiencies.

As can be seen from these figures, the strip efficiencies vary significantly from one region to the next and are affected by large statistical fluctuations due to the lack of sufficient muon tracks. We have, hence, parameterised the measured efficiencies by building an average value of the same strips over all functional detector planes. From this average we fixed the shape as a function of strip number for each of the 6×4 regions. If then, on a given detector plane, the average efficiency deviated significantly from the obtained average level, the normalisation of each region was adjusted to best describe the measured efficiencies. These parameterisations are shown as a line.

Typical strip efficiencies for the regions A–E are around 90–97%, while in the region F the efficiencies vary from ~ 75 to $\sim 90\%$.

D.) p_T -y Correlated Acceptances

The following figures show the p_T -y correlated acceptance for opposite-sign dimuons in the mass ranges 0.70–0.85 GeV (“ ω ”) and 0.9–1.1 GeV (“ ϕ ”), in different projections. Figures 8.21 and 8.22 show the p_T differential acceptances for different rapidity windows. In order to separate the individual curves, offsets of 10 and 15, in case of the ω and the ϕ , respectively, were added to the acceptances of different rapidity curves. Figure 8.23 shows the same acceptances but in a 2 dimensional view, and from two different perspectives.

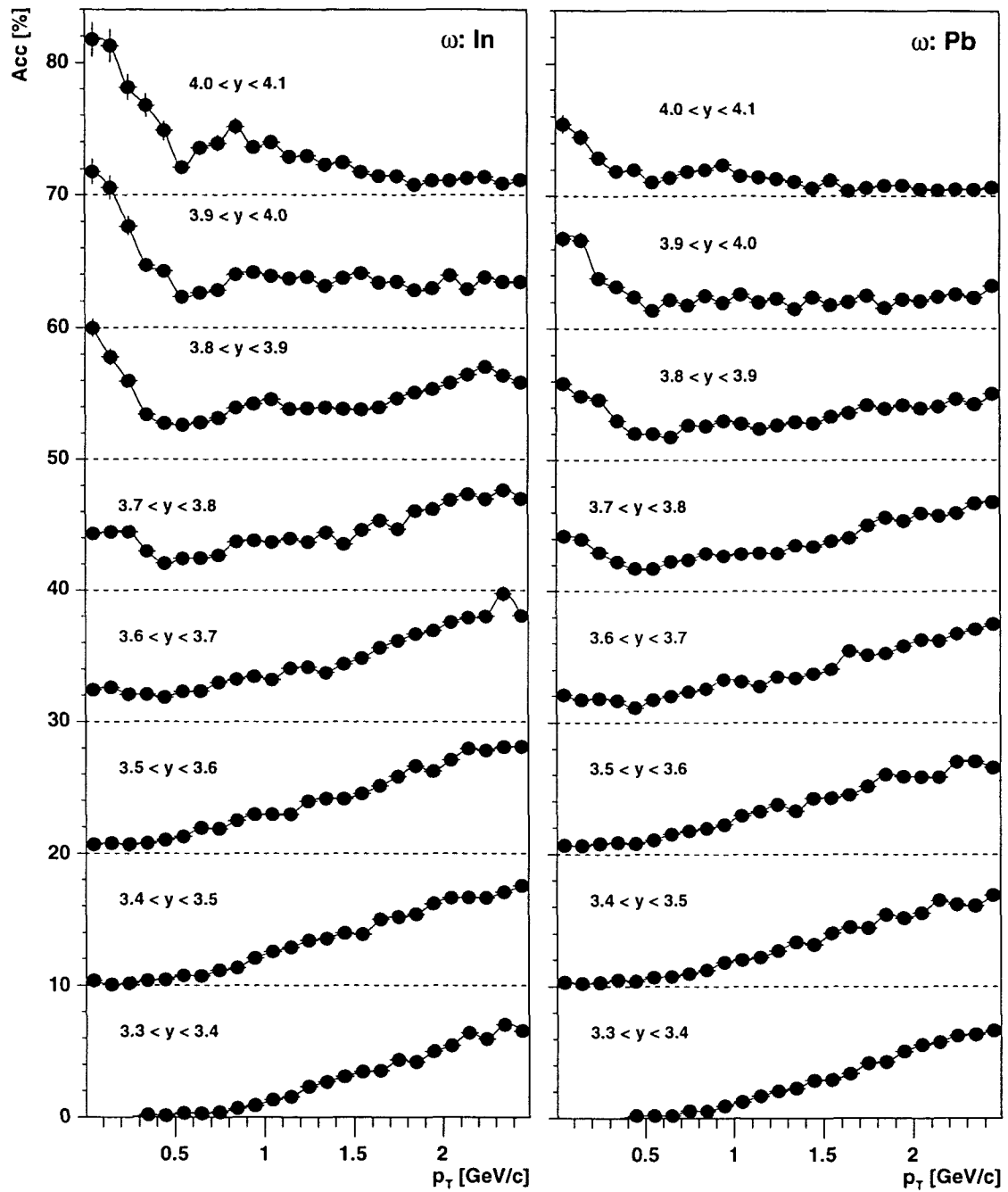


Figure 8.21: p_T differential acceptances for opposite-sign dimuons in the mass range 0.70–0.85 GeV for 8 different rapidity windows. An offset of 10 was added between the individual curves.

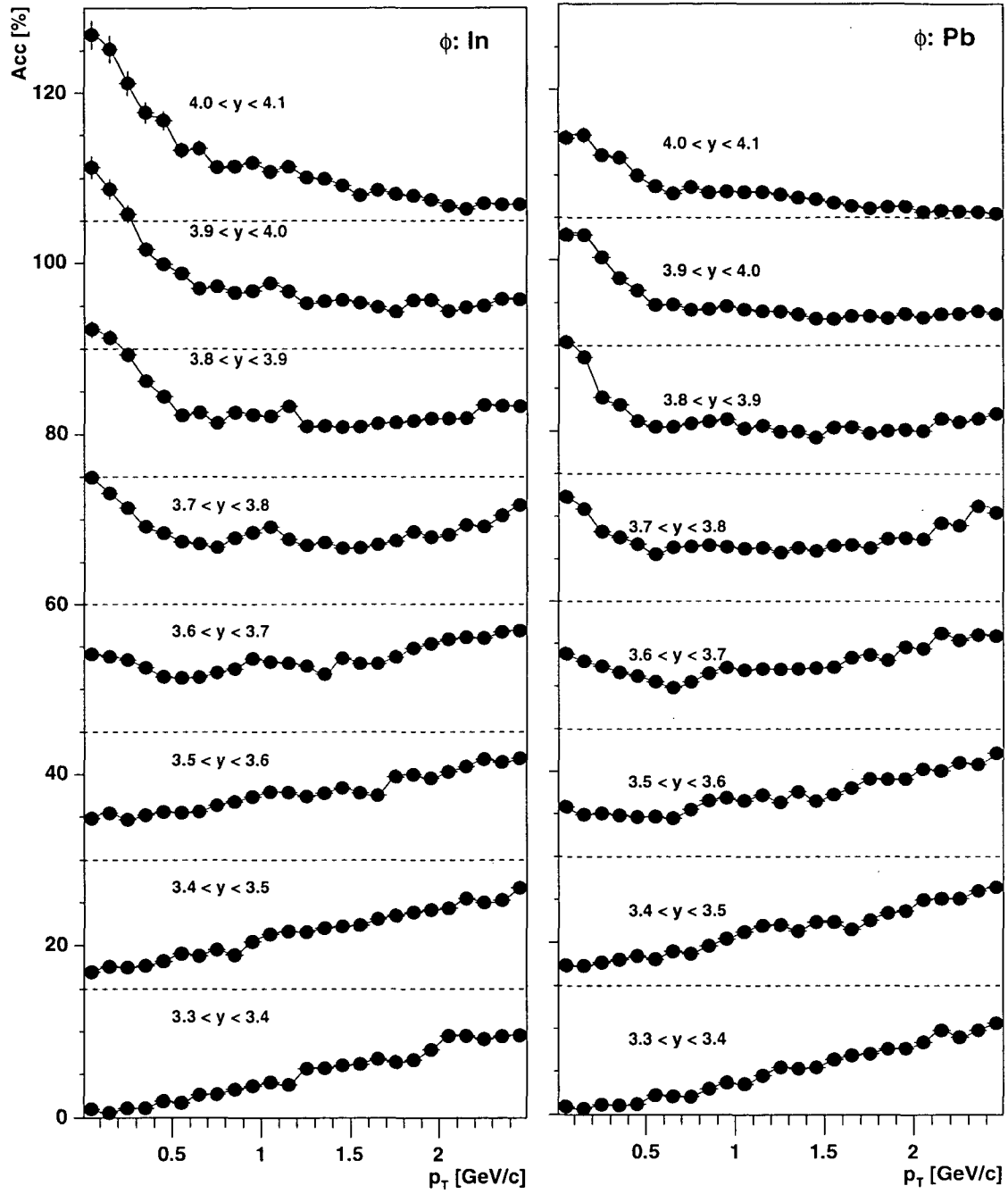


Figure 8.22: p_T differential acceptances for opposite-sign dimuons in the mass range 0.9–1.1 GeV for 8 different rapidity windows. An offset of 15 was added between the individual curves.

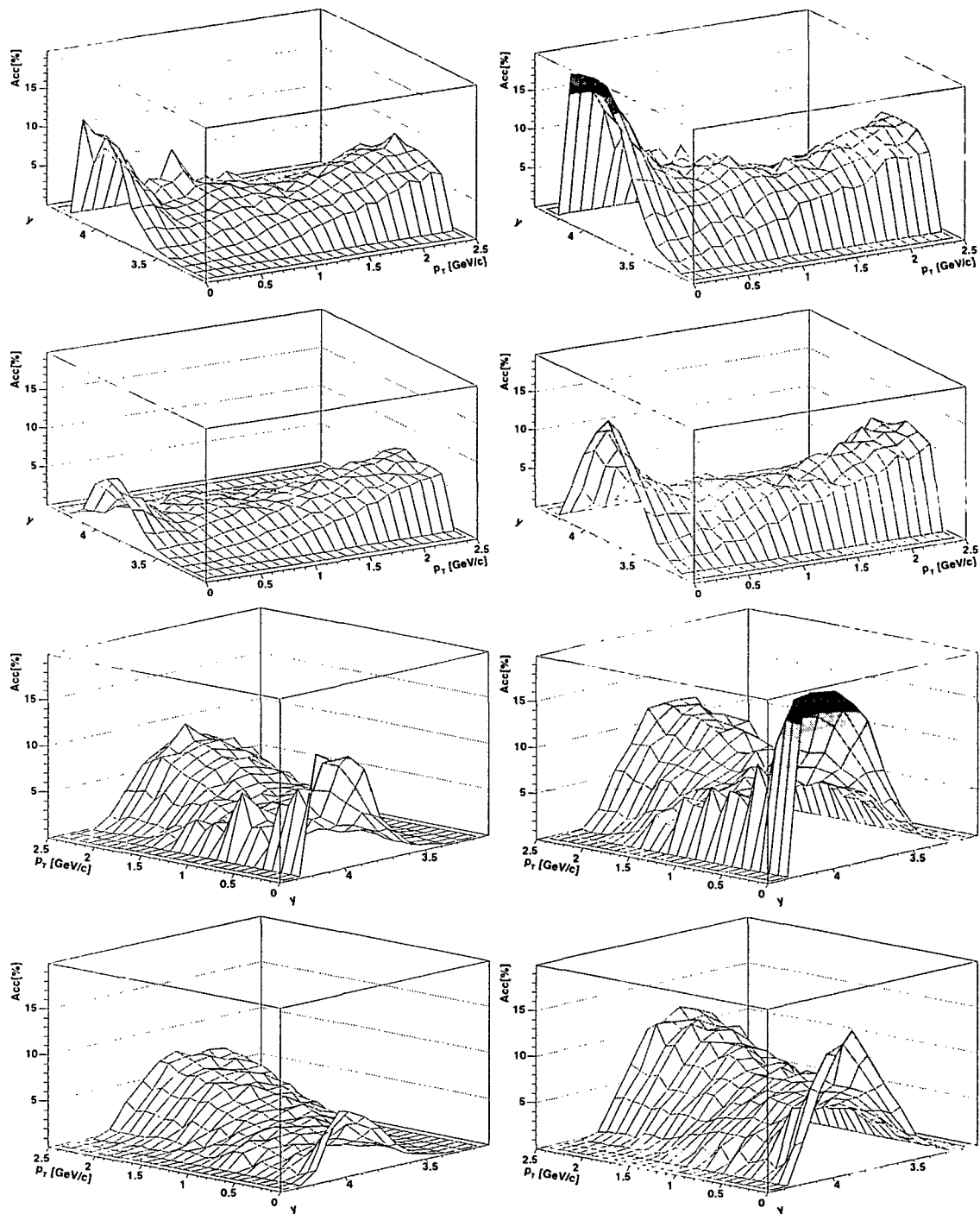


Figure 8.23: 2D acceptances in p_T and y_{lab} for opposite-sign dimuons within the mass windows 0.70–0.85 (left) and 0.9–1.1 GeV (right). The first and third rows show the acceptances in the Indium target; the second and fourth in the Lead target.

Bibliography

- [1] F. Karsch, *Lattice QCD at high temperature and density*, Lect. Notes Phys. 583, (2002) 209, hep-lat/0106019, and references therein.
- [2] *Study of prompt dimuon and charm production with proton and heavy ion beams at the SPS*, CERN/SPSC 2000-010, March 2000;
See <http://na60.cern.ch/www/experiment/spsc/> for updated information.
- [3] M.C. Abreu *et al.* (NA50 Coll.), *Evidence for Deconfinement of Quarks and Gluons from the J/ψ Suppression Pattern measured in Pb-Pb Collisions at the CERN-SPS*, Phys. Lett. **B477** (2000) 28;
L. Ramello *et al.* (NA50 Coll.), *Results on Leptonic Probes from NA50*, Nucl. Phys. **A715** (2003) 243c.
- [4] M.C. Abreu *et al.* (NA38 and NA50 Coll.), *Dimuon and Charm Production in Nucleus-Nucleus Collisions at the CERN SPS*, Eur. Phys. J. **C14** (2000) 443.
- [5] G. Agakichiev *et al.* (CERES Coll.), *Low-mass e^+e^- Pair Production in 158 A GeV Pb-Au Collisions at the CERN SPS, Its Dependence on Multiplicity and Transverse Momentum*, Phys. Lett. **B422** (1998) 405.
J.P. Wessels *et al.* (CERES Coll.), *Latest Results From CERES/NA45*, Nucl. Phys. **A715** (2003) 262c.
- [6] G. Agakichiev *et al.* (CERES Coll.), *Systematic Study of Low-Mass Electron Pair Production in p-Be and p-Au Collisions at 450 GeV/c*, Eur. Phys. J. **C4** (1998) 231.
- [7] T. Akesson *et al.* (HELIOS-1 Coll.), *Low-Mass Lepton-Pair Production in p-Be Collisions at 450 GeV/c*, Z. Phys. **C 68** (1995) 47.
- [8] M.C. Abreu *et al.* (NA38 and NA50 Coll.), *Low Mass Dimuon Production in Proton and Ion Induced Interactions at the SPS*, Eur. Phys. J. **C13** (2000) 69.
- [9] M. Brugger, S. Graham, *Simulation of the Radiation Field around the NA60 Experiment for Damage and Background Purposes*, NA60 Note 2002-4,
http://na60.cern.ch/www/experiment/notes/note_2002_4.pdf
- [10] C. Lourenço, *J/ψ , ψ' and Dimuon Production in p-A and S-U Collisions at 200 GeV/Nucleon*, PhD thesis, Instituto Superior Técnico, Lisbon, 1995,
<http://cern.ch/NA38/theses/carlosl.ps.gz>
- [11] L. Anderson *et al.* (NA10 Coll.), *A High-Resolution Spectrometer for the Study of High-Mass Muon Pairs Produced by Intense Hadron Beams*, Nucl. Instr. Meth. **223** (1984) 26.
- [12] V. Granata *et al.*, *Cryogenic Technology for Tracking Detectors*, Nucl. Instr. Meth. **A461** (2001) 197;

- RD39 Coll., *RD39 Status Report*, CERN/LHCC 2002-004, February 2002.
- [13] K. Borer *et al.* (RD39 Coll.), *Charge Collection Efficiency of Irradiated Silicon Detectors Operated at Cryogenic Temperatures*, Nucl. Instr. Meth. **A440** (2000) 5.
 - [14] K. Banicz, F. Bergsma, H. Wöhri, *The PT7 Magnet*, NA60 Note 2001-2, http://na60.cern.ch/www/experiment/notes/note_2001_2.pdf.
 - [15] R.L. Gluckstern, *Uncertainties in Track Momentum and Direction due to Multiple Scattering and Measurement Errors*, Nucl. Instr. Meth. **24** (1963) 381.
 - [16] K. Banicz *et al.*, *Status of the NA60 Silicon Pixel Telescope*, NA60 Note 2002-3, 11 March 2002, http://na60.cern.ch/www/experiment/notes/note_2003_3.pdf
M. Keil *et al.*, *Operation and Performance of the NA60 Silicon Pixel Telescope*, CERN-PH-EP-2004-021, to be published in Nucl. Instr. Meth. **A**.
 - [17] K. Wyllie *et al.*, *A Pixel Readout Chip for Tracking at ALICE and Particle Identification at LHCb*, Proceedings of the Fifth Workshop on Electronics for LHC Experiments, Snowmass, Colorado, 1999.
 - [18] J.J. van Hunen *et al.*, *Irradiation and SPS Beam Tests of the ALICE1LHCb Pixel Chip*, CERN-ALI-2001-015, 2001.
 - [19] R. Arnaldi *et al.*, *The NA60 Silicon Pixel Telescope*, Proceedings of the “12th International Workshop on Vertex Detection (VERTEX 2003)”, submitted to Nucl. Instr. Meth. **A**.
 - [20] K. Hagiwara *et al.* (PDG), *Review of Particle Physics*, Phys. Rev. **D66** (2002) 010001.
 - [21] W.R. Leo, *Techniques for Nuclear and Particle Physics Experiments*, 1994, 2nd edition, Springer-Verlag.
 - [22] G. Lutz, *Semiconductor Radiation Detectors*, 1999, Springer-Verlag.
 - [23] J. Buytaert *et al.*, *The NA60 Silicon Tracking Telescope for Proton Running*, NA60 Note 2001-5,
http://na60.cern.ch/www/experiment/notes/note_2001_5.pdf
 - [24] *SCTA128VG User Reference, Version 1.3*, February 2003,
<http://cern.ch/chipinfo>.
 - [25] E. Belau *et al.*, *Charge Collection in Silicon Strip Detectors*, Nucl. Instr. Meth. **214** (1983) 253.
 - [26] A. Bocardi, *Processing of Data from a Silicon Detector Readout-ASIC*, diploma thesis, Univ. of Pisa, 2001, <http://cern.ch/ep-div-ed/archive.htm>
 - [27] A. David, *The NA60 Microstrip Telescope Readout Electronics*, 4th International Workshop on Radiation Imaging Detectors, Amsterdam, The Netherlands, September 9–12, 2002,
http://na60.cern.ch/www/experiment/conferences/index_html
 - [28] http://www.caen.it/nuclear/power_family.php
 - [29] J. Grognez, C. Lourenço, H. Wöhri, *Cooling of the NA60 Microstrip Detector Modules*, NA60 Note 2001-7,
http://na60.cern.ch/www/experiment/notes/note_2001_7.pdf
 - [30] W.M.C. Sansen *et al.*, *Limits of Low Noise Performance of Detector Readout*

- Front Ends in CMOS Technology*, IEEE **37** (1990) 1375.
- [31] L.F. Figueira, *Noise on NA60 Microstrip Detectors*, NA60 Note 2002-5, http://na60.cern.ch/www/experiment/notes/note_2002_5.ps.Z
 - [32] V. Bartsch *et al.*, *Lorentz Angle Measurements in Silicon Detectors*, Nucl. Instr. Meth. **A478** (2002) 330.
 - [33] R. Shahoyan, *J/ψ and ψ' Production in 450 GeV pA Interactions and Its Dependence on the Rapidity and x_F* , PhD thesis, Instituto Superior Técnico, Lisbon, April 2001, <http://cern.ch/NA50/theses/ruben.ps.gz>
 - [34] J. Castor and J. Fargeix, private communications.
 - [35] G. Agakichiev *et al.* (CERES Coll.), *A New Robust Fitting Algorithm for Vertex Reconstruction in the CERES Experiment*, Nucl. Inst. Meth. **A 394** (1997) 225.
 - [36] P. Sonderegger, private communications.
 - [37] L.G. Landsberg, *Electromagnetic Decays of Light Mesons*, Phys. Rep. **128** (1985) 301.
 - [38] S. Eidelman *et al.* (PDG), *Review of Particle Physics*, Phys. Lett. **B592** (2004) 1.
 - [39] M. Diakonou *et al.*, *Inclusive High- p_T ω and η' Production at the ISR*, Phys. Lett. **B89** (1980) 432.
 - [40] R.J. Veenhof, *Low Mass Muon Pair Production in 450 GeV p-Be Collisions*, PhD thesis, Universiteit van Amsterdam.
 - [41] M. Bourquin and J.M. Gaillard, *A Simple Phenomenological Description of Hadron Production*, Nucl. Phys. **B114** (1976) 334.
 - [42] G. Agakichiev *et al.* (CERES-TAPS Coll.), *Neutral Meson Production in p-Be and p-Au Collisions at 450 GeV Beam Energy*, Eur. Phys. J. **C4** (1998) 249.
 - [43] S. Kartik, *Vector Meson Production in Meson-Nucleus and Proton-Nucleus Collisions at 530 GeV/c*, PhD thesis, Indiana University, 1991, FERMILAB-THESIS-1991-22.
 - [44] M. Binkley *et al.* (E358 Coll.), *Dimuon Production on Nuclear Targets*, Phys. Rev. Lett. **37** (1976) 571.
 - [45] A. Zieminski *et al.* (E672 and E706 Coll.), *Production of Vector Mesons in Hadron-A Interactions*, AIP Conf. Proc. **243** (1992) 891.
 - [46] R. Bailey *et al.* (NA11 Coll.), *A-Dependence Study of Inclusive ϕ Production*, Z. Phys. **22** (1984) 125.
 - [47] M. Symalla, *Produktion von ϕ -Mesonen in Inelastischen Proton-Kern-Wechselwirkungen*, PhD thesis, Universität Dortmund, 2004, DESY-THESIS-2004-020.
 - [48] W. M. Lee, *A Measurement of the Nuclear Dependence of J/ψ and ψ' Production*, PhD thesis, Georgia State University, 1999, FERMILAB-THESIS-1999-30.
 - [49] H. Frisch *et al.* (E258 Coll.), *Inclusive Production of Hadrons at high p_T in 200 and 300 GeV π^- -p and π^- -Nucleus Collisions*, Phys. Rev. **D27** (1983) 1001.
 - [50] G.B. Osborne, *Direct Photon and Neutral Meson Production at High Transverse Momentum by Negative 515 GeV/c Pions and 530 GeV/c Protons Incident upon Hydrogen, Beryllium and Copper Targets*, PhD thesis, University of Rochester, New York, 1996;

- J. Kühler, *An Analysis of π^0 Meson Production in Minimum Bias 515 GeV/c π^- Nuclear Collisions*, PhD thesis, University of Oklahoma, 1995.
- [51] S.V. Afanasiev *et al.* (NA49 Coll.), *Production of ϕ -mesons in pp, p-Pb and Central Pb-Pb Collisions at $E_{\text{beam}} = 158A$ GeV*, Phys. Lett. **B491** (2000) 59.
 - [52] T. Alber *et al.* (NA35 Coll.), *Charged Particle Production in Proton-, Deuteron-, Oxygen- and Sulphur-Nucleus Collisions at 200 GeV per Nucleon.*, Eur. Phys. J. **C2** (1998) 643.
 - [53] G.J. Gounaris and J.J. Sakurai, *Finite-width Corrections to the Vector-Meson-Dominance Prediction for $\rho \rightarrow e^+e^-$* , Phys. Rev. Lett. **21** (1968) 244.
 - [54] F. Klingel, N. Kaiser and W. Weise, *Effective Lagrangian Approach to Vector Mesons, their Structure and Decays.*, Z. Phys. **A356** (1996) 193.
 - [55] S. Damjanovic, A.De Falco and H. Wöhri, *The GENESIS $\mu^+\mu^-$ Generator in NA60*, NA60 internal Note in preparation.
 - [56] R. Hagedorn, *Statistical Thermodynamics of Strong Interactions at High-Energies*, Nuovo Cim. Suppl. **3** (1965) 147.
 - [57] J. Knoll and B. Frimann, private communications.
 - [58] N.M. Kroll and W. Wada, *Internal Pair Production Associated with the Emission of High-Energy Gamma Rays*, Phys. Rev. **98** (1955) 1355.
 - [59] J.C. Collins, D.E. Soper, *Angular Distribution of Dileptons in High-Energy Hadron Collisions*, Phys. Rev. **D16** (1977) 2219.
 - [60] T. Sjöstrand *et al.*, *PYTHIA 6.2, Physics and Manual*, Comp. Phys. Comm. **135** (2001) 238, hep-ph/0108264.
 - [61] A.D. Martin *et al.*, *Parton Distributions for Low Q^2* . Phys. Rev. **D51** (1995) 4756.
 - [62] W.J. Stirling and M.R. Whalley, *A Compilation of Drell-Yan Cross Sections*, J. Phys. G: Nucl. Part. Phys. **19** (1993) D1.
 - [63] P.L. McGaughey, *Recent Measurements of Quarkonia and Drell-Yan Production in Proton-Nucleus Collisions*, Nucl. Phys. **A610** (1996) 394c.
 - [64] J. Badier *et al.* (NA3 Coll.), *Experimental Cross-Section for Dimuon Production and the Drell-Yan Model*, Phys. Lett. **89B** (1979) 145.
 - [65] A.S. Ito *et al.* (E288 Coll.), *Measurement of the Continuum of Dimuons Produced in High-Energy Proton-Nucleus Collisions*, Phys. Rev. **D23** (1981) 604.
 - [66] B. Alessandro *et al.* (NA50 Coll.), *Charmonia and Drell-Yan Production in Proton-Nucleus Collisions at the CERN SPS*, Phys. Lett. **B553** (2003) 167.
 - [67] D.M. Alde *et al.* (E772 Coll.), *Nuclear Dependence of Dimuon Production at 800 GeV*, Phys. Rev. Lett. **64** (1990) 2479.
 - [68] J. Badier *et al.* (NA3 Coll.), *Drell-Yan Events from 400-GeV/c Protons: Determination of the K Factor in a Large Kinematical Domain*, Z. Phys. **C26** (1984) 489.
 - [69] H.K. Wöhri and C. Lourenço, *Heavy Flavour Production Cross-Sections from Fixed Target to Collider Energies*, J. Phys. G: Nucl. Part. Phys. **30** (2004) S315; H.K. Wöhri and C. Lourenço, *Heavy Flavour-Production Cross-Sections*, AIP Conf. Proc. **698** (2004) 704, ISBN 0-7354-0169-1.
 - [70] J. Pumplin *et al.*, *New Generation of Parton Distributions with Uncertainties*

- from Global QCD Analysis, JHEP 0207 (2002) 012.
- [71] M.J. Leitch *et al.* (E789 Coll.), *Nuclear Dependence of Neutral D Meson Production by 800 GeV/c Protons*, Phys. Rev. Lett. **72** (1994) 2542.
 - [72] M. Adamovich *et al.*, (WA82 Coll.), *Nuclear Dependence of Charm Production by a 340 GeV π^- Beam*, Phys. Lett. **B284** (1992) 453.
 - [73] G.A. Alves *et al.*, (E769 Coll.), *Atomic Mass Dependence of D^\pm and D^0 , \bar{D}^0 Production in 250 GeV π^\pm -Nucleon Interactions*, Phys. Rev. Lett. **70** (1993) 722.
 - [74] M. Adamovich *et al.* (WA92 Coll.), *Measurements of Charmed-Meson Production in Interactions between 350 GeV/c π^- Particles and Nuclei*, Nucl. Phys. **B495** (1997) 3.
 - [75] L. Apanasevich *et al.* (E706 Coll.), *Production of Charm Mesons at High Transverse Momentum in 515 GeV/c π^- -Nucleon Collisions*, Phys. Rev. **D56** (1997) 1391.
 - [76] K.J. Eskola *et al.*, *The Scale Dependent Nuclear Effects in Parton Distributions for Practical Applications*, Eur. Phys. J. **C9** (1999) 61.
 - [77] K. Werner, *Strings, Pomerons and the VENUS Model of Hadronic Interactions at Ultrarelativistic Energies*, Phys. Rep. **232** (1993) 87.
 - [78] M.C. Abreu *et al.* (NA50 Coll.), *Pseudorapidity Distributions of Charged Particles as a Function of Centrality in Pb-Pb Collisions at 158 and 40 GeV per Nucleon Incident Energy*, Phys. Lett. **B530** (2002) 33;
M.M. Aggarwal *et al.* (WA98 Coll.), *Event-by-event Fluctuations in Particle Multiplicities and Transverse Energy produced in 158A GeV Pb+Pb Collisions*, Phys. Rev. **C65** (2002) 054912.
 - [79] M.A. Mazzone *et al.* (HELIOS-3 Coll.), *Dimuon and Vector-Meson Production in p-W and S-W Interactions at 200 GeV/c per Nucleon*, Nucl. Phys. **A566** (1994) 95c.
 - [80] R. Shahoyan, *Combinatorial Background in the NA60 Muon Spectrometer*, NA60 Note 2004-3, http://na60.cern.ch/www/experiment/notes/2004/combin_210604.ps
 - [81] B. Alessandro *et al.* (NA50 Coll.), *ϕ Production in Pb-Pb Collisions at 158 GeV/c per Nucleon Incident Momentum*, Phys. Lett. **B555** (2003) 147; Phys. Lett. **B561** (2003) 294;
 - [82] M. Aguilar-Benitez *et al.* (NA27 Coll.), *Inclusive Particle Production in 400 GeV/c pp-Interactions*, Z. Phys. **C 50** (1991) 405.